

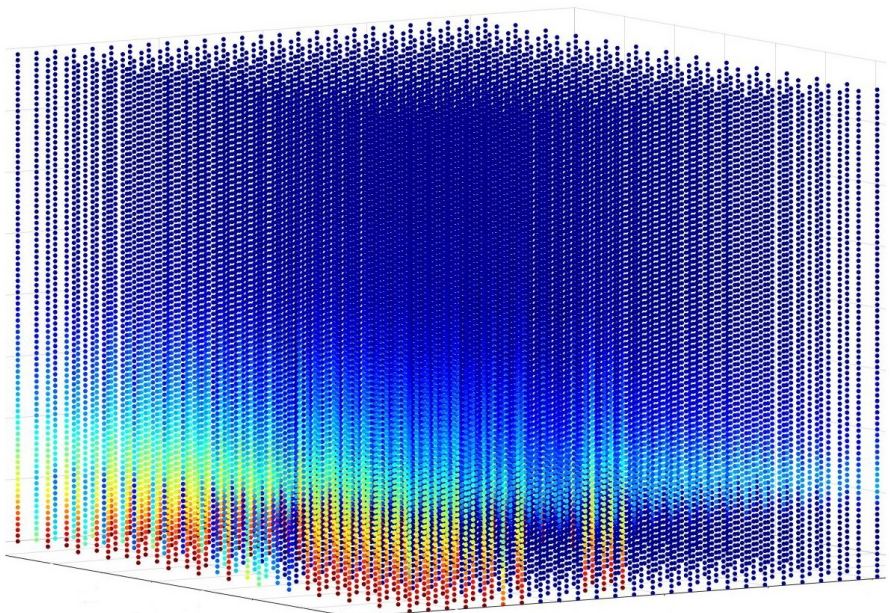
# Master's thesis

**NTNU**  
Norwegian University of Science and Technology  
Faculty of Information Technology and Electrical  
Engineering  
Department of Engineering Cybernetics

Monica Lapadatu

## Simulation Tool And Analysis For Hyperspectral Imaging Of Algal Blooms From Satellites

Master's thesis in MTTK  
Supervisor: Tor Arne Johansen  
June 2019

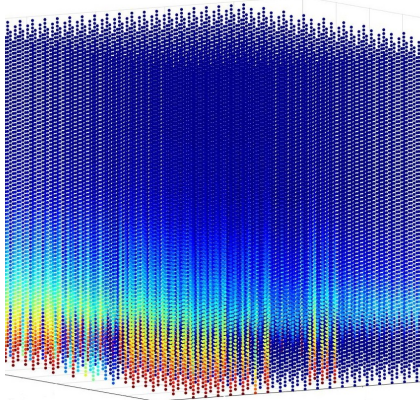


Norwegian University of  
Science and Technology



Monica Lapadatu

# Simulation Tool And Analysis For Hyperspectral Imaging Of Algal Blooms From Satellites



Master's thesis in MTTK  
Supervisor: Tor Arne Johansen  
June 2019

Norwegian University of Science and Technology  
Faculty of Information Technology and Electrical Engineering  
Department of Engineering Cybernetics



Norwegian University of  
Science and Technology



# **MSC Thesis Description**

**Name:** Monica Lapadatu

**Department:** Engineering Cybernetic

**Thesis title (English):** Simulation tool and analysis for hyperspectral imaging of algal blooms from satellites

**Thesis title (Norwegian):** Simuleringsverktøy og analyse for hyperspektral bildebehandling av algeoppblomstring fra satellitter

**Thesis Description:** The purpose of the thesis is to develop a simulation tool for the expected radiance from oceanic geophysical parameters through the atmosphere as perceived by a hyperspectral remote sensing satellite. This involves utilizing the coupled physical and ecological ocean model SINMOD. Furthermore, the effects of varying off-nadir viewing angles, solar zenith angles and the presence of water clouds on the resulting radiance should be analyzed, water leaving radiance lookup tables should be created and a temporal sensitivity of data acquisition analysis should be performed.

**Start date:** 2019 - 01 - 07

**Due date:** 2019 - 06 - 03

**Thesis performed at:** Department of Engineering Cybernetics, NTNU

**Supervisor:** Professor Tor Arne Johansen, Dept. of Eng. Cybernetics, NTNU



# Abstract

Motivated by the Center for Autonomous Marine Operations and Systems (NTNU-AMOS) at the Department of Engineering Cybernetics together with the Department of Electronic Systems plan to develop, launch and operate a series of small satellites specially made for maritime observation and surveillance, this thesis presents a tool created for simulating the expected radiance from oceanic geophysical parameters through the atmosphere as perceived by a hyperspectral remote sensing satellite. The effects of varying off-nadir viewing angles, solar zenith angles and the presence of water clouds on the resulting radiance has been analyzed. The developed simulation tool is based on the software for modelling light PlanarRad and the atmospheric radiative transfer model COART, and utilizes the coupled physical and ecological ocean model SINMOD. Water leaving radiance lookup tables were created in order to make the simulation more temporal efficient. Further, a temporal sensitivity of data acquisition analysis was performed.

The simulations revealed that the selection of viewing angles is of greater impact than the selection of solar angles with regard to the resulting water leaving radiance. The resulting water leaving radiance is larger than the resulting radiance at the ocean surface due to atmospheric effects regardless of solar or viewing angles. Further it is found that the viewing zenith angles affect the resulting radiance at the ocean surface due to atmospheric effects more than the viewing azimuth angles do, as the resulting radiance is roughly the same regardless of viewing azimuth angle. The selection of viewing azimuth angle is of less importance than the selection of viewing zenith angle with regard to the radiance at TOA due to atmospheric effects. In the same manner, the selection of viewing zenith angle is of greater importance than the selection of solar zenith angle. It was found that the utilized viewing and solar angles do not affect the resulting radiance with regard to wavelength dependent variations. The simulation further revealed that the locations resulting in high water leaving radiance values are spread out geographically, and more frequent at lower wavelengths. Further, the resulting radiance at TOA due to atmospheric effects is higher for all wavelengths when water clouds are present.

Simulated TOA radiance values coincide well with real world data. The water leaving radiance calculated by PlanarRad and the water leaving radiance calculated by the lookup table are identical. The temporal analysis concludes that the longer time period of observance, the greater the maximum water leaving radiance variation. The development of the

simulation tool has made the calculation and computation of water leaving radiance just above the ocean surface given chlorophyll a concentration, as well as of radiance at TOA due to atmospheric effects, less complicated and more rapid.

# Sammendrag

Motivert av senter for autonome marine operasjoner og systemer (NTNU-AMOS), på instituttet for teknisk kybernetikk, sammen med instituttet for elektroniske systemer sin plan om å utvikle, utskyte og operere en serie av små satellitter lagd spesielt for maritim observasjon og overvåking, presenterer denne avhandlingen et verktøy skapt for simulering av forventet radians fra maritime geofysiske parametere gjennom atmosfæren som oppfattet av en hyperspektral fjernanalyse satellitt. Effektene av å variere innsynsvinkel, sol vinkel og tilstedevarelsen av skyer på den resulterende radiansen har blitt analysert. Det utviklede simuleringsverktøyet er basert på lysmodellerings programvaren PlanarRad og den atmosfærisk strålings overføringsmodellen COART, og bruker den koblede fysiske og økologiske havmodellen SINMOD. Vannforlatende radians oppslagstabeller ble skapt for å gjøre simuleringen mer tidseffektiv. Videre ble en temporal sensitivitetsanalyse for data tilegnelse utført.

Simuleringene viste at valget av innsynsvinkel er viktigere enn valget av solvinkel med tanke på vannforlatende radians. Den resulterende vannforlatende radiansen er større enn den resulterende radiansen ved havoverflaten grunnet atmosfæriske effekter, uavhengig av sol- eller innsynsvinkel. Videre ble det funnet at senit innsynsvinkelen påvirker den resulterende radiansen ved havoverflaten grunnet atmosfæriske bidrag mer enn asimut innsynsvinkelen gjør, ettersom den resulterende radiansen er omtrent den samme uavhengig av asimut innsynsvinkel. Valget av asimut innsynsvinkel er ikke like betydelig som valget av senit innsynsvinkel når det gjelder radians ved toppen av atmosfæren grunnet atmosfæriske effekter. Likedan er valget av senit innsynsvinkel mer betydelig enn valget av senit solvinkel. Videre ble det funnet at valg av innsyns- og solvinkler ikke påvirker den resulterende radiansen med tanke på bølgelengdeavhengige variasjoner. Simuleringen avslørte videre at datapunktene som resulterer i høy vannforlatende radians er geografisk spredt og mer hyppigere ved lave bølgelengder. Den resulterende radiansen ved toppen av atmosfæren grunnet atmosfæriske effekter er høyere ved alle bølgelengder når vann-skyer er tilstede.

Simulerte radiansverdier ved toppen av atmosfæren sammenfaller godt med virkelighetsdata. Vannforlatende radians utregnet av PlanarRad og vannforlatende radians utregnet av oppslagstablene er identiske. Den temporale analysen konkluderer at jo lengre observeringstidsperiode, jo større maksimal vannforlatende radians variasjon. Utviklingen

av simuleringsverktøyet har gjort beregningen av vannforlatende radians rett over havoverflaten gitt klorofyll a konsentrasjon, i tillegg til radians ved toppen av atmosfæren grunnet atmosfæriske effekter, mindre komplisert og mer tidsbesparende.

# Preface

This thesis is submitted as part of the requirements for the Master of Science degree at the Norwegian University of Science and Technology. The work presented in this thesis has been carried out at the Department of Engineering Cybernetics, and is part of the HYPSO mission. The HYPSO mission is being carried out by The Center for Autonomous Marine Operations and Systems (NTNU-AMOS) at the Department of Engineering Cybernetics together with the Department of Electronic Systems. This thesis would not have been possible without the inputs and contributions from many of their associates.

This work was supported by the Norwegian Research Council through the Centre of Autonomous Marine Operations and Systems (grant no. 223254), the MASSIVE project (grant no. 270959).

I would like to thank Professor Tor Arne Johansen for his academic guidance. I would like to acknowledge the HYPSO team, especially Sivert Bakken and Evelyn Honoré-Livermore, who have provided information and guidance whenever necessary. Sivert Bakken has been of great help with guidance and planning throughout this thesis and the preliminary work. Mariusz Eivind Grøtte has also assisted with guidance and ideas for this thesis.

I am grateful for Sivert Bakken, Mariusz Eivind Grøtte, Morten Alver and Tor Arne Johansen for their assistance regarding the writing and editing of the conference paper that has been submitted based on this work. Furthermore, I am grateful to Ingrid Ellingsen, Morten Alver and SINTEF Ocean for assisting with the SINMOD simulation data. I am also grateful to Associate Professor Rune Storvold who assisted with guidance regarding the calculations of atmospheric effects in the preliminary work. Thanks to my family, friends and partner for their support throughout the years.

The information and dataset made available at the start of the thesis, and that has formed the basis for this thesis, is information regarding the HYPSO mission, provided by the HYPSO team, and the SINMOD dataset. This thesis is a continuation of the semester project report *Simulation of hyperspectral imaging of algal blooms from satellites* submitted to the Norwegian University of Science and Technology as part of the course TTK4550. This thesis overlaps with the preliminary work with regard to theory, background, and the

fact that the simulation tool created in the preliminary work has been utilized, with some alterations, for several analyses in this thesis. The simulation tool created in the preliminary work has been the basis for the creation of a more temporal efficient, user friendly and comprehensive simulation tool created in this thesis.

*Monica Lapadatu*

*Trondheim, June 2019*

# Table of Contents

<b>Abstract</b>	<b>i</b>
<b>Sammendrag</b>	<b>iii</b>
<b>Preface</b>	<b>v</b>
<b>Table of Contents</b>	<b>vii</b>
<b>List of Tables</b>	<b>xi</b>
<b>List of Figures</b>	<b>xiii</b>
<b>Nomenclature</b>	<b>xix</b>
<b>I Introduction and Background Material</b>	<b>1</b>
<b>1 Introduction</b>	<b>2</b>
1.1 Motivation . . . . .	2
1.2 Objective . . . . .	4
1.3 The HYPSO Mission . . . . .	6
1.4 Literature Review . . . . .	8
1.4.1 Simulating Geophysical Variables As A Hyperspectral Cube At TOA	8
1.4.2 Geophysical Variables To Spectral Signatures . . . . .	9
1.4.3 Calculating Absorption And Scattering . . . . .	10
1.4.4 Calculating Atmospheric Effects . . . . .	10
1.4.5 The Effect Of Different Viewing And Solar Angles . . . . .	11
1.4.6 Lookup Tables For Resulting Water Leaving Radiance . . . . .	12
1.4.7 Temporal Sensitivity . . . . .	12
1.5 Main Contributions . . . . .	12
<b>2 Theory</b>	<b>14</b>
2.1 Ocean Optics . . . . .	14
2.1.1 Light And Radiometry . . . . .	14
2.1.2 Optical Oceanography . . . . .	18
2.1.3 Absorption And Scattering . . . . .	22

2.1.4	Optical Constituents Of The Ocean . . . . .	23
2.1.5	Radiative Transfer Theory . . . . .	24
2.1.6	Remote Sensing . . . . .	27
2.1.7	Atmospheric Correction . . . . .	28
2.1.8	Surfaces . . . . .	32
2.2	Hyperspectral Remote Sensing . . . . .	35
<b>3</b>	<b>Background</b>	<b>39</b>
3.1	The SINMOD Data . . . . .	39
3.2	NetCDF Files . . . . .	41
3.2.1	MATLAB . . . . .	41
3.2.2	Panoply . . . . .	42
3.3	PlanarRad . . . . .	50
3.4	COART . . . . .	58
<b>II</b>	<b>Method</b>	<b>61</b>
<b>4</b>	<b>Combining The MATLAB Files From The Preliminary Work</b>	<b>63</b>
<b>5</b>	<b>Developing Batch Runs For PlanarRad</b>	<b>66</b>
5.1	Installation And Python Interface . . . . .	66
5.2	Inputs And Outputs . . . . .	67
<b>6</b>	<b>Examining Different Scenarios</b>	<b>70</b>
6.1	Viewing Zenith Angle Definitions . . . . .	71
6.2	Radiance Definitions . . . . .	71
6.3	Solar Azimuth Angle . . . . .	72
6.4	Solar Zenith Angle . . . . .	73
6.5	Viewing Angles . . . . .	73
6.5.1	Viewing Zenith Angle . . . . .	74
6.5.2	Viewing Azimuth Angle . . . . .	74
6.6	Clouds . . . . .	74
<b>7</b>	<b>Creating A Lookup Table For Simulation Of A Whole Scene</b>	<b>75</b>
7.1	The Creation Of A Lookup Table . . . . .	75
7.1.1	Panoply . . . . .	75
7.1.2	MATLAB And PlanarRad . . . . .	76
7.2	Simulating A Whole Scene . . . . .	77
<b>8</b>	<b>Temporal Sensitivity Of Data Acquisition Analysis</b>	<b>78</b>
<b>9</b>	<b>User Friendly Interface For The Software</b>	<b>80</b>
9.1	The Python Files . . . . .	80
9.2	The MATLAB Files . . . . .	80

<b>III Results</b>	<b>82</b>
<b>10 Combining The MATLAB Files From The Preliminary Work</b>	<b>83</b>
<b>11 Developing Batch Runs For PlanarRad</b>	<b>85</b>
11.1 The Difference Between Initial And Batched PlanarRad Version . . . . .	85
<b>12 Examining Different Scenarios</b>	<b>92</b>
12.1 Solar Azimuth Angle . . . . .	95
12.2 Solar Zenith Angle . . . . .	97
12.2.1 Radiance Due To Atmospheric Effects . . . . .	97
12.2.2 Water Leaving Radiance . . . . .	100
12.2.3 Solar Zenith Angles Summary . . . . .	100
12.3 Viewing Angles . . . . .	102
12.3.1 Radiance Due To Atmospheric Effects . . . . .	102
12.3.2 Water Leaving Radiance . . . . .	106
12.3.3 Viewing Angles Summary . . . . .	110
12.4 Clouds . . . . .	114
<b>13 Creating A Lookup Table For Simulation Of A Whole Scene</b>	<b>117</b>
13.1 The Creation Of A Lookup Table . . . . .	117
13.2 Simulating A Whole Scene . . . . .	124
<b>14 Temporal Sensitivity Of Data Acquisition Analysis</b>	<b>131</b>
14.1 Panoply . . . . .	131
14.2 The Lookup Table . . . . .	134
<b>15 User Friendly Interface For The Software</b>	<b>144</b>
<b>IV Discussion and Conclusions</b>	<b>145</b>
<b>16 Discussion</b>	<b>146</b>
16.1 Combining The MATLAB Files From The Preliminary Work . . . . .	146
16.2 Developing Batch Runs For PlanarRad . . . . .	146
16.3 Examining Different Scenarios . . . . .	146
16.3.1 Frequent Observations . . . . .	147
16.3.2 Solar Azimuth Angle . . . . .	148
16.3.3 Solar Zenith Angle . . . . .	149
16.3.4 Viewing Angles . . . . .	150
16.3.5 Clouds . . . . .	154
16.3.6 Comparison Between Several Presented Scenarios . . . . .	154
16.4 Creating A Lookup Table For Simulation Of A Whole Scene . . . . .	158
16.4.1 The Creation Of A Lookup Table . . . . .	158
16.4.2 Simulating A Whole Scene . . . . .	160
16.5 Temporal Sensitivity Of Data Acquisition Analysis . . . . .	161
16.5.1 Panoply . . . . .	161

16.5.2 The Lookup Table . . . . .	162
16.6 User Friendly Interface For The Software . . . . .	163
<b>17 Conclusion</b>	<b>164</b>
17.1 Combining The MATLAB Files From The Preliminary Work . . . . .	164
17.2 Developing Batch Runs For PlanarRad . . . . .	164
17.3 Examining Different Scenarios . . . . .	165
17.3.1 Solar Azimuth Angle . . . . .	165
17.3.2 Solar Zenith Angle . . . . .	165
17.3.3 Viewing Angles . . . . .	166
17.3.4 Clouds . . . . .	167
17.3.5 Comparison Between Several Presented Scenarios . . . . .	168
17.4 Creating A Lookup Table For Simulation Of A Whole Scene . . . . .	172
17.4.1 The Creation Of A Lookup Table . . . . .	172
17.4.2 Simulating A Whole Scene . . . . .	172
17.5 Temporal Sensitivity Of Data Acquisition Analysis . . . . .	172
17.5.1 Panoply . . . . .	172
17.5.2 The Lookup Table . . . . .	172
17.6 User Friendly Interface For The Software . . . . .	173
17.7 Summary . . . . .	173
17.7.1 Effects On The Various Types Of Radiance . . . . .	175
17.8 Further Work . . . . .	177
<b>V Appendices</b>	<b>178</b>
<b>A Documentation And User Guide For The RadPhyll Simulator</b>	<b>179</b>
A.1 Introduction . . . . .	179
A.2 The Input File . . . . .	181
A.3 The Manual Chl <sub>a</sub> Values Version . . . . .	182
A.4 The Manual Chl <sub>a</sub> Values Version With Specific Viewing Angles . . . . .	183
A.5 The Whole Scene Version . . . . .	185
A.6 The COART (Atmospheric Effects) Version . . . . .	189
A.7 The General Angle Variation Demonstration Version . . . . .	192
A.8 Expanding The RadPhyll Simulator . . . . .	195
<b>B The Lookup Tables</b>	<b>196</b>
<b>C Conference Paper</b>	<b>203</b>
<b>Bibliography</b>	<b>209</b>

# List of Tables

17.1 Summarized conclusion regarding solar and viewing angles' effect on the water leaving radiance at the ocean surface. . . . .	175
17.2 Summarized conclusion regarding solar and viewing angles' effect on the radiance at the ocean surface due to atmospheric effects. . . . .	176
17.3 Summarized conclusion regarding solar and viewing angles' effect on the radiance at TOA due to atmospheric effects. . . . .	176
A.1 Description of the available program versions. . . . .	180
A.2 Available input values to the variable <i>input_version</i> . . . . .	181
A.3 The manual chl_a values version input variables. . . . .	182
A.4 The manual chl_a values version with specific viewing angles input variables.	185
A.5 The whole scene version input variables. . . . .	187
A.6 The COART (atmospheric effects) version input variables. . . . .	190
A.7 The general angle variation demonstration version input variables. . . . .	193



# List of Figures

1.1	Oceanic remote sensing. Originally presented in Hirata. . . . .	3
1.2	Illustration of HYPSO's coordinated missions proposition. Created by the HYPSO team. . . . .	4
1.3	Overall HYPSO mission idea illustration. Created by the HYPSO team. . . . .	5
1.4	Thesis tasks. . . . .	6
1.5	Graphic illustration of the HYPSO mission. Created by the HYPSO team. . . . .	7
1.6	HSI V6. Originally presented in Sigernes et al. [2018] . . . . .	7
1.7	Summary table HYPSO mission. . . . .	8
2.1	Geometry associated with the definition of plane angle (panel a) and solid angle (panel b). Originally presented in Mobley. . . . .	15
2.2	Geometry used to obtain an element of solid angle in spherical coordinates. Originally presented in Mobley. . . . .	16
2.3	Radiance as a function of polar viewing direction and wavelength, in the azimuthal plane of the sun, in air just above the level sea surface. Originally presented in Mobley. . . . .	17
2.4	Radiance as a function of polar and azimuthal viewing directions, just above the sea surface and at wavelength 355 nm. Originally presented in Mobley. . . . .	18
2.5	Radiances in selected directions as a function of depth, at wavelength 555 nm. Originally presented in Mobley. . . . .	18
2.6	Geometry for defining the volume scattering function. Originally presented in Mobley. . . . .	20
2.7	Geometry used to define inherent optical properties. Originally presented in Mobley. . . . .	20
2.8	Illustration of light rays contributing to the irradiance reflectance $R$ . Originally presented in Mobley. . . . .	21
2.9	Illustration of light rays contributing to the remote-sensing reflectance $R_{rs}$ . Originally presented in Mobley. . . . .	22
2.10	Absorption spectrum for pure water on a semilog scale. (Data from various sources: Smith and Baker (1981); Sogandares Fry (1997); Pope and Fry (1997); Segelstein (1981)). Originally presented in Mobley. . . . .	24
2.11	Organization chart for optical oceanography. Originally presented in Mobley. . . . .	26
2.12	Illustration of terms used in validating measurements. Originally presented in Mobley. . . . .	28

2.13 Qualitative illustrations of the various processes contributing to the total TOA radiance. Originally presented in Mobley. . . . .	30
2.14 Example of the fraction of $L_t$ due to various processes. Originally presented in Mobley. . . . .	31
2.15 Left panel: Illustration of sun glint as seen from the TOA, which is described by a direct transmittance. Right panel: Illustration of water-leaving radiance as seen from the TOA, which is described by a diffuse transmittance. Originally presented in Mobley. . . . .	32
2.16 Illustration of incident, reflected, and transmitted rays for air- and water-incident light. Originally presented in Mobley. . . . .	33
2.17 Geometry for discussion of surface reflectance. Originally presented in Mobley. . . . .	33
2.18 Pushbroom HSI. Figure made by the HYPSO team. . . . .	36
2.19 Optical diagram of a spectrometer. Originally presented in Sigernes [2018].	36
3.1 Polar stereographic grids, presented as Polar Spatial Coverage Maps for the northern and southern hemispheres. Originally presented in (Snow and Center). . . . .	41
3.2 Panoply: Available options for which variables to present. . . . .	42
3.3 Panoply: Plotting on a map example. . . . .	43
3.4 Panoply: Example of the <i>Array</i> option. . . . .	44
3.5 Panoply: Zonal averages plotting example. . . . .	45
3.6 Panoply: Choices and menus available for the map-plotting. . . . .	46
3.7 Panoply: Several available maps. . . . .	47
3.8 Panoply: Several examples of available maps. . . . .	48
3.9 Panoply: Example of maneuvering towards the data of interest. . . . .	49
3.10 Panoply: Utilized values under the <i>map</i> option. . . . .	49
3.11 Panoply: Chl <sub>0.50</sub> m example, with utilized map variables. . . . .	50
3.12 PlanarRad: Band specification file example. . . . .	51
3.13 PlanarRad: Example of where to save the band specification file. . . . .	52
3.14 PlanarRad: Directional structure. Originally presented in Hedley [a]. . . . .	52
3.15 PlanarRad: Setting the diffuse irradiance ratio. . . . .	53
3.16 PlanarRad: Relative refractive indices. . . . .	54
3.17 PlanarRad: Medium properties. . . . .	54
3.18 PlanarRad: Depth options. . . . .	55
3.19 PlanarRad: Lower boundary properties. . . . .	55
3.20 PlanarRad: Illustration of the profile of downwelling planar irradiance in the slab of media. . . . .	56
3.21 PlanarRad: Hemispherical views. . . . .	57
3.22 PlanarRad: Location of the report file. . . . .	57
3.23 PlanarRad: Mean point theta. . . . .	58
3.24 Angle definitions in COART. Originally presented in Jin [a]. . . . .	60
5.1 Example of a batch report from PlanarRad, before the alterations. . . . .	68

6.1	Illustration of water leaving radiance, radiance due to atmospheric effects at the ocean surface and radiance due to atmospheric effects at TOA. Originally presented in Council . . . . .	72
7.1	Illustration of a satellite observing a scene. Originally presented in Honoré-Livermore. . . . .	77
10.1	HICO radiance. . . . .	84
11.1	Input radiance distribution specifications for the initial PlanarRad version.	87
11.2	Input interface properties specifications for the initial PlanarRad version. .	87
11.3	Input medium properties for the initial PlanarRad version. . . . .	88
11.4	Input depth options for the initial PlanarRad version. . . . .	88
11.5	Input lower boundary properties for the initial PlanarRad version. . . . .	88
11.6	The right hand side of the initial PlanarRad version. Figures, e.g. illustrating the depth profile, will be displayed here after a run. . . . .	89
11.7	Inputs for the batch PlanarRad version. . . . .	90
11.8	The right hand side of the batch PlanarRad version. . . . .	91
12.1	Top figure: Percentage water leaving radiance of the total reflected radiance at the ocean surface. Bottom figure: Percentage water leaving radiance of the total radiance at TOA. Originally presented in Lapadatu [2018]	94
12.2	Resulting water leaving radiance at the ocean surface while varying the solar azimuth angle. . . . .	95
12.3	Resulting water leaving radiance at the ocean surface while varying the solar azimuth angle (without the solar azimuth angle of 180°). . . . .	96
12.4	Resulting water leaving radiance at the ocean surface with the solar azimuth angles of 0° and 60°. . . . .	96
12.5	Resulting radiance at the ocean surface due to atmospheric effects, with various solar zenith angles. . . . .	97
12.6	Resulting radiance at TOA due to atmospheric effects, with various solar zenith angles. . . . .	98
12.7	Resulting radiance due to atmospheric effects with the solar zenith angle of 60°. . . . .	99
12.8	The visible spectrum. Originally posted in Smith [2000]. . . . .	99
12.9	Resulting water leaving radiance at the ocean surface for various solar zenith angles. . . . .	100
12.10	Radiance difference at the ocean surface for various solar zenith angles. Water leaving radiance at the ocean surface subtracted from the radiance due to atmospheric effects at the ocean surface. . . . .	101
12.11	Radiance difference at the ocean surface for various solar zenith angles. Water leaving radiance at the ocean surface subtracted from the radiance due to atmospheric effects at the ocean surface. . . . .	101
12.12	Resulting radiance at TOA due to atmospheric effects for various viewing zenith angles. . . . .	102

12.13	Resulting radiance due to atmospheric effects for the viewing zenith angle of 30° . . . . .	103
12.14	Resulting radiance at the ocean surface due to atmospheric effects for various viewing zenith angles. . . . .	103
12.15	Resulting radiance at the ocean surface due to atmospheric effects for various viewing azimuth angles. . . . .	104
12.16	Resulting radiance at TOA due to atmospheric effects for various viewing azimuth angles. . . . .	105
12.17	Resulting radiance due to atmospheric effects with the viewing azimuth angle 60°. . . . .	105
12.18	Resulting water leaving radiance at the ocean surface for various viewing zenith angles. . . . .	106
12.19	Water leaving radiance at the ocean surface with viewing zenith angle 120°. . . . .	107
12.20	Water leaving radiance at the ocean surface with viewing zenith angle 150°. . . . .	107
12.21	Water leaving radiance at the ocean surface with viewing zenith angle 170°. . . . .	108
12.22	Resulting water leaving radiance at the ocean surface for various viewing azimuth angles. . . . .	109
12.23	Resulting water leaving radiance at the ocean surface for three viewing azimuth angles. . . . .	109
12.24	Water leaving radiance at the ocean surface with viewing azimuth angle 0°. . . . .	110
12.25	Radiance difference at the ocean surface for the viewing zenith angle 30°. Water leaving radiance at the ocean surface subtracted from the radiance due to atmospheric effects at the ocean surface. . . . .	111
12.26	Radiance difference at the surface for various viewing azimuth angles. Water leaving radiance at the ocean surface subtracted from the radiance due to atmospheric effects at the ocean surface. . . . .	112
12.27	Radiance difference at the surface for various viewing azimuth angles. Water leaving radiance at the ocean surface subtracted from the radiance due to atmospheric effects at the ocean surface. . . . .	113
12.28	Radiance at the ocean surface due to atmospheric effects. With water clouds. . . . .	114
12.29	Radiance at TOA due to atmospheric effects. With water clouds. . . . .	115
12.30	Radiance due to atmospheric effects. With water clouds. . . . .	115
12.31	Radiance due to atmospheric effects. Comparison between water clouds and no clouds. . . . .	116
13.1	Chl.a in time frame 501 visualized in Panoply. . . . .	118
13.2	Water leaving radiance at the ocean surface for different SINMOD data points, i.e. for different chl_a values. . . . .	119
13.3	Absorption due to chl_a concentration values, and pure water, for varying SINMOD data points. . . . .	120
13.4	Absorption due to chl_a concentration values, and pure water, for varying SINMOD data points. A closer view. . . . .	121
13.5	Scattering due to chl_a concentration values for varying SINMOD data points. . . . .	122

13.6 Comparing the water leaving radiance calculated by the lookup table and the water leaving radiance calculated by PlanarRad for chl_a = $3.409 \times 10^{-1}$ mg chl_a m <sup>-3</sup> . . . . .	122
13.7 Scattering due to pure water for varying SINMOD data points. . . . .	123
13.8 Several results from the lookup table, presented together with several results from PlanarRad. . . . .	123
13.9 Illustration of water leaving radiance for a whole scene (view 1). . . . .	125
13.10 Illustration of water leaving radiance for a whole scene (view 2). . . . .	126
13.11 Illustration of water leaving radiance for a whole scene (view 3). . . . .	127
13.12 Illustration of water leaving radiance for a whole scene (view 4). . . . .	128
13.13 Illustration of water leaving radiance for a whole scene (view 5). . . . .	129
13.14 Illustration of water leaving radiance for a whole scene (view 6). . . . .	130
14.1 Illustrations from Panoply at time stamp 160, 161 and 162. . . . .	132
14.2 Illustrations from Panoply at time stamp 162, 167 and 172. . . . .	133
14.3 Water leaving radiance [sr <sup>-1</sup> ] from time frames 160, 161 and 162, respectively. . . . .	135
14.4 Water leaving radiance [sr <sup>-1</sup> ] from time frame 162, 167 and 172, respectively. . . . .	136
14.5 Water leaving radiance difference [sr <sup>-1</sup> ] from time frame 160 to time frame 161. . . . .	137
14.6 Water leaving radiance difference [sr <sup>-1</sup> ] from time frame 162 to time frame 172. . . . .	138
14.7 Water leaving radiance [sr <sup>-1</sup> ] percentage change between the time frame 160 and the time frame 161. . . . .	139
14.8 Water leaving radiance [sr <sup>-1</sup> ] percentage change between the time frame 162 and the time frame 172. . . . .	140
14.9 Maximum water leaving radiance change over 1 hour. . . . .	141
14.10 Maximum water leaving radiance change over 5 hours. . . . .	142
14.11 Maximum water leaving radiance change over 10 hours. . . . .	142
14.12 Maximum water leaving radiance change over 1 hour, 5 hours and 10 hours.	143
16.1 Absorption by water. . . . .	161
17.1 Illustration of a Lambertian surface. Originally presented in Mobley. . . . .	169
17.2 Illustration of the observation distance being correlated to the viewing zenith angle. . . . .	169
A.1 Illustration of version selection in the program input file. . . . .	182
A.2 The manual chl_a values section in the program input file. . . . .	183
A.3 The manual chl_a values version of the program output example. . . . .	183
A.4 Illustration of the section of the input file of the program regarding the manual chl_a values version with specific viewing angles. . . . .	185
A.5 The section of the program input file regarding the whole scene version. .	188
A.6 The input file, with regard to The COART (atmospheric effects) version. .	191

A.7 Some of the inputs from the input file of the program regarding the general angle variation demonstration version. . . . .	194
B.1 Lookup table for the viewing azimuth angle of 0°. . . . .	197
B.2 Lookup table for the viewing azimuth angle of 30°. . . . .	197
B.3 Lookup table for the viewing azimuth angle of 60°. . . . .	198
B.4 Lookup table for the viewing azimuth angle of 90°. . . . .	198
B.5 Lookup table for the viewing azimuth angle of 120°. . . . .	199
B.6 Lookup table for the viewing azimuth angle of 150°. . . . .	199
B.7 Lookup table for the viewing azimuth angle of 180°. . . . .	200
B.8 Lookup table for the viewing zenith angle of 100°. . . . .	200
B.9 Lookup table for the viewing zenith angle of 120°. . . . .	201
B.10 Lookup table for the viewing zenith angle of 140°. . . . .	201
B.11 Lookup table for the viewing zenith angle of 160°. . . . .	202



# Nomenclature

## Ocean Optics

*Absorption* Any process where radiant energy is converted to non-radiant energy (Mobley). Absorption results in the disappearance of photons.

*Albedo of a surface* The ratio of the plane irradiance leaving a surface to the plane irradiance incident onto it. Both are measured just above the surface (Mobley).

*Apparent optical property (AOP)* An optical quantity that depends weakly on the external environment, and strongly on the water absorption and scattering properties (IOPs) (Mobley).

*Bidirectional reflection distribution function (BRDF)* The ratio of the radiance reflected by a surface into a specific direction to the collimated irradiance incident from a particular direction onto the surface (Mobley). Units: [ $\text{sr}^{-1}$ ].

*Chlorophyll* Chemical compounds occurring in plants that enable radiant energy to be converted to chemical energy in the process of photosynthesis (Mobley).

*Inherent optical property (IOP)* In optical oceanography, any optical quantity that depends only on the properties of the water and is independent of the ambient light field (Mobley).

$L_{\text{atm}}$  Atmospheric scattering.

$L_{\text{surf}}^{\text{TOA}}$  Sun and sky radiance reflected back upward by the ocean surface (Mobley).

$L_t$  Total radiance measured at TOA.

$L_w^{\text{TOA}}$  Water leaving radiance that reaches TOA

*Lambertian surface* A surface that reflected or emits light at each point of the surface in an angular pattern that is proportional to the cosine of the angle to normal to the surface (Mobley).

*Mie scattering theory* An exact solution of Maxwell's equations that describes the scattering of electromagnetic waves by homogeneous spheres of any size (Mobley). Utilizing the theory requires knowledge of the complex index of refraction of the sphere relative to the surrounding medium and the ratio of the sphere's circumference to the wavelength of light in the medium. It is a mathematical model for scattering under certain conditions, not a physical scattering process (Mobley).

*Optical oceanography* The subdiscipline of oceanography concerned with the propagation of radiant energy through ocean water and with the interactions of light with ocean water constituents (Mobley). The wavelengths of interest are usually between 300 nm and 1000 nm.

*Phase function* The ratio of the volume scattering function [ $\text{m}^{-1} \text{ sr}^{-1}$ ] to the scattering coefficient [ $\text{m}^{-1}$ ] (Mobley). Units: [ $\text{sr}^{-1}$ ]

*Phytoplankton* Small, i.e. linear sizes from less than 1 to tens of  $\mu\text{m}$ , usually single-cell, aerobic, photosynthetic, oxygenic organisms (Mobley).

*Radiance* The radiant power in a beam per unit solid angle, per unit area perpendicular to the beam, per unit wavelength interval (Mobley). Units: [ $\text{W m}^{-2} \text{ sr}^{-1} \text{ nm}^{-1}$ ].

*Radiometer* An instrument that measures radiant energy.

*Radiometry* The science of the measurement of radiant energy.

*Rayleigh scattering theory* A mathematical model that describes elastic scattering by very small, i.e. relative to the wavelength of the light being scattered, particles (Mobley). It is characterized by a volume scattering function that depends inversely with the fourth power of the wavelength and has forward-backward directional symmetry (Mobley). It is a mathematical model for scattering under certain conditions, not a physical scattering process (Mobley).

*Reflectance* Refers to any measures of how much light leaves a region normalized by how much light is incident onto the region (Mobley).

*Refraction* The change in direction of a light beam when crossing an interface between two media that have different real indices of refraction (Mobley).

*Scattering coefficient* The scatterance per unit distance of photon travel in a medium, i.e., the limit of the ratio of the spectral scatterance to the distance of photon travel as that distance becomes vanishingly small (Mobley). Units: [ $\text{m}^{-1}$ ]

*Zooplankton* Animal forms of plankton.

## **Remote Sensing**

*Hyperspectral imaging* Collects and processes information from across the electromagnetic spectrum, with a goal of obtaining the spectrum for each pixel in the image of a scene. The purpose is to find objects, identify materials, or detect processes (Chang [2003]).

*Nadir angle* The angle between a given direction and the downward vertical (nadir) direction (Mobley).

$R_{rs}$  Spectral remote sensing reflectance

*Remote sensing reflectance* The ratio of the water leaving radiance [ $\text{W m}^{-2} \text{ sr}^{-1} \text{ nm}^{-1}$ ] in air to the downward plane irradiance [ $\text{W m}^{-2} \text{ nm}^{-1}$ ] incident onto the sea surface, with both measured just above the sea surface (Mobley). The remote sensing reflectance is an AOP. It is the fundamental optical quantity used in ocean color remote sensing (Mobley). Units: [ $\text{sr}^{-1}$ ].

*Water leaving radiance* Radiance leaving the ocean surface, due to e.g. chl<sub>a</sub> concentration in the water and reflected radiance due to atmospheric effects.

## Utilized Software And Datasets

*COART* An atmospheric radiative transfer model.

*Panoply* A netCDF, HDF and GRIB Data Viewer.

*PlanarRad* Software for modelling light in natural waters or other homogenous scattering and absorbing media (Hedley [b]).

*SINMOD* Dataset consisting of approximately one month of recorded data with a temporal resolution of 1 hour. The variables included are temperature [ $^{\circ}\text{C}$ ], chlorophyll in the surface layer [ $\text{mg chl}_a \text{ m}^{-3}$ ], chlorophyll integrated over 0 - 50 meter per square metre [ $\text{mg chl}_a \text{ m}^{-2}$ ], and the concentration of diatoms [ $\text{mmol N m}^{-3}$ ] and flagellates [ $\text{mmol N m}^{-3}$ ] in the surface layer (Alver [2018]).

## Abbreviations

*AOP* Apparent Optical Property

*AOT* Aerosol Optical Thickness

*BRDF* The Bidirectional Reflectance Distribution Function

*CDISORT* Coupled Discrete Ordinate Radiative Transfer

*CDOM* Colored Dissolved Organic Matter

*Chl<sub>a</sub>* Chlorophyll a

*COART* Coupled Ocean and Atmosphere Radiative Transfer

*CPU* Central Processing Unit

*DISORT* Discrete Ordinate Radiative Transfer

*ESA* The European Space Agency

*GRIB* GRIdded Binary (or General Regularly-distributed Information in Binary form)

*GUI* Graphical User Interface

*HDF* Hierarchical Data Format

*HSI* Hyperspectral Imager

*HSI V6* The Hyperspectral Imager V6

*HYPSO* Hyperspectral smallsat for ocean observation

*IOP* Inherent Optical Property

*MERIS* The MEdium Resolution Imaging Spectrometer

*MODIS* Moderate Resolution Imaging Spectroradiometer

*MODTRAN* MODerate resolution atmospheric TRANsmission

*NASA* The National Aeronautics and Space Administration

*NetCDF* Network Common Data Form

*NTNU* The Norwegian University of Science and Technology

*NTNU – AMOS* The Center for Autonomous Marine Operations and Systems

*RGB* Red, Green and Blue

*SDR* Software Defined Radio

*TOA* Top Of The Atmosphere

*VSF* The Volume Scattering Function



## **Part I**

# **Introduction and Background Material**

# Introduction

Sections 1.1, 1.2, 1.3, 1.4.1, 1.4.2, 1.4.3, 1.4.4 and 1.5 are heavily based on the preliminary work, i.e. the project thesis created for the course *TTK4550 - Engineering Cybernetics, Specialization Project*, which can be found here [Lapadatu [2018]].

## 1.1 Motivation

The Center for Autonomous Marine Operations and Systems (NTNU-AMOS) at the Department of Engineering Cybernetics together with the Department of Electronic Systems are planning to develop, launch and operate a series of small satellites specially made for maritime observation and surveillance (Johansen). In such operations, the tasks of the small satellites will be tightly integrated with the tasks of unmanned aerial, surface and underwater vehicles that will operate as an autonomous coordinated network of robots that are cooperating in order to research the overall mission objectives. Ocean color remote sensing satellites, such as for this mission, are currently being used for maritime observation and surveillance, e.g. monitoring of phytoplankton, zooplankton, river plumes, oil spills, water sediments and ice. Past and present operational satellites are mainly concerned with multispectral data, but hyperspectral sensors are being considered more frequently for upcoming missions (Ibrahim et al. [2018], Ortiz et al. [2019]). By utilizing hyperspectral sensors it is expected to enhance the capabilities to detect targets of interest and estimate their characteristics (Guelman and Ortenberg [2009]). Experimental space-based hyperspectral sensors include HICO and Hyperion (Keith et al. [2014], Soukup et al. [2016]).

Examples of applications of ocean color data include mapping of chlorophyll concentrations, measurement of inherent optical properties (IOP's), determination of phytoplankton characteristics, studies of ocean carbon cycling, monitoring of ecosystem changes re-

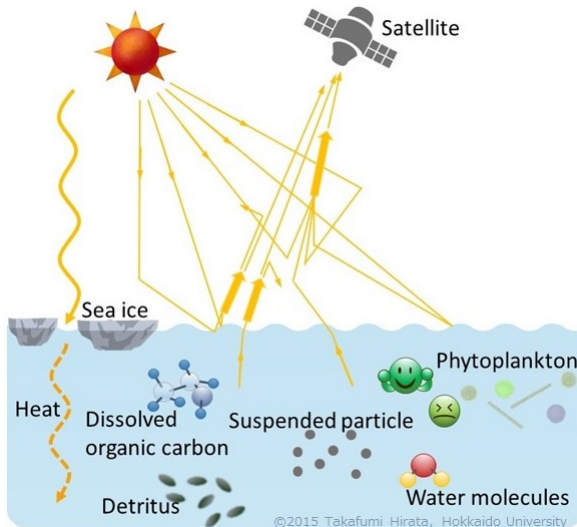


**Figure 1.1:** Oceanic remote sensing. Originally presented in Hirata.

sulting from climate change, fisheries management, mapping of coral reefs, mapping of sea grass beds, monitoring of water quality for recreation, and detection of harmful algal blooms and pollution events. These applications are fundamental to understanding and monitoring the global ecosystem, and are therefore of great interest (Mobley). Figure 1.1 illustrates oceanic remote sensing.

The motivation and objective of the overall mission is to provide data for oceanographers and to perform on-demand and coordinated missions with unmanned vehicles. The actors who will benefit from the collected data are all who are interested in ocean color, whether it is due to the interest in algae, cyanobacteria/toxins, river plumes, oil spill or other phenomena (Honoré-Livermore). Examples are the Norwegian fish farms, actors interested in global climate change and actors interested in micro plastics (Honoré-Livermore).

An example illustrating the mission's motivation is fish farms. Currently, fish farms get their research data from huge satellites, such as Sentinel, lengthy and costly planned missions with boats and personnel, and manned missions performed by drones or airplanes (Honoré-Livermore). It is therefore hard to influence where and when the data can be gathered. Solving this difficulty is part of the mission's motivation (Honoré-Livermore). See figure 1.2 for an illustration of coordinated missions.

This thesis performs several analysis' and examinations regarding the observed radiance, as well as develops a simulation process that is more user friendly and time efficient than current non commercial methods. The motivation for this thesis is to provide information regarding the effects of various solar angles, various viewing angles and various weather on the resulting radiance, as well as information regarding the temporal sensitivity of data

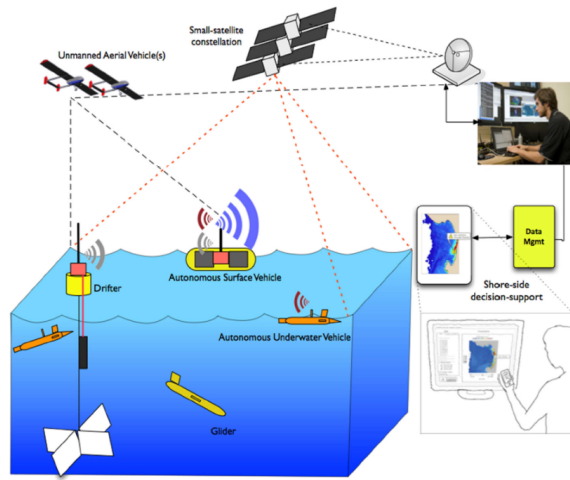


**Figure 1.2:** Illustration of HYPSO’s coordinated missions proposition. Created by the HYPSO team.

acquisition, to the overall mission. Providing the possibility for the team working with the overall mission to perform more simulations, if desired, time efficiently without needing assistance, is also a motivation for this thesis.

## 1.2 Objective

Two payloads are foreseen in the first phase of the mission. One payload is for communication based on Software Defined Radio (SDR), while the other will be a hyper-spectral imager (HSI) (Johansen). This thesis will regard the HSI segment of the mission.

The long term objective of the mission is to develop an ocean observation system that can exploit the complementary capabilities of small satellites, unmanned aerial vehicles, unmanned surface vehicles and autonomous underwater vehicles carrying different sensors to observe the same spatially distributed phenomena (Johansen). These robotic agents have different positions, mobility and abilities to carry sensors and communicate. By a cooperative approach the fast space and aerial vehicles can guide the slower surface and underwater vehicles to locations of interest, where they can gather more detailed information (Johansen). Furthermore, another objective of the overall mission is to simulate what the different sensors on board of the different robot agents record, let the agents share obtained knowledge and update models (a)synchronous (Berget and Fossum), as illustrated in figure 1.3.

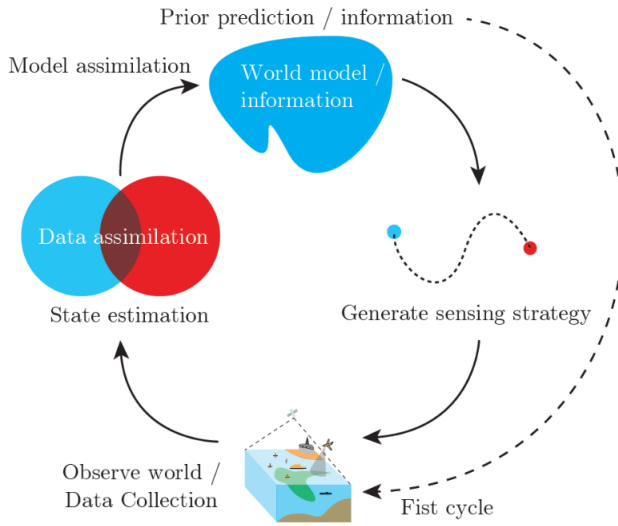


**Figure 1.3:** Overall HYPSSO mission idea illustration. Created by the HYPSSO team.

This thesis focuses on simulation and analysis of hyperspectral imaging of algal blooms from satellites. More precisely, it focuses on the simulation of TOA radiance as perceived by a hyperspectral sensor in Low Earth Orbit, without taking the sensor characteristics such as the optical efficiency into account, as well as simulation of water leaving radiance at the ocean surface. The objective is to analyze different scenarios with varying off-nadir viewing angles, solar zenith angles and the presence of water clouds. As an alternative to existing remote sensing tools, e.g. SeaDas, SNAP and Ocean Virtual Laboratory, that use real satellite data, the simulation tool uses output data from the coupled physical and ecological ocean model SINMOD to calculate the resulting spectral response in radiance. Further, estimated atmospheric effects at TOA are added. The result is the hyperspectral image cube sensed at TOA. The simulation is performed by revising, upgrading and utilizing the simulation created in the preliminary work. Moreover, the objective included developing a temporal efficient software for such simulation. Furthermore, the objective of this thesis includes performing a temporal sensitivity of data acquisition analysis.

Figure 1.4 illustrates the procedure for this thesis. The figure demonstrates that the first task regards combining the MATLAB files from the preliminary work. The second task regards developing batch runs for the software PlanarRad. The third task regards examining different scenarios by utilizing the batched PlanarRad. The fourth task regards creating lookup tables, in order to be able to calculate water leaving radiance more time efficient. The fifth task regards performing a temporal sensitivity of data acquisition analysis. Figure 1.4 illustrates that the final task regards developing a user friendly program for simulating geophysical variables as water leaving radiance or radiance at TOA.

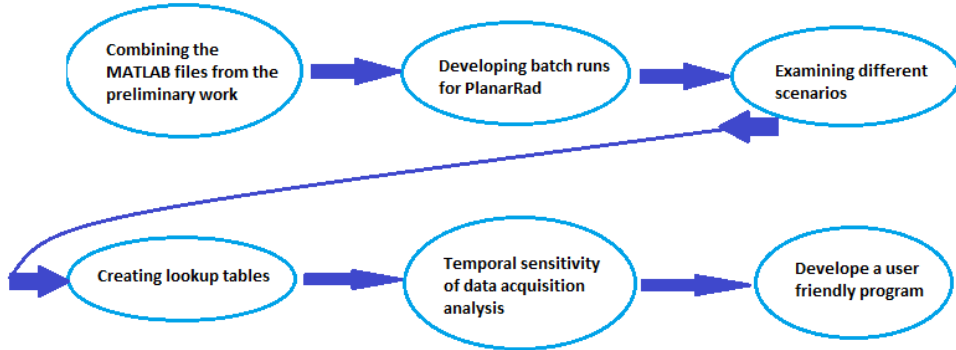


**Figure 1.4:** Thesis tasks.

### 1.3 The HYPSO Mission

The Norwegian University of Science and Technology's (NTNU's) hyper-spectral smallsat for ocean observation (HYPSO) mission will be the execution of the long-term-overall-objective mentioned in section 1.2. The mission will provide and support ocean color mapping and monitoring along the Norwegian coast through a HSI payload, autonomously onboard-processed data, on-demand autonomous communications and a concert of robotic agents (Grøtte). Figure 1.5 illustrates the HYPSO mission.

Essential characteristics, regarding the orbit, the payload, the S/C Bus, the autonomy and the communications, of the HYPSO mission are presented in figure 1.7. The Hyperspectral Imager V6 (HSI V6), based on [Sigernes et al. [2018]], will be utilized as part of the hyperspectral payload of the HYPSO SmallSat (Grøtte). The characteristics of the HSI V6 are therefore relevant to this thesis. The simulation is based on the HSI V6. The HSI V6 has a maximum frame rate of 39.56 FPS, spectral range of 400 - 800 nm, and spectral resolution of 5 nm (Grøtte).

A picture of the HSI V6 is presented in figure 1.6. The numbers presented in the figure represent the following: 1. front lens, 2. CP12 cage plate, 3. collimator lens, 4. 3D printed grating holder, 5. camera lens, 6. CP03/M cage plate, 7. steel rods, 8. 3D printed camera mount insert, and 9. iDS CMOS camera head (Grøtte). The optical design of the HSI will utilize the pushbroom technique, which will be shortly explained in section 2.2.

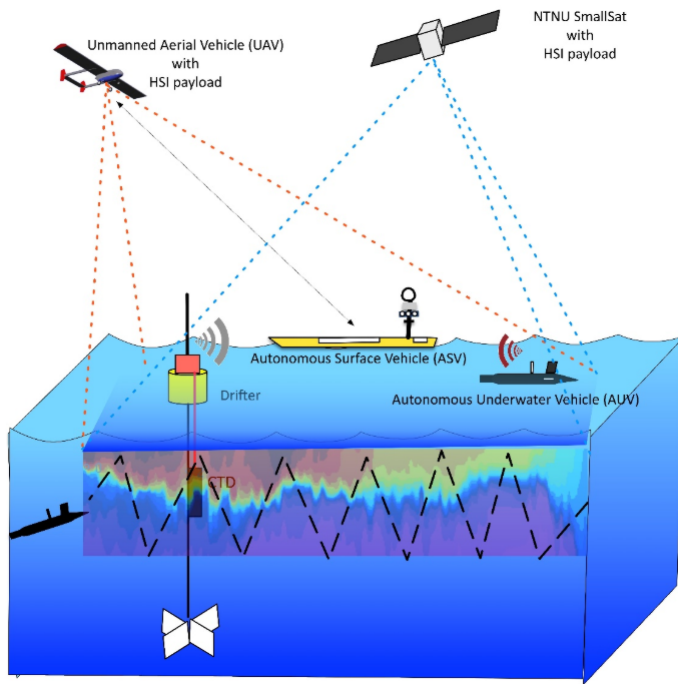


**Figure 1.5:** Graphic illustration of the HYPSO mission. Created by the HYPSO team.

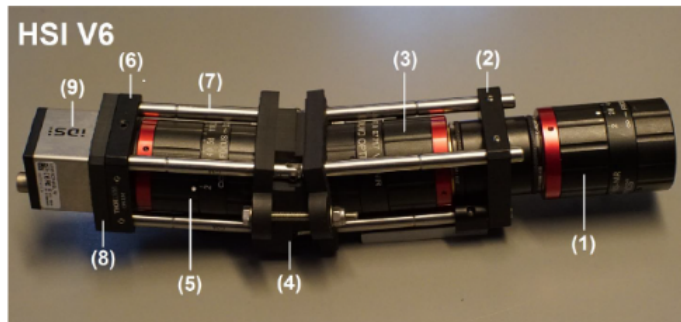


**Figure 1.6:** HSI V6. Originally presented in Sigernes et al. [2018]

General	Definition
Objective Subjects	Ocean color Coast of Norway, Greenland, Svalbard, Barents Sea, Baltic, Chiloe, Cape Point, Antarctica, Monterey Bay, Azores
Target Location (baseline)	Lat: 63.867608 °, Lon: 8.663644 ° (Frøya, Norway)
Target area	70 km × 70 km <sup>2</sup>
Orbit	
Type	Syn-Synchronous
Altitude	500 km
Passes over target	3
Launch	10:00 AM LTAN in Q1 2020
Payload	
Type	Pushbroom Hyperspectral Imager
Spectral Range	400-800 nm
Spectral Resolution	5 nm
Operating Modes	High Res; Medium Res
Spatial resolution	560 m
Swath Width	70.32 km
Ground Sampling Distance	38 m
Max SNR	269
S/C Bus	
Size	6U
Energy	94 Wh
Mass	5.7 kg
Autonomy	
Data Processing	On-board compression, geometric, radiometric, spectral and spatial processing
Downlinked Data Products	Level 1A and Operational data (spectral+map coordinates)
Autonomy	Uplink and downlink to Ground Station, uploaded scheduling and tasks determined by mission control
Communications	
Bands	S-band (uplink/downlink), UHF (back-up and commissioning)
Ground Stations	NTNU Trondheim, KSAT Svalbard & Tromsø

**Figure 1.7:** Summary table HYPSO mission.

## 1.4 Literature Review

Section 1.4 presents literature review regarding the simulation of geophysical variables as a hyperspectral cube at TOA, the process of calculating spectral signatures from geophysical variables, the calculation of absorption and scattering, the calculation of atmospheric effects, the effect of different viewing and solar angles on the resulting radiance, lookup tables for resulting water leaving radiance and temporal time sensitivity of the resulting water leaving radiance with respect to chlorophyll a (chl\_a) concentration.

### 1.4.1 Simulating Geophysical Variables As A Hyperspectral Cube At TOA

Regarding the process of simulating geophysical variables in the ocean as a hyperspectral cube observed at TOA, there are no programs, procedures or models available. There are however several models, algorithms and simulations for starting with a hyperspectral image and estimating the amount of geophysical variables, such as chl\_a concentration.

Procedures for performing the process of interest do exist. However, they involve combining several, more specified, models. The common way to simulate geophysical variables in the ocean as hyperspectral radiance received by a satellite sensor is to combine

the underwater radiative transfer code HydroLight and the atmospheric code MODTRAN (Mobley). Both are widely used for radiative transfer calculations in their respective geo-physical domains (Mobley). The combination of the two software can compute the in-water and atmospheric radiances, both just above the ocean surface and at TOA (Mobley). The MODTRAN atmospheric code can be utilized to propagate sunlight from TOA to the ocean surface. Then, this atmospheric radiance incident onto the sea surface can be used to initialize the HydroLight in-water code (Mobley). HydroLight can then transmit the radiance through the sea surface, compute its interaction with the water constituents, and return the water-leaving radiance back to MODTRAN. MODTRAN can then propagate the water-leaving radiance, plus the glint radiance and atmospheric path radiance, to the sensor (Mobley). This way one can simulate the sunlight going from the sun, to the ocean surface, through the water and back up to a sensor on board a satellite. However, both HydroLight and MODTRAN are commercial software, and they are not designed to work together, i.e. the interactions and data transference between the two must be developed by the user.

The combination of HydroLight and MODTRAN will not be utilized in this thesis, as one of the objectives was to develop a single complete, open source, model to simulate the discussed process.

Other existing remote sensing tools include SeaDAS, SNAP and Ocean Virtual Laboratory. SeaDAS is a software package for the processing, display, analysis, and quality control of ocean color data provided by the National Aeronautics and Space Administration (NASA) (Feldman). SNAP is a toolbox for Earth Observation processing provided by the European Space Agency (ESA) (ESA [a]). The Ocean Virtual Laboratory is a virtual platform that displays various Earth Observation dataset with a different multifacet point of view (ESA [b]). The Ocean Virtual Laboratory is provided by ESA. These remote sensing tools utilize real satellite data, and are thus not able to simulate the desired radiance given specific geophysical variables (Feldman) (ESA [a]) (ESA [b]).

Summarizing, the available option is expensive, as well as not developed as one whole system. The process provided in this thesis is a non commercial option where the only required inputs are the geophysical variables one wishes to simulate and the properties of the mediums of interest, e.g. water, surface and atmospheric properties. That is, the simulation tool is an alternative to existing remote sensing tools, that uses output data from the coupled physical and ecological ocean model SINMOD to calculate the resulting spectral response in radiance.

## 1.4.2 Geophysical Variables To Spectral Signatures

As presented in section 1.4.1, the common way to calculate spectral radiance from geo-physical variables is through HydroLight. The issues with utilizing HydroLight are stated in the same section. An open source alternative is to utilize a program titled PlanarRad (Hedley [b]).

The difficulties with PlanarRad is that it is set up to calculate the light field and reflectances at a single point in space and time, based on the optical properties of the water at that moment (Hedley [2018]). Another issue is that PlanarRad requires the user to manually insert all the required inputs (Hedley [a]). This extremely inefficient. However, this issue was taken care of by batching PlanarRad. See chapter 5.

### 1.4.3 Calculating Absorption And Scattering

The inputs required by models such as HydroLight and PlanarRad are not directly the geophysical variables (Hedley [a]). This means that a process of converting the geophysical variables to the required inputs, such as absorption, scattering and attenuation, is required. There are ways of performing such calculations, and they are based on physical properties (Mobley). Such properties and equations are presented in section 2.1.2 and 2.1.3.

There are no general simulations or programs made for such calculations, and so it is necessary to compute scripts for this purpose. However, scripts exist for parts of the scattering calculation, such as the MATLAB script *betaswZHH2009* that calculates scattering by pure seawater, and the MATLAB script *bhmie* that calculates the scattering efficiency due to phytoplankton. These scripts are utilized as parts of the scattering calculations required in this thesis. See chapter 4.

### 1.4.4 Calculating Atmospheric Effects

There exists several atmospheric radiative transfer models, which calculate radiative transfer of electromagnetic radiation through a planetary atmosphere, such as the Earth's (Wallace and Hobbs [2006]), such as 4A/OP (Scott and Chedin [1981]), 6S/6SV1 (Kotchenova et al. [2006]), ATRS (Eriksson et al. [2011]), BTRAM (Chapman et al. [2009]), COART (Jin et al. [2006a]), CRM (Zender), CRTM (van Delst), DART radiative transfer model (Gastellu-Etchegorry et al. [1996]), DISORT (Stamnes et al. [1988]), FARMS (Xie et al. [2016]), Fu-Liou (Fu and Liou [1993]), FUTBOLIN (andA. Kutepov et al. [2003]), GENLN2 (Edwards [1992]), libRadtran (Mayer et al. [2017]), MODTRAN (Berk et al. [1998]) and more. The ones that are free of charge are 4A/OP, COART, CRM, FARMS, libRadtran, and ARTS.

The issue with these models is their input, as most of them are not able to intake user specified water leaving radiance, but rather presents predefined modes to select from. As an example, LibRadtran can calculate the radiation field in the Earth's atmosphere, given the input of constituents of the atmosphere, such as various molecules, aerosols and clouds (Mayer et al. [2017]). The absorption and scattering properties of the constituents can be selected from databases provided by libRadtran, or be provided by the user. The boundary conditions for the model are the solar spectrum at TOA and the reflecting surface at the bottom. These can be selected from provided solar spectra and surface models by libRadtran (Mayer et al. [2017]). However, the most fundamental input, i.e. the water leaving

radiance, can not be provided. The water leaving radiance has to be selected from predefined situations (Mayer et al. [2017]).

The most frequently utilized process of calculating the atmospheric effect for personal water leaving radiance data, is to calculate only the effects from the atmosphere, i.e ignore the water leaving radiance, and add the resulting atmospheric effects to the water leaving radiance later (Storvold [2018a]). This process can be performed by utilizing most of the mentioned algorithms above.

As illustrated, the issue with LibRadtran, and the other atmospheric radiative transfer models, is that they utilize a general starting point, such as either ocean, forest, or a specific surface albedo, and then utilize different methods to compute a general BRDF (Mayer et al. [2017]).

Once again, the user must manually calculate the total effect of the atmosphere by summing the atmospheric effects at TOA, the atmospheric radiance that is reflected back from the ocean surface, and the specific water leaving radiance at TOA. There are ways to achieve these individual calculations. In this thesis COART was utilized as the atmospheric radiative transfer model. See section 3.4. Thus, it is illustrated that there is a desire for a procedure that combines all the separate calculations into one process. In the procedure presented in the preliminary work scripts have been written that include required collected data, and thus only require the water leaving radiance to be simulated as input.

#### 1.4.5 The Effect Of Different Viewing And Solar Angles

Examinations regarding the viewing angle's and solar angle's effect on the water leaving radiance and on the radiance at TOA do exist. A measurement of water leaving radiance on smooth water surfaces at different viewing angles using high-resolution spectroradiometer has been performed (Lv et al. [2012]). Effects of the ocean surface reflection for solar irradiance on the normalized water leaving radiance in the visible wavelengths have been evaluated and discussed for various conditions of the atmosphere, solar-zenith angles, and wind speeds, in an article by Menghua Wang (Wang [2006]). This evaluation was also partly performed for the radiance at TOA. Furthermore, the Multi-angle Imaging Spectro-Radiometer (MISR) data illustrates the effect of viewing angle on TOA radiance (NASA [a]).

However, it is challenging to compare different viewing and solar angles with regard to water leaving radiance from different reports as some are based on actual water leaving radiance measurements while others are based on evaluated water leaving radiance. In the same manner, the spectral resolution is not the same for every analysis and neither is the underlying chl<sub>a</sub> concentration in the ocean. In the same manner, it is challenging to compare different viewing and solar angles from different reports and satellite images regarding the radiance at TOA. This is due to the spectral resolution, the atmospheric conditions and the geographical location varying. Moreover, the utilized viewing angle can vary from analysis to analysis when the variation in solar angles are discussed. In the same

manner, the solar angle can vary when the viewing angle is discussed.

Therefore, an examination is performed in this thesis, where different combinations of viewing angles and solar angles are utilized in order to examine specific scenarios on the same underlying chl<sub>a</sub> concentration values. That is, all examinations are performed with only the angle of interest varying, while all other variables are kept constant. This way, the variation in the resulting water leaving radiance, or radiance at TOA, is due to the variation of the variable of interest, e.g. when an analysis regarding the effects of the viewing zenith angle on the water leaving radiance is performed, the viewing azimuth angle, solar angle, atmospheric conditions and chl<sub>a</sub> concentration are kept constant.

#### **1.4.6 Lookup Tables For Resulting Water Leaving Radiance**

There are several lookup tables for obtaining water leaving radiance given the radiance at TOA (Mobley). Lookup tables for obtaining Rayleigh scattering in the atmosphere and for obtaining atmospheric correction also exist (Wang)(Gordon and Voss). However, there are no publicly available lookup tables for obtaining water leaving radiance given geophysical variables in the ocean.

#### **1.4.7 Temporal Sensitivity**

Several temporal sensitivity analyses have been performed for the variation of chl<sub>a</sub> concentrations by utilizing remote sensing methods. Many of these analyses regard the chl<sub>a</sub> concentration in lakes. An example is the observation of the short-term variations of chl<sub>a</sub> concentrations in Poyang Lake, China, by utilizing data from the MEdium Resolution Imaging Spectrometer (MERIS) satellite (Li et al.). Another example is the chl<sub>a</sub> concentration estimation in lake Kinneret, Israel, by utilizing remote sensing techniques (Yacobi [2006]). An example of temporal analyses made regarding the chl<sub>a</sub> concentration by utilizing satellite data that is not performed on a lake is the detecting of temporal variability of chl<sub>a</sub> concentration in Apalachicola Bay, Florida, utilizing Moderate Resolution Imaging Spectroradiometer (MODIS) imagery (Wang et al. [2010]).

However, as the HYPSO mission desired a temporal sensitivity analysis of data acquisition for the oceans outside of Norway, that should not be based on satellite data, but rather actual chl<sub>a</sub> concentration data, a new analysis was performed by utilizing the SINMOD data. See chapter 8.

### **1.5 Main Contributions**

The simulation tool created in the preliminary work, i.e. simulating water leaving radiance and radiance at TOA given geophysical variables in the ocean, was altered in order to be more user friendly and time efficient.

The simulation tool is based on the utilization of a hyperspectral imager, as described in [Sigernes [2018]]. Furthermore, a dataset, titled the SINMOD data, is utilized in combination with the program PlanarRad in order to calculate water leaving radiance from the ocean surface. The radiance due to atmospheric effects is calculated utilizing the program COART. Combining the two results in the hyperspectral radiance at TOA.

Via PlanarRad and COART, open-source alternatives, a system of lookup tables were computed to make the simulation process more time effective. A temporal sensitivity of data acquisition analysis was performed, and a user friendly interface for radiance simulation was developed. In addition the simulation tool was utilized in order to examine the effects of various viewing angles, various solar angles and various weather on the resulting radiance.

The simulation tool, and thus the results from the examined scenarios and from the temporal data acquisition analysis, is intended to be used for feasibility and analytic studies during the space mission design phase as well as improve the mission operations of a possibly custom-designed hyperspectral imaging satellite that is configured to observe specific targets. This includes design and validation of the hyperspectral instrument, spacecraft attitude control during imaging, data processing algorithms and data products.

The Radiance given Chlorophyll Simulator (RadPhyll Simulator) was developed in order to make the calculation and computation of water leaving radiance just above the ocean surface given chl<sub>a</sub> concentration, as well as of radiance at TOA due to atmospheric effects, less complicated and more rapid. The software differs from existing software, by being developed as one whole system, i.e. the several specific processes needed for the radiance computation mentioned in section 1.4.1 are combined. That is, utilizing the developed program the user needs only specify inputs in one input file, and is not required to transfer data between several different software.

A conference paper has been submitted based on this work:

- Monica Lapadatu, Sivert Bakken, Mariusz E. Grøtte, Morten Alver, Tor A. Johansen, "Simulation Tool for hyper-spectral imaging from a satellite", IEEE Whispers, Pending, 2019

The paper is presented in appendix C.

# Chapter 2

# Theory

This chapter presents the basic theory that the decisions made in the preliminary work and this thesis are based upon, as well as complementing theory needed for a general understanding of the domain the simulation and analysis tool is to be used in. The chapter consists of theory regarding ocean optics and hyperspectral remote sensing.

The entire theory chapter is based on the preliminary work, i.e. the project thesis which can be found here: [Lapadatu [2018]], which is based on [Mobley].

## 2.1 Ocean Optics

Optics is a branch of physics. It regards the behaviour and properties of light, including its interactions with matter and the construction of instruments that use or detect it. Optics usually describes the behaviour of visible, ultraviolet, and infrared light (McGraw-Hill [1993]). Ocean optics is the study of optics in the ocean. This subchapter will regard light and radiometry, optical oceanography, absorption and scattering, optical constituents of the ocean, radiative transfer theory, remote sensing, atmospheric correction and surfaces.

### 2.1.1 Light And Radiometry

It is useful to describe "light" and "radiometry", as these two are central concepts to the theory that will be presented later. Light is "electromagnetic radiation within a certain portion of the electromagnetic spectrum" (CIE [1987]), while radiometry is "a set of techniques for measuring electromagnetic radiation, including visible light" (Stroebel and Za-

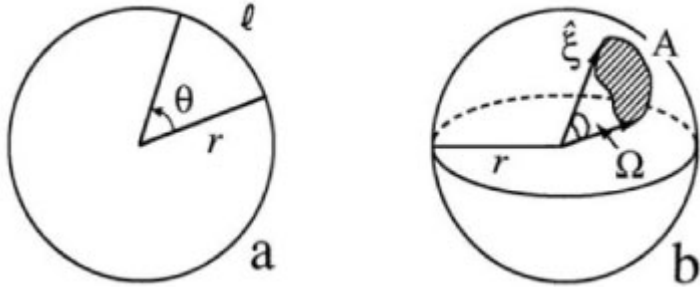


**Figure 2.1:** Geometry associated with the definition of plane angle (panel a) and solid angle (panel b). Originally presented in Mobley.

kia [1993]). Radiometry plays a significant role in remote sensing, as will be presented later on.

An important specification regarding radiometry is that of a solid angle. A solid angle is an extension of two-dimensional angle measurement (Mobley). The plane angle  $\theta$  between two radii of a circle of radius  $r$  is

$$\theta \equiv \frac{\text{arc length}}{\text{radius}} = \frac{\ell}{r} \quad [\text{rad}] \quad (2.1)$$

This is illustrated in part (a) of figure 2.1. Part (b) of figure 2.1 illustrates a patch of area,  $A$ , on the surface of a sphere of radius  $r$ . The boundary of  $A$  is traced out by a set of directions  $\hat{\xi}$ . The solid angle of the set of directions defining the patch  $A$  is illustrated as  $\Omega$  in the figure, and is defined by equation 2.2 given below.

$$\Omega \equiv \frac{\text{area}}{\text{radius squared}} = \frac{A}{r^2} \quad [\text{sr}] \quad (2.2)$$

Note that even though both plane and solid angle are dimensionless numbers, they are given the units of respectively radians and steradians (Mobley). This is to make it clear that they are measures of angle.

Several computations in the field of radiometry use the convenient form for a differential element of solid angle, which the definition of the solid angle, i.e. equation 2.2, gives (Mobley). The blue patch shown in figure 2.2 represents a differential element of area  $dA$  on the surface of a sphere of radius  $r$ . Using trigonometry one can show that this area is  $dA = (r \sin\theta d\phi)(r d\theta)$ , and so the element of solid angle  $d\Omega(\hat{\xi})$  about the direction  $\hat{\xi} = (\theta, \phi)$  is given in polar coordinate form by equation 2.3.

$$d\Omega(\hat{\xi}) = \frac{dA}{r^2} = \frac{(r \sin\theta d\phi)(r d\theta)}{r^2} = \sin\theta d\theta d\phi = d\mu d\phi \quad [\text{sr}] \quad (2.3)$$

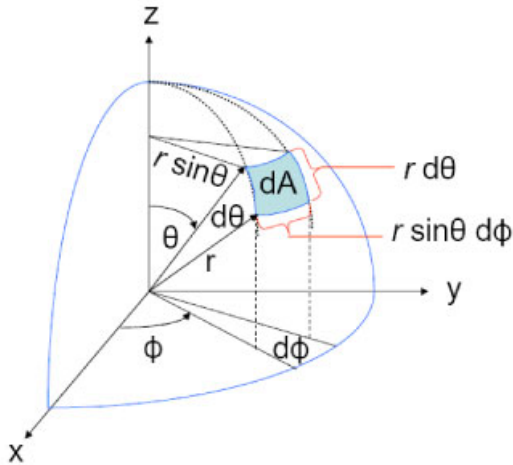


**Figure 2.2:** Geometry used to obtain an element of solid angle in spherical coordinates. Originally presented in Mobley.

Note that the last equation holds even though  $d\mu = d \cos\theta = -\sin\theta d\theta$ . This is due to the fact that when the differential element is used in an integral and variables are changed from  $(\theta, \phi)$  to  $(\mu, \phi)$ , the Jacobian of the transformation involves an absolute value (Mobley).

Having defined the solid angle, radiance, spectral radiance, irradiance and spectral irradiance can be presented. Radiance is the radiant flux emitted, reflected, transmitted or received by a given surface, per unit solid angle per unit projected area. Spectral radiance is the radiance of a surface per unit frequency or wavelength (Palmer [2012]). Spectral radiance specifies the spatial, directional, temporal and wavelength structure of the light field being described. Irradiance is the radiant flux received by a surface per unit area. Spectral irradiance is the irradiance of a surface per unit frequency or wavelength (ISO [1989]). The spectral radiance is the fundamental radiometric quantity of interest, and all other radiometric quantities can be derived from it (Mobley). It is given by

$$L(\vec{x}, t, \hat{\epsilon}, \lambda) = \frac{\partial^4 Q}{\partial t \partial A \partial \Omega \partial \lambda} \quad (2.4)$$

As spectral radiance is a fundamental quantity, it is often desirable to present it graphically. However, this is challenging due to the fact that even in the simplest case of horizontally homogeneous water and time independence, the radiance distribution is a function of four variables, namely depth  $z$ , polar angle  $\theta$ , azimuthal angle  $\phi$ , and wavelength  $\lambda$  (Mobley). As there is a lot of information contained in  $L(z, \theta, \phi, \lambda)$ , it is important to evaluate how to display the information. The following figures present some of the commonly used

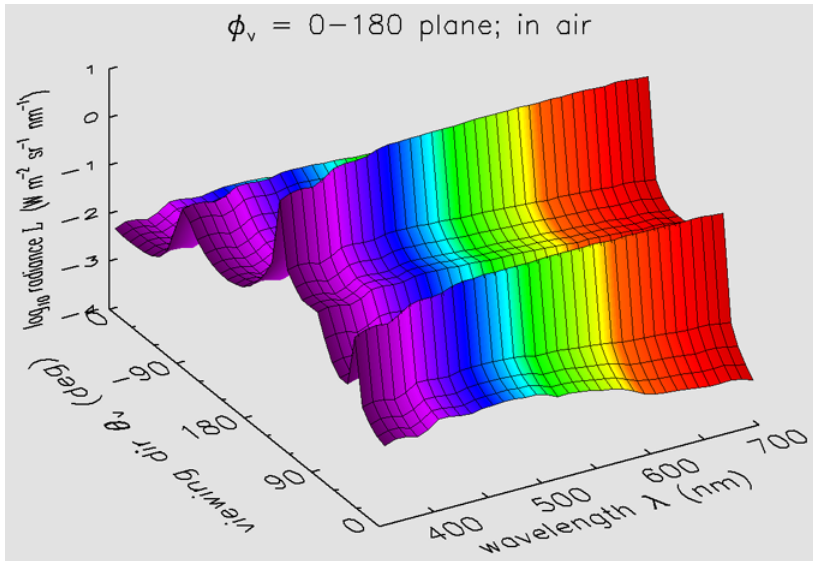


**Figure 2.3:** Radiance as a function of polar viewing direction and wavelength, in the azimuthal plane of the sun, in air just above the level sea surface. Originally presented in Mobley.

graphical representations of radiance distributions.

Figure 2.3 presents an example of radiance distribution in air just above the sea surface, computed by the HydroLight software [Sequoia Scientific]. It is presented as depending on polar viewing direction and wavelength, in the azimuthal plane containing the sun. The colors roughly correspond to the visual colors of the various wavelengths.

The information presented in figure 2.3 does not show the azimuthal dependence of the radiance, except in the plane containing the sun. Figure 2.4 presents a different way to illustrate the radiance. This illustration shows both the polar and azimuthal dependence of the radiance, but the information is only available for one depth and one wavelength, i.e. 355 nm. This plot can be interpreted as if one is at the center of the sphere, the solid black line around the "equator" is looking horizontally, i.e.  $\theta_v = 90$  deg, and the solid black line drawn from "pole to pole" is the  $\phi_v = 0$  azimuthal direction. The colors in this figure represent the magnitude of the  $\log_{10}$  (radiance), with violet being lowest. Another characteristic of figure 2.4 is that the "northern hemisphere" represents looking upward toward the sky, while the "southern hemisphere" represents looking downward toward the sea surface. This can be extremely helpful, and is used in bidirectional reflectance distribution functions (BRDFs). More on this in section 3.3.

Figure 2.3 and 2.4 present very detailed directional information, and while this can be interesting it is generally not necessary in optical oceanography. In most cases it is sufficient to display the radiance in a few selected directions as a function of depth and wavelength. An example of such a plot is figure 2.5, which illustrates the radiance in five directions.

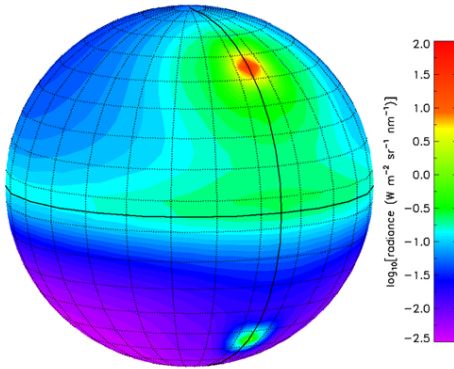


**Figure 2.4:** Radiance as a function of polar and azimuthal viewing directions, just above the sea surface and at wavelength 355 nm. Originally presented in Mobley.

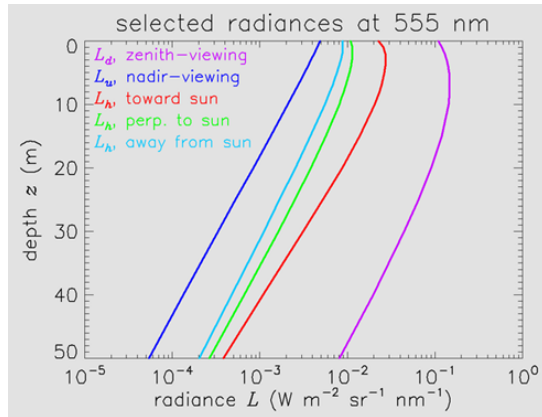


**Figure 2.5:** Radiances in selected directions as a function of depth, at wavelength 555 nm. Originally presented in Mobley.

The radiances are plotted as functions of depth at one wavelength, namely 555 nm.

## 2.1.2 Optical Oceanography

Optics is critical in aquatic research, as one can learn about the state of the water by looking at its optical properties (Mobley). This is due to the connections between the optical properties and the biological, chemical and geological constituents of natural waters, which several disciplines are interested in (IOCCG et al. [2008]). This regards, among others, the disciplines mentioned in section 1.1.

Optical properties of water are divided into two mutually exclusive classes, i.e. inherent and apparent optical properties (AOPs). The difference between the two is that the first

only depends on the medium, i.e. it is independent of the surrounding light field within the medium, while the second depends both on the medium and on the geometric, or directional, structure of the surrounding light field. The apparent optical properties must display enough regular features and stability to be useful as descriptors of the water body. Examples of AOPs are different kinds of reflectances, average cosines and diffuse attenuation coefficients (Mobley).

The two fundamental inherent optical properties (IOPs) are the absorption coefficient and the volume scattering function (Mobley). The absorption coefficient describes how a medium absorbs light, while the volume scattering function describes how the medium scatters light (Mobley). More generally, the two fundamental IOPs are absorption,  $a(\lambda)$ , and scattering,  $b(\lambda)$ . These two properties are only dependent on the water itself and the substances in it. Absorption captures photons from the light field, while scattering changes the direction and/or energy of the photons. More precisely,  $a(\lambda)$  is the exponential rate of decay of flux per unit path-length of light in the water, whereas  $b(\lambda)$  is the exponential rate of decay of the flux due to scattering. Another important property is the total volume attenuation coefficient,  $c(\lambda)$ , which describes the light beam attenuation. It is the sum of the absorption,  $a(\lambda)$ , and scattering coefficients,  $b(\lambda)$  (Johnsen et al. [2009]).

In contrast to AOPs, which are passive measurements of natural light conditions, IOPs are actively measured by instruments with their own artificial light sources, such as spectrophotometers and spectrofluorometers (Johnsen et al. [2009]). Due to this, IOPs can be measured at night, in the laboratory, and in situ in the ocean. IOPs modify the underwater light conditions, such as the information-carrying water leaving and reflected light. This light is recorded by satellite sensors, and so is of great interest for researchers. The total optical effect of the IOPs is the sum of the IOP of each component present in the medium being observed (Mobley).

The angular distribution of the scattered power has a great impact regarding optical oceanography. When discussing this two assumptions are commonly made, namely that the medium is isotropic, i.e. its influence on light is the same in all directions at a given point, and that the light is unpolarized. The first assumption is reasonable for natural waters in which the particles are randomly oriented by turbulence (Mobley). If these two assumptions hold, then the scattering process is azimuthally symmetric, i.e. the scattering depends only on the scattering angle  $\psi$ , which is measured from the direction of the unscattered beam (Mobley). Figure 2.6 illustrates this. The following holds:

$$0 \leq \psi \leq \pi \quad (2.5)$$

Figure 2.7 is the key to defining the IOPs. If the two assumptions given earlier hold, then  $B(\psi, \lambda)$  is the fraction of incident power scattered out of the beam through an angle  $\psi$  into a solid angle  $\Delta\Omega$  centered on  $\psi$  (Mobley). See figure 2.6. The solid angle  $\Delta\Omega$  includes all directions within the two red rings in figure 2.6. This corresponds to all directions between scattering angles  $\psi$  and  $\psi + \Delta\psi$ .

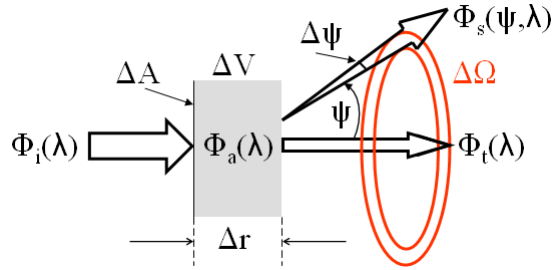


**Figure 2.6:** Geometry for defining the volume scattering function. Originally presented in Mobley.

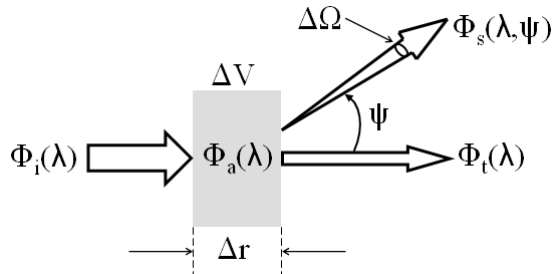


**Figure 2.7:** Geometry used to define inherent optical properties. Originally presented in Mobley.

For presenting some general equations, figure 2.7 will be used. The figure illustrates a small volume  $\Delta V$  of water, of thickness  $\Delta r$ , which is illuminated by a collimated beam of monochromatic light,  $\Phi_i(\lambda)$ , of spectral radiant power at some wavelength  $\lambda$ . A part of the incident power  $\Phi_i(\lambda)$  is absorbed within the volume of water. This part is denoted  $\Phi_a(\lambda)$ . Another part,  $\Phi_s(\lambda, \psi)$ , is scattered out of the beam at an angle  $\psi$ . The remaining power,  $\Phi_t(\lambda)$ , is transmitted through the volume with no change in direction.  $\Phi_s(\lambda)$  denotes the total power that is scattered into all directions (Mobley). Note that it is assumed that no photons undergo a change in wavelength during the scattering process. Then by conservation of energy one has that

$$\Phi_i(\lambda) = \Phi_a(\lambda) + \Phi_s(\lambda) + \Phi_t(\lambda). \quad (2.6)$$

The absorptance  $A(\lambda)$  is the fraction of incident power that is absorbed within the volume:

$$A(\lambda) \equiv \frac{\Phi_a(\lambda)}{\Phi_i(\lambda)} \quad (2.7)$$

The scatterance  $B(\lambda)$  is the fractional part of the incident power that is scattered out of the beam into all directions:

$$B(\lambda) \equiv \frac{\Phi_s(\lambda)}{\Phi_i(\lambda)} \quad (2.8)$$

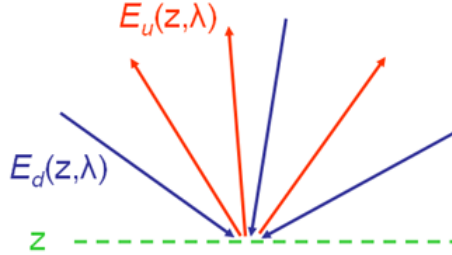


**Figure 2.8:** Illustration of light rays contributing to the irradiance reflectance  $R$ . Originally presented in Mobley.

The transmittance  $T(\lambda)$ , is the fraction of the incident power that passes through the volume without interacting with the medium, is

$$T(\lambda) \equiv \frac{\Phi_t(\lambda)}{\Phi_i(\lambda)} \quad (2.9)$$

$A(\lambda) + B(\lambda) + T(\lambda) = 1$  holds (Mobley).

As mentioned earlier, the beam attenuation coefficient  $c(\lambda)$  is defined as

$$c(\lambda) \equiv a(\lambda) + b(\lambda) \quad [\text{m}^{-1}] \quad (2.10)$$

Figure 2.8 illustrates spectral irradiance reflectance, also called irradiance ratio. It is denoted by  $R(z, \lambda)$ , and defined as the ratio of spectral upwelling to downwelling plane irradiances (Mobley):

$$R(z, \lambda) \equiv \frac{E_u(z, \lambda)}{E_d(z, \lambda)}. \quad (2.11)$$

The depth  $z$  can be any depth within the water column or in the air just above the sea surface.  $R(z, \lambda)$  is thus a measure of how much of the radiance traveling in all downward directions is reflected upward into any direction, as measured by a cosine collector (Mobley).

Irradiance reflectance can be measured by a single, uncalibrated, plane irradiance detector (Mobley). It can be performed by measuring the downwelling irradiance,  $E_d$ , and then turning the detector "upside down" to measure  $E_u$ .

Figure 2.9 illustrates the spectral remote-sensing reflectance  $R_{rs}$ , which is a measure of how much of the downwelling radiance, that is incident onto the water surface in any direction, is returned through the surface into a small solid angle,  $\Delta\Omega$ , centered on a particular direction  $(\theta, \phi)$  (Mobley). The spectral remote-sensing reflectance is defined as

$$R_{rs}(\theta, \phi, \lambda) \equiv \frac{L_w(\text{in air}, \theta, \phi, \lambda)}{E_d(\text{in air}, \lambda)} \quad [\text{sr}^{-1}] \quad (2.12)$$

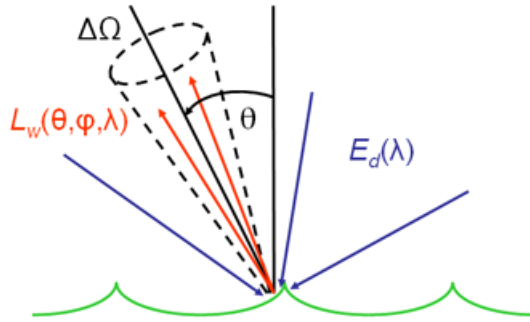


**Figure 2.9:** Illustration of light rays contributing to the remote-sensing reflectance  $R_{rs}$ . Originally presented in Mobley.

The depth argument of equation 2.12 is "in air". This indicates that  $R_{rs}$  is evaluated using the water-leaving radiance,  $L_w$ , and  $E_d$  in the air just above the water surface.

$R_{rs}$  is the property that is being used for remote sensing, not  $R$ . This is due to the advantage of  $R_{rs}$ , compared to  $R$ , which is that  $R_{rs}$  is less sensitive to environmental conditions, such as sun angle or sky conditions. However, determination of the spectral remote-sensing reflectance  $R_{rs}$  is more difficult than determination of the spectral irradiance reflectance  $R$  (Mobley).

### 2.1.3 Absorption And Scattering

This section presents, in depth, theory regarding absorption and scattering, as these properties are crucial to understanding ocean optics.

The magnitude and spectral features of the absorption coefficient varies linearly with the concentration of the absorbing material in the water. This is due to the fact that the inherent optical properties (IOPs) are conservative properties. The optically important components in the ocean, regarding total absorption, are water, phytoplankton, non-algal particles, colored dissolved organic matter (CDOM) and colored dissolved inorganic matter (Mobley).

The volume scattering function (VSF),  $\beta(\lambda, \Psi)$ , describes scattering, as it describes angular distribution of light that is scattered towards a direction,  $\Psi$  [rad], at a wavelength,  $\lambda$ . As information about the VSF of oceanic waters was desired, several early researchers in optical oceanography built instruments to measure it (Mobley). The most carefully made, and widely cited, scattering measurements are found in the report of Petzold [1972].

The VSF is defined as the radiant intensity,  $dI(\Omega, \lambda)$  [ $W sr^{-1} nm^{-1}$ ], emitting at an angle  $\Psi$  from an indefinitely small volume element,  $dV$  [ $m^3$ ], for a given incident irradiant intensity,  $E(0, \lambda)$  [ $W m^2 nm^{-1}$ ] (Mobley). This definition is presented in equation 2.13

below.

$$\beta(\Psi) = \frac{1}{E(0, \lambda)} \frac{dI(\Omega, \lambda)}{dV} \quad [m^{-1} sr^{-1}] \quad (2.13)$$

It is generally assumed that scattering is azimuthally symmetric so that  $\beta(\lambda, \Psi) = \beta(\lambda, \theta)$ , where  $\theta$  [rad] is the angle between the initial direction of light propagation and that to which the light is scattered regardless of azimuth (Mobley).

The scattering coefficient,  $b(\lambda)$  [ $m^{-1}$ ], is a measure of the overall magnitude of the scattered light, without regard to its angular distribution (Mobley). That is to say, the scattering coefficient is the integral of the VSF over all angles ( $4\pi$  [sr]), as presented in equation 2.14.

$$b \equiv \int_0^{4\pi} \beta(\Psi) d\Omega = \int_0^{2\pi} \int_0^\pi \beta(\theta, \phi) \sin \theta d\theta d\phi = 2\pi \int_0^\pi \beta(\theta) \sin \theta d\theta \quad (2.14)$$

where  $\phi$  [rad] is the azimuth angle.

Scattering is often described by the phase function,  $\tilde{\beta}$  (Mobley). The phase function is the VSF normalised to the total scattering, and so it provides information about the shape of the VSF regardless of the intensity of the scattered light. It is defined as in equation 2.15.

$$\tilde{\beta} \equiv \frac{\beta}{b} \quad (2.15)$$

It is usually desired to have an analytic formula that approximates the shape of an actual phase function. In oceanography, the Fournier-Forand phase function is commonly used as such an approximation. It is more realistic than other phase functions that have been used in the past (Mobley). Fournier and Forand derived this approximate analytic form for the phase function in 1994.

Mie scattering theory describes the scattering of electromagnetic waves by homogeneous spheres of any size (Mobley).

## 2.1.4 Optical Constituents Of The Ocean

Ocean colour is dependent on the IOPs of water, and the spectral composition and angular distribution of the incident light (Johnsen et al. [2009]).

The in-water components that affect the optical properties of water, are traditionally divided into water, inorganic dissolved materials, phytoplankton, CDOM, non-phytoplankton organic particles, inorganic particles and bubbles (Mobley).

The following section will examine the contributions from sea water and phytoplankton more closely. The other components will not be presented in more detail as the calculations regarding their contributions were not performed in the preliminary work and will not be performed in this thesis either.

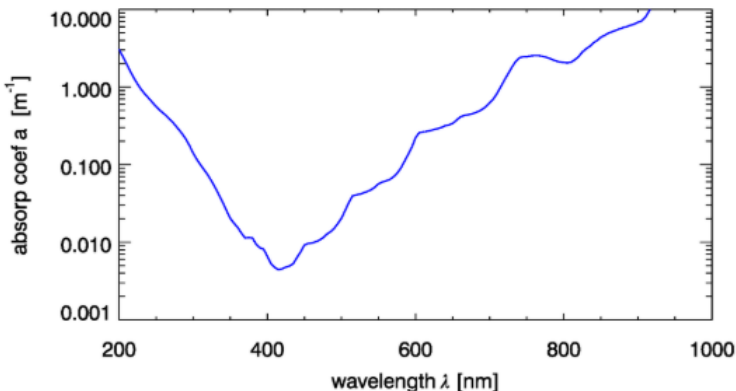


**Figure 2.10:** Absorption spectrum for pure water on a semilog scale. (Data from various sources: Smith and Baker (1981); Sogandares Fry (1997); Pope and Fry (1997); Segelstein (1981)). Originally presented in Mobley.

Sea water contributes to both absorption and scattering. The absorption in the near infrared (NIR) is often dominated by the contribution from water (Mobley). The temperature and salinity of the water affect both the absorption and the scattering. That is to say, one must take the two properties into consideration when computing the optical properties of water. Regardless, figure 2.10 illustrates the absorption spectrum of pure water.

Phytoplankton are microscopic, single cell, free-floating organisms that possess chlorophyll (Johnsen et al. [2009]). Chlorophyll is a pigment that allows the phytoplankton to perform photosynthesis. Phytoplankton are one of the primary reasons for studying ocean color, and they have a major effect on it. They are the most significant primary producers in the ocean, the base of the oceanic food web and an important component of the global carbon cycle (Mobley). Hence, it is of interest to study phytoplankton. The chlorophyll causes two dominant peaks, at 440 nm (blue) and 675 nm (red), in the absorption spectra (Mobley). The scattering properties of phytoplankton are also important as they are directly related to remote sensing reflectance calculations.

## 2.1.5 Radiative Transfer Theory

As presented, there are several IOPs that are used to describe the optical properties of the medium that light propagates through. Radiative transfer theory provides the connection between these IOPs and the AOPs (Mobley). The radiative transfer equations tie the two sets of properties together and so provides the theoretical framework for all optical oceanography and ocean-color remote sensing. Figure 2.11 illustrates the central role of radiative transfer theory, through the radiative transfer equation. Simply explained, IOPs and boundary conditions are the inputs to the equation, and radiance is the resulting output (Martin [2014]). Boundary conditions are represented by the physical environment of a

water body, such as the waves on its surface, its depth, the characteristics of its bottom, and the incident radiance from the sky (Mobley).

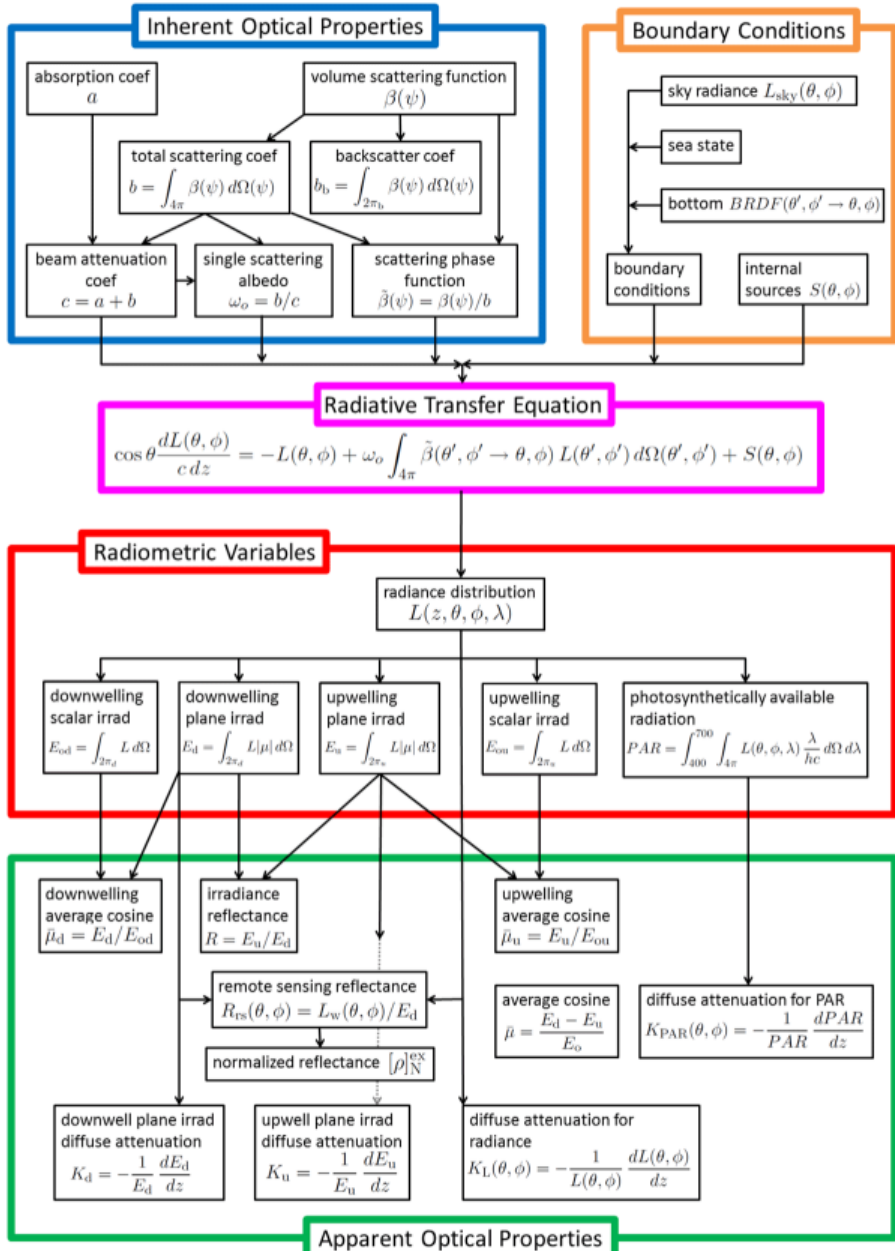


**Figure 2.11:** Organization chart for optical oceanography. Originally presented in Mobley.

## 2.1.6 Remote Sensing

The inverse problem of radiative transfer theory is "given radiometric measurements of underwater or water-leaving light fields, determine the inherent optical properties of the water" (Mobley). This is remote sensing, and the problem is regarded as unsolved, and has both conceptual and practical limits. The difficulties regarding inverse problems include uniqueness of the solution, stability of the solution, and that inversions are always based on an assumed model that relates what is known to what is desired (Mobley). The details of inverse problems will not be discussed, as the thesis will not attempt to solve such problems. However, a description of remote sensing is presented in this section, as it is essential to the HYPSO mission.

Remote sensing refers to the use of optical measurements, made from aircraft or satellites, with the desire to obtain information about the constituents of natural waters, the IOPs, or the bottom depth and type (Martin [2014]). The type of remote sensing which is of most importance for this thesis is oceanic remote sensing. Ocean color remote sensing, commonly utilizes visible light, i.e. wavelengths between 400 nm and 700 nm, and near-IR light, i.e. wavelengths from 700 to just under 2000 nm (Mobley).

Remote sensing is divided into two categories, i.e. active and passive (Mobley). Active remote sensing is performed by sending a signal of known characteristics from the sensor platform to the ocean, and then detecting the return signal after a time delay. Passive remote sensing on the other hand, observes the light that is naturally emitted or reflected by the ocean. An example of passive remote sensing is the use of sunlight that has been backscattered within the water and returned to the sensor (Martin [2014]).

The quality of remote sensing data is determined by the spatial, spectral, radiometric and temporal resolutions (Mobley). Spatial resolution regards the ground size of an image pixel. For satellites this might be more than 1000 meters (Mobley). Spectral resolution regards the number, spacing, and width of the different wavelength bands recorded. The spectral resolution is quantified by the sampling interval and the band width. Radiometric resolution regards the number of different intensities of light the sensor is able to distinguish, and so it determines how small of a change in the measured quantity can be recorded by the instrument. Temporal resolution refers to the frequency of flyovers by the sensor (Mobley). This is relevant for example when clouds cover over the area of interests, thus making it necessary to repeat the data collection.

The objective of remote sensing is to convert the radiance measured by the sensor to the desired information (Mobley). This is the processing of remotely sensed imagery, and it consists of several steps that result in different levels of processed data. These different levels of processed data range from unprocessed instrument data at full resolution, to results obtained from a combination of satellite data and model output (such as the output from an ocean ecosystem model) (Mobley).

It is of interest to compare remotely sensed values with the ground truth values of the

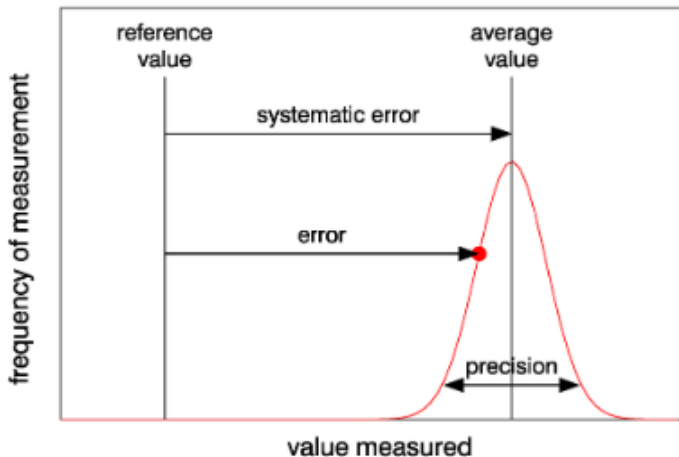


**Figure 2.12:** Illustration of terms used in validating measurements. Originally presented in Mobley.

quantity being determined by the remote sensing, i.e. to perform validation. Put simply, validation refers to checking the model output against reference values. Validation is performed to make sure that both the model physics and the computer programming are correct (Mobley). There are several ways to describe the difference in remotely sensed and in situ values of the same quantity, such as reliability (the certainty with which the value of a remotely sensed quantity is actually a measure of the quantity of interest), reference value (the quantity, often measured in situ, being used for comparison with a remotely sensed value), error (the difference between a measurement and a reference value), and precision (the reliability with which an instrument will give the same value when repeated measurements of the same quantity are made) (Mobley). See figure 2.12 for an illustration of the different terms.

Summarizing, the goal of remote sensing of ocean colour is to obtain information regarding substances and particles present in the water. The idea is that since different substances have different absorption and scattering characteristics in the visible wavelength band, they can be detected remotely through the spectral characteristics of the upwelling light of the sea surface (Johnsen et al. [2009]).

## 2.1.7 Atmospheric Correction

The satellite-borne sensors measure the radiance at TOA. There are various contributions to this TOA radiance, and they come from solar radiance (which is scattered by atmospheric molecules and aerosols), sun and sky radiance (which is reflected by the sea surface, i.e by the water surface itself or by the foam from whitecaps), and from water leaving radiance (Mobley). Atmospheric correction regards extracting the radiance of interest, i.e. the water leaving radiance, from the TOA radiance (Mobley).

The various steps of the atmospheric correction process are the corrections for absorption and scattering by gases and aerosols, corrections for sun and sky reflectance by the sea surface, correction for whitecap reflectance, and corrections for sensor out-of-band response and polarization effects (Mobley). The end result is, as mentioned above, an estimate of the water leaving radiance.

The resulting normalized reflectance is the input to several algorithms, which are made for retrieval of various quantities of scientific interest such as the chlorophyll a concentration, the water-column diffuse attenuation for downwelling plane irradiance, water-column absorption, and water-column backscatter coefficients (Mobley).

As presented, the total radiance,  $L_t$ , measured at TOA comes from contributions by atmospheric scattering ( $L_{atm}$ ), sun and sky radiance reflected back upward by the sea-surface ( $L_{surf}^{TOA}$ ), and water leaving radiance that reaches the TOA ( $L_w^{TOA}$ ). This can be summarized in the following equation:

$$L_t = L_{atm} + L_{surf}^{TOA} + L_w^{TOA} \quad (2.16)$$

Note that the atmospheric contribution,  $L_{atm}$ , is always considered to be at the TOA. Generally, the surface-reflected radiance and the water leaving radiance are formulated both at the sea surface and at the TOA, and so for these radiances a superscript TOA is used to specify that the given value is at TOA (Mobley). That is to say,  $L_w$  denotes the water leaving radiance just above the sea surface, while  $L_w^{TOA}$  denotes how much of  $L_w$  reaches the TOA.

The atmospheric contribution in equation 2.16 is usually called atmospheric path radiance, and comes from scattering by atmospheric gases and aerosols (Mobley). The part that is due to scattering by atmospheric gas molecules alone is customarily called the Rayleigh radiance,  $L_R$  (Mobley). The atmospheric path radiance is equal to the Rayleigh radiance if there is an absence of aerosols.

The total surface reflectance consists of reflectance due to direct sun glint from the water surface ( $L_g^{TOA}$ ), background sky radiance reflected by the water surface ( $L_{sky}^{TOA}$ ), and sun and sky radiance reflected by whitecaps and foam ( $L_{wc}^{TOA}$ ) (Mobley). Figure 2.13 illustrates the contributions to the TOA radiance.

As the goal of atmospheric correction is to convert the measured TOA radiance,  $L_t$ , into the corresponding sea-level water leaving radiance,  $L_w$ , and  $L_t$  is the only measured value, it requires estimation of the different reflectances due to the atmosphere and sea surface (Mobley). The way to obtain the sea-level water leaving radiance is to subtract the different atmospheric and surface-reflectance terms from  $L_t$ .

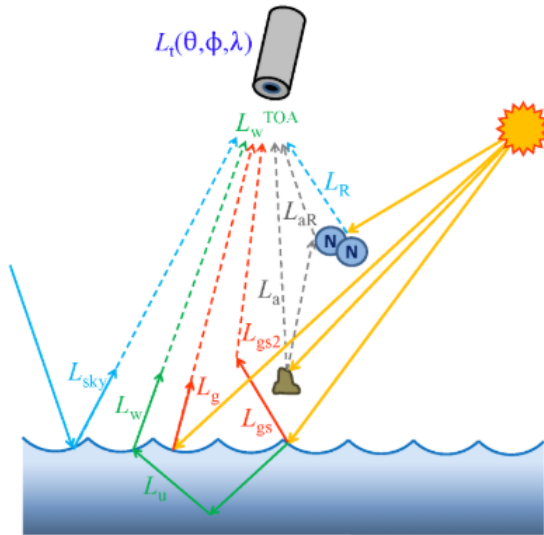


**Figure 2.13:** Qualitative illustrations of the various processes contributing to the total TOA radiance. Originally presented in Mobley.

For illustration purposes figure 2.14 presents the fractional contributions by various processes to the total TOA radiance  $L_t$ , for a specific example. For this particular case, the water leaving radiance is at most 10% of the total TOA radiance. This gives an impression of how small-scale the radiance of interest is compared to the measured radiance. The atmospheric path radiance contributes to between 70% and 90% of  $L_t$ . Furthermore, figure 2.14 demonstrates that Rayleigh scattering by atmospheric gases is the largest contributor to the TOA radiance for wavelengths below 500 nm. Aerosols are mostly located near the sea surface, as figure 2.14 demonstrates as the aerosols are the greatest contributors to the TOA radiance for wavelengths between 500 nm and 1350 nm.

In general, approximately 90% of the visible light returned to space over the ocean is contributions from the atmosphere. The water leaving irradiance only makes up approximately 10%, and this is where the signal of interest is contained (Storvold [2018b]).

The process performed in the preliminary work and in this report is the opposite of atmospheric correction. The objective was to add atmospheric effects onto the water leaving radiance values. Nonetheless, numerous choices made later on are based on the theory that has been presented here, as well as the following theory.

The following section will more closely consider the water leaving radiance, as this is the radiance of interest. Regarding water leaving radiance,  $L_w$ , every point of the sea surface is emitting an upward distribution of radiance  $L_w(\theta, \phi)$  (Mobley). This is illustrated in the right part of figure 2.15. Radiance from all locations and various directions can be scattered into the direction of interest via only one scattering (Mobley), as illustrated in

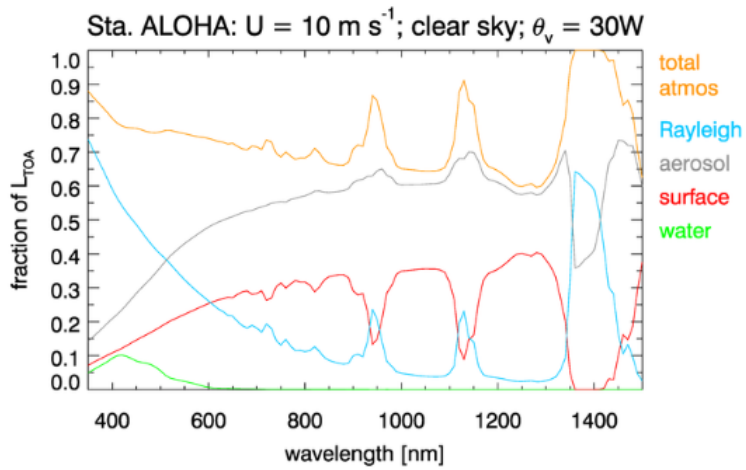


**Figure 2.14:** Example of the fraction of  $L_t$  due to various processes. Originally presented in Mobley.

the right part of figure 2.15, by the dotted line.

Absorption, emission and scattering by aerosols play a role in the atmospheric effects on the TOA recorded radiance (Mobley). There exist several aerosol models that characterize physical and optical properties of the particles. These models span a wide range of compounds such as soot, mineral dust, salt, chemical compounds, and organic matter (Mobley). Optical properties depend on relative humidity and temperature. The variable amounts of relative humidity causes the particle size to change and hence the optical properties. General models regarding aerosols are urban, rural, maritime (oceanic and coastal) and tropospheric (background) (Mobley).

Absorption, emission and scattering by water particles that radiative properties depend on are phase (liquid or ice), overall cloud shape, particle size and shape distribution, contaminants and temperature (Storvold [2018b]).

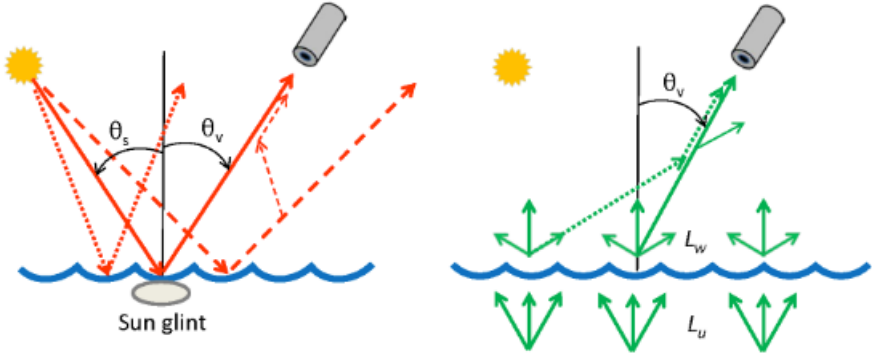


**Figure 2.15:** Left panel: Illustration of sun glint as seen from the TOA, which is described by a direct transmittance. Right panel: Illustration of water-leaving radiance as seen from the TOA, which is described by a diffuse transmittance. Originally presented in Mobley.

## 2.1.8 Surfaces

The surface of the water, or ocean, is interesting to study as it affects how light is reflected by and transmitted through air-water surfaces (Mobley). Another interesting scene regards how light is reflected by opaque surfaces such as the ocean bottom. The bidirectional reflectance distribution function (BRDF) is the fundamental quantity for specifying how an opaque surface reflects light (Mobley). The ocean is generally affected by wind, and so has a rough surface. Reflection and transmission by such ocean surfaces are modeled using the equations for a flat surface applied to each small patch of the ocean surface (Mobley).

Figure 2.16 illustrates a level surface with light incident onto the surface from the air (panel a), and from the water (panel b). The real index of refraction of the air is  $n_a$ , and the real index of refraction of the water is  $n_w$ , which is approximately 1.34 at visible wavelengths (Mobley).  $\hat{n}$  represents a unit vector normal to the surface,  $\hat{\xi}_i$  represents a unit vector in the incident direction, and  $\hat{\xi}_r$  and  $\hat{\xi}_t$  are the directions of the reflected and transmitted rays respectively.

Another helpful figure of the geometry for discussion of surface reflectance is figure 2.17. The figure illustrates a cartesian (x,y,z) coordinate system with a surface, colored light blue, lying in the x-y plane. The figure also presents a collimated light source providing the incident light, and a detector which receives the reflected light. Surface optical properties usually depend on the wavelength  $\lambda$ , so the complete description of the reflectance properties of a surface will be a function of five variables:  $\theta_i, \phi_i, \theta_r, \phi_r, \lambda$  (Mobley).

It is mainly assumed that an ocean bottom is a Lambertian reflecting surface, i.e. a surface that reflects radiance equally into all directions (Mobley). This assumption is due to the fact that actual measurements of BRDFs of ocean bottom materials have rarely been made. Stated differently, measurements and models of the BRDF for actual ocean bottom

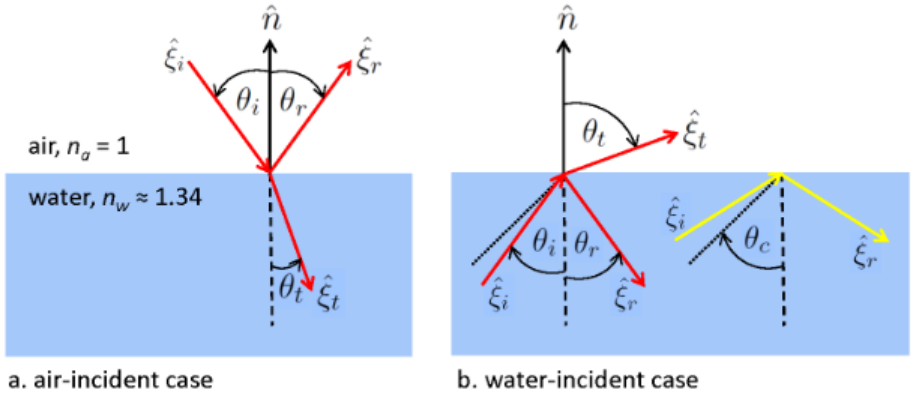


**Figure 2.16:** Illustration of incident, reflected, and transmitted rays for air- and water-incident light. Originally presented in Mobley.

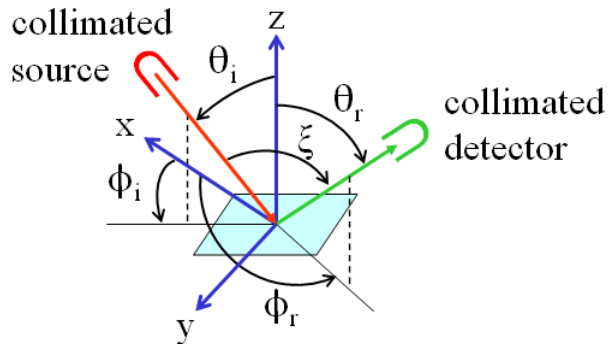


**Figure 2.17:** Geometry for discussion of surface reflectance. Originally presented in Mobley.

materials are lacking.

## 2.2 Hyperspectral Remote Sensing

Hyperspectral imaging (HSI), also called imaging spectroscopy, is an emerging field that combines two-dimensional object visualization with spectroscopy, resulting in a hypercube image. A hypercube image is an image cube that in addition to containing the two-dimensional image also contains the spectral information in each pixel. Hyperspectral imaging has become an established remote sensing technique over the past few decades, and is widely used for mapping and monitoring of mineral deposits, vegetation cover and ocean color (Goetz [2009]).

The difference between hyperspectral imaging and traditional RGB imaging is the hyperspectral imaging's ability to record spectral information. The spectral range of hyperspectral imagers depends on both the sensor and the application. However, typical values are between 400 - 2500 nm (Goetz [2009]).

The most common type of hyperspectral imagers are the push-broom scanners (Sigernes [2018]). These scanners record the imagery by moving across the area of interest. Push-broom hyperspectral imagers work by light entering a narrow entrance slit, which corresponds to one hyperspectral pixel row. Then, to acquire an image transect, the imager has to be moved in a straight line across the target area (x-axis) with the slit oriented perpendicularly to the direction of movement (y-axis). As the imager is moved, slit images (pixel rows) are continuously captured. The frame rate is predefined. The result is, as mentioned above, an hyperspectral cube. Each pixel row has a fixed number of monochromatic levels corresponding to the imager's spectral range and resolution, which can be interpreted as the z-axis of the cube (Sigernes [2018]). The resulting hyperspectral image cube is obtained by placing all the captured pixel rows together. Recapitulating, the x-, y- and z-axes represent, respectively, transect length, swath width and monochromatic level (wavelength). The push-broom technique is illustrated in figure 2.18.

A spectrometer is an instrument used to separate and measure spectral components of physical phenomena. Hyperspectral remote sensing uses spectrometers to record data (Sigernes [2018]). Figure 2.19 is an illustration of an optical diagram of a spectrometer. The light source and its area are depicted as  $S$ . A spectrometer works by a source illuminating the first lens  $L_1$ , which is at the distance  $p$ , and then the lens focuses the rays onto the entrance slit area,  $S_2$ , as the imaged area  $S_1$  of  $S$ . The entrance slit is at a distance  $q$  from the first lens. The light is then emitted onto the second lens,  $L_2$ , that is at a distance  $f_2$  from the entrance slit. This action collimates the beam onto a grating  $G$ . The diffracted light will then be focused by the third lens,  $L_3$ , onto the exit slit with area  $S_3$  at a distance  $f_3$  from the third lens. All lenses may be exchanged with mirrors as long as the light is focused, and the front optics, i.e.  $L_1$  in figure 2.19, may be exchanged by multi-lens elements, such as telescopes or microscopes (Sigernes [2018]).

Essential properties regarding hyperspectral imaging are intensity, throughput, flux and etendue (Sigernes [2018]). These are properties of the combination of light and the optics. Next follows a brief presentation of the mentioned properties.

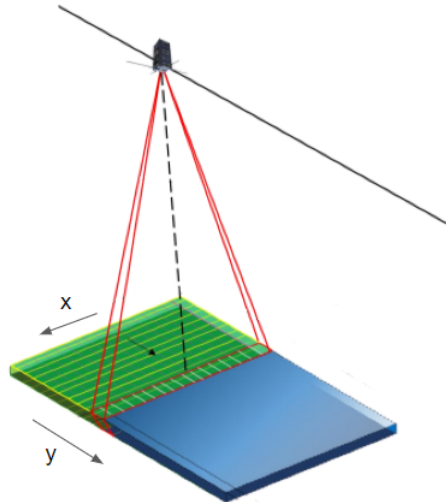


**Figure 2.18:** Pushbroom HSI. Figure made by the HYPSO team.

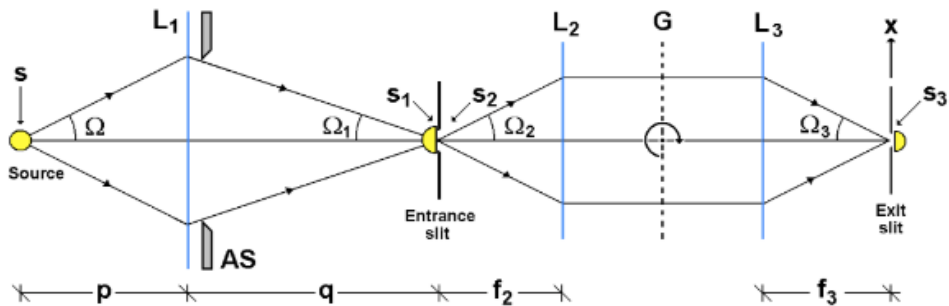


**Figure 2.19:** Optical diagram of a spectrometer. Originally presented in Sigernes [2018].

The flux is the number of emitted photons from a source S per unit time into a solid angle Q (Sigernes [2018]).

The intensity is defined as the flux per unit solid angle and is proportional to the square of the amplitude (Sigernes [2018]). The property is imperative as it is measured in order to obtain the spectral information. This is presented in equation 2.17, where  $b$  is the slit width,  $\beta$  is the diffraction angle and  $\lambda$  the wave length.

$$I = I_0 \left[ \frac{\sin(\pi b \sin(\beta)/\lambda)}{\pi b \sin(\beta)/\lambda} \right]^2 \quad (2.17)$$

Equation 2.17 makes it possible to vary the angle so that one can observe various peaks for different wave lengths of interest.

Etendue is a geometrical property of the system. Etendue represents the maximum geometric beam size the instrument can handle, i.e. it measures an optical system's capability of gathering flux (Sigernes [2018]). The etendue is a function of the emitting area of the source and the angle the light propagates into or out of. The optimal construction, with respect to etendue, will keep the property constant throughout the system. Thus, a spectrometer will be etendue optimized if equation 2.18 holds.

$$G = \pi S \sin^2 \Omega = \pi S_1 \sin^2 \Omega_1 = \pi S_2 \sin^2 \Omega_2 = \pi S_3 \sin^2 \Omega_3 \quad (2.18)$$

The final equality is required in order not to overfill the field of view of the second lens (Sigernes [2018]). An conspicuous property of this is that the input etendue of a spectrometer is equal to its output etendue.

Throughput regards the fact that the flux will be reduced throughout the system (Sigernes [2018]). This is due to aberrations and transmission factors. The remaining flux at the exit slit, which is available to the detector, is defined as the throughput (Sigernes [2018]). The throughput is defined as the efficiency of the grating, transmission factor and spectral radiance multiplied by the etendue of the exit slit, as presented in equation 2.19.

$$\Phi_2 = B_\lambda E_\lambda^n T_\lambda \times G_3 \quad (2.19)$$

Another fundamental property in hyperspectral imaging is diffraction. Diffraction separates the different wavelengths, which makes it possible to record the intensity and thus obtain the spectral signature (Sigernes [2018]). Diffraction is the effect of a wave being distorted by an obstacle with comparable dimensions to the wavelength of the wave (Sigernes [2018]). The phenomenon occurs when a wave encounters an obstacle, which in HSI is represented by a slit or grating. In order to obtain the desired diffraction multiple slits, i.e. a grating can be used. The grating will result in a number of new waves equal to the number of slits in the grating. The resulting intensity is therefore the interference caused by the the number of slits,  $N$ , modulated by the diffraction from one slit, as

presented by equation 2.20.

$$I = I_0 \left[ \frac{\sin(N\pi a \sin(\beta)/\lambda)}{\sin(\pi a \sin(\beta)/\lambda)} \right]^2 \times \left[ \frac{\sin(\pi b \sin(\beta)/\lambda)}{\pi b \sin(\beta)/\lambda} \right]^2 \quad (2.20)$$

The last property that is going to be presented in this section regards the signature of the pixels in the hyperspectral image. In hyperspectral imaging each pixel contains the intensity of the different wavelengths (Sigernes [2018]). If the intensity is plotted as a continuous curve, with the intensity on the vertical axis and the wavelength on the horizontal axis, the result is the signature of the pixel. This signature will vary depending on what is depicted in the pixel, and thus it may be used to reveal patterns that may be invisible to the human eye (Sigernes [2018]).

# Background

This chapter will present needed background regarding the dataset utilized in the preliminary work and in the thesis at hand. Theory regarding Network Common Data Form (NetCDF) files and the programs PlanarRad and COART will be presented as well. PlanarRad and COART will be presented using examples.

NetCDF files will be presented as it is the file format of the SINMOD data processed in this thesis. It will be demonstrated how to work with NetCDF files utilizing Matlab and Panoply. PlanarRad is utilized for calculating water leaving radiance given absorption and attenuation. COART is a model utilized for calculation of radiances due to atmospheric effects.

The entire background chapter is based on the preliminary work, i.e. the project thesis which can be found here: [Lapadatu [2018]].

## 3.1 The SINMOD Data

A dataset was provided for this project, i.e. for the preliminary work and the thesis at hand, by SINTEF Ocean. The dataset is titled the SINMOD data. SINMOD is developed by SINTEF (Slagstad and Mc Climans [2005], Wassmann et al. [2006]). It is based on the primitive Navier-Stokes equations and uses a regular horizontal grid and z-layers. High resolution simulations are achieved using a nesting scheme where larger scale simulations provide outer boundary conditions for higher resolution simulations. The top level domain covers the Norwegian Sea and Arctic Ocean in 20 km horizontal resolution, and the resolution is increased by a factor of 5 through each nesting step. The model forcing includes atmospheric reanalysis data from Era Interim (Dee et al. [2011]) and climatological freshwater runoff data. Tidal dynamics are applied on the outer boundaries of the top level

domain, based on 8 tidal components from TPXO (Egbert and Erofeeva). The model calculates physical oceanographic variables such as surface elevation, current speed, temperature and salinity. The ecological model additionally estimates nutrient concentrations (nitrate, silicate, ammonium), phytoplankton (diatoms and flagellates), zooplankton (*Calanus finmarchicus* and *C. glacialis*) and variables such as heterotrophic nanoflagellates, microzooplankton, and fast and slow sinking detritus (Alver [2018]).

The SINMOD dataset was provided as a NetCDF file titled *plankton.nc*. The dataset consists of approximately one month of recorded data with a temporal resolution of 1 hour, produced from model domain covering the areas outside of Mid Norway, including Hitra, Frøya, Froan and Frohavet in 160 m horizontal resolution. The surface layer thickness is 3 m on average, but varies with surface elevation. The thickness of the layers below ranges from 0.5 m (layers 2 and 3) to 500 m below 1000 m depth (Alver [2018]). The variables included are temperature [ $^{\circ}\text{C}$ ], chlorophyll in the surface layer [ $\text{mg chl}_a \text{ m}^{-3}$ ], chlorophyll integrated over 0 - 50 meter per square metre [ $\text{mg chl}_a \text{ m}^{-2}$ ], and the concentration of diatoms [ $\text{mmol N m}^{-3}$ ] and flagellates [ $\text{mmol N m}^{-3}$ ] in the surface layer.

The concentration of diatoms and flagellates were not given in the units regarding chlorophyll, but rather in mmol nitrogen per cubic meters, and so it was necessary to multiply with the nitrogen-to-carbon ratio (which is 7.6 in SINMOD), the atomic weight of carbon, i.e. 12 u, and the amount of chlorophyll per gram carbon in the two classes of algae, i.e. 0.035 and 0.013 respectively, to obtain the units of mg chl<sub>a</sub>. Thus, the conversion factor for converting from mmol diatoms to mg chl<sub>a</sub> is  $12*7.6*0.035$ , and in the same manner  $12*7.6*0.013$  for flagellates. These calculations were performed by SINTEF Ocean when calculating the chlorophyll values given in the dataset (Alver [2018]).

The SINMOD data is saved in a polar stereographic grid. In geometry, the stereographic projection is a particular mapping, or function, that projects a sphere onto a plane. The projection preserves angles at which curves meet, but it preserves neither distances nor the areas of figures (Casselman). Figure 3.1 illustrates an example of a polar stereographic grid, used by the National Snow and Ice Data Center (Snow and Center). There are two ways to relate the SINMOD data to latitude and longitude values. The first option is to utilize the available variables *latitude* and *longitude*, which give the position per grid-cell. The second option is to utilize the characteristics of the polar stereographic grid, which are given as attributes in the file containing the dataset (Alver [2018]).

The SINMOD data was, as mentioned in the introduction to chapter 3, provided as a NetCDF file. Hence, the next section regards NetCDF files.

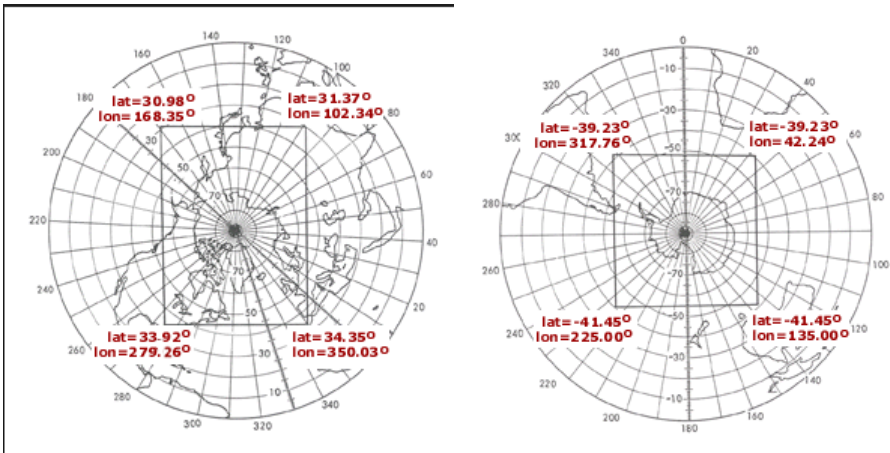


**Figure 3.1:** Polar stereographic grids, presented as Polar Spatial Coverage Maps for the northern and southern hemispheres. Originally presented in (Snow and Center).

## 3.2 NetCDF Files

Network Common Data Form is a set of software libraries and machine-independent data formats that support the creation, access and sharing of scientific data that is array-oriented (UCAR [a]). NetCDF is used by a wide range of disciplines, as it offers a standard way to store data, and thus makes sharing data between disciplines simpler. NetCDF files can be used to store substantial amounts of data, as well as keep track of where the data comes from, in space and time (UCAR [b]).

### 3.2.1 MATLAB

MATLAB can work with huge NetCDF files, by utilizing MATLAB's own routines made for this purpose. The correct way to read data from NetCDF files depends on how the file is set up. MATLAB can, among other functionalities, read data from a given variable in the data source (MathWorks [a]).

MATLAB's own high-level functions simplify the process of importing data from NetCDF files, while MATLAB's low-level functions enable further control over the importing process (MathWorks [b]).

Running the *ncdisp* command on the SINMOD data file, i.e. the plankton.nc file, results in the format, global attributes, dimensions, variables, and information about the variables such as their size, dimensions, data type and attributes being presented in the output.

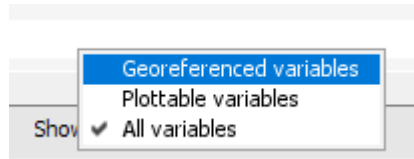


**Figure 3.2:** Panoply: Available options for which variables to present.

### 3.2.2 Panoply

The first objective for the preliminary work was to obtain an impression regarding the values of the dataset. This was achieved by creating a visualization illustrating the algae concentration and the chlorophyll in space and time. That is, a video presenting the values of the variables chl\_0\_50m, chl\_a, diatoms and flagellates was generated. The application Panoply was utilized for this purpose.

Panoply was utilized for similar tasks, such as obtaining a period in time from the SINMOD data set with huge chl\_a concentration variation, in this thesis. Panoply is a netCDF, HDF and GRIB Data Viewer provided by NASA. The program can, among other functions, plot georeferenced arrays from a NetCDF file, and export animations as MP4 video or as a collection of individual frame images (Schmunk). Panoply is a cross-platform application that can be run on Macintosh, Windows, Linux and other desktop computers. The following sections will highlight some of the capabilities of Panoply.

Information regarding the loaded file, e.g. the plankton.nc file, and its variables are presented immediately when opening Panoply. For the file at hand, the available variables are chl\_0\_50m, chl\_a, diatoms, flagellates, latitude, longitude, temperature and time. Information regarding whether the variables are georeferenced or not is available. More information regarding the file, such as dimensions, units and coordinates are available as well. Figure 3.2 demonstrates options regarding which variables to present in the Panoply overview.

A variable can be selected from the overview to work further with. The options available for the chosen variable regard different types of plots that can be created. The main categorizations of the plots are georeferenced plot, 2D plot and line plots along one axis. Several options are available for the three plot types. Figure 3.3 was created by selecting the georeference plot. The figure displays a map with different options regarding the visualization.

Selecting the option "Array" instead of "Plot" results in a visualization of the values of the variable. This is helpful with regard to obtaining an overview of the values stored in the variable. This is a functionality that MATLAB, among other programs, does not have any suitable options for performing, due to the NetCDF files containing too many values. An example of a value-visualization in Panoply is presented in figure 3.4.

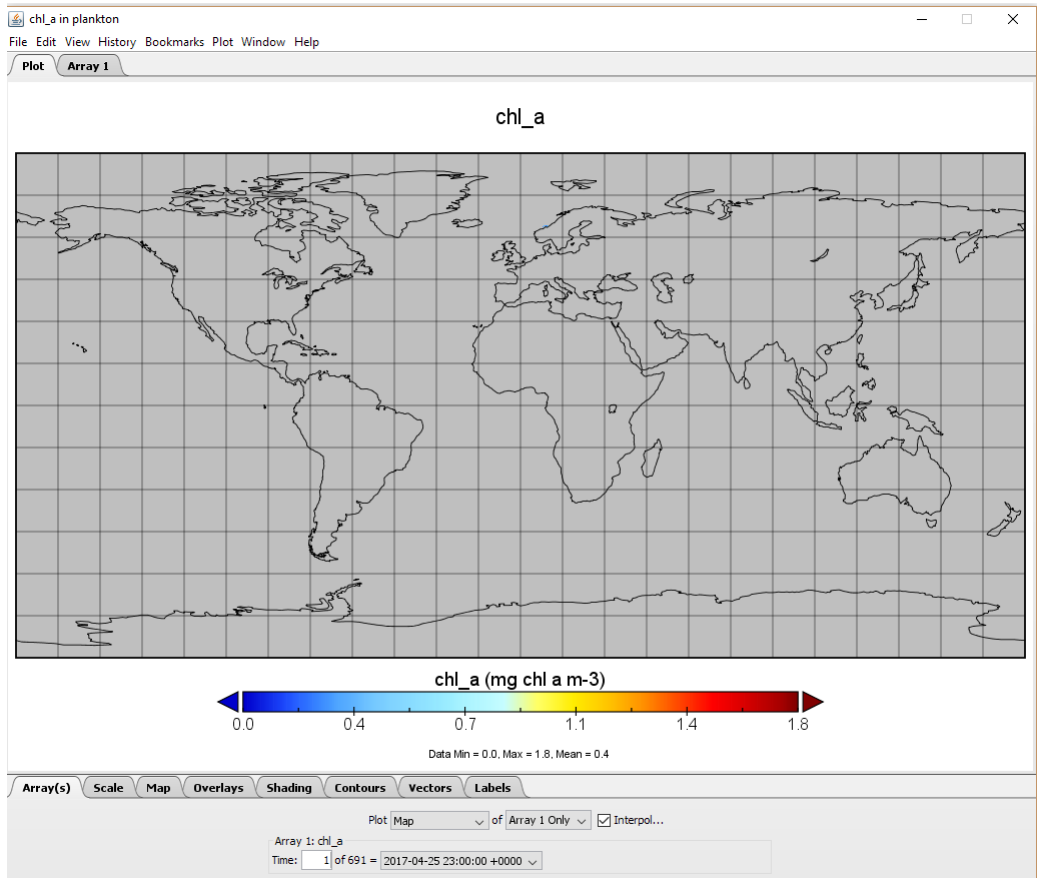


**Figure 3.3:** Panoply: Plotting on a map example.

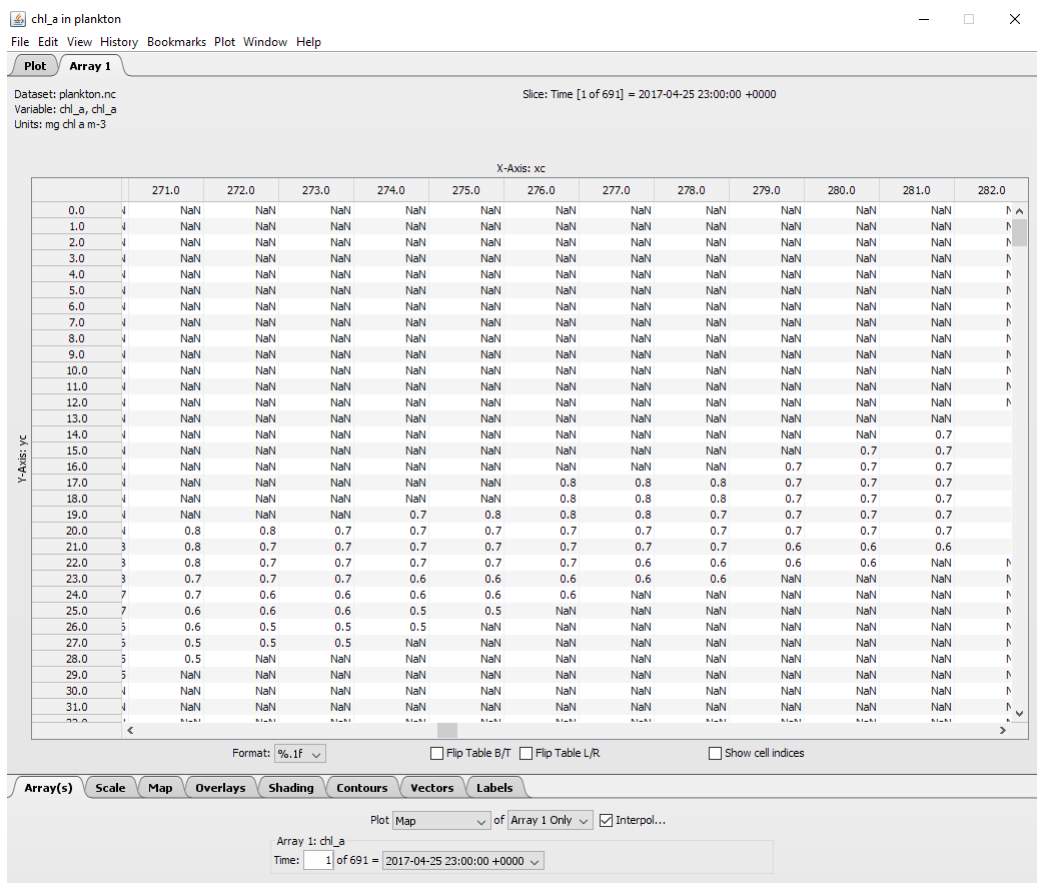
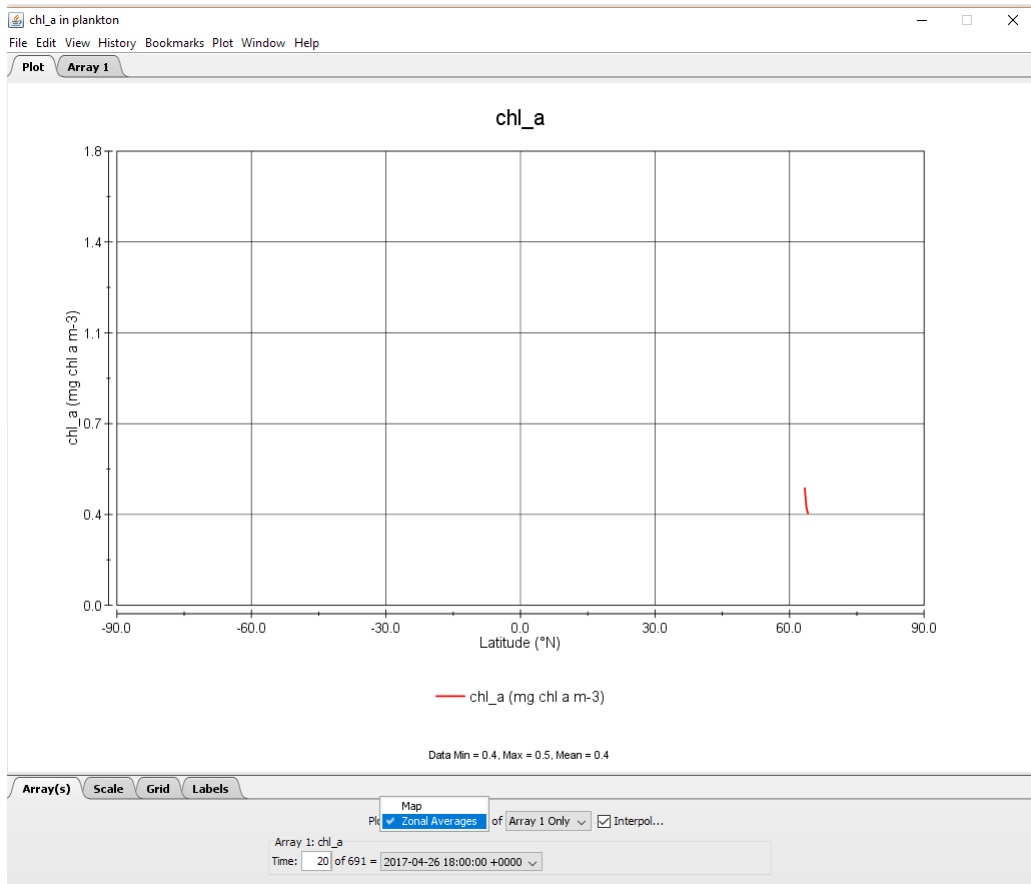


Figure 3.4: Panoply: Example of the Array option.



**Figure 3.5:** Panoply: Zonal averages plotting example.

Utilizing the "Plot" option, the data can be plotted as a map or as zonal averages, as demonstrated in figure 3.5. The plot option presenting the data on a map was utilized in the generation of the videos in the preliminary work. Figure 3.6 presents a few different options available for map-plotting.

Several maps are available for visualization, as demonstrated in figure 3.7. Several of the available maps are presented in figure 3.8.

Utilizing the equirectangular regional map, coordinates can be provided to manoeuvre to the data of interest. This is illustrated for the insertion of the coordinates of Norway in figure 3.9.

The *Map* input values were constant throughout the preliminary work and this thesis. The utilized values are given below, and presented in figure 3.10.

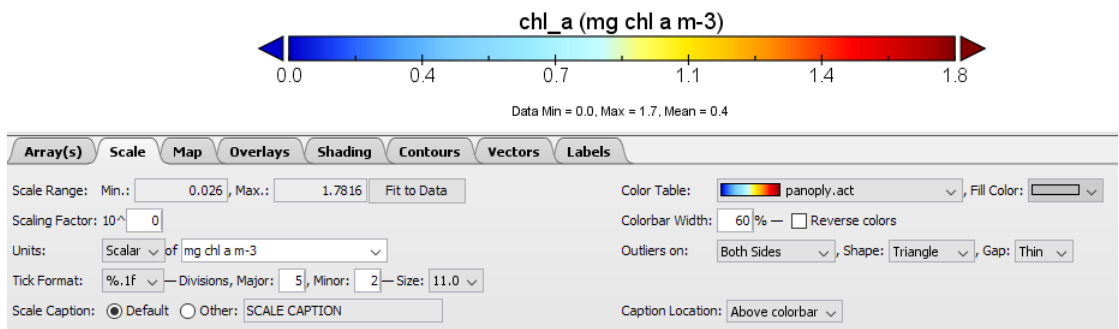
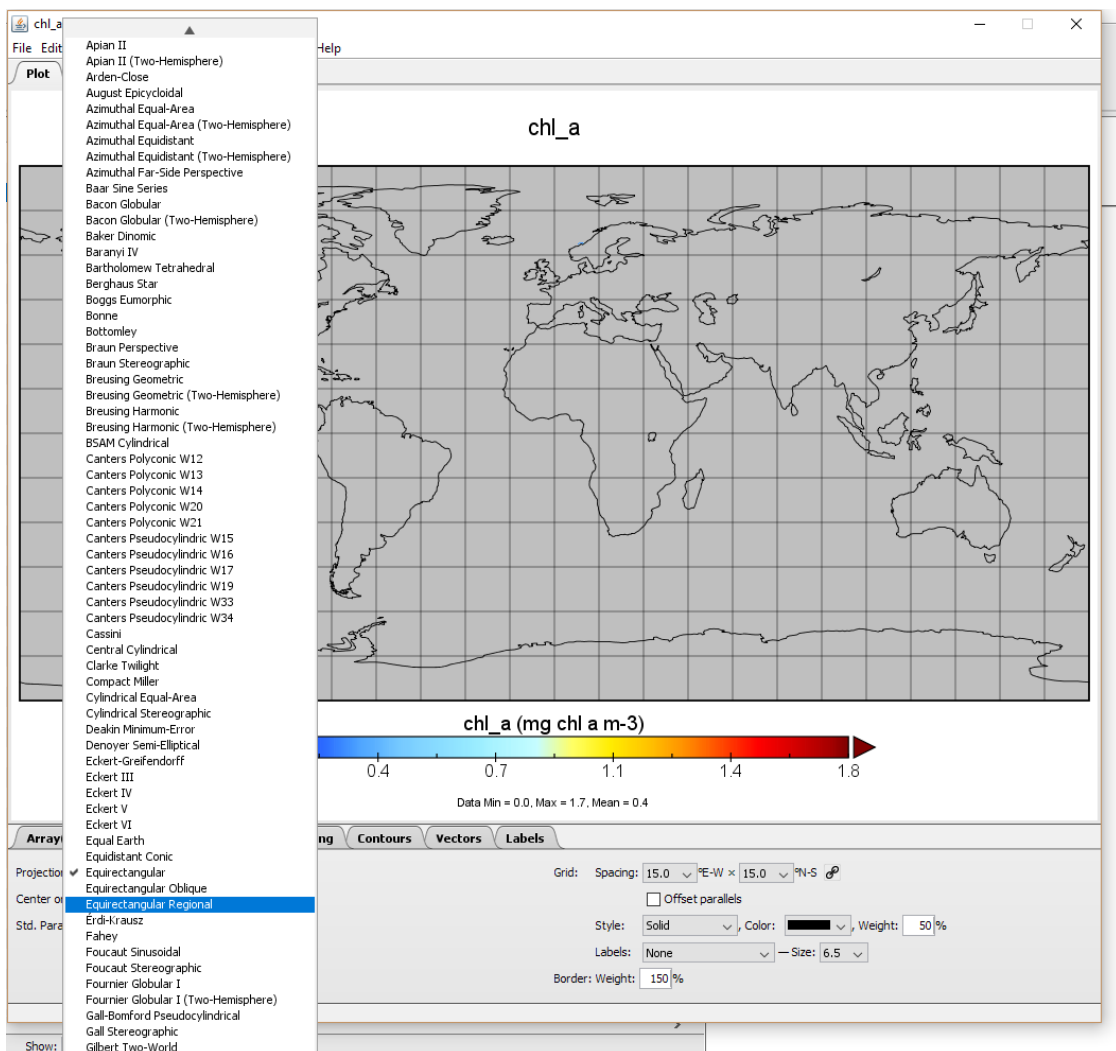


**Figure 3.6:** Panoply: Choices and menus available for the map-plotting.

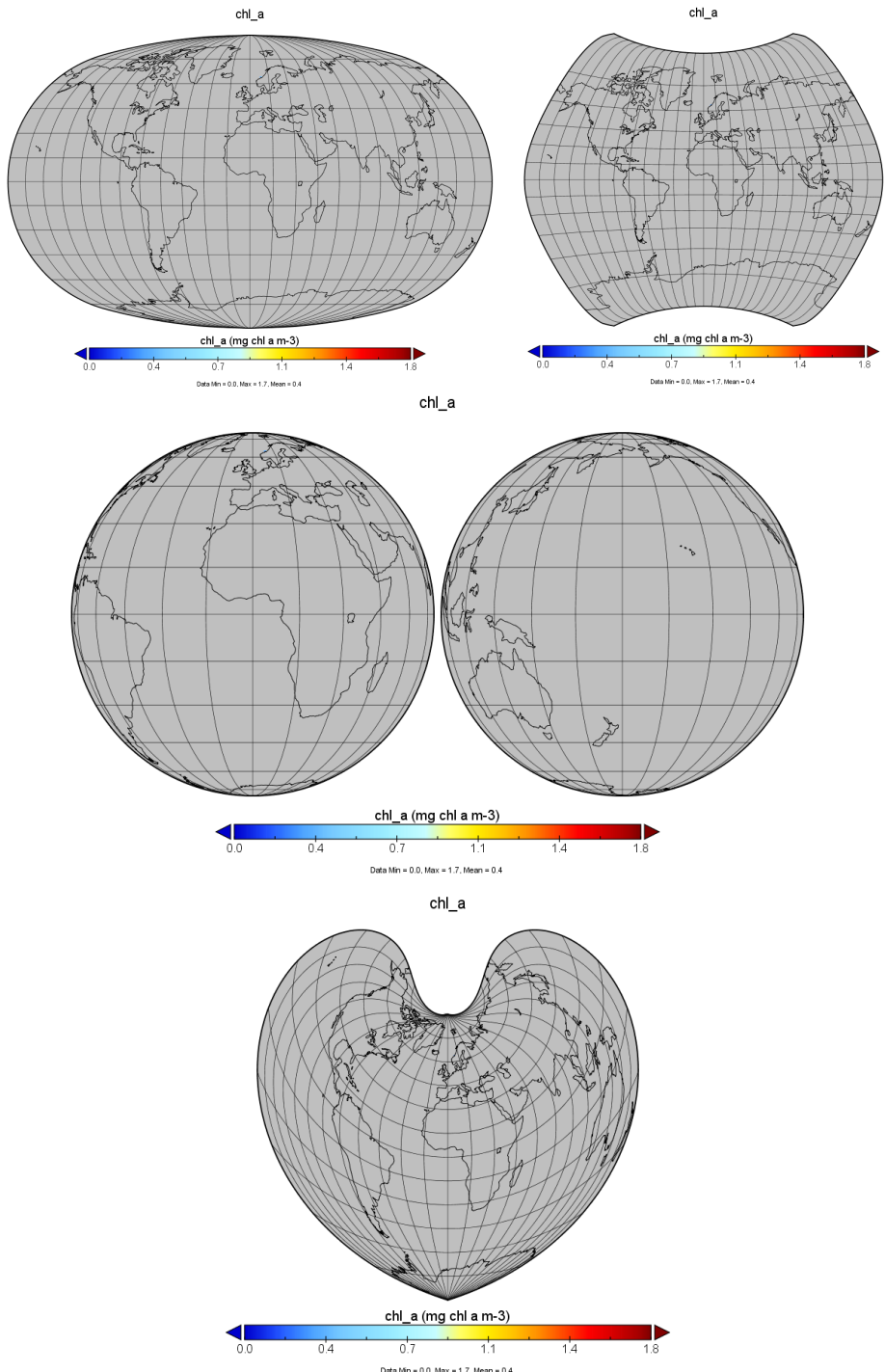
- Projection: Equirectangular Regional
- Center on: Lon. 8.8 E, Lat. 63.8 N
- Width: 3, Height: 1.5

Figure 3.11 delineates an example of a visualization given the variables set as above. The figure illustrates one time instance for the variable chl\_0\_50m.

Panoply provides the opportunity to create a video of the entire dataset. An option is to utilize the "time" variable, thus arranging all the time instances consecutively, resulting in a video.



**Figure 3.7:** Panoply: Several available maps.



**Figure 3.8:** Panoply: Several examples of available maps.

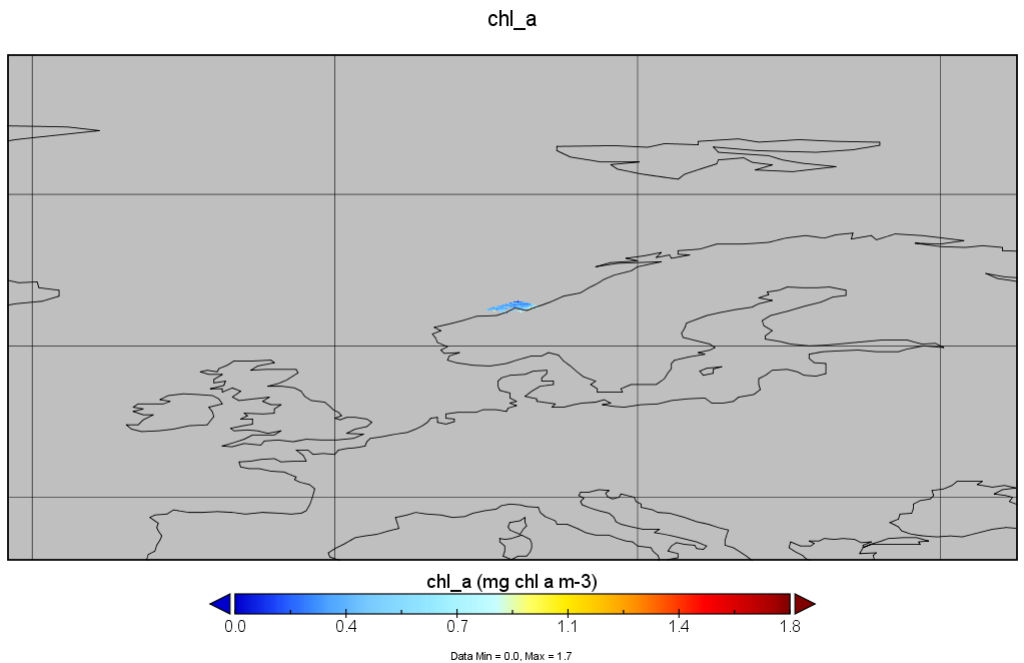


**Figure 3.9:** Panoply: Example of maneuvering towards the data of interest.



**Figure 3.10:** Panoply: Utilized values under the *map* option.

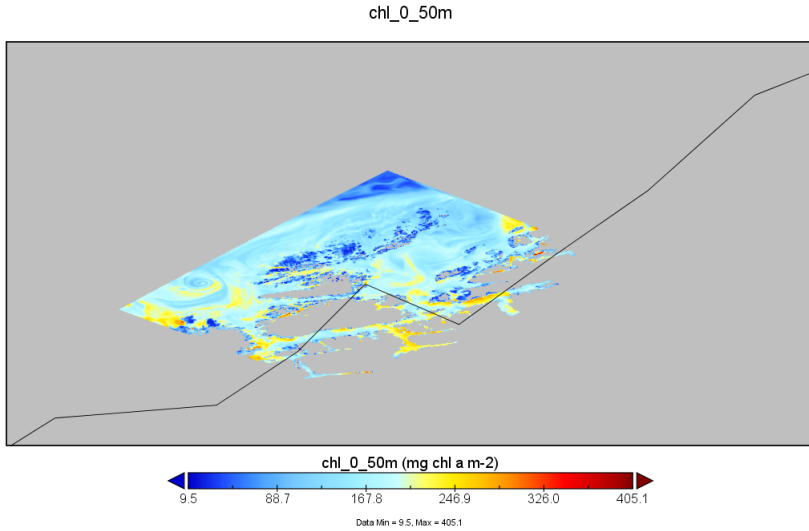


**Figure 3.11:** Panoply: Chl\_0\_50 m example, with utilized map variables.

### 3.3 PlanarRad

HydroLight is well suited for mapping geophysical variables to spectral signatures (Mobley). However, as HydroLight is a commercial software, PlanarRad, a functionally similar open source alternative, was utilized instead.

PlanarRad is a free open source code for modelling light in natural waters or other homogeneous scattering and absorbing media (Hedley [2008]). Some of the functionality offered by PlanarRad is a highly scriptable command-line interface, GUI front-end with interactive visualizations and plots, and nearly identical results to HydroLight, which can be verified by the user (Hedley [c]). PlanarRad is a C++ implementation of the invariant imbedded numerical integration technique for calculating radiative transfer in plane-parallel media with an opaque bottom boundary (Hedley [2008]). It is based on the algorithm described in Curt Mobley's book Light and Water. PlanarRad was designed for modelling light propagation in, and reflection from, shallow water environments. However, by setting a suitably large depth, an infinite depth solution is approximated. PlanarRad was developed by John Hedley.

PlanarRad calculates the light field and reflectances at a single point in space and time, based on the optical properties of the water at that moment (Hedley [2008]).

The options and possibilities made available by PlanarRad, and how they are performed, will be presented through an example. The example illustrates how to model the BRDF of a material for which the extinction and absorption coefficients are known, and for which

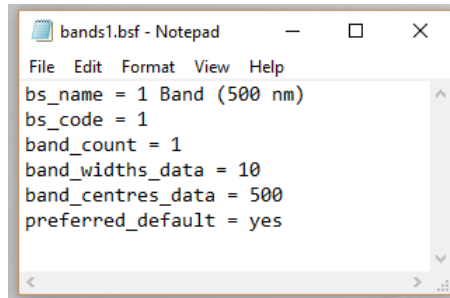


**Figure 3.12:** PlanarRad: Band specification file example.

it is assumed that the phase function is isotropic. The example will regard a volume of a material that is sufficiently thick that the material underneath it has negligible effect on its reflectance. The method, and explanation, regarding the utilization of PlanarRad is presented through the aforementioned example instead of through the actual utilization of PlanarRad performed in the preliminary work, as the project dealt with a huge data set, including 87 wavelength bands. For illustration purposes and explicit explanations, the example will be presented for one run with one wavelength.

Firstly, a band run must be set up (Hedley [a]). A single wavelength will be utilized in this example, thus a band specification file is set up to specify this. A text file called 'bands1.bsf' is created, and is presented in figure 3.12.

The explanation for the different elements in figure 3.12 is as follows (Hedley [a]):

- bs\_name - What will appear in PlanarRad to refer to this band specification.
- bs\_code - Will be appended onto the name of some automatically generated files.
- band\_count - Number of bands.
- band\_widths\_data - A comma separated list of the widths of the bands in nanometre.
- band\_centres\_data - A comma separated list of the centre wavelengths of the bands in nanometre.
- preferred\_default - If 'yes' the PlanarRad GUI will offer this band specification as the default.

A new folder titled e.g. 'testslab' is created, and 'bands1.bsf' is saved in it, as illustrated in figure 3.13.

At this point, PlanarRad can be run. The directory containing the band specification file, e.g. the "testslab" directory, is chosen by selecting "File > Change current working directory" from the menu. The information in "Bands:" under the "Model" tab, should read "1 Band (500 nm)". The run must be named, e.g. "run1". During the processing of the run, a folder titled as the run will be saved in the directory (Hedley [a]). This is where all outputs

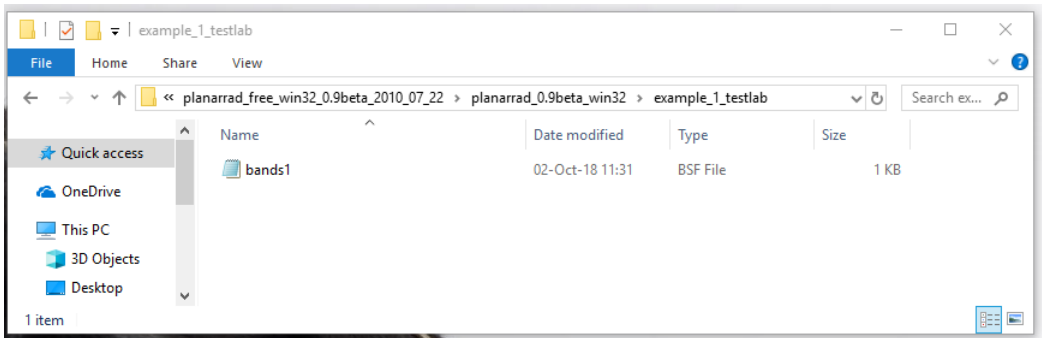


**Figure 3.13:** PlanarRad: Example of where to save the band specification file.

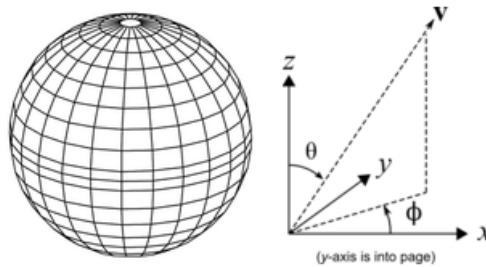


**Figure 3.14:** PlanarRad: Directional structure. Originally presented in Hedley [a].

will be saved.

Selecting the directional structure as HL Standard results in PlanarRad decomposing the sphere of all directions into segments in the same way HydroLight does (Hedley [2008]). That is, the upward and downward hemispheres are split into 9 by 24 segments of constant zenith and azimuth angle, as well as an end-cap. This is illustrated in figure 3.14.

The diagram on the right hand side of figure 3.14 indicates how the zenith angle  $\theta$  and azimuth angle  $\phi$  specifies a direction in PlanarRad. Every direction lies within a corresponding segment. PlanarRad, like HydroLight, works with the "quad averaged radiance", meaning the radiance in a particular direction is the radiance averaged over one of the segments (Hedley [2008]).

The average radiance in a particular segment can be considered an approximation of the radiance at the  $\theta$  angles. However, because the segments are wider at the bottom than at the top (Hedley [a]), they are not perfect rectangles. Thus, the centre with respect to solid angle is not the midpoint of the theta limits.

The segment at  $(\theta, \phi)$  of  $(0, 0)$  or  $(180, 0)$  is the end-cap, and thus the total number of segments in a hemisphere is a table of  $9 \times 24$ , with the end-cap in addition, i.e. 217

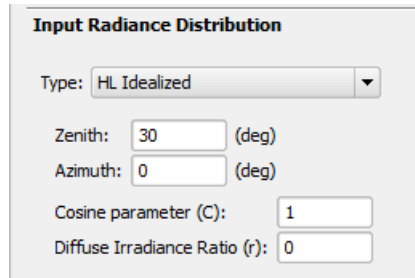


**Figure 3.15:** PlanarRad: Setting the diffuse irradiance ratio.

values. The whole sphere consists of 432 segments.

In hydrological optics the direction  $z$  is the depth into the water, and thus it increases downwards (Hedley [2008]). Therefore,  $z$  should be zero at the air-water interface and point downwards through the water. Figure 3.14 is thus frequently upside-down compared to the situation being modelled.

A straightforward use of PlanarRad is to model the directional radiance leaving the top of the slab of media for a given incident radiance distribution (Hedley [a]). The following sections describe how to perform the modelling for one incident direction (Hedley [2008]).

The radiance distribution must be defined. The example at hand models the directional reflectance arising from a light incident at zenith  $\theta = 30^\circ$  and azimuth  $\phi = 0^\circ$ . This is obtained by defining the input radiance to be zero in all segments except the one centred at the specified angles. The HL Idealized sky model is utilized by setting the diffuse irradiance ratio to zero, as illustrated in figure 3.15. In this context the cosine parameter has no effect, and can thus be left as 1 (Hedley [a]).

In the example at hand it is assumed that the interface between the slab of material and the air is perfectly flat. Thus, the relative refractive indices are given as presented in figure 3.16.

If the refractive index of the material is greater than the refractive index of air, as in this example, the slab will be slightly shiny (Hedley [a]). Since the surface is perfectly flat, the specular reflection should be very narrow in angular terms. However, since PlanarRad works with the average radiances in the segments of the sphere, it won't be fully captured by the outputs. That is to say, the angular resolution is limited to that of the discretization of the sphere. However, this is not an inaccuracy in itself, as it is an average radiance. If a bright spot exists within a segment its radiance is effectively spread over that segment (Hedley [a]).

The section regarding medium properties specifies the attenuation coefficient,  $c$ , and the absorption coefficient,  $a$ . Due to the fact that this example models a single wavelength

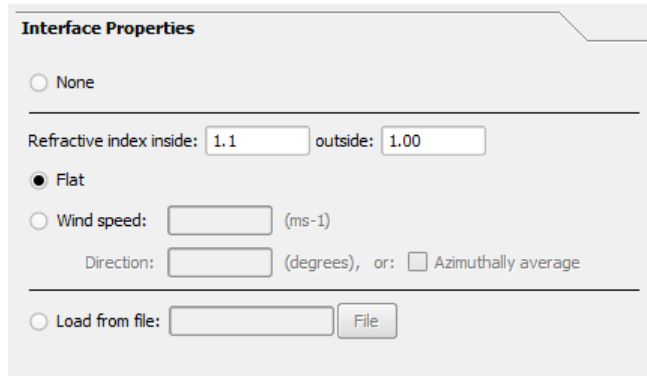


**Figure 3.16:** PlanarRad: Relative refractive indices.

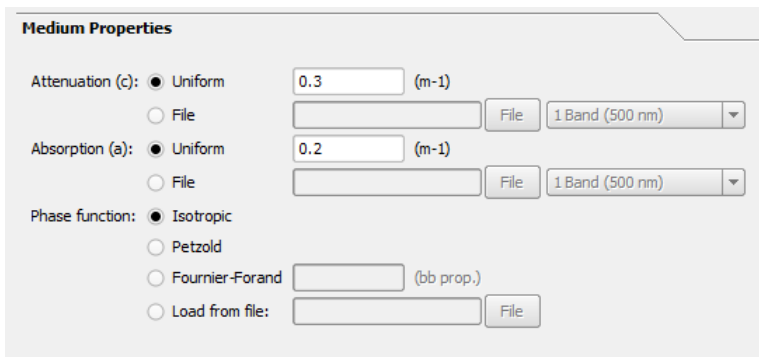


**Figure 3.17:** PlanarRad: Medium properties.

run, the attenuation and absorption coefficients are entered directly. An isotropic phase function is selected. Figure 3.17 demonstrates the mentioned medium properties inputs.

The units for the attenuation and absorption are expressed as per metre. However, in PlanarRad "metre" can be replaced by any dimension and the result will remain correct. This holds as long as the change is consistently applied. Stated otherwise, if every instance of "metre" is assumed to be "mm", the results remain correct (Hedley [a]).

Depth options must be specified. The depth is set to 20 m for this particular example. The entries "Sample interval" and "Delta evaluation distance" are for capturing the light field at certain points within the media. It is suggested that values around one tenth, or less, of the total depth for the sample interval are specified, and that the delta evaluation distance is set to a value that is small compared to the sample interval. The delta evaluation distance is utilized for internal calculation of the rate of change of the light field at the sample points. Figure 3.18 presents an example of specified depth options.

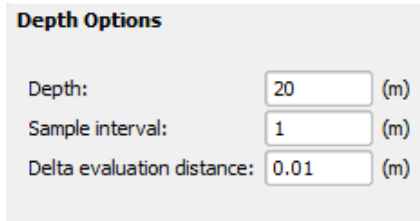


**Figure 3.18:** PlanarRad: Depth options.

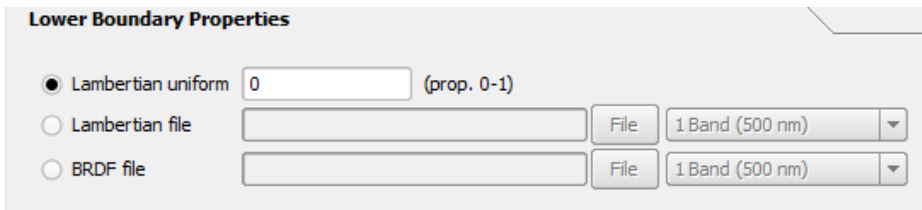


**Figure 3.19:** PlanarRad: Lower boundary properties.

The lower boundary properties describe the reflectance of the material underneath the water at the depth specified previously under depth options (Hedley [2008]). As this example assumes that the medium is sufficiently thick that what is below it is irrelevant, the reflectance is set to zero. This is demonstrated in figure 3.19.

After the mentioned specifications are defined and selected, PlanarRad is ready to process the run. After the run is processed several resulting visualizations are available.

One of the resulting visualizations will be similar to figure 3.20. The figure illustrates the profile of downwelling planar irradiance in the media. The downwelling planar irradiance value is zero from roughly 16 m and below in figure 3.20. This is expected as it corresponds to the specification of the media being thick enough that the light penetrating through it will not be reflected by the bottom underneath.

Another resulting figure is presented in figure 3.21. The figure illustrates a hemispherical fisheye view from just below the air-media interface, i.e. inside the media. The hemisphere on the left hand side of the figure illustrates the scene of the fish-eye looking upwards. This is to say that the figure illustrates the distribution of downwelling radiance. The white segment in the figure is the light source. The bright colored bands at the edge of the fish-eye view represent internal reflection from just below the air-media interface. The colors are meaningless, as they are PlanarRad's interpretation of 500 nm as a color (Hedley [a]).

The hemisphere on the right hand side of figure 3.21, illustrates the scene with the hemispherical view downwards, i.e. it presents the upwelling radiance distribution. This figure provides an impression of the reflected light distribution needed for the BRDF. However,

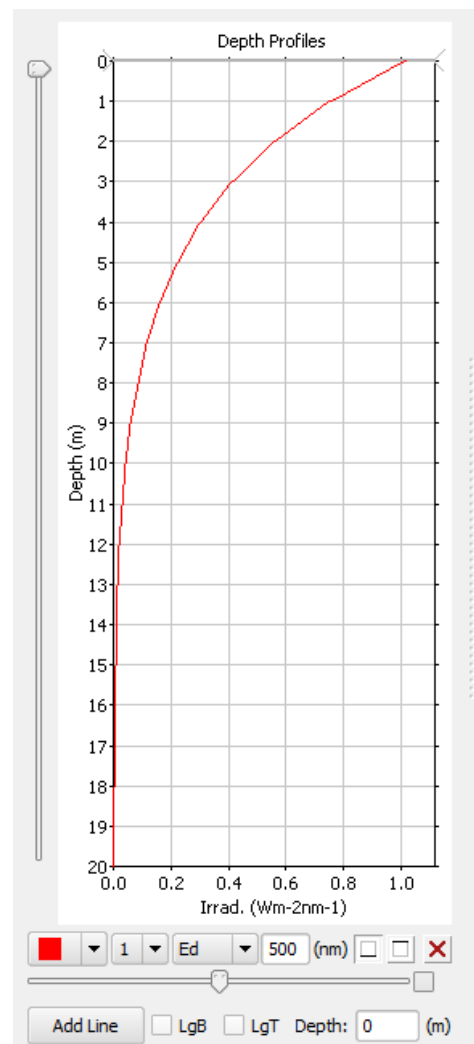


**Figure 3.20:** PlanarRad: Illustration of the profile of downwelling planar irradiance in the slab of media.

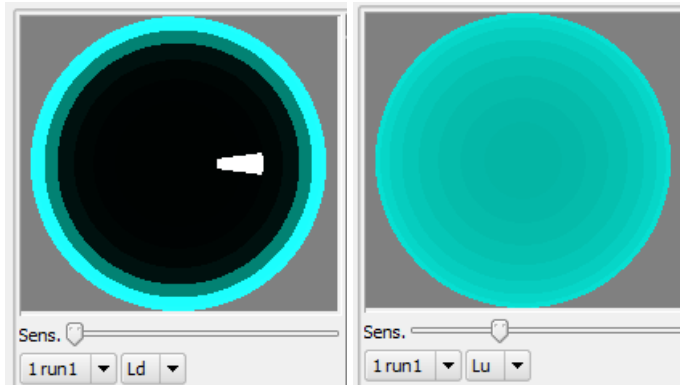


**Figure 3.21:** PlanarRad: Hemispherical views.

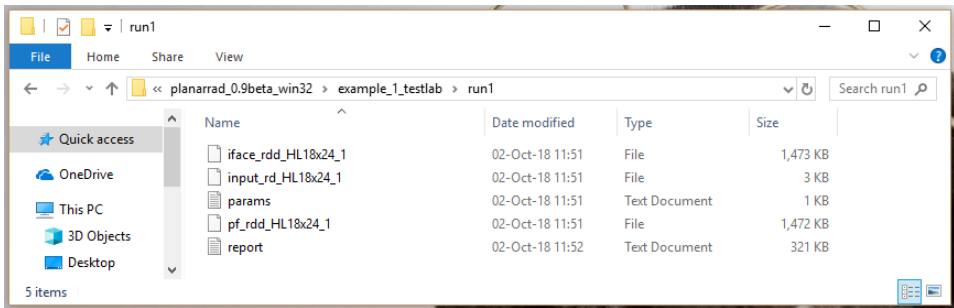


**Figure 3.22:** PlanarRad: Location of the report file.

the figure illustrates the values just below the air-media interface, not just above (Hedley [a]), as is required for the BRDF. The water leaving radiance distribution will be directionally modified by refracted transmission through the air-media interface (Hedley [a]).

The values of interest for the creation of the BRDF are available in the output report file, titled "report.txt". The report is saved in the run directory. Figure 3.22 presents an example of the contents of a run directory.

The report file can be opened with WordPad, Notepad++, Excel or similar programs, and contains several outputs of interest, such as the entry titled "L\_a Band 1". This entry represents the segment averaged radiances over the sphere of all directions just above the air-media interface. Each row of numbers represents one horizontal band around the sphere, i.e. for a specific zenith angle. The numbers start at azimuth  $0^\circ$  and increment with  $15^\circ$  for each step. The top row corresponds to a zenith angle  $\theta = 0^\circ$ , the next row represents  $\theta = 10^\circ$ , etc. (Hedley [a]). The last row has a single entry, which represents the bottom cap.

The values presented in the L\_a tables represent the radiance in the given direction. In this particular example, the values in the entire upward-looking hemisphere, i.e. the top

$$2.2817E-02 \times \cos(30.376) \times 50.800 = 1.0000 \text{ W m}^{-2}$$

**Figure 3.23:** PlanarRad: Mean point theta.

rows of the table, are zero, except for the entry corresponding to  $\theta = 30^\circ$  and  $\phi = 0^\circ$ . This direction has a value of 50.8 [ $\text{W m}^{-2} \text{ sr}^{-1} \text{ nm}^{-1}$ ], which confirms that the media has been illuminated with light from one segment only. The lower part of the table is the downward-looking hemisphere, and thus the values are the BRDF response to the illuminated direction (Hedley [a]).

There are several options regarding the units of the given values of the BRDF. The BRDF can be presented as a radiance-to-radiance ratio. In this case, in the example above, all the output values should be divided by 50.8, as this results in the BRDF response being presented as radiance for an unit incident radiance (Hedley [a]). However, a more common representation is to express the BRDF as a radiance response per unit incident planar irradiance, i.e. in the units  $\text{sr}^{-1}$ . In such a situation, the resulting radiances must be scaled to correspond to a unit incident irradiance on the plane. Nonetheless, this scaling is already performed in PlanarRad, as this method is integrated in the input radiance model. Put simply, the scaling of values is not necessary. This assertion will be demonstrated by performing the conversion. The incident radiance of 50.8 [ $\text{W m}^{-2} \text{ sr}^{-1} \text{ nm}^{-1}$ ] is multiplied by the solid angle of the segment weighted by the cosine of  $\theta$ . The solid angle of each segment is available in the table named 'Quad solid angles' in the report. For the segment at hand, the solid angle value is  $2.2817 \times 10^{-2} \text{ sr}$ . The calculation of the incident irradiance from the segment at  $\theta = 30.376^\circ$  is presented in figure 3.23. The mean point theta  $\theta = 30.376^\circ$  is utilized due to the wedge-shaped segments.

As demonstrated, the radiance values in the lower half of the 'L\_a' tables are the BRDF for the specified incident illumination direction, in units of  $\text{sr}^{-1}$ .

PlanarRad can be utilized to generate a BRDF file that can be used as the bottom boundary condition for a different run (Hedley [a]). Thus, a layered media can be implemented. However, this was not performed in the preliminary work, nor in this thesis, and will therefore not be discussed further.

## 3.4 COART

Coupled Ocean and Atmosphere Radiative Transfer (COART) is a tool provided by NASA, which is public on their internet sites. The tool is able to calculate and simulate radiance and irradiance at any levels in the atmosphere and ocean (Jin [b]). The calculations can be controlled by specifying inputs. The following section describes the input values in detail.

COART can be reduced to a conventional atmospheric radiative transfer model, i.e. at-

mosphere - surface system, by setting the ocean depth as zero (Jin [a]). The surface albedo must still be provided. That is, the atmosphere-ocean system is reduced to a atmosphere-land system. In this case, the bottom albedo will be assumed as the Lambert surface albedo.

The COART model was based on the Coupled Discrete Ordinate Radiative Transfer (CDISORT) code, which was developed from DISORT. DISORT is a publicly distributed software for radiative transfer, provided by NASA (Jin [a]).

The atmospheric absorption calculated in COART is based on the LOWTRAN7 band model (Jin [a]). The default amounts of trace gases, such as total precipitable water, Ozone,  $CO_2$ , and  $CH_4$ , which are defined in the standard atmospheric models, are utilized in COART. However, these values can be altered if desired.

COART offers several standard aerosol models. Any one of these can be utilized in the COART calculations. The tropospheric and stratospheric aerosol models are based on the MODTRAN models (Jin [a]). The aerosol loading can be defined by user input, through variables such as visibility and Aerosol Optical Thickness (AOT) at 500 nm or 550 nm, or by uploading an aerosol scattering phase function file. User defined aerosol loading requires the aerosol optical properties as inputs. Up to 10 wavelengths are available for user inputs.

COART offers the opportunity to select clouds from three available types, i.e. water clouds, spheric ice clouds, and non-spheric ice clouds. Inputs regarding the cloud modeling, such as the bottom and top heights (km) above surface, effective radius and either liquid water path or cloud optical depth, can be defined by the user. The optical properties for modelling water clouds in COART are based on Hu and Stamnes (1993). The modelling of spheric ice clouds is based on Mie calculations, and the modelling of non-spheric ice clouds is based on Fu's (1996) parameterization for Cirrus clouds (Jin [a]). Not including clouds in the system is also an option.

Figure 3.24 illustrates how the angles  $\phi$ ,  $\theta$  and  $\theta_0$  are defined in COART.  $\theta_0$  represents the solar zenith angle,  $\theta$  is the radiance zenith angle, and  $\phi$  is the relative radiance azimuth angle.  $\theta$  has a range of  $0^\circ$  -  $180^\circ$ , where  $0^\circ$  is straight-up,  $90^\circ$  is at the horizon and  $180^\circ$  is straight-down.  $\phi$  has a range of  $0^\circ$  -  $360^\circ$ , where  $0^\circ$  represents forward scattering and  $180^\circ$  represents back scattering. The origin is just above the ocean, or land, surface. Thus only the angles illustrated in figure 3.24 are of interest.

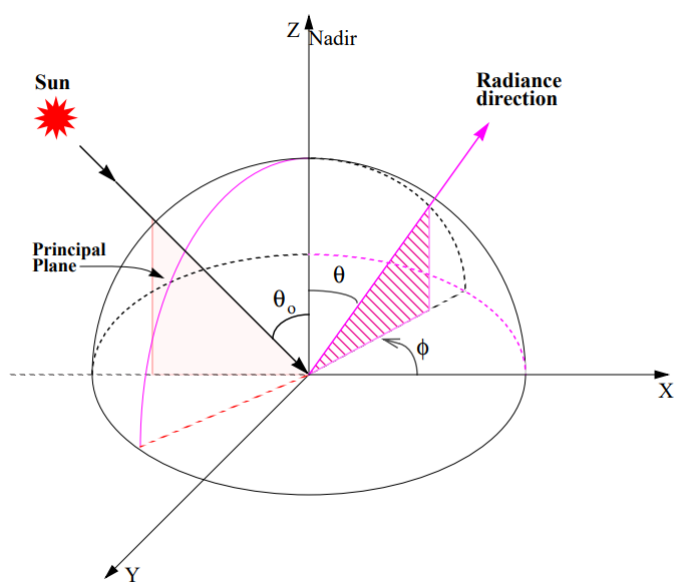


**Figure 3.24:** Angle definitions in COART. Originally presented in Jin [a].

## **Part II**

# **Method**

This section details how the research was conducted, the research methods utilized and the reasons for applying the presented methods. The part includes six chapters. The first chapter regards the altering of the MATLAB files created in the preliminary work. The second chapter regards the development of batch runs for PlanarRad. The third chapter regards examining the resulting radiance in different scenarios, with regard to viewing angles, solar angles and cloud states. The fourth chapter regards the development of a lookup table. The fifth chapter presents a temporal sensitivity of data acquisition analysis. The final chapter regards the development of a user friendly interface for the created software.

The altered MATLAB files were employed together with the batch runs for PlanarRad in order to examine the different scenarios. However, in order to simulate a whole scene and perform a temporal sensitivity of data acquisition analysis, developing several lookup tables was essential. Finally, a user friendly software interface was developed. The program is titled the RadPhyll Simulator and uses the created lookup tables.

# Chapter 4

## Combining The MATLAB Files From The Preliminary Work

The first performed task for the thesis at hand was to combine the MATLAB scripts created the previous semester, as part of the preliminary work, into two compact and further automated scripts. The motivation was to simplify the simulation process, by not being dependent on several input files nor on numerous manual inputs. The 11 scripts created in the preliminary work were combined into two scripts, i.e. one for calculations prior to PlanarRad, and one for calculations post PlanarRad. That is to say, one script calculates the inputs required by PlanarRad, while the other script utilizes the outputs from PlanarRad to calculate, and create, the final hyperspectral cube.

The first script is titled "Pre\_PlanarRad.m" and regards absorption calculations, scattering calculations and attenuation calculations. The second script is titled "Post\_PlanarRad" and regards calculating the hyperspectral cube radiance values [ $W\ m^{-2}\ \mu m^{-1}\ sr^{-1}$ ], creating the hyperspectral cube, and several plotting possibilities. Calculating the hyperspectral cube radiance values consists of calculating the water leaving radiance at TOA, the radiance due to atmospheric effects that is reflected to TOA by the ocean surface, and the total radiance at TOA.

The six following sections regard *Pre\_PlanarRad.m*. The band-centers are specified in correspondence to the HSI V6, i.e. the camera that is to be used by the HYPSO mission, wavelengths. The HSI V6 and the HYPSO mission are presented in section 1.3.

The absorption calculations include absorption due to chl.a concentration and due to pure water, as well as total absorption calculation. The absorption values [ $m^2 g^{-1}$ ] due to chl.a concentration are given by [Bidigare et al. [1990]] for certain wavelengths. These values are converted to the unit of  $m^{-1}$ , by being multiplied with 1000 as well as with the

SINMOD chl\_a concentration values of interest. The values from [Bidigare et al. [1990]] corresponding to the wavelengths that coincide with the specified band-centers are saved for further calculations.

The calculation of the pure water absorption is performed by utilizing absorption values [ $cm^{-1}$ ] from [Buiteveld et al.]. These values are converted to the unit of  $m^{-1}$  by being multiplied with 100. The absorption values of interest are obtained from the provided dataset, i.e. from [Buiteveld et al.], by selecting the values corresponding to the wavelengths that coincide with the specified band-centers. The total absorption is calculated by summing the absorption due to chl\_a concentration and absorption due to pure water.

The scattering calculation consists of calculating scattering due to phytoplankton and water, as well as calculating the total scattering.

The calculation of scattering due to phytoplankton utilizes a script from [Bohren and Huffman], titled *bhmie*, in order to obtain the scattering efficiency, which is used in order to calculate the scattering coefficient. The phytoplankton in the SINMOD dataset consists of diatoms and flagellates. Thus, the scattering efficiency must be calculated separately for the two algae groups. The function *bhmie* is based on Mie scattering theory, presented in section 2.1.3, and requires size parameter =  $\frac{2\pi*\lambda}{radius}$ , refractive index in complex form, and the number of viewing zenith angles between 0 and  $\frac{\pi}{2}$  to be used in the phase function corresponding function, as inputs. The size parameter is required for the diatoms and for the flagellates, and is dependent on their radii and on the specified wavelength. The radii of diatoms and flagellates are specified as 55 [ $\mu m$ ] (UCL) and 5.5 [ $\mu m$ ] (Leadbeater and Green [2000]) respectively. The refractive index is specified as  $1.03 + 0.02 * i$  (Aas [1981]). The number of viewing zenith angles is set to three. The results from the *bhmie* function are a function corresponding to a phase function, extinction efficiency, scattering efficiency, backscatter efficiency and an asymmetry parameter. The only variable of interest is the scattering efficiency. The given number of viewing zenith angles is applied in the calculation of the function corresponding to a phase function, and is required to be set to at least two. However, as the resulting function is not of interest, the number of viewing zenith angles does not affect the desired results. The two scattering efficiencies are employed in the scattering coefficients calculations, which are separate for diatoms and flagellates. The aforementioned calculations are performed by multiplying the diatoms and flagellates concentration [ $mmol\ N\ m^{-3}$ ] values from the SINMOD data with  $\pi$ , as well as with their respective *diameter*<sup>2</sup>, and dividing the result by 4. Furthermore, the resulting value is multiplied with the calculated scattering efficiency value. The total scattering coefficient for phytoplankton is calculated by summing the coefficients of diatoms and flagellates.

The scattering due to water is calculated by utilizing a function, titled *betasw\_ZHH2009* (Zhang et al. [2009]). *betasw\_ZHH2009* requires wavelength [nm], temperature [C], viewing angle  $\theta$ , salinity and depolarization ratio as inputs. The function results in several outputs. Nonetheless, the only output of interest regarding the task at hand is the total scattering coefficient. The specified band centers are applied as input wavelengths, while

$\theta$  is set to the viewing angle of interest. The temperatures are provided in the SINMOD dataset. The salinity value is defined as 34.9 [ppt] (Gordon). The default depolarization ratio value, i.e. 0.039, is selected. The total scattering is calculated by summing the scattering due to phytoplankton and the scattering due to water.

The total attenuation is the summation of the total absorption and the total scattering.

The following sections will regard *Post\_PlanarRad.m*. *Post\_PlanarRad.m* requires the water leaving radiance [ $sr^{-1}$ ] from PlanarRad for 87 wavelength bands as input. These input values are arranged into a cube. The script includes radiance values [ $W\ m^{-2}\ \mu m^{-1}\ sr^{-1}$ ] obtained from COART at the height of 100 km, and at 1m, above the ocean surface. The mentioned radiance values are utilized to calculate the radiance ratio between 1m and 100 km. The calculated ratio is used in the calculation of the water leaving radiance at TOA, by multiplying it with the water leaving radiance.

The radiance at 1 m above the ocean surface due to atmospheric effects that is reflected by the ocean surface and propagates to TOA is calculated by multiplying the radiance values at 1 m with the aforementioned ratio. The total radiance at TOA is calculated by summing the water leaving radiance at TOA, the radiance values at 100 km obtained from COART, and the radiance due to atmospheric effects that is reflected to TOA by the ocean surface.

The resulting total radiance at TOA is saved as a cube, resulting in the hyperspectral cube with radiance values at TOA. The hyperspectral cube represents the radiance values [ $W\ m^{-2}\ \mu m^{-1}\ sr^{-1}$ ] the HYPSO satellite, see section 1.3, would measure while in orbit.

Several calculations were performed in order to provide distinct plotting options, such as calculations of the total radiance at TOA due to atmospheric effects. The calculation of the percentage of water leaving radiance out of the total radiance at the surface, as well as at TOA, is also part of the script. Other plotting calculations include water leaving radiance at the surface and at TOA, and the total radiance at TOA. The possibility of plotting different combinations of the mentioned values is available.

# Developing Batch Runs For PlanarRad

## 5.1 Installation And Python Interface

The program PlanarRad was employed in the preliminary work for calculating the water leaving radiance given absorption and attenuation, see sections 3.3 and 2.1.5 for theory regarding this process. For this thesis it was essential to modify PlanarRad so that it could calculate several runs at once, i.e. run batches, due to the objective of developing temporal and data handling efficiency for the simulation tool. This was more challenging than first assumed. The intention was to utilize a python interface, titled PlanarRadPy, developed for this specific purpose by Daniel Marrable. The source code can be found here: [Marrable [a]].

PlanarRadPy is a tool, more precisely a front end, written in Python that can execute PlanarRad (Marrable). The tool can be utilized for running PlanarRad in batches, i.e. the tool makes it easier to run copious different parameters as well as collating the results, rather than running PlanarRad individually each time different parameters are desired (Marrable [2019]). It is possible to distribute the computations over many CPUs. This is performed by running an instance for PlanarRad on each available core, or for the number of cores specified by the user (Marrable). A unique directory is created to save the outputs for every possible combination of the batchable parameters (Marrable). Thus, one can specify several variations of parameter values at the time.

Several issues occurred with regard to the utilization of PlanarRadPy. The first difficulties regarded the Python version. The interface was written in python 2.7, and thus some functionality and syntax were outdated for the Python 3 version on which the interface

was run. The solution was to update the scripts. A period of time was spent altering the interface to work properly. However, as issues still occurred, it was attempted to run the interface on Python 2.7. This was unsuccessful as well. It was therefore attempted to run the interface on Linux, instead of on Windows. For this purpose partition was performed on the computers hard drive. Partition enabled the possibility of utilizing both Windows and Linux without utilizing a virtual machine, which is an emulation of a computer system (Smith and Nair [2005]).

PlanarRad was downloaded for Linux. The procedure can be found here: [Hedley [d]]. However, it did not run properly. Thus, Ubuntu 18 was uninstalled and replaced by Ubuntu 13. PlanarRad had been tested on Ubuntu 13 in 2013 by John Hedley, the developer of PlanarRad (Hedley [e]). The installation of Ubuntu 13 proved to be difficult, possibly due to Ubuntu 13 not being compatible with the used motherboards chip set. Ubuntu 16 was therefore installed instead. PlanarRad ran successfully on Ubuntu 16.

Making the python interface to run properly was still difficult. Many errors occurred, and thus the batching did not work properly for a long period of time. As a result, several wavelengths had to be run alone, while other wavelengths, i.e. 503.5 - 535.7 and 558.7 - 572.5, had to use different attenuation values. The issues were due to the scattering input file having been written over at an earlier point. The scattering input file was corrected, and thus all the wavelengths could be run together, as intended. Furthermore, after several paths and the input file were altered, the interface worked as intended. The input file was altered due to PlanarRad not managing all possible input values for the solar zenith angle, initially believed to be due to missing sky-files for these values. Sky files are files created by PlanarRadPy in order to simulate conditions such as cloud state. However, the reason was due to the attenuation input file containing values that contradicted the values in the scattering input file. PlanarRad was able to run batches. The Python interface could be run through a GUI or through the command-line. A test was performed regarding whether the same results are produced regardless of whether one utilizes the GUI or not. The test revealed that the same results are indeed produced.

## 5.2 Inputs And Outputs

The batched version of PlanarRad can be run from a command-line by typing "python planarradpy.py -i <input\_parameter\_file>" (Marrable [b]).

A folder is created for each combination of input variables when PlanarRad is run on batches. Each folder contains a text-file, "batch.txt", and the report created by PlanarRad, as explained in section 3.3. The batch file contains information regarding the input variables, file paths and variables such as the Euler steps per optical depth. In addition to these results, a batch report is created. If the batch report is opened as a .csv file in a fit program, each column corresponds to the IOP bio-optical model parameters followed by the values of interest at each wavelength. This is illustrated in figure 5.1. The batch report obtains the values of interest from each individual report, and combines them into one file. More

Sun Azimuth (deg)	Sun Zenith (deg)	Phytoplankton	Scattering X	Scattering Y	CDOM G	CDOM S	Depth (m)	#wave length (nm) ->	402.3	406.9	411.5	416.1
0	20	1	1	1	1	1	4		0.017328	0.017328	0.017328	0.017328
0	60	1	1	1	1	1	4		0.70379	0.70379	0.70379	0.70379
0	80	1	1	1	1	1	4		8.5917	8.5917	8.5917	8.5917
0	40	1	1	1	1	1	4		0.025419	0.025419	0.025418	0.025418

**Figure 5.1:** Example of a batch report from PlanarRad, before the alterations.

precisely, PlanarRadPy offers the possibility to retrieve specified values from the different reports, e.g. the spectral remote sensing reflectance values of interest can be obtained by specifying `rrs@<zenith-theta>:<azimuth-phi>` in the variable `report_parameter` in the input file.

The values of interest from the PlanarRad reports for the preliminary work were the values placed first in the 11th row in the L\_a table. This corresponds to the values for the viewing angles  $\theta = 80^\circ$  and azimuth =  $0^\circ$ . Therefore, the input "rrs@80.0:0.0" should have been able to be used for the batched version of PlanarRad to retrieve the same values for this thesis. However, due to two parameters being out of order in the call for `interpolate.py`, an error occurred. This was fixed. Nonetheless, the retrieval of the values of interest was hard-coded into the script. This was done to ensure the retrieval of the correct values in a time effective way, as the Python interface was to be applied in the creation of lookup tables, and not as a final solution.

The initial values which were available for batching, that is before the Python interface was altered, were the sun azimuth angle [deg], the sun zenith angle [deg], phytoplankton linear scaling factor, the scattering scaling factor, the scattering slope factor, CDOM absorption scaling factor, CDOM absorption slope factor and the depth [m] (Marrable [b]).

The phytoplankton linear scaling factor should be a normalized vector such that the absorption is '1' at 440 nm. The scaling factor adjusts the total absorption (Marrable [2019]). More sophisticated models do exist (Marrable [2019]). This model was not employed in this thesis as the calculations performed in the preliminary work are more intricate. Thus, specific input files are applied instead.

Several available input parameters for batching, e.g. phytoplankton linear scaling factor, scattering scaling factor, scattering slope factor, CDOM absorption scaling factor and CDOM absorption slope factor, are not utilized in this thesis due to their purpose being calculating the absorption and attenuation files. The absorption and attenuation files are, in this thesis, provided beforehand. Furthermore, the scripts defining PlanarRadPy initially contained functions that were not necessary for this thesis. These functions were ones regarding the calculation of total absorption, water absorption, phytoplankton absorption, CDOM absorption, total scattering, backscattering, attenuation from absorption, attenuation from scattering, and several scaling functions. The scripts were initially also able to calculate directional AOP, more precisely the subsurface spectral remote sensing reflectance values. However, as this was not of interest for the thesis, the values of interest were retrieved directly from the desired table.

This section will present the inputs for the batch version of PlanarRad after the Python interface was altered. A batch name must be specified. The bio-optical parameters list only includes solar azimuth angle, solar zenith angle and depth options. The wavelengths of interest must be provided by the user, as well as the number of CPUs. The PlanarRad path is required. Furthermore, it is required to specify paths for the absorption, attenuation, scattering and bottom reflectance files. Finally, a new input, that can specify the IOP type was added. This variable can be set to "isotropic", "isotropic\_integ", "petzold" or "pure\_water".

# Examining Different Scenarios

Several scenarios, e.g. different viewing and solar angles, were of interest regarding examining what affects the water leaving radiance being measured at the surface and the radiance being measured at TOA. The results will assist with making informed system and mission choices, as well as with understanding the possible mission scenarios, and thus facilitate proper resource management. The tests were performed with the batched version of PlanarRad and with COART. The viewing and solar angle tests are motivated by the fact that the recorded radiance could be dependent on the viewing and solar angles due to absorption and scattering in the atmosphere, as well as due to the ocean surface not being a Lambertian surface. That is, the ocean surface will not reflect radiance equally into all directions.

The following tests regard the effect on the water leaving radiance, and the radiance at TOA, due to variation of solar azimuth angle, solar zenith angle, viewing azimuth angle and viewing zenith angle. Tests regarding the impact of clouds being present were also executed.

The following tests were performed with the same environmental surroundings, phase functions and depth options. Thus, the variations in the results are only due to the variation of the input parameters.

The following sections present the applied COART inputs, unless otherwise stated.

COART was prescribed to calculate radiances [ $W\ m^{-2}\ \mu m^{-1}\ sr^{-1}$ ] at multiple wavelengths from 0.4 to 0.8 [ $\mu m$ ] at every 0.005 [ $\mu m$ ]. The water leaving radiance output was not included, as these are provided by PlanarRad. Thus, the output represent only the radiances due to the atmosphere. The resulting radiances were presented at TOA and at the ocean surface. The wavelengths were selected as presented in order to correspond to the wavelengths of interest for the HYPSO mission.

The solar zenith angle was directly inputted to  $60^\circ$ . COART operates with mean Earth-sun distance when solar zenith angles are user defined.

COART was specified to use less atmospheric layers in order to save computation time. The effect of this varies slightly with regard to wavelength and specified height above the ocean surface. However, using less atmospheric layers generally results in a variation in results between 0.02% and 0.4%. As long as all calculations use this specification, the analyses will not be significantly affected (Jin et al. [2006b]). Furthermore, the trace gas amounts of  $CO_2$  and  $CH_4$  were set to the values recommended by COART. The mixed layer aerosol was set to the MODTRAN maritime model, while the stratospheric aerosol was set to a background model. The aerosol loading was specified by the aerosol optical thickness (AOT) at  $0.5 \text{ } [\mu\text{m}]$  of 0.2, as recommended by COART. Generally COART was not to model clouds. The intention was to model general radiance values, i.e. with no specific amounts of gases or clouds. Furthermore, the aerosol model was chosen to be maritime due to the SINMOD data being recorded in maritime conditions.

The depth was 0 meters. Thus, COART ignored the inputs regarding ocean conditions. That is, COART modelled an atmosphere-land case. The bottom albedo was defined to be 0, as modelling a black surface prevents the COART outputs to include values of reflected radiance from the ocean surface.

## 6.1 Viewing Zenith Angle Definitions

The viewing zenith angles are defined differently in PlanarRad and in COART. Figure 3.24 illustrates the angles definition in COART. Figure 3.14 illustrates the angles definition in PlanarRad. The origin in COART is just above the ocean surface. Thus, only the angles presented in the figure are above the ocean surface. In PlanarRad however, the whole illustrated sphere is just above the ocean surface. Thus the lower half of the illustrated sphere has a direction down towards the ocean surface. Furthermore, the viewing zenith angle direction in PlanarRad is defined as the direction of an observer in the origin. The viewing zenith angle direction in COART is defined as the direction the observed radiance propagates. The viewing zenith angle in PlanarRad must be specified between  $90^\circ$  and  $180^\circ$  in order to obtain water leaving radiance values. The viewing zenith angle in COART must be specified between  $0^\circ$  and  $90^\circ$  in order to obtain radiance reflected by the ocean surface or radiance due to atmospheric effects that propagates from below the observation point.

## 6.2 Radiance Definitions

Generally, three different resulting radiances are discussed, i.e. water leaving radiance, radiance due to atmospheric effects at the ocean surface, and radiance due to atmospheric

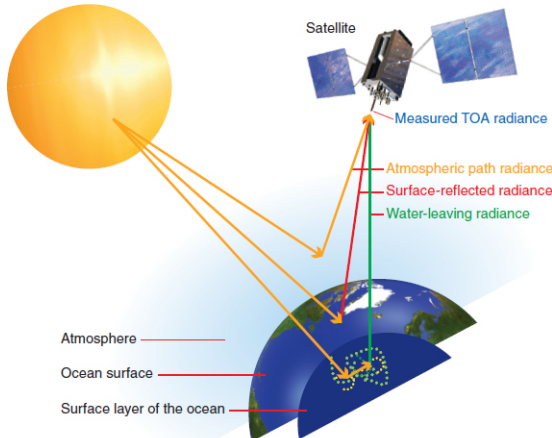


**Figure 6.1:** Illustration of water leaving radiance, radiance due to atmospheric effects at the ocean surface and radiance due to atmospheric effects at TOA. Originally presented in Council

effects at TOA. Figure 6.1 presents an illustration of different radiances. The water leaving radiance is the radiance resulting from geophysical variables such as chl<sub>a</sub> concentration in the ocean. The radiance due to atmospheric effects at the ocean surface does not include the water leaving radiance, only radiance due to atmospheric effects. The same holds for the radiance due to atmospheric effects at TOA. This radiance does not include the water leaving radiance propagated to TOA, only the radiance due to atmospheric effects at TOA and the radiance due to atmospheric effects at the ocean surface that has been reflected by the ocean surface and propagated to TOA. This differs from the preliminary work.

The water leaving radiance is presented in the unit of  $sr^{-1}$ , as this is the unit employed by PlanarRad. The radiance due to atmospheric effects is presented in the unit of  $W m^{-2} \mu m^{-1} sr^{-1}$ , as this is the unit utilized by COART. Nonetheless, the the presented values are the same regardless of units, as the values computed by PlanarRad do not need calculations in order to be presented as  $W m^{-2} \mu m^{-1} sr^{-1}$ . See section 3.3 for details.

### 6.3 Solar Azimuth Angle

The following test regards the solar azimuth angle's effect on the water leaving radiance. The test was executed by utilizing the batched version of PlanarRad. No test was performed regarding the effect on the radiance at TOA as there is no option for varying the sun azimuth angle in COART.

Four different solar azimuth angle values were utilized in the test, i.e.  $0^\circ$ ,  $60^\circ$ ,  $120^\circ$  and  $180^\circ$ . These solar azimuth angles were selected as four values are sufficient to observe variations in the water leaving radiance, while not being too computationally time consuming. The solar azimuth angle values were selected to be integers that cover the range

of interest.

The sun zenith angle was set to  $20^\circ$ . The resulting water leaving radiance values were obtained from the viewing azimuth angle of  $0^\circ$  and the viewing zenith angle of  $170^\circ$ , as defined by PlanarRad.

## 6.4 Solar Zenith Angle

A test was performed regarding the solar zenith angle's effect on the water leaving radiance at the ocean surface and on the radiance at TOA. Only the solar zenith angles of  $0^\circ$  -  $90^\circ$  were of interest, as these angles represent the sun above the horizon.

The test was performed for the solar zenith angles  $20^\circ$ ,  $40^\circ$ ,  $60^\circ$  and  $80^\circ$ . The solar zenith angles were selected based on the same reasoning as for the solar azimuth angles mentioned in the previous section. The batched version of PlanarRad, as well as COART, were used. The reason for utilizing both PlanarRad and COART was the desire of investigating the effect directly on the water leaving radiance at the ocean surface as well as the total effect on the radiance at TOA. PlanarRad was used to observe the water leaving radiance at the ocean surface, while COART was used to observe the effect from the atmosphere.

PlanarRad was run with the solar azimuth angle of  $0^\circ$ . The resulting water leaving radiance at the ocean surface was retrieved with the viewing azimuth angle  $0^\circ$  and the viewing zenith angle  $170^\circ$ , as defined by PlanarRad. The viewing zenith angle was selected in order to be observing the water leaving radiance. See section 6.1 for details.

COART was run with the inputs presented in the introduction to chapter 6. The viewing zenith angle was  $20^\circ$ , as defined by COART, while the viewing azimuth angle was  $0^\circ$ . Thus, the outputs would be, after calculating the reflected radiance from the surface to TOA in Matlab, the radiance due to the atmosphere [ $W\ m^{-2}\ \mu m^{-1}\ sr^{-1}$ ] at the surface and at TOA.

## 6.5 Viewing Angles

Two tests were performed regarding the viewing angle's effect on the water leaving radiance at the ocean surface and on the radiance at TOA. The tests were performed by utilizing the batched version of PlanarRad and COART.

The viewing angle in PlanarRad was varied by varying which values from the individual L\_a tables were to be retrieved and added to the batch report. The available viewing zenith angles start at  $10^\circ$  and increment with  $10^\circ$  until  $170^\circ$ . The L\_a table indices start at 0 and end at 17. Regarding the azimuth viewing angles the indices 0, 4, 8 and 12 correspond to the angles  $0^\circ$ ,  $60^\circ$ ,  $120^\circ$  and  $180^\circ$  respectively.

### 6.5.1 Viewing Zenith Angle

The test performed with PlanarRad regarding the viewing zenith angle was performed for the angles  $120^\circ$ ,  $150^\circ$  and  $170^\circ$ . These viewing zenith angle values were selected as they cover the range of interest. The viewing azimuth angle was constant at  $0^\circ$ . The solar azimuth angle was constant at  $0^\circ$ , while the solar zenith angle was constant at  $40^\circ$ .

The test performed by utilizing COART was executed with the inputs mentioned in the introduction to chapter 6, except for the *radiance output angles* inputs. The azimuth was selected to be  $0^\circ$  and the zenith was chosen to be at every  $30^\circ$  from  $0^\circ$  to  $90^\circ$ .

### 6.5.2 Viewing Azimuth Angle

The test performed by utilizing PlanarRad regarding the viewing azimuth angles was performed for the angles  $0^\circ$ ,  $60^\circ$ ,  $120^\circ$  and  $180^\circ$ . The viewing zenith angle was constantly  $130^\circ$ . The solar azimuth angle was constant at  $0^\circ$ , while the solar zenith angle was  $40^\circ$ .

The test performed by utilizing COART was executed with the inputs mentioned in the introduction to chapter 6, except for the *radiance output angles* inputs. The zenith was chosen to be  $20^\circ$  and the azimuth was chosen to be at every  $60^\circ$  from  $0^\circ$  to  $180^\circ$ .

## 6.6 Clouds

A test regarding the effect of clouds on the radiance at TOA was performed via COART. COART was ran for two different scenarios, i.e. for one with water clouds and one without clouds.

The test regarding the water clouds was performed by specifying spheric water clouds from 3 km to 4 km of the size 10 RE [ $\mu m$ ] and 200 liquid water path (LWP) [ $g/m$ ]. RE is effective size for nonspherical clouds (Jin et al. [2006b]). These were the recommended options by COART (Jin et al. [2006b]). The remaining inputs were as in the introduction to chapter 6.

The test regarding no clouds was performed by specifying this in the cloud input. The remaining inputs were the same as for the water clouds scenario. Thus, only the inputs regarding clouds were varied.

The outputs from the tests resulted in radiances for 81 wavelengths. As 87 wavelengths are required for this thesis the tests described above were also performed for single wavelengths. This was performed by selecting to present the outputs as radiances [ $W\ m^{-2}\ \mu m^{-1}\ sr^{-1}$ ] at one single wavelength. This was performed for the wavelengths of 402 nm, 448 nm, 503 nm, 628 nm, 743 nm and 798 nm. The stated wavelengths were selected to correspond to the missing wavelengths of interest.

# Chapter 7

## Creating A Lookup Table For Simulation Of A Whole Scene

This section presents the motive and objective behind creating a water leaving radiance lookup table, as well as the creation process.

### 7.1 The Creation Of A Lookup Table

Several lookup tables were created with the purpose of saving computational time regarding the calculation of water leaving radiance at the ocean surface. The lookup tables are especially relevant for computation of whole scenes. Panoply, MATLAB and PlanarRad were utilized to compute the water leaving radiance lookup tables. Panoply was used for selecting a time frame to provide the chl\_a concentration values. Matlab was employed in order to read the SINMOD dataset and calculate the absorption, attenuation and scattering for the PlanarRad input files. PlanarRad was used to calculate the water leaving radiance for the chosen chl\_a concentration values. This section presents the creation of one lookup table. The created lookup tables are presented in appendix B.

#### 7.1.1 Panoply

Panoply was applied to visualize the chl.a concentration values in the different time frames in the dataset. Such an visualization is not possible in Matlab. The objective was to identify a time frame containing the minimum chl\_a concentration value, the maximum chl\_a concentration value, and a range of values in between the two. This would provide range

and variation for the lookup table calculation. A time frame was selected.

The Panoply *Map* inputs were set to:

- Projection: Equirectangular Regional
- Center on: Lon.: 8.8 degrees E, Lat.: 63.8 degrees N
- Width: 3 degrees
- Height: 1.5 degrees

The smallest value of chl<sub>a</sub> concentration is 0.0 mg chl<sub>a</sub> m<sup>-3</sup>, while the largest is, generally, 1.8 mg chl<sub>a</sub> m<sup>-3</sup>. A number of frames include higher maximum values. However, these values regard limited areas at imperceptible time instances. Therefore, 1.8 mg chl<sub>a</sub> m<sup>-3</sup> is a more representative maximum chl<sub>a</sub> concentration value, and is thus utilized. The chl<sub>a</sub> concentration values used in the calculation of the lookup tables were 0.0, 0.3, 0.6, 0.9, 1.2, 1.5 and 1.8 mg chl<sub>a</sub> m<sup>-3</sup>. The presented values were chosen due to them representing variation in the value-range, as well as not being to computationally time consuming.

The data points of interest, i.e. the geographical locations in the selected time frame, were found via Panoply, and were used in order to obtain the values of interest in Matlab.

The absorption calculations, which PlanarRad needs as an input file, only requires chl<sub>a</sub> concentration [mg m<sup>-3</sup>] values. The scattering calculations require the values of the diatoms concentrations [mmol N m<sup>-3</sup>], flagellates concentrations [mmol N m<sup>-3</sup>] and water temperatures [C] for the chosen data points as well.

### 7.1.2 MATLAB And PlanarRad

After the values of interest, i.e. the chl<sub>a</sub> concentrations, diatoms concentrations, flagellates concentrations and water temperature, for the seven data points had been obtained in Matlab, the input files for PlanarRad, i.e the absorption file, the scattering file and the attenuation file, were calculated and created.

PlanarRad was run with the input files created in Matlab. The rest of the essential inputs were the solar azimuth and zenith angles, which were 0° and 40° respectively. The wavelengths were 400 - 800 nm and the number of CPUs was defined to be 1. The result was the water leaving radiance [sr<sup>-1</sup>] for the 87 wavelength bands, for the seven data points. The resulting water leaving radiances were used in Matlab in the calculation and creation of the lookup tables.

The lookup table was created in MATLAB utilizing the water leaving radiance for the seven locations and interpolation. The calculations of the water leaving radiance for an arbitrary chl<sub>a</sub> concentration value is performed by interpolation through the Matlab function *interp1()*. The function *interp1()* requires the chl<sub>a</sub> concentration values for which

the resulting water leaving radiance is known, i.e. for the seven locations in this particular case, the resulting water leaving radiance for these chl<sub>a</sub> concentration values, and the chl<sub>a</sub> concentration value for which the water leaving radiance is to be calculated as inputs (MATLAB). The chl<sub>a</sub> concentration value for which the lookup tables can calculate the resulting water leaving radiance must be a value in between 0.0 and 1.8 mg chl<sub>a</sub> m<sup>-3</sup>.

## 7.2 Simulating A Whole Scene

The motivation behind being able to compute the water leaving radiance for a whole scene rather than for only a few location-points, is to be able to investigate properties such as the time sensitivity of the data and be able to simulate what a sensor at TOA would record in its entirety. Figure 7.1 illustrates a satellite observing a scene. Such analyses require the water leaving radiance for several data points at the same time instance. A whole scene was created in MATLAB by utilizing the lookup table.

The created scene was calculated by selecting a number of chl<sub>a</sub> concentration values from the chosen time frame from the SINMOD dataset. The chl<sub>a</sub> concentration values were applied as inputs to the lookup table. Thus, their respective water leaving radiance values were calculated. The result was a hyperspectral cube.

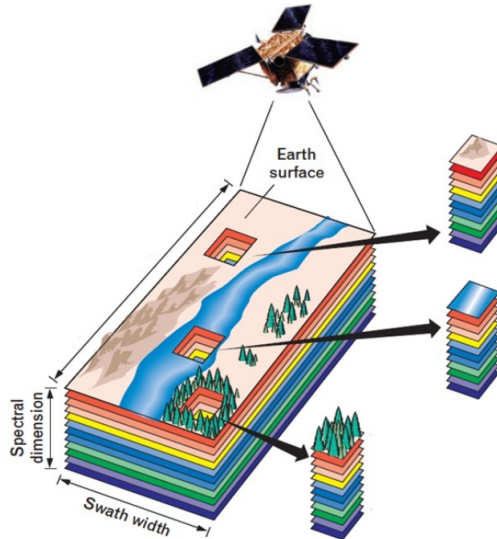


**Figure 7.1:** Illustration of a satellite observing a scene. Originally presented in Honoré-Livermore.

# Temporal Sensitivity Of Data Acquisition Analysis

An objective of being able to simulate a whole scene was to investigate the temporal sensitivity of data acquisition with respect to ocean color products for a multi-agent system. Such an analysis was of interest due to the HYPSO project desiring to know how fast they need to be able to send agents to the location of interest, in order to further investigate the data of interest. HYPSO will not benefit from sending a drone to the location of interest in three hours if the phenomenon of interest only lasts for one hour.

The temporal sensitivity of data acquisition analysis was performed by utilizing Panoply and a lookup table. Panoply was used to examine the illustrations of the chl\_a concentration values. The objective was to obtain a first impression of how the chl\_a concentration values vary with time. The lookup table was employed in order to analyze how the resulting water leaving radiance values vary over time.

The Panoply analysis was performed by identifying a period of time, i.e. several consecutive time frames, with variation in the chl.a concentration values by examining the visualizations while varying the time-stamp. A period of time as desired was identified. Three consecutive time frames were saved. Thus, an impression of the variation in the chl\_a concentration values over the time period of one hour could be created. Three time frames, with five time frames in between them were saved as well, for the same reason as previously mentioned. Three time frames with 10 time frames in between them were also saved.

The lookup table was used in order to acquire a more precise understanding of the chl.a concentration variation with regard to time. The time frames detected with Panoply were used for this analysis as well. Panoply was utilized once again, in order to identify which

part of the data in the selected time frames contains the changing chl\_a concentration values. The resulting information was used in Matlab together with the lookup table. That is, the water leaving radiance was calculated for the selected chl\_a concentration values. The result was the variation of the water leaving radiance at the ocean surface with regard to time, for the scene of interest.

# User Friendly Interface For The Software

This chapter regards the process of combining and altering all the files and processes created for this thesis into one user friendly and straightforwardly program. The program is titled *RadPhyll Simulator*. The motivation was to create the possibility for the HYPSO mission, and other interested parties, to utilize the work and data created in this thesis at any time, without requiring help from the creator.

The chapter is divided into two sections. The first regards the Python files, while the second regards the MATLAB files. Appendix A presents the documentation, as well as a user guide, for the RadPhyll Simulator.

## 9.1 The Python Files

The python interface to PlanarRad was altered in order to be more appropriate for the objective at hand. The files were shortened and cleaned up, by removing unnecessary inputs and functions. Several properties were added in order to make the interface more automatic. These properties include it not being required to change the inputs of interest in several locations in a handful of files, but rather only in the input file.

## 9.2 The MATLAB Files

The MATLAB files from the preliminary work were altered as presented in chapter 4. Furthermore, an input Matlab file was created. This is the only file where the user is required

to provide inputs. The user provided inputs are automatically saved in a *.mat* file named "input\_data\_RadPhyll\_version" when the input file is run. A *.mat* file is a data file that is in the binary data container format that MATLAB uses (MathWorks [c]). The input file is loaded in the main script called "RadPhyll.m". This is the script that is to be run in order to use the program. The script reads the input file and calculates the desired results. The results are automatically saved in a *.mat* file as well as in a *.csv* file. The results are saved in two different files as *.mat* files are advantageous for potential further calculations in MATLAB, while *.csv* files are more straightforward with regard to being interpreted by a user.

The developed software is written in MATLAB, but can be translated to any programming language, as it is purely based on computation of provided data.

## **Part III**

# **Results**

# Combining The MATLAB Files From The Preliminary Work

The results from combining the Matlab files from the preliminary work include fewer files, faster computational time, more robust and straightforwardly scripts, as well as more user friendly scripts.

A comparison of the results and real-world TOA radiance values obtained from The Hyperspectral Imager for the Coastal Ocean (HICO) was performed in the preliminary work. The results will be shortly presented here as they are relevant for this thesis as well. The following sections are heavily based on [Lapadatu [2018]].

HICO is the first spaceborne imaging spectrometer designed to sample coastal oceans (Nahorniak). Data files recorded by HICO are available for download from their internet sites. This holds for MATLAB code for processing the data as well (Nahorniak). The main data file, available for download, from HICO contains a hyperspectral image cube of TOA radiances, 400 - 900 nm, in the unit of  $W\ m^{-2}\ \mu m^{-1}\ sr^{-1}$ . The image downloaded from HICO, and used in the comparison, was from Tiburon, California, taken on 2013-04-18 at 00:14:52. The HICO data was recorded from the ISS which had an altitude of approximately 350 km. Figure 10.1 illustrates the data from HICO in the units  $W\ m^{-2}\ \mu m^{-1}\ sr^{-1}$ .

The resulting radiance at TOA from the preliminary work, and from this thesis, are similar to the HICO data, as they share general absolute value and wavelength dependent variations. For further results, discussion and conclusion regarding the comparison to the HICO data, see [Lapadatu [2018]].

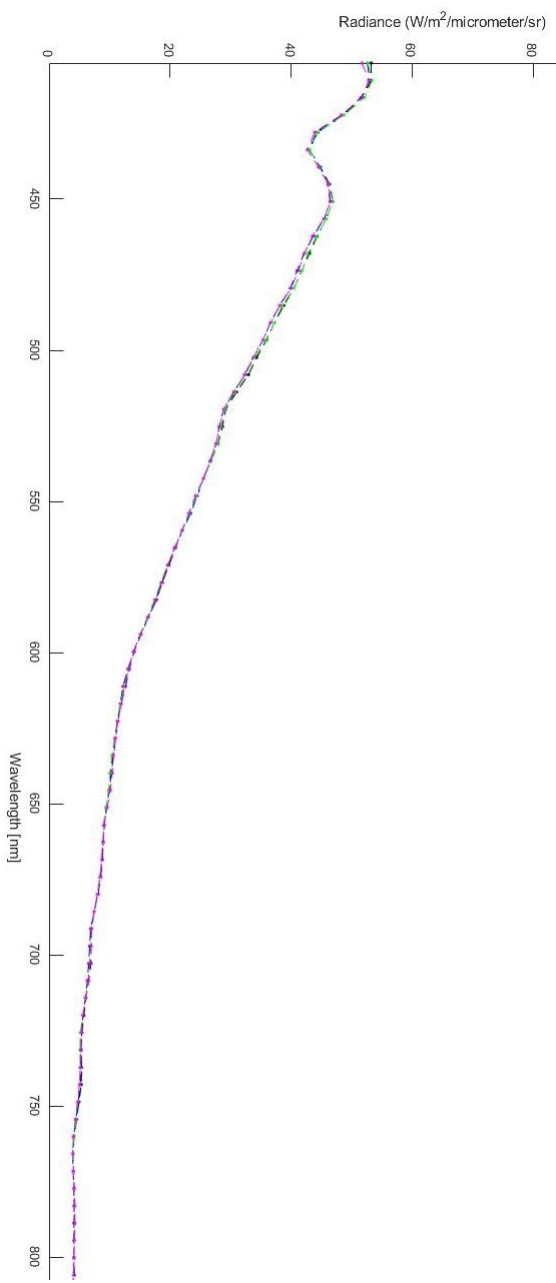


**Figure 10.1:** HICO radiance.

# Developing Batch Runs For PlanarRad

The development of the batch runs for PlanarRad was successful and resulted in a more user friendly method of providing inputs, a more robust method, less computational time, and a more straightforwardly output report.

The test regarding whether the same results are produced regardless of whether one utilizes the GUI or not was successful, and resulted with the same results being produced in both cases.

## 11.1 The Difference Between Initial And Batched Planar-Rad Version

This section regards the differences between the initial PlanarRad, and the initial setup of the batched version of PlanarRad, i.e. before it was altered as presented in chapter 5.

Figure 11.1, 11.2, 11.3, 11.4, 11.5 and figure 11.6 illustrate the initial PlanarRad, i.e. the version that runs one run at the time, while figure 11.7 and figure 11.8 illustrate the batched PlanarRad version. Both versions include options for giving the run, or batch, a name, zenith and azimuth solar angle, depth, wavelengths and lower boundary properties, i.e. the bottom reflectance value. The two versions differ on the fact that the initial PlanarRad version has total irradiance (or diffuse irradiance) as input while the batched version has particle scattering, phytoplankton linear scaling factor and organic absorption as inputs. That is, the batched version is set up to calculate the irradiance itself. This was changed, as some inputs were removed. Nonetheless, the results are the same as absorp-

tion, attenuation and scattering files are provided as inputs.

Another distinction between the two versions is that the initial version has the possibility of choosing the cloud state, while the batched version applies the sky-state *clear*, i.e. it is not directly an input. However, this can be made an input if desired. The initial version has the interface properties as input as well, while the batched version defines these properties in the script. These variables can be altered to become user defined inputs if desired. Furthermore, the initial version enables the possibility of choosing sample interval and delta evaluation distance for the depth. The batched version has this integrated in the script, and thus it must be changed manually if desired. It is possible to enable these variables to be input variables, but as these values were to be unchanged for this thesis, this was not developed. These differences can be changed by altering the scripts for the batched PlanarRad.

The resulting outputs are the same regardless of PlanarRad being run on batches or not. Both versions compute the same report file. However, the batched version creates a batch report file in addition, and runs faster, as the user is not required to change the inputs for every run. The batched version saves the resulting figures in a folder instead of displaying them in the GUI.

The batched version of PlanarRad requires a scattering file as well as attenuation and absorption files, due to the internal calculations not taking into account that scattering values can be calculated from the absorption and attenuation values.

**Model**   **Data**

Name:

Bands: **17 Bands (400-740 nm)**   Directional Structure: **HL Standard**

**Input Radiance Distribution**

Type: **Grant Model**

Zenith:  (deg)  
Azimuth:  (deg)

Total Irradiance (Wm-2nm-1):  File **17 Bands (400-740 nm)**  
Diffuse Irradiance (Wm-2nm-1):  File **17 Bands (400-740 nm)**

Cloud State:  Clear Sky  High Cloud  Low Cloud  Overcast

**Interface Properties**

**Medium Properties**

**Depth Options**

**Lower Boundary Properties**

**Figure 11.1:** Input radiance distribution specifications for the initial PlanarRad version.

**Interface Properties**

None  
 Flat  
 Height S.D.:   
 Wind speed:  (ms-1)  
Direction:  (degrees), or:  Azimuthally average

Load from file:  File

**Medium Properties**

**Depth Options**

**Lower Boundary Properties**

**Figure 11.2:** Input interface properties specifications for the initial PlanarRad version.

**Medium Properties**

Attenuation (c):  Uniform  File (m-1)

Absorption (a):  Uniform  File (m-1)

Phase function:  Isotropic  Petzold  Fournier-Forand (bb prop.)

Load from file: (bb prop.)

Depth Options

Lower Boundary Properties

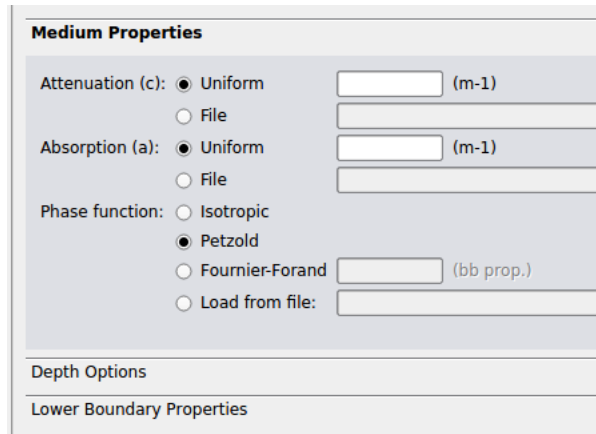


**Figure 11.3:** Input medium properties for the initial PlanarRad version.

**Depth Options**

Depth: (m)

Sample interval: (m)

Delta evaluation distance: (m)

Lower Boundary Properties

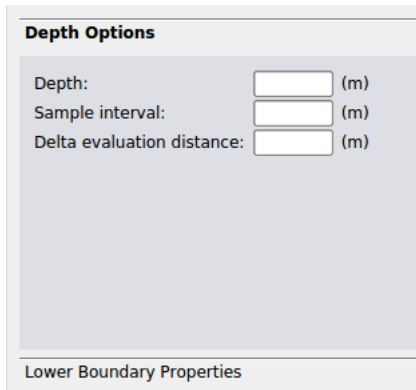


**Figure 11.4:** Input depth options for the initial PlanarRad version.

**Lower Boundary Properties**

Lambertian uniform (prop. 0-1)

Lambertian file

BRDF file

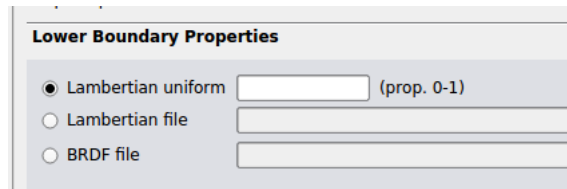


**Figure 11.5:** Input lower boundary properties for the initial PlanarRad version.

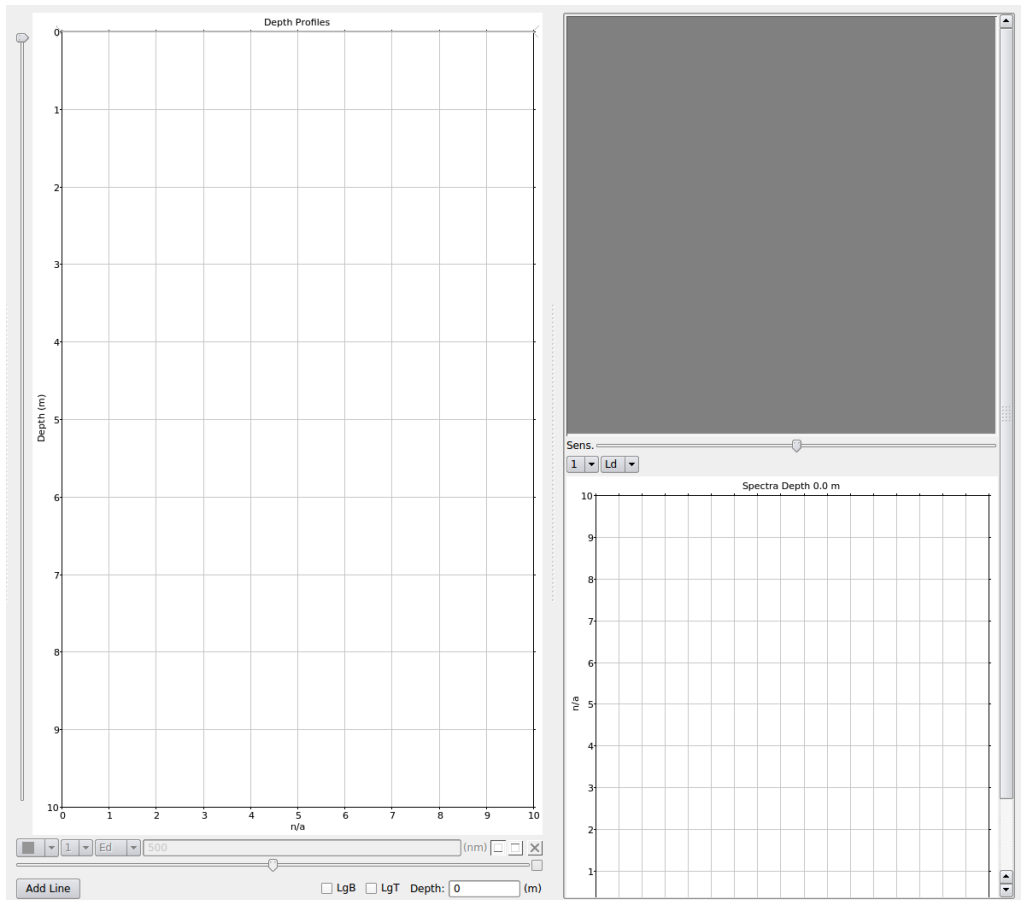


**Figure 11.6:** The right hand side of the initial PlanarRad version. Figures, e.g. illustrating the depth profile, will be displayed here after a run.

**Radiative Transfer Model** **Inverse**

Set the optical parameters list (comma seperated)

Batch name	<input type="text" value="default"/>
SAA values	<input type="text" value="0.0"/> (deg)
SZA values	<input type="text" value="0.0"/> (deg)
P values	<input type="text" value="0.1"/>
Particle scattering $b_{bp}$	<input type="text" value="0.01"/> <input type="text" value="1.0"/>
Organic absorption $a_g$	<input type="text" value="0.01"/> <input type="text" value="0.015"/>
Depth (Z)	<input type="text" value="10.0"/> (m)
Wavelengths	<input type="text" value="570.0, 590.0, 610.0, 630.0, 650.0, 670.0, 690.0, 710.0, 730.0"/> (nm)

---

Bottom reflectance	<input type="button" value="File"/>
<input type="text" value="/home/marrabld/Projects/planarradpy/inputs/bottom_files/ger_sand17.txt"/>	
Phytoplankton absorption	<input type="button" value="File"/>
<input type="text" value="/home/marrabld/Projects/planarradpy/inputs/iop_files/a_phi.csv"/>	

---

Report parameter	<input type="text" value="Rrs"/>	View Azimuth	<input type="text" value="0.0"/> (deg)
Verbose	<input type="text" value="6"/> (1 -> 6)	View Zenith	<input type="text" value="0.0"/> (deg)
Number of CPU	<input type="text" value="-1"/> (-1 means all CPUs)		
Path to Planarrad	<input type="button" value="Directory"/>	<input type="text" value="/home/marrabld/Apps/jude2_install/bin"/>	

---

<input type="button" value="Run"/>	<input type="button" value="Cancel"/>
------------------------------------	---------------------------------------

**Figure 11.7:** Inputs for the batch PlanarRad version.

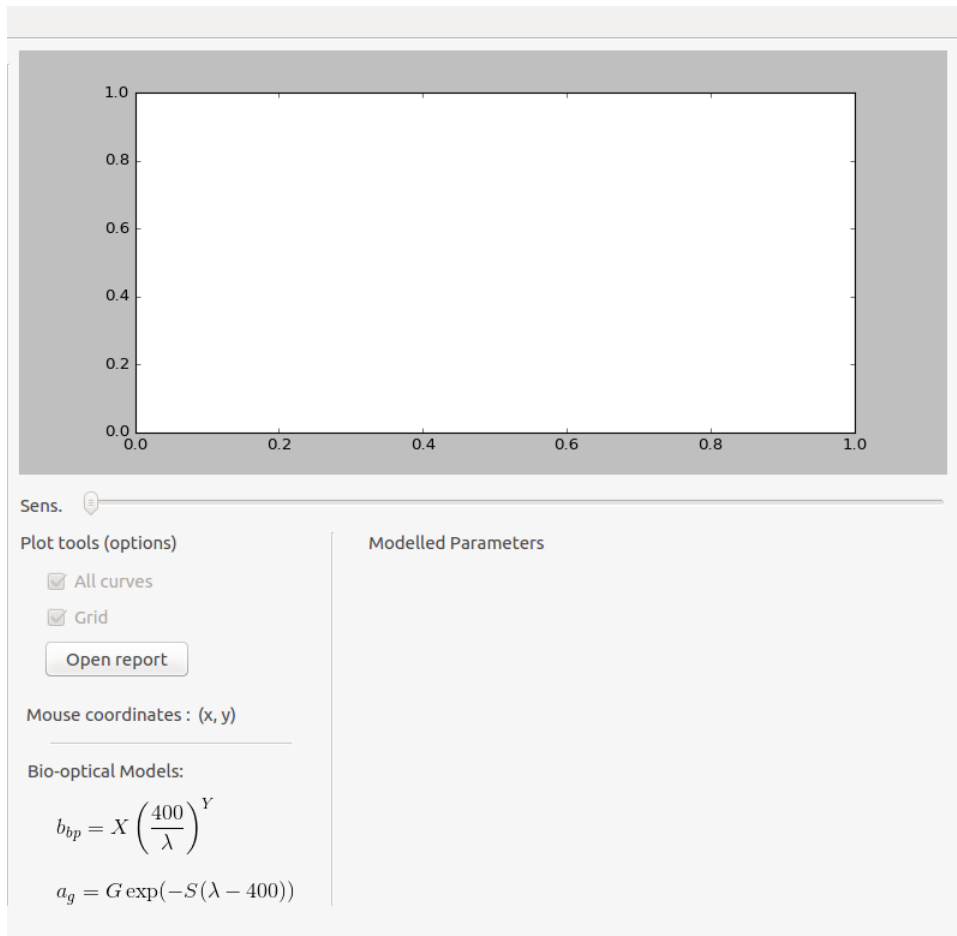


**Figure 11.8:** The right hand side of the batch PlanarRad version.

# Examining Different Scenarios

This chapter will present the results regarding the effect on the water leaving radiance, and the radiance due to atmospheric effects, at the ocean surface due to the solar azimuth angle, the solar zenith angle, the viewing azimuth angle and the viewing zenith angle. The chapter will also present the results regarding the effects on the radiance at TOA due to the solar zenith angle, the viewing azimuth angle, the viewing zenith angle and the presence of clouds.

The presented results generally include resulting water leaving radiance, resulting radiance at the ocean surface due to atmospheric effects, and resulting radiance at TOA due to atmospheric effects. That is the presented resulting radiance at TOA does not include the water leaving radiance that has propagated to TOA, only the radiance due to atmospheric effects at TOA, i.e. the radiance due to atmospheric effects at TOA and the radiance due to atmospheric effects just above the ocean surface that has been reflected by the ocean surface and propagated to TOA. The reason for this is that the preliminary work revealed how small the water leaving radiance at TOA is compared to the resulting radiance due to atmospheric effects. See figure 12.1 (Lapadatu [2018]). Thus, the results presented in this chapter regard the effects of solar and viewing angles on the water leaving radiance, and on the radiance due to atmospheric effects separately, as this was the objective of interest. The water leaving radiance at the ocean surface and the radiance at the ocean surface due to atmospheric effects are compared, as this is of interest.

Figure 12.1 illustrates that the percentage water leaving radiance of total reflected radiance at the ocean surface varies between 2% and 35%, but generally, is approximately 10%. Furthermore, the figure illustrates that the percentage water leaving radiance of total radiance at TOA is small. The maximum percentage is of  $8 * 10^{-7}\%$ , and generally approximately  $3 * 10^{-7}\%$ . The scene, and presented percentages, illustrated in figure 12.1, vary with chl<sub>a</sub> concentration, atmospheric properties, viewing angles and solar angles. Thus, the percentage water leaving radiance of total radiance at the ocean surface varies

quite a bit. However, the comparison between percentage water leaving radiance at the surface and at TOA stands valid.

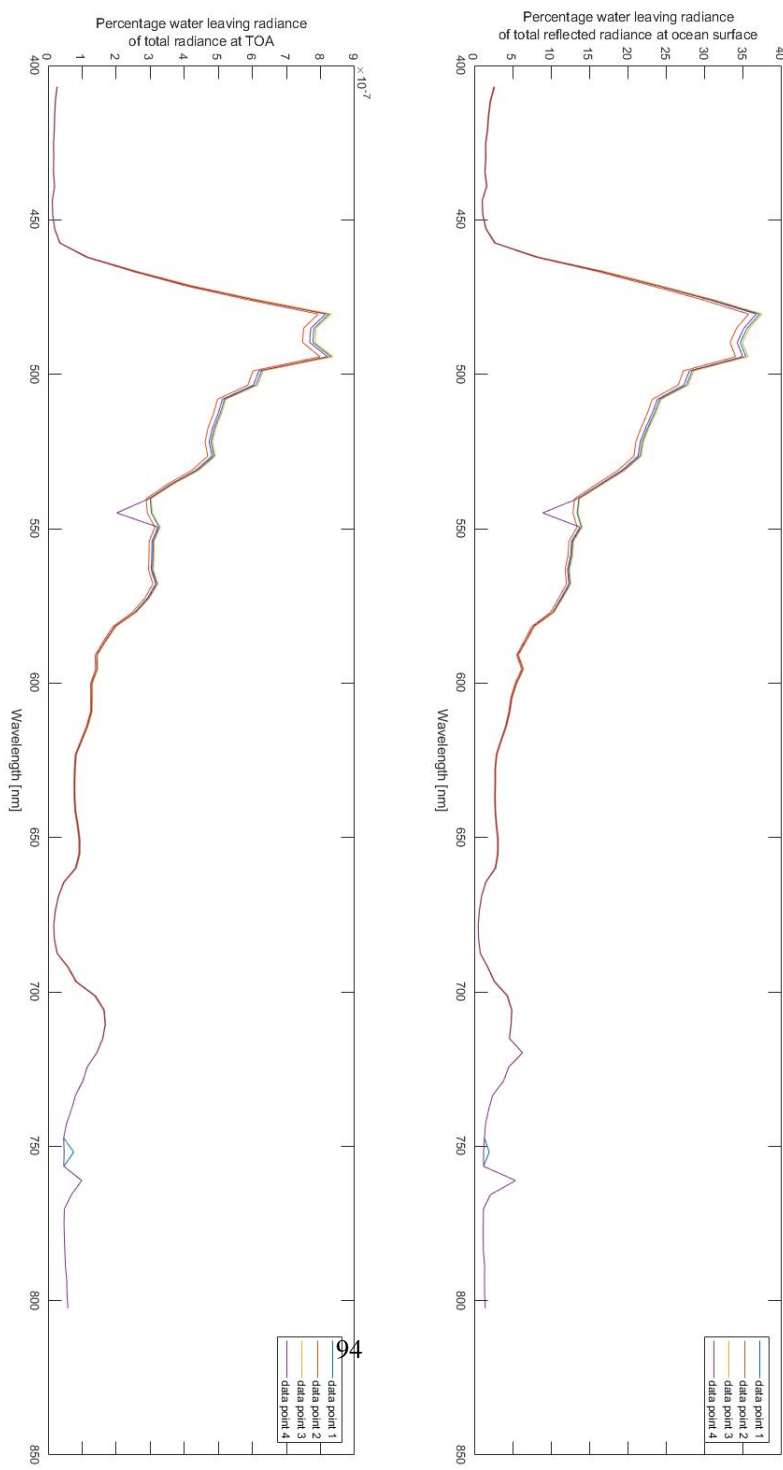


**Figure 12.1:** Top figure: Percentage water leaving radiance of the total reflected radiance at the ocean surface. Bottom figure: Percentage water leaving radiance of the total radiance at TOA. Originally presented in Lapadatu [2018]

## 12.1 Solar Azimuth Angle

Figure 12.2 and 12.3 present the water leaving radiance at the ocean surface for different solar azimuth angles. The two figures differ by the fact that figure 12.3 does not include the solar azimuth angle of  $180^\circ$ . Figure 12.4 illustrates the water leaving radiance at the ocean surface for the solar azimuth angles  $0^\circ$  and  $60^\circ$ .

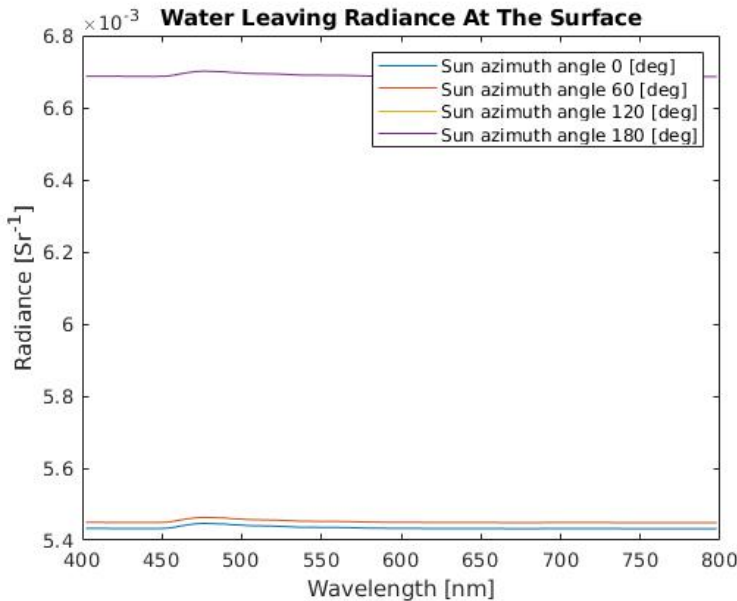


**Figure 12.2:** Resulting water leaving radiance at the ocean surface while varying the solar azimuth angle.

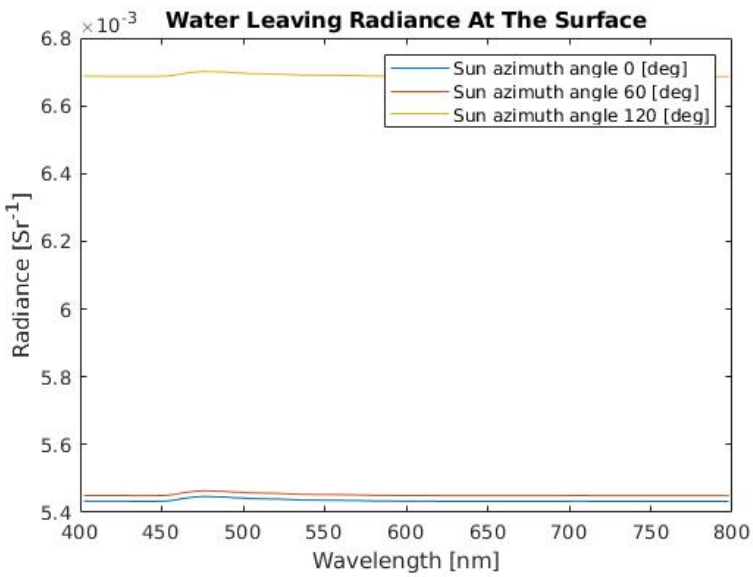


**Figure 12.3:** Resulting water leaving radiance at the ocean surface while varying the solar azimuth angle (without the solar azimuth angle of  $180^\circ$ ).

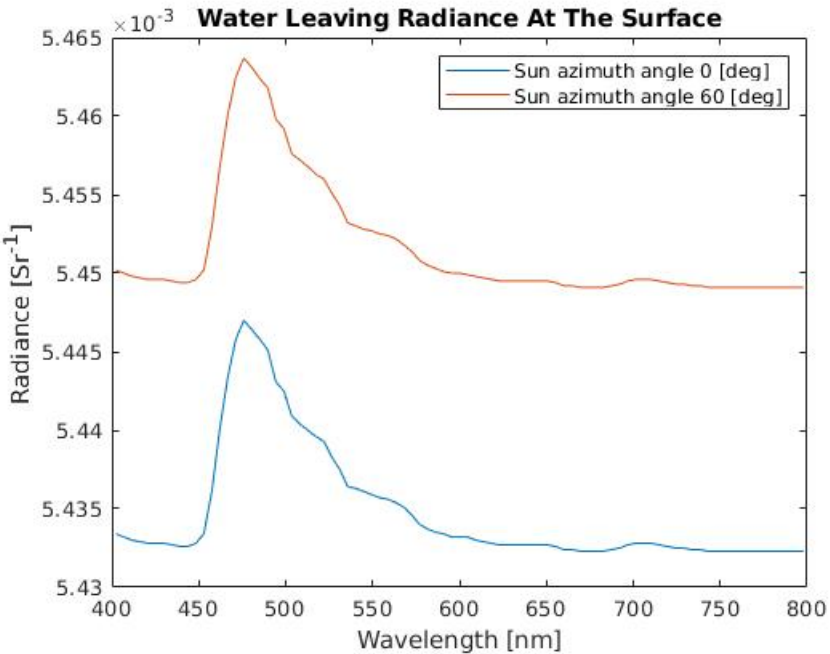


**Figure 12.4:** Resulting water leaving radiance at the ocean surface with the solar azimuth angles of  $0^\circ$  and  $60^\circ$ .

## 12.2 Solar Zenith Angle

This section presents the results regarding the effects on the water leaving radiance, and the radiance due to atmospheric effects, at the ocean surface and on the radiance at TOA due to variations in the solar zenith angle. As mentioned in section 6.4, these tests were performed by utilizing both PlanarRad and COART. The two parts of the tests will be presented separately. Finally, a combined summary will be presented.

### 12.2.1 Radiance Due To Atmospheric Effects

The figures presented in this section regard the radiance due to atmospheric effects. Figure 12.5 presents the resulting radiance at the ocean surface, figure 12.6 presents the resulting radiance at TOA, and figure 12.7 presents the difference between the two at one chosen solar zenith angle, i.e.  $60^\circ$ . More precisely, figure 12.5 and figure 12.6 regard the four solar zenith angles  $20^\circ$ ,  $40^\circ$ ,  $60^\circ$  and  $80^\circ$ .

As mentioned, figure 12.7 compares the resulting radiance at the ocean surface and the resulting radiance at TOA for the solar zenith angle of  $60^\circ$ . The solar zenith angle of  $60^\circ$  was chosen for display purposes, as it is one of the three solar zenith angles with little deviation from the radiance resulting from the other solar zenith angles. Figure 12.7 is purely for the purpose of illustrating how small the atmospheric noise is at the ocean surface compared to at TOA.

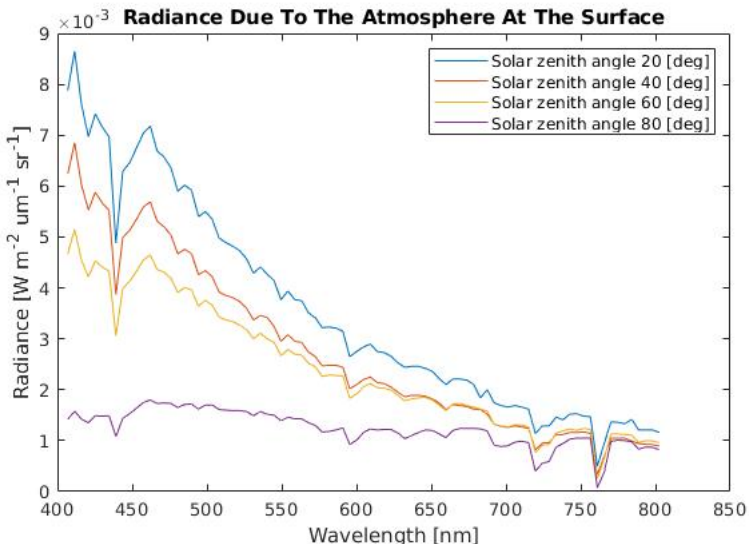


**Figure 12.5:** Resulting radiance at the ocean surface due to atmospheric effects, with various solar zenith angles.

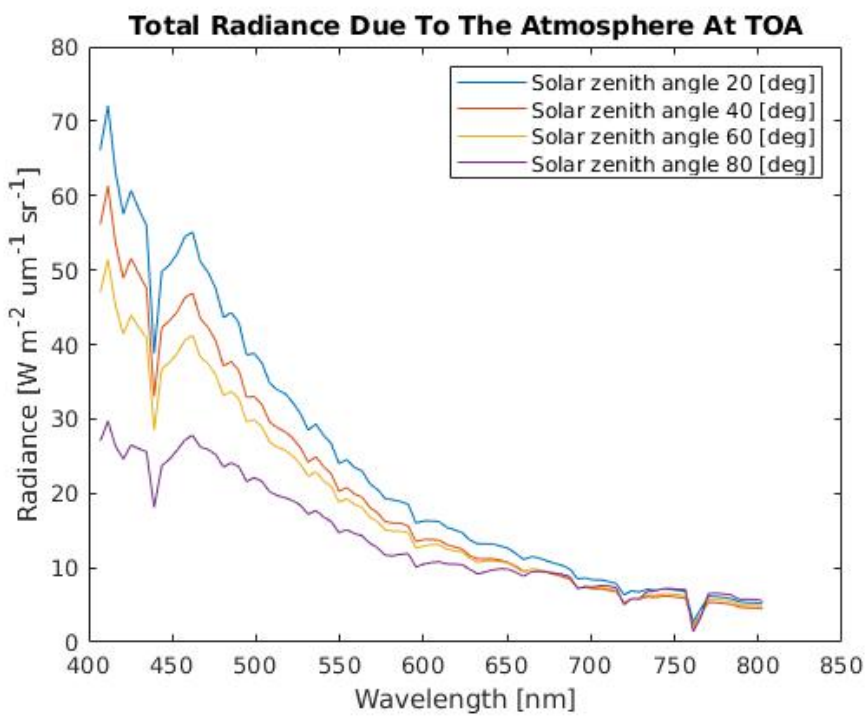


**Figure 12.6:** Resulting radiance at TOA due to atmospheric effects, with various solar zenith angles.

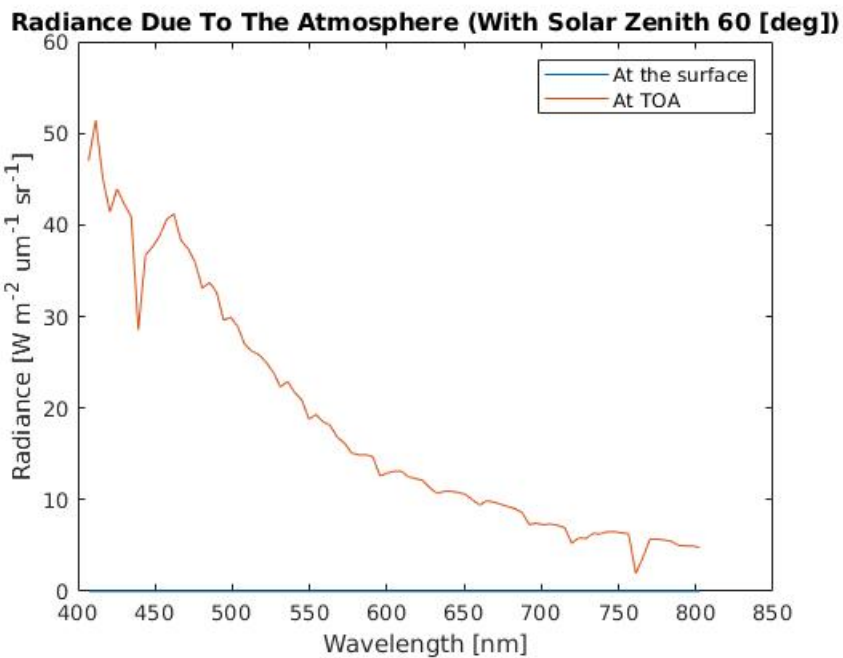


**Figure 12.7:** Resulting radiance due to atmospheric effects with the solar zenith angle of 60°.

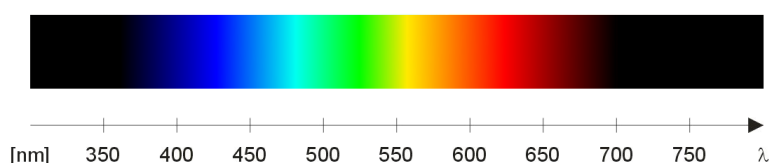


**Figure 12.8:** The visible spectrum. Originally posted in Smith [2000].

## 12.2.2 Water Leaving Radiance

Figure 12.9 presents the water leaving radiance at the ocean surface for different solar zenith angles, namely for the angles  $20^\circ$ ,  $40^\circ$ ,  $60^\circ$  and  $80^\circ$ .

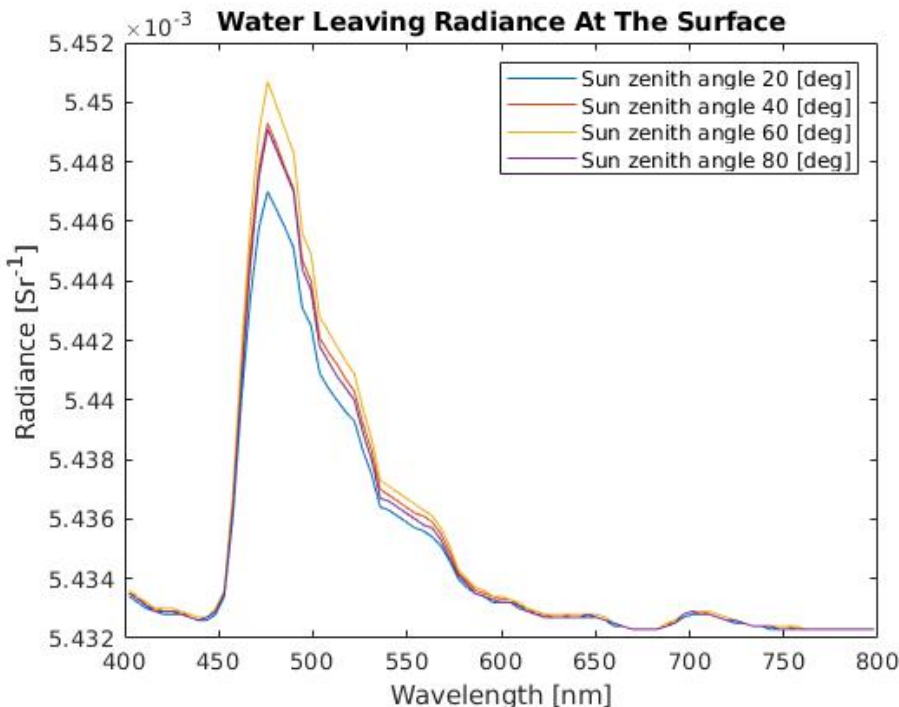


**Figure 12.9:** Resulting water leaving radiance at the ocean surface for various solar zenith angles.

## 12.2.3 Solar Zenith Angles Summary

Figure 12.10 and 12.11 illustrates the radiance difference between the radiance due to atmospheric effects and the water leaving radiance at the ocean surface, with regard to solar zenith angles. The difference is presented as the water leaving radiance subtracted from the radiance due to atmospheric effects. The solar zenith angles in figure 12.10 are  $20^\circ$ ,  $40^\circ$ ,  $60^\circ$  and  $80^\circ$ , while in figure 12.11 the solar zenith angles are  $20^\circ$  and  $40^\circ$ .

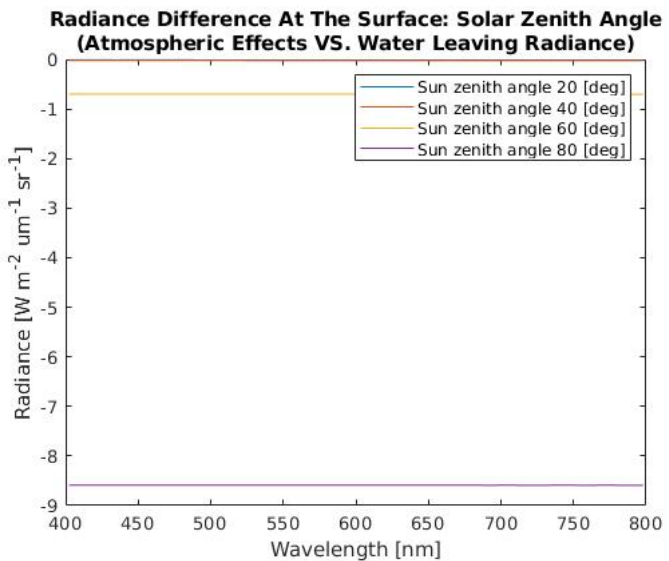


**Figure 12.10:** Radiance difference at the ocean surface for various solar zenith angles. Water leaving radiance at the ocean surface subtracted from the radiance due to atmospheric effects at the ocean surface.

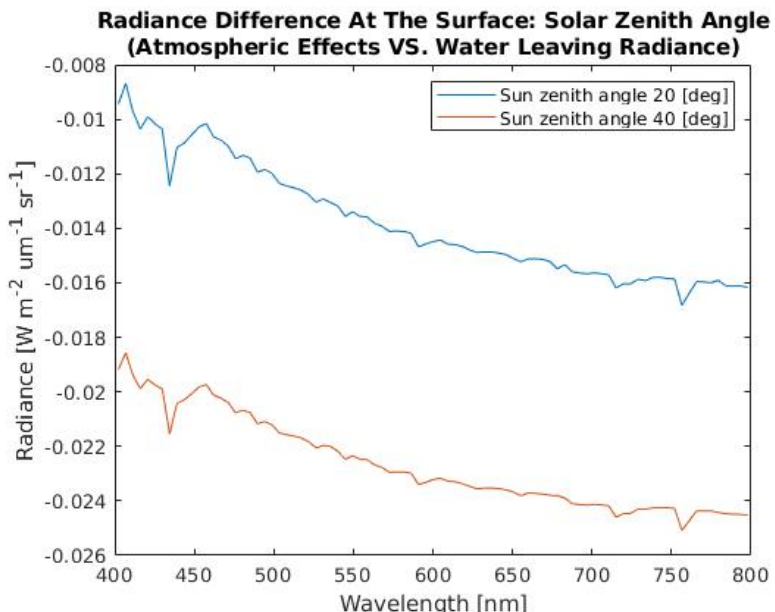


**Figure 12.11:** Radiance difference at the ocean surface for various solar zenith angles. Water leaving radiance at the ocean surface subtracted from the radiance due to atmospheric effects at the ocean surface.

## 12.3 Viewing Angles

This section will present the results regarding the effect of the viewing azimuth angle and the viewing zenith angle on the water leaving radiance, and the radiance due to atmospheric effects, at the ocean surface, as well as on the radiance at TOA. These tests were performed by utilizing both PlanarRad and COART. The tests performed in PlanarRad and COART will be presented separately. Lastly, a summary is presented.

### 12.3.1 Radiance Due To Atmospheric Effects

#### Viewing Zenith Angles

Figure 12.14 illustrates the radiance due to atmospheric effects at the ocean surface for three different viewing zenith angles, namely for  $0^\circ$ ,  $30^\circ$  and  $60^\circ$ . Figure 12.12 presents the same scenario, except for the illustrated radiance being at TOA. Figure 12.13 compares the radiance at the ocean surface to the radiance at TOA for the described scenario.

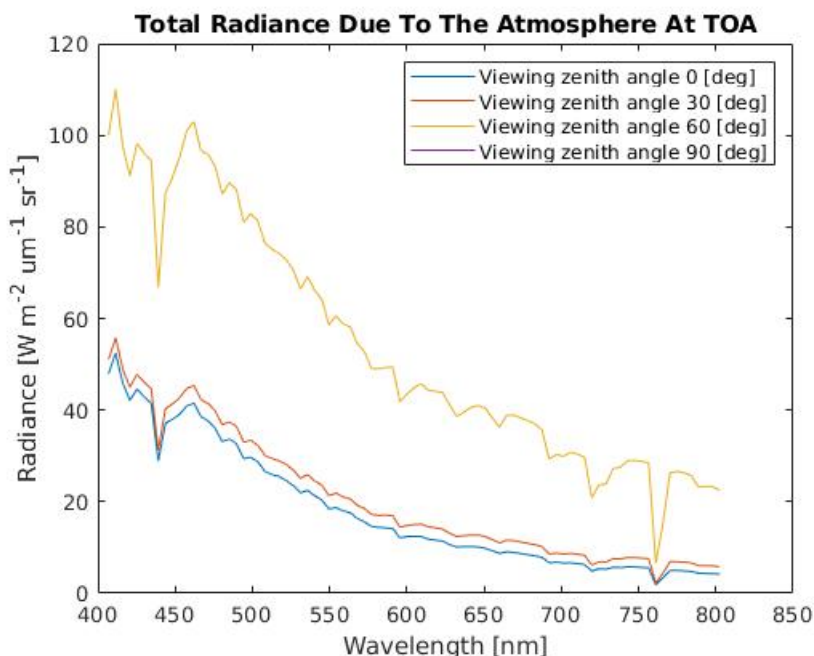


**Figure 12.12:** Resulting radiance at TOA due to atmospheric effects for various viewing zenith angles.

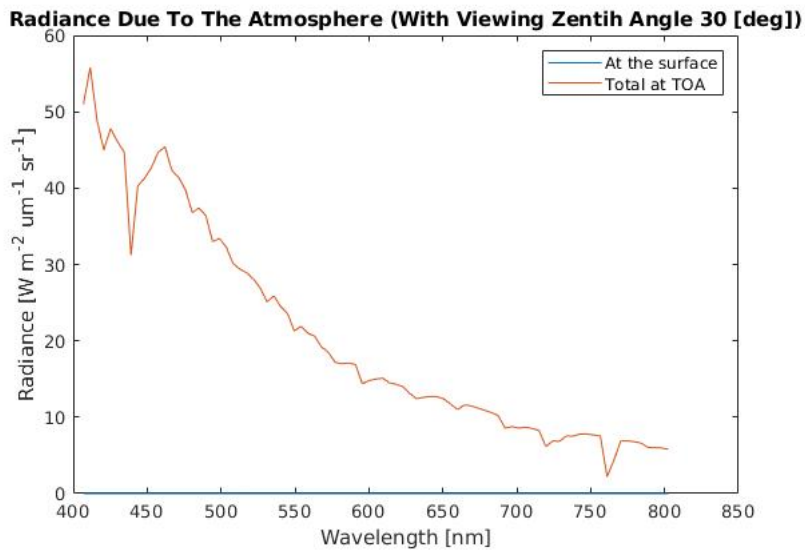


**Figure 12.13:** Resulting radiance due to atmospheric effects for the viewing zenith angle of  $30^\circ$ .

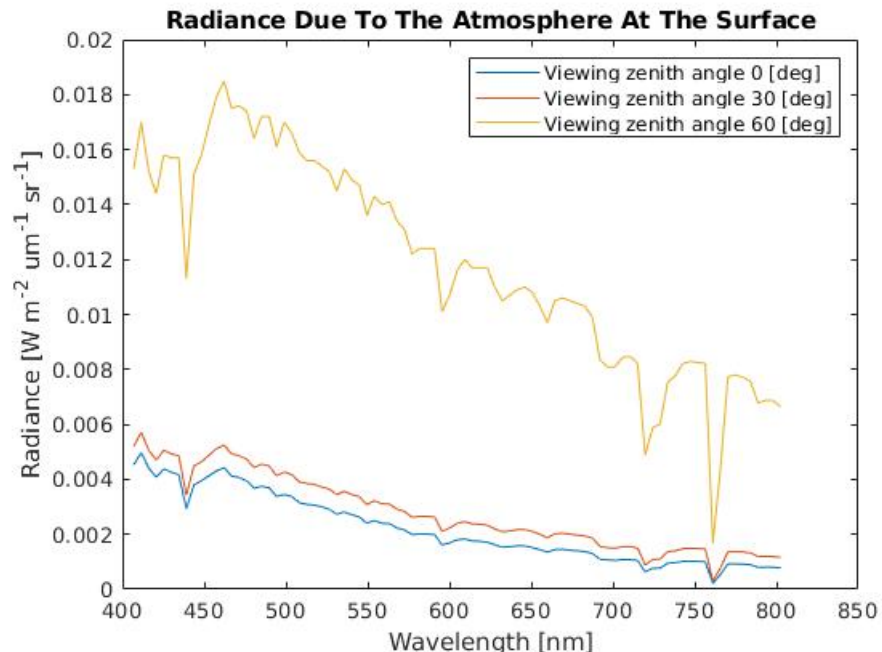


**Figure 12.14:** Resulting radiance at the ocean surface due to atmospheric effects for various viewing zenith angles.

## Viewing Azimuth Angles

Figure 12.15 illustrates the resulting radiance due to the atmosphere at the ocean surface with regard to four viewing azimuth angles, namely for  $0^\circ$ ,  $60^\circ$ ,  $120^\circ$  and  $180^\circ$ . Figure 12.16 presents the same scenario, except for the resulting radiance being presented at TOA, while figure 12.17 compares the radiances at the ocean surface and at TOA. The viewing azimuth angle utilized in figure 12.17 is  $60^\circ$ .

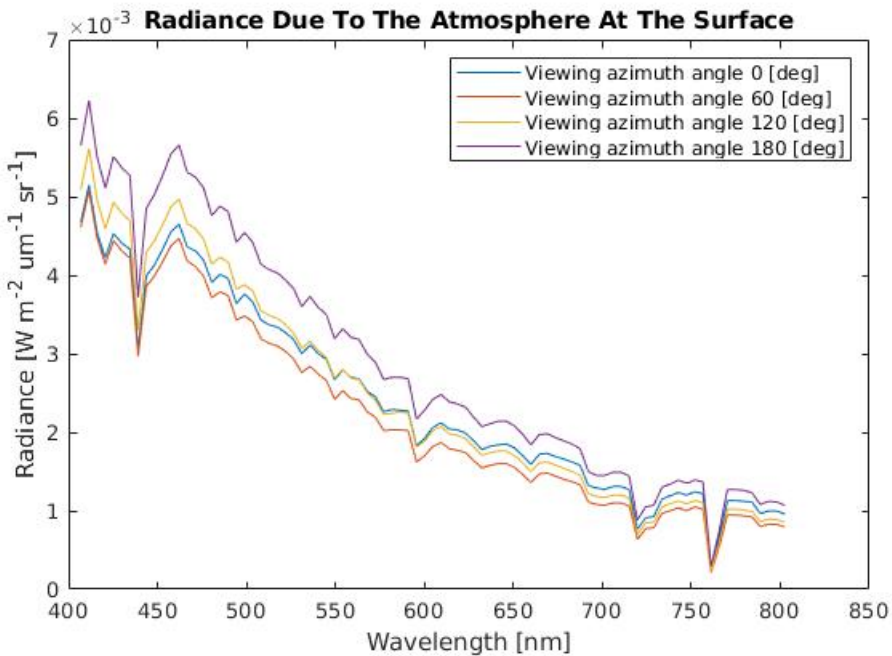


**Figure 12.15:** Resulting radiance at the ocean surface due to atmospheric effects for various viewing azimuth angles.

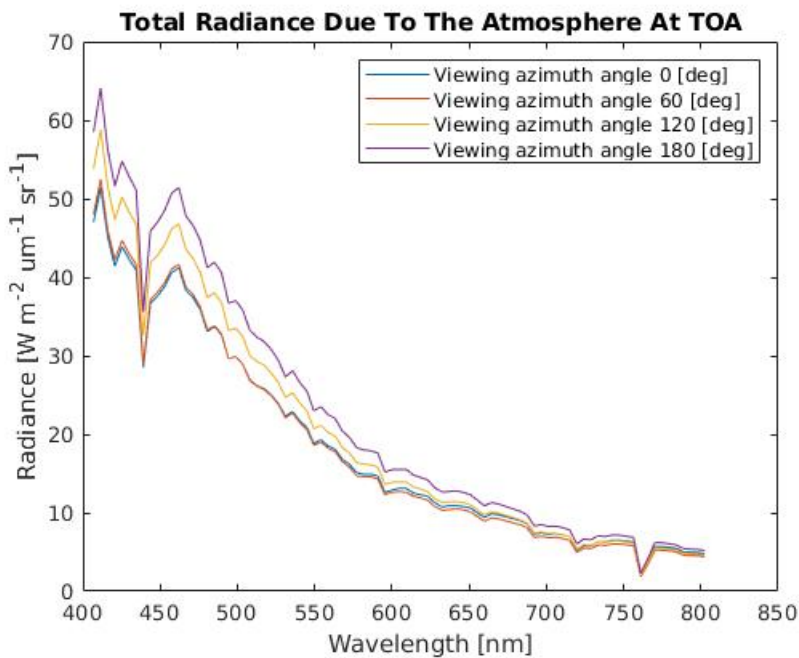


**Figure 12.16:** Resulting radiance at TOA due to atmospheric effects for various viewing azimuth angles.

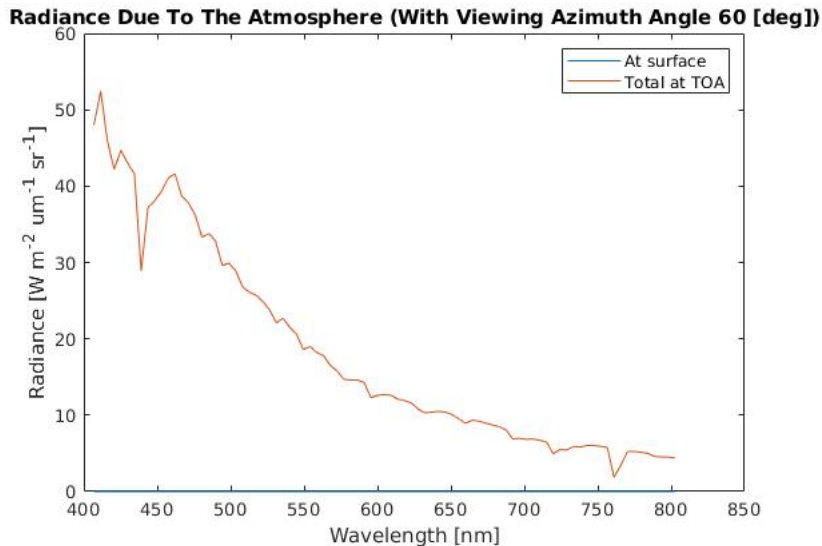


**Figure 12.17:** Resulting radiance due to atmospheric effects with the viewing azimuth angle 60°.

### 12.3.2 Water Leaving Radiance

#### Viewing Zenith Angles

Figure 12.18 illustrates the water leaving radiance at the ocean surface with the viewing zenith angle varying, more precisely for the viewing zenith angles  $120^\circ$ ,  $150^\circ$  and  $170^\circ$ . Figure 12.19, 12.20 and 12.21 present the three viewing zenith angles in separate figures, with the intention of demonstrating the wavelength dependent variations in the resulting radiance.

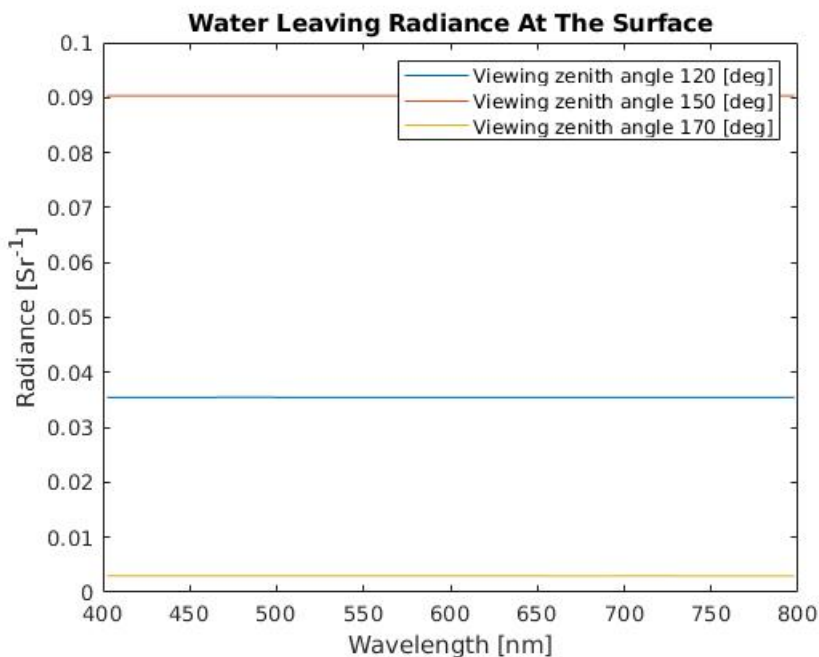


**Figure 12.18:** Resulting water leaving radiance at the ocean surface for various viewing zenith angles.

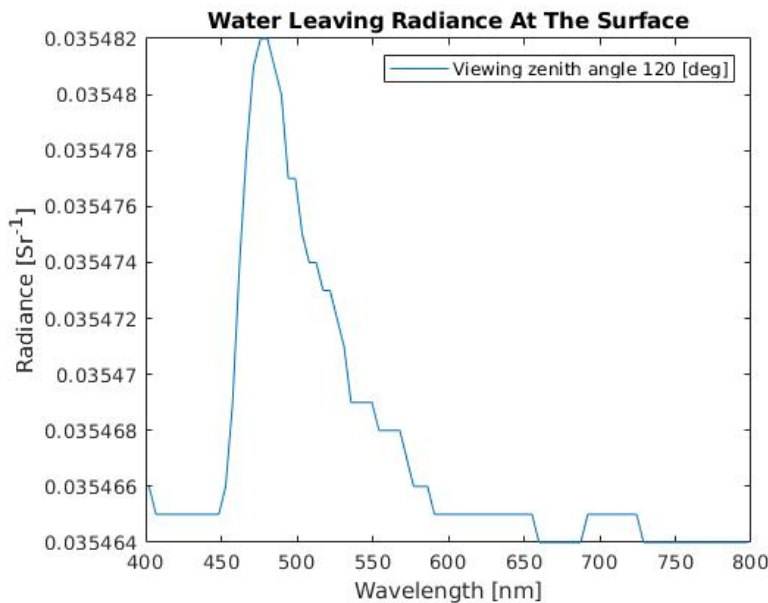


**Figure 12.19:** Water leaving radiance at the ocean surface with viewing zenith angle  $120^\circ$ .

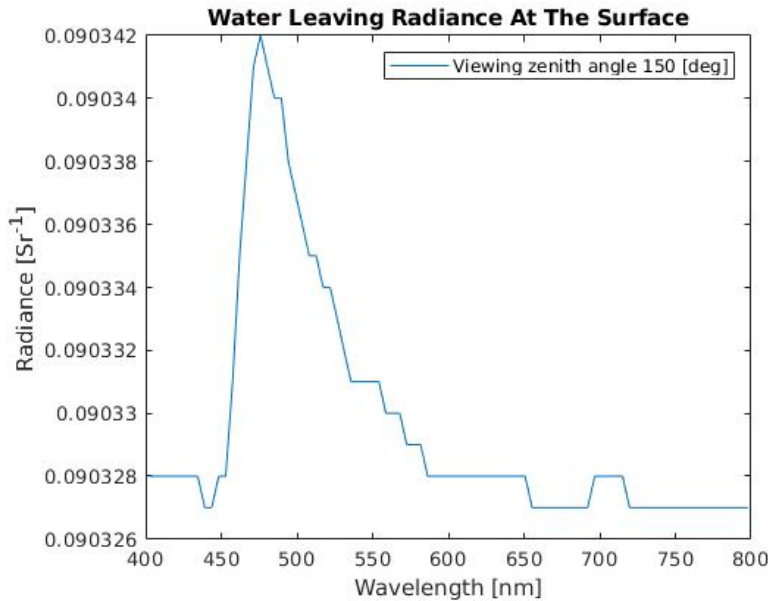


**Figure 12.20:** Water leaving radiance at the ocean surface with viewing zenith angle  $150^\circ$ .

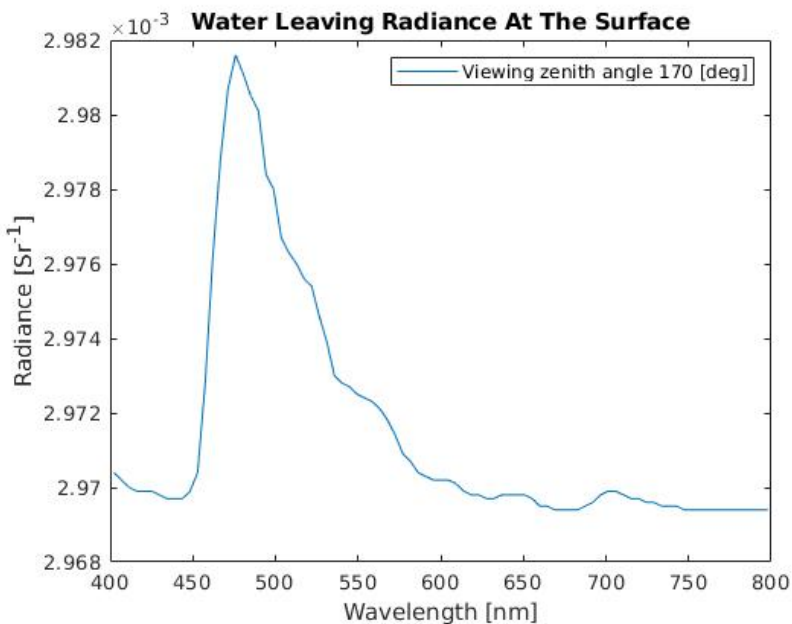


**Figure 12.21:** Water leaving radiance at the ocean surface with viewing zenith angle 170°.

### Viewing Azimuth Angles

Figure 12.22 presents the resulting water leaving radiance at the ocean surface while varying the viewing azimuth angle. The presented viewing azimuth angles are 0°, 60°, 120° and 180°. Figure 12.23 presents the same scenario, for the viewing azimuth angles of 60°, 120° and 180°. Figure 12.24 presents the water leaving radiance at the ocean surface for the viewing azimuth angle of 0°.

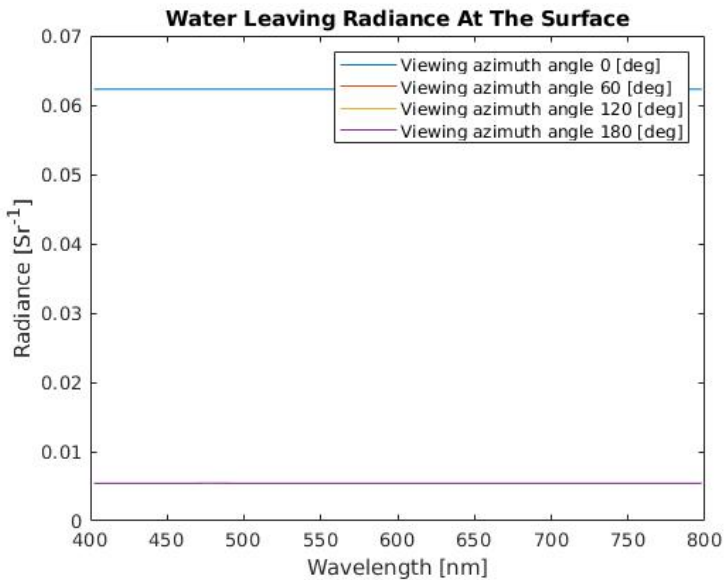


**Figure 12.22:** Resulting water leaving radiance at the ocean surface for various viewing azimuth angles.

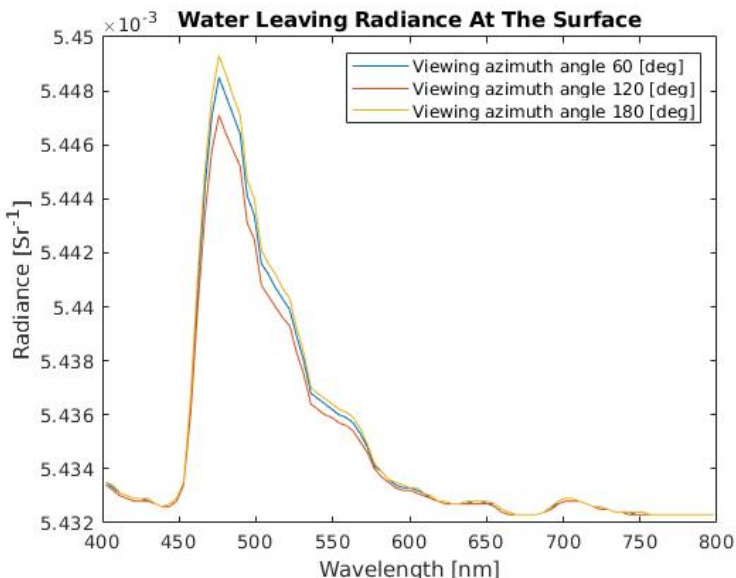


**Figure 12.23:** Resulting water leaving radiance at the ocean surface for three viewing azimuth angles.

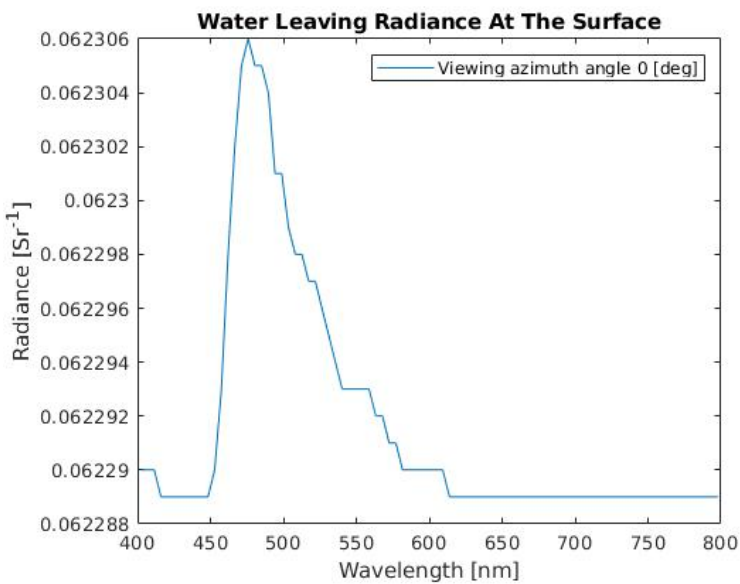


**Figure 12.24:** Water leaving radiance at the ocean surface with viewing azimuth angle  $0^\circ$ .

### 12.3.3 Viewing Angles Summary

#### Viewing Zenith Angles

Figure 12.25 illustrates the radiance difference between the radiance due to atmospheric effects and the water leaving radiance, at the ocean surface, with regard to the viewing zenith angle of  $30^\circ$ . The difference is presented as the water leaving radiance subtracted from the radiance due to atmospheric effects.

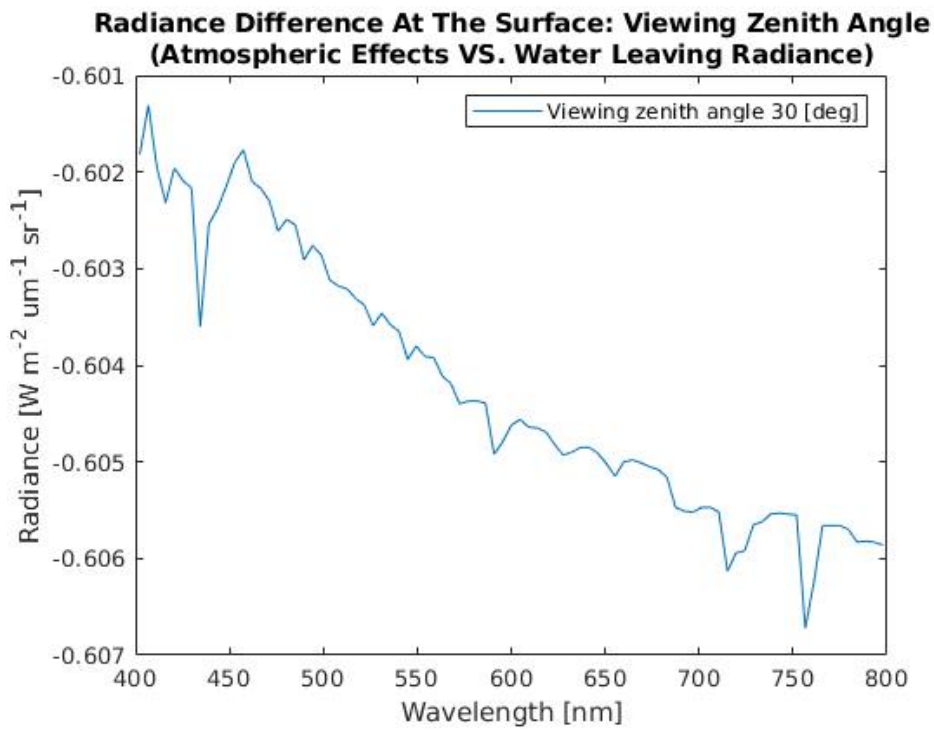


**Figure 12.25:** Radiance difference at the ocean surface for the viewing zenith angle  $30^\circ$ . Water leaving radiance at the ocean surface subtracted from the radiance due to atmospheric effects at the ocean surface.

## Viewing Azimuth Angles

Figure 12.26 and 12.27 illustrate the radiance difference between the radiance due to atmospheric effects and the water leaving radiance, at the ocean surface, with regard to viewing azimuth angle. The viewing azimuth angles in figure 12.26 are  $0^\circ$ ,  $60^\circ$ ,  $120^\circ$  and  $180^\circ$ . Figure 12.27 does not include the viewing azimuth angle of  $0^\circ$ . The difference is presented as the water leaving radiance subtracted from the radiance due to atmospheric effects.

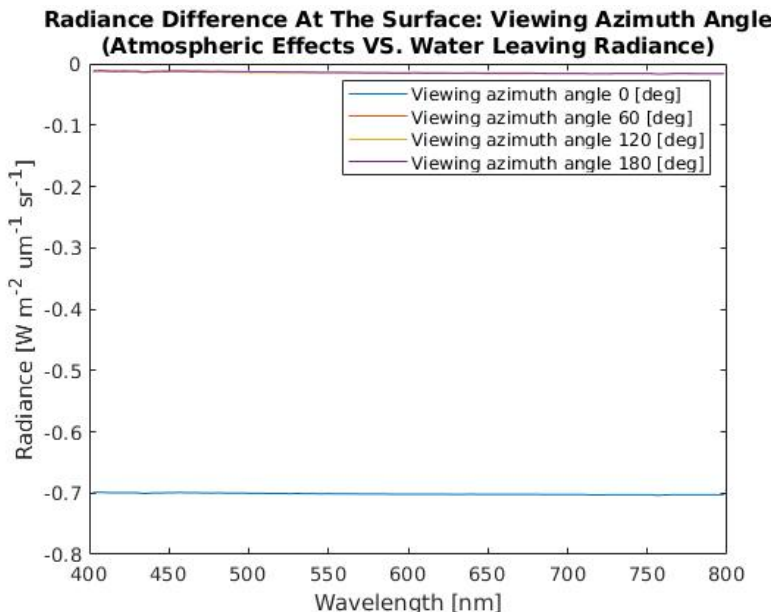


**Figure 12.26:** Radiance difference at the surface for various viewing azimuth angles. Water leaving radiance at the ocean surface subtracted from the radiance due to atmospheric effects at the ocean surface.

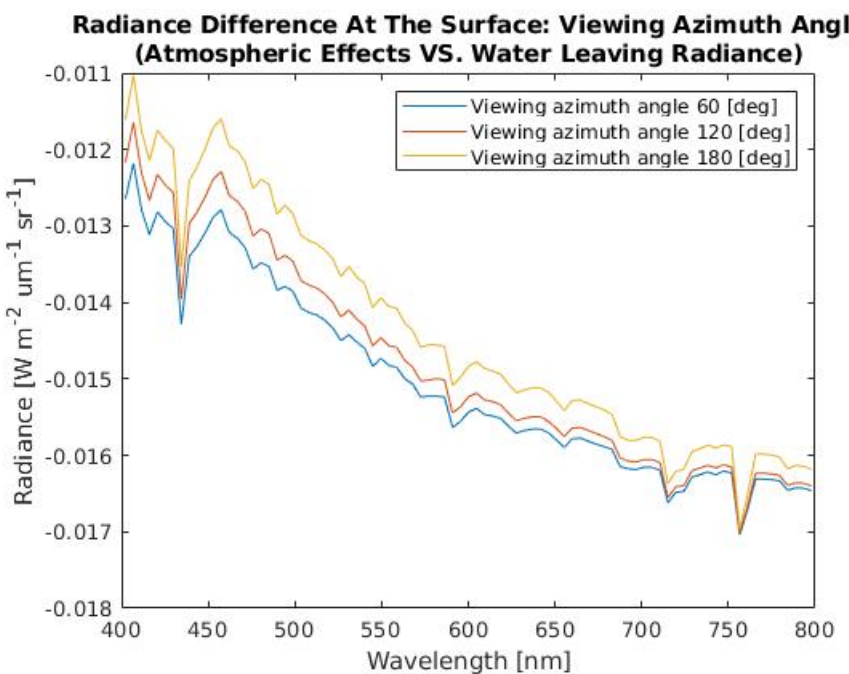


**Figure 12.27:** Radiance difference at the surface for various viewing azimuth angles. Water leaving radiance at the ocean surface subtracted from the radiance due to atmospheric effects at the ocean surface.

## 12.4 Clouds

Figure 12.28 presents the radiance due to atmospheric effects at the ocean surface for a scenario with water clouds above the ocean. Figure 12.29 presents the same scenario, but illustrates the radiance at TOA, rather than at the ocean surface. Figure 12.30 compares the radiances at the ocean surface and at TOA. Figure 12.31 presents the difference in radiance at TOA with respect to there being water clouds and there not being any clouds.

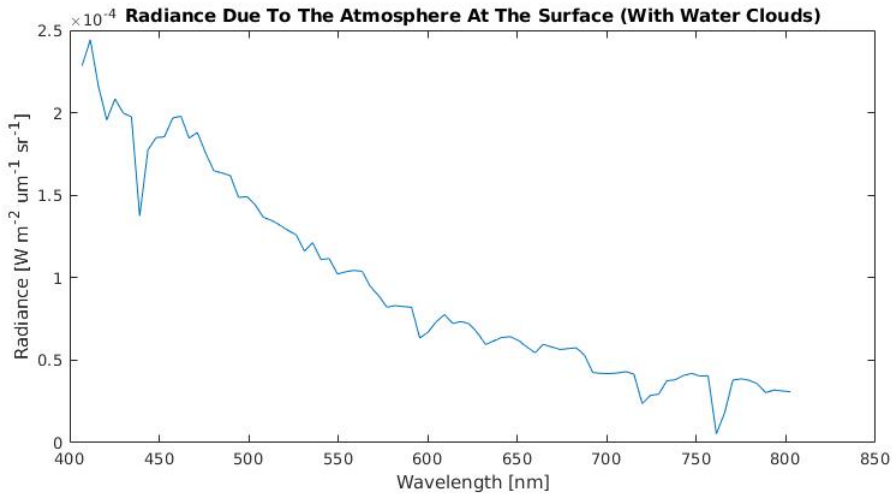


**Figure 12.28:** Radiance at the ocean surface due to atmospheric effects. With water clouds.

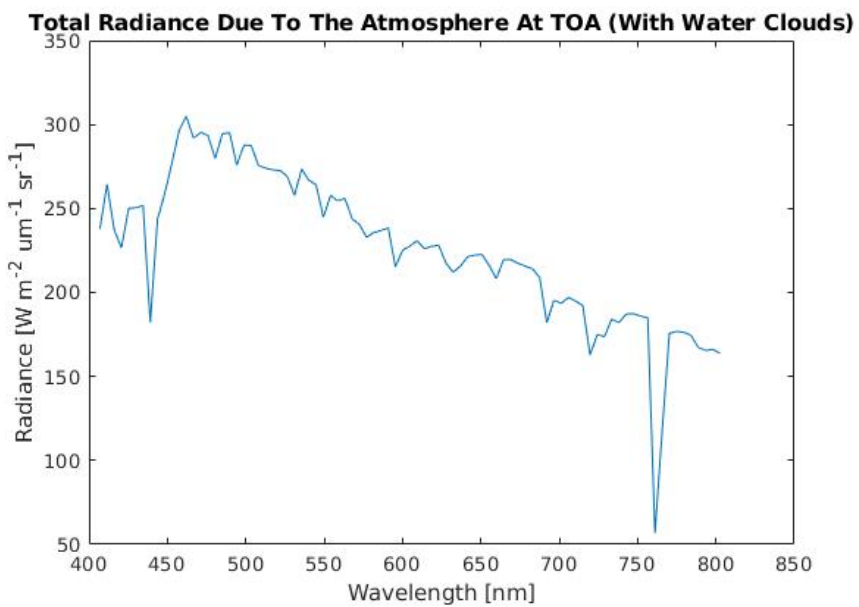


**Figure 12.29:** Radiance at TOA due to atmospheric effects. With water clouds.

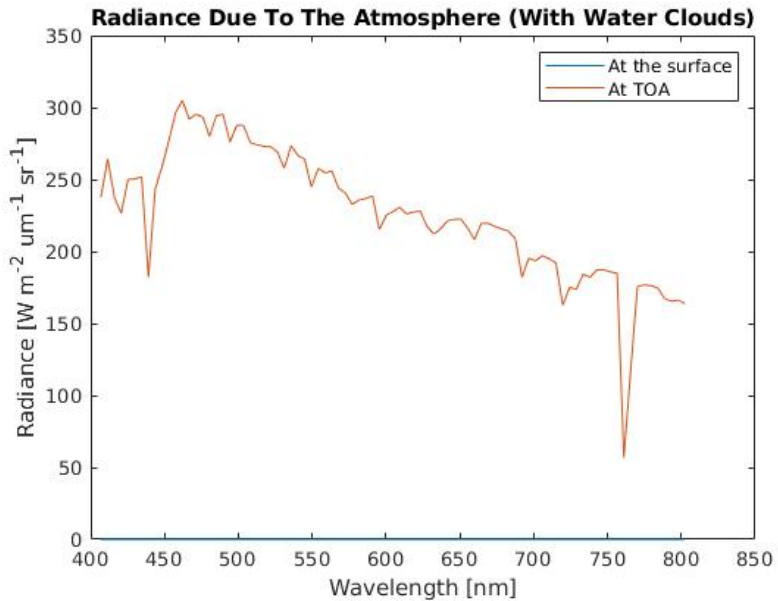


**Figure 12.30:** Radiance due to atmospheric effects. With water clouds.

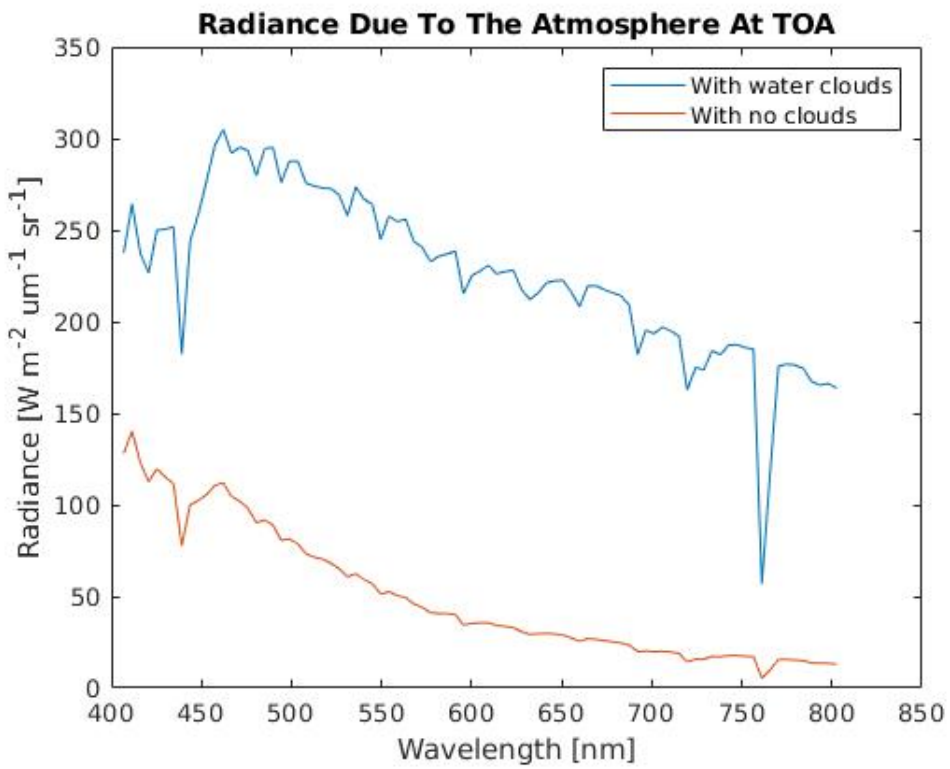


**Figure 12.31:** Radiance due to atmospheric effects. Comparison between water clouds and no clouds.

# Creating A Lookup Table For Simulation Of A Whole Scene

This chapter presents the results regarding the creation of the water leaving radiance lookup table and the simulation of the whole scene.

## 13.1 The Creation Of A Lookup Table

This section presents the results regarding the created lookup table. The time frame 501 was chosen in Panoply and utilized for providing range and variation, with regard to chl.a concentration values, for the lookup table calculation. Figure 13.1 illustrates the Panoply visualization of the time frame 501.

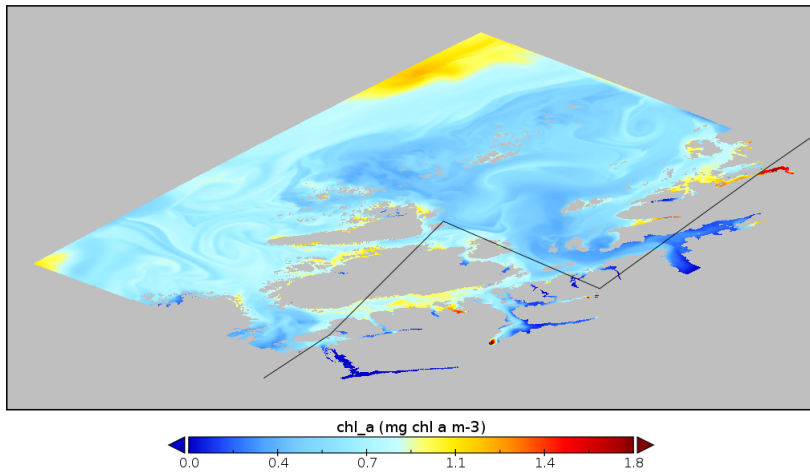


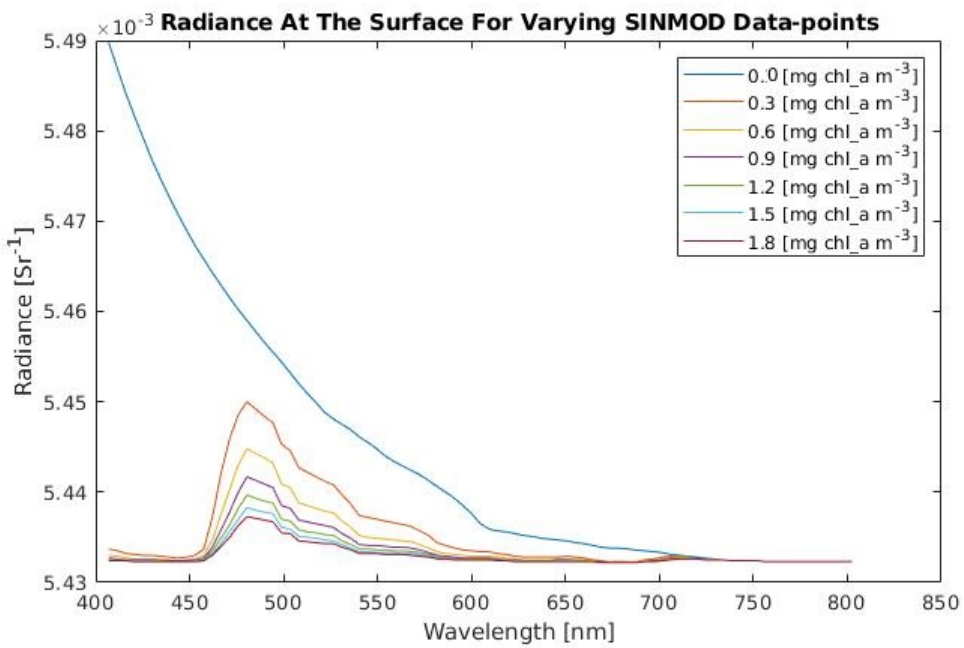
**Figure 13.1:** Chl<sub>a</sub> in time frame 501 visualized in Panoply.

The data points of interest, i.e. the geographical locations in time frame 501 used to obtain the chl<sub>a</sub> concentration values of interest in Matlab, were found utilizing Panoply, and are presented as MATLAB indices below.

- 0.0 [mg chl<sub>a</sub> m<sup>-3</sup>]: (4, 121, 501)
- 0.3 [mg chl<sub>a</sub> m<sup>-3</sup>]: (770, 269, 501)
- 0.6 [mg chl<sub>a</sub> m<sup>-3</sup>]: (713, 131, 501)
- 0.9 [mg chl<sub>a</sub> m<sup>-3</sup>]: (715, 133, 501)
- 1.2 [mg chl<sub>a</sub> m<sup>-3</sup>]: (721, 101, 501)
- 1.5 [mg chl<sub>a</sub> m<sup>-3</sup>]: (722, 102, 501)
- 1.8 [mg chl<sub>a</sub> m<sup>-3</sup>]: (727, 103, 501)

where each index represents (x, y, time).

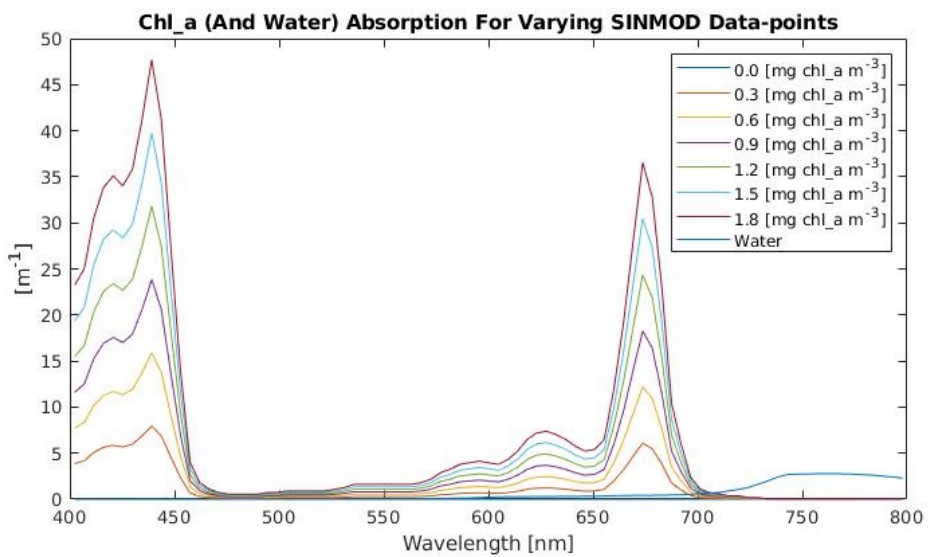
Figure 13.2 presents the water leaving radiance at the ocean surface for different SINMOD data points, i.e. for different values of the chl<sub>a</sub> concentration [mg chl<sub>a</sub> m<sup>-3</sup>]. Figure 13.3 presents the absorption due to chl<sub>a</sub> concentrations and due to pure water for the same SINMOD data points. Figure 13.4 illustrates the same phenomena, but only for the wavelengths 400 - 700 nm, thus presenting the variations more straightforwardly for the wavelengths of interest. Figure 13.5 presents the scattering due to the selected chl<sub>a</sub> concentrations, while figure 13.7 presents the water scattering for the same chl<sub>a</sub> concentration values. More precisely, figure 13.2, 13.3, 13.5 and 13.7 presents their respective scenarios for seven SINMOD data points.



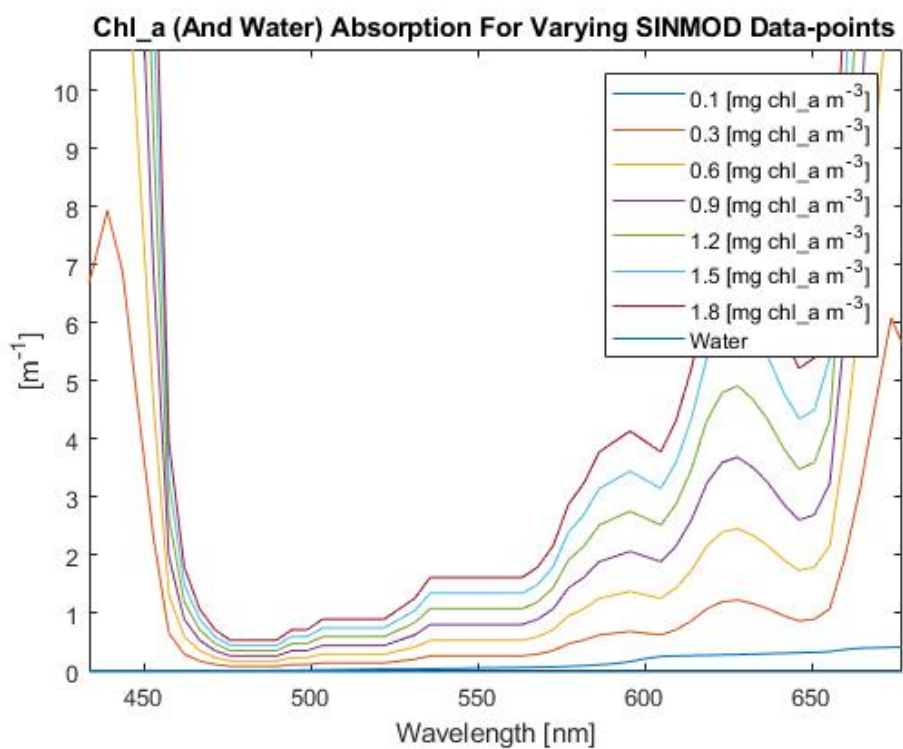
**Figure 13.2:** Water leaving radiance at the ocean surface for different SINMOD data points, i.e. for different chl<sub>a</sub> values.

Figure 13.6 compares the water leaving radiance at the ocean surface calculated by Planar-Rad for a chosen SINMOD data point and the water leaving radiance at the ocean surface for the same value calculated by utilizing the lookup table. The chl<sub>a</sub> concentration value applied in figure 13.6 is  $3.409 \times 10^{-1} \text{ mg chl}_a \text{ m}^{-3}$ .

Figure 13.8 presents several resulting water leaving radiance values from the lookup table together with several resulting water leaving radiance values from PlanarRad. The stippled lines are results from the lookup table, while the filled lines are results from PlanarRad.



**Figure 13.3:** Absorption due to chl<sub>a</sub> concentration values, and pure water, for varying SINMOD data points.



**Figure 13.4:** Absorption due to chl<sub>a</sub> concentration values, and pure water, for varying SINMOD data points. A closer view.

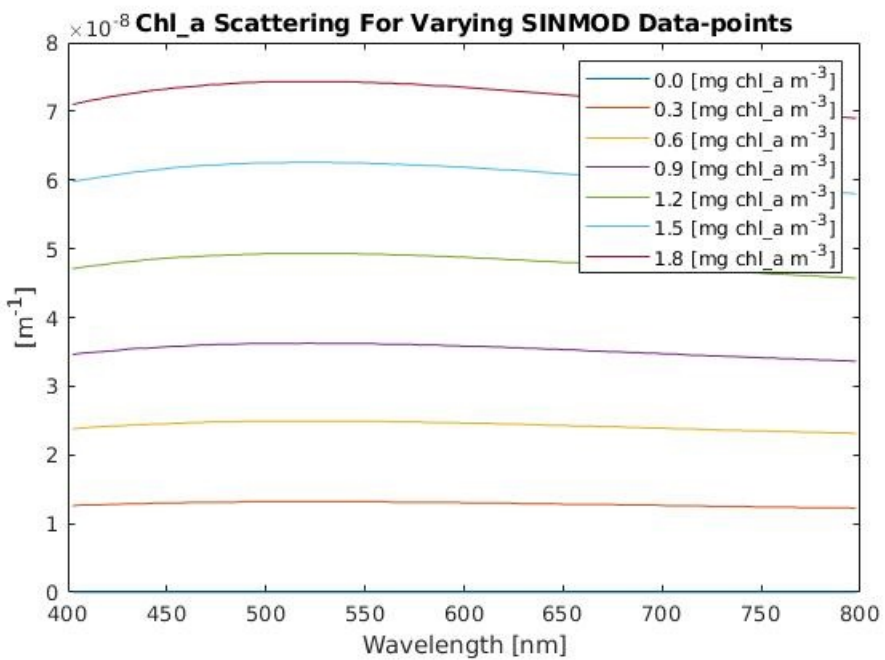


**Figure 13.5:** Scattering due to chl\_a concentration values for varying SINMOD data points.

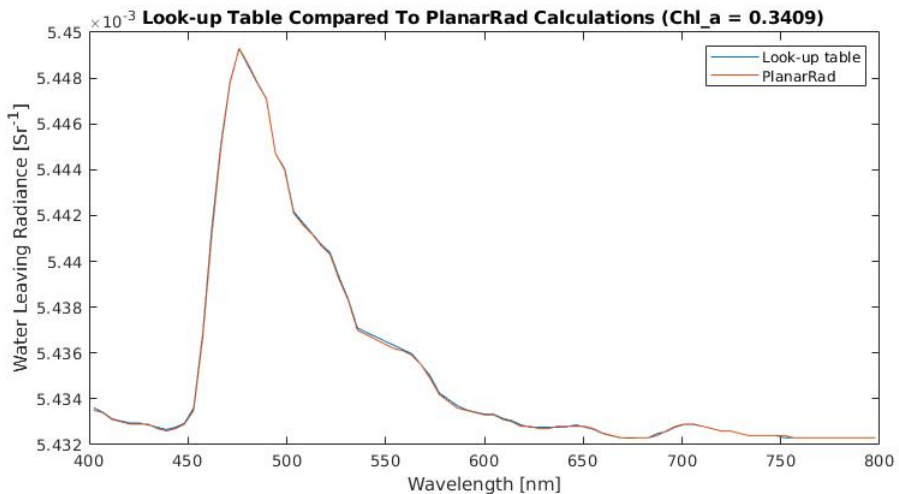


**Figure 13.6:** Comparing the water leaving radiance calculated by the lookup table and the water leaving radiance calculated by PlanarRad for  $\text{chl\_a} = 3.409 \times 10^{-1} \text{ mg chl\_a m}^{-3}$ .

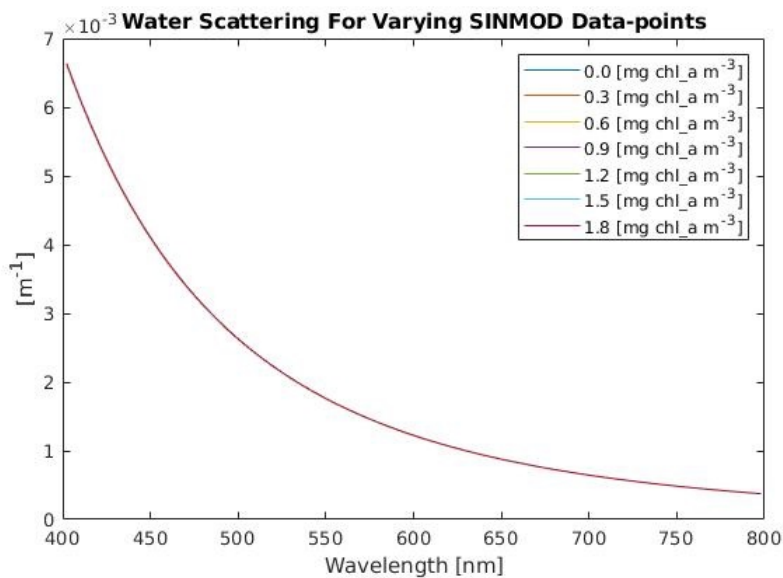


**Figure 13.7:** Scattering due to pure water for varying SINMOD data points.

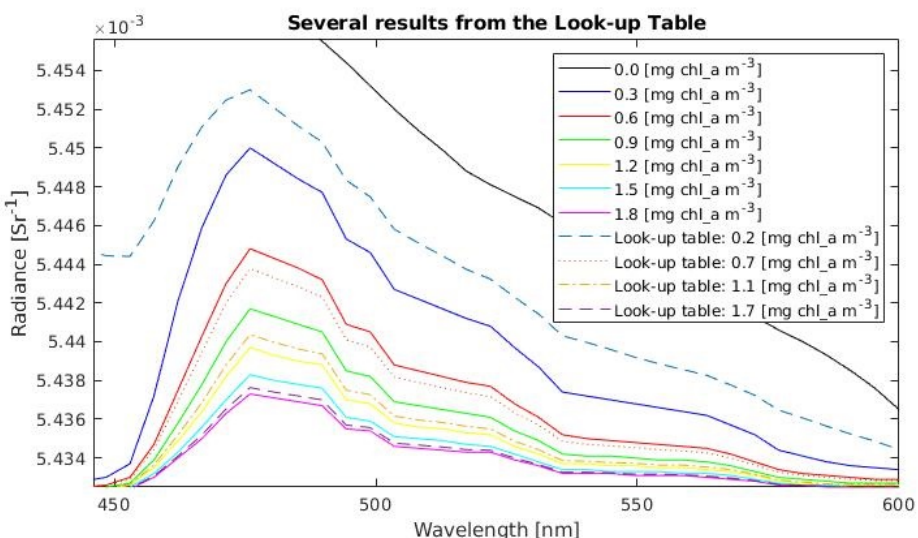


**Figure 13.8:** Several results from the lookup table, presented together with several results from PlanarRad.

## 13.2 Simulating A Whole Scene

The created scene was calculated by selecting a number of chl\_a concentration values from the time frame 501 in the SINMOD dataset. The resulting hyperspectral cube had the dimensions 13 X 25 X 87. The dimensions represent 13 latitude values, 25 longitude values, and 87 wavelength bands.

Figures 13.9, 13.10, 13.11, 13.12, 13.13 and 13.14 present the same result, a 4D plot, from different views. The figures present a 4D plot representing the water leaving radiance for a whole scene. Two of the axes represent latitude and longitude from the starting data point. The third axis represents the wavelengths of interest, i.e. 400 to 800 nm. The color in the plots represents the water leaving radiance values. That is to say, the color of a point represents the water leaving radiance at that latitude, longitude and wavelength. The water leaving radiances were calculated utilizing the lookup table. Figure 13.12 presents the perspective from above the scene.

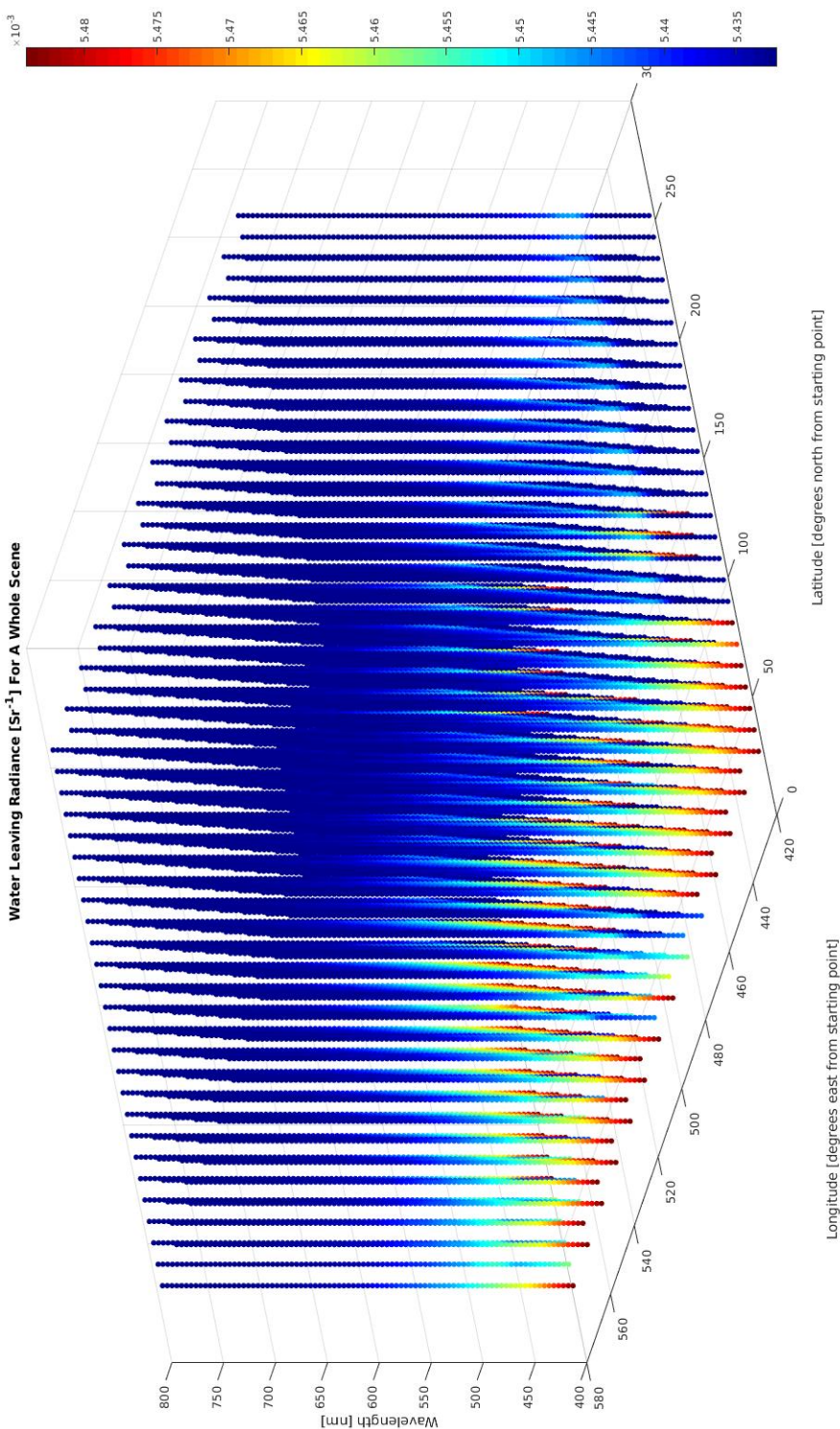


**Figure 13.9:** Illustration of water leaving radiance for a whole scene (view 1).

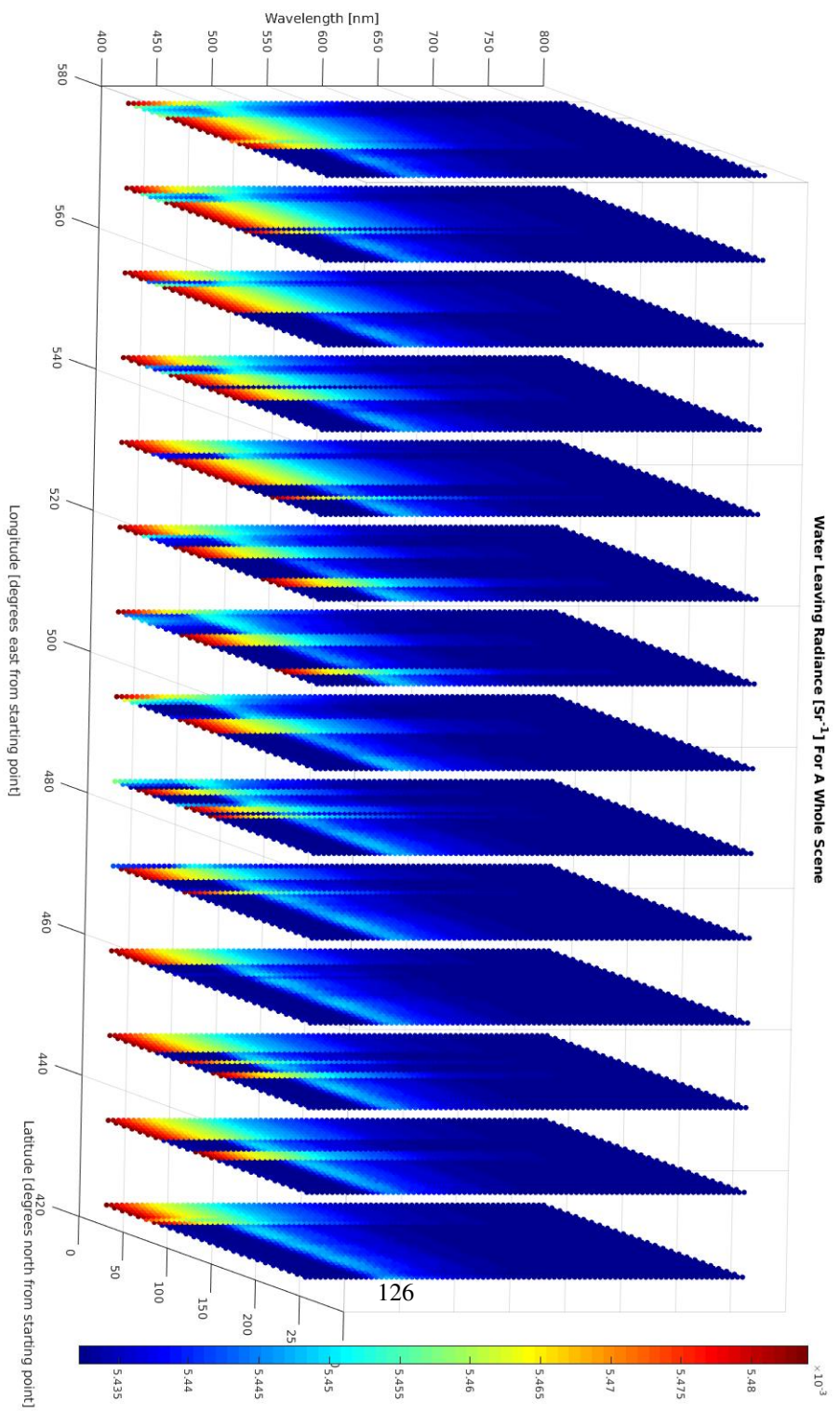


**Figure 13.10:** Illustration of water leaving radiance for a whole scene (view 2).

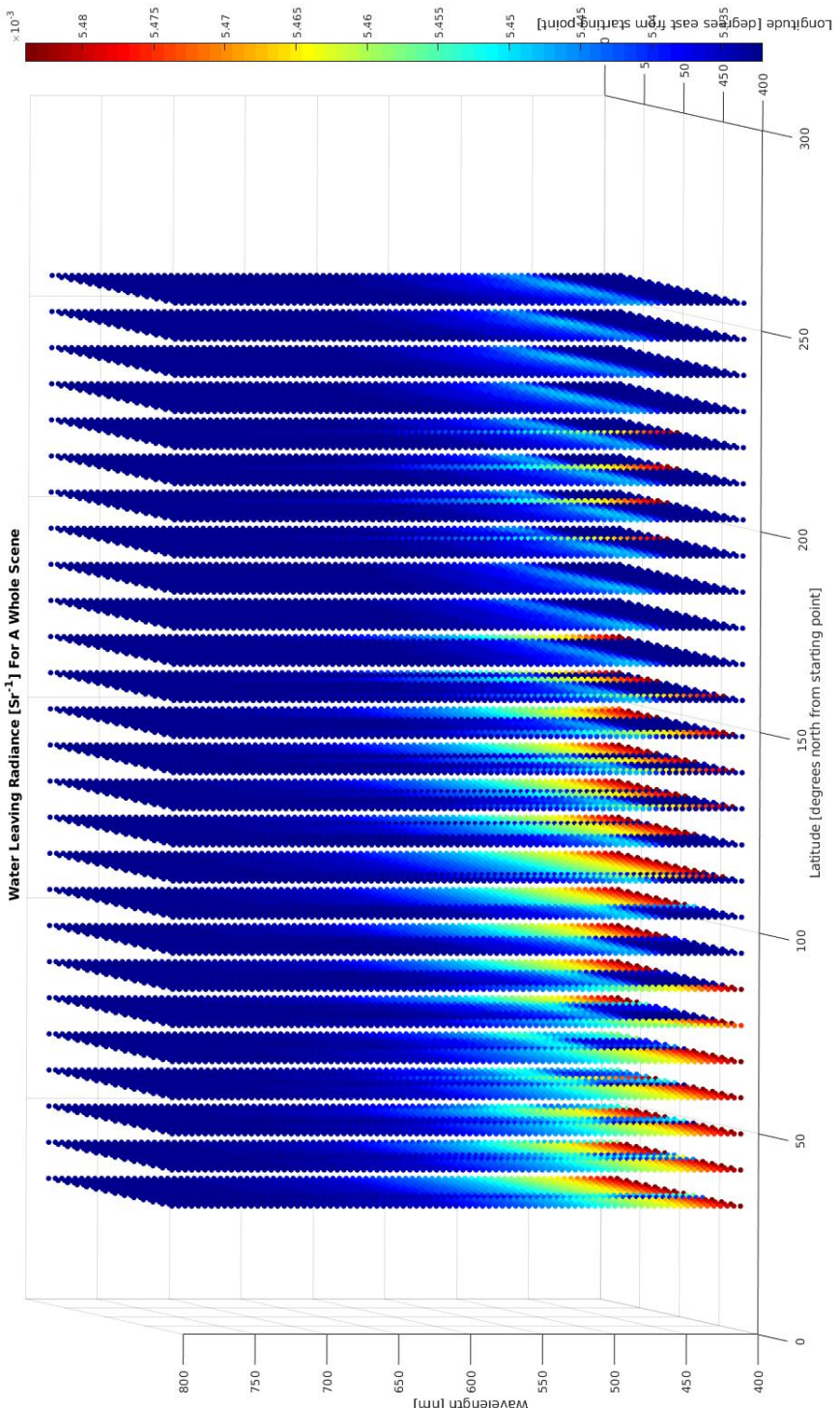


Figure 13.11: Illustration of water leaving radiance for a whole scene (view 3).

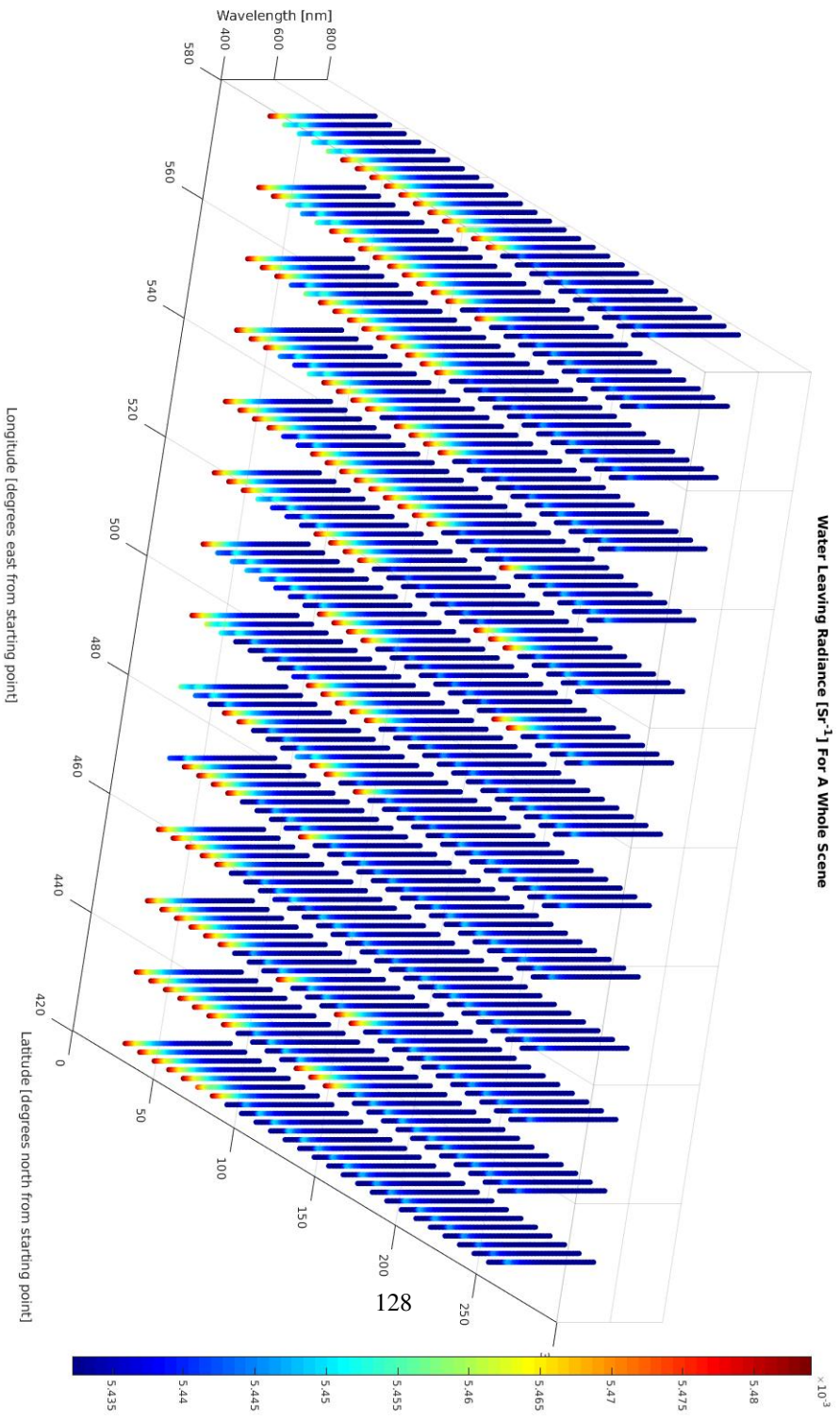
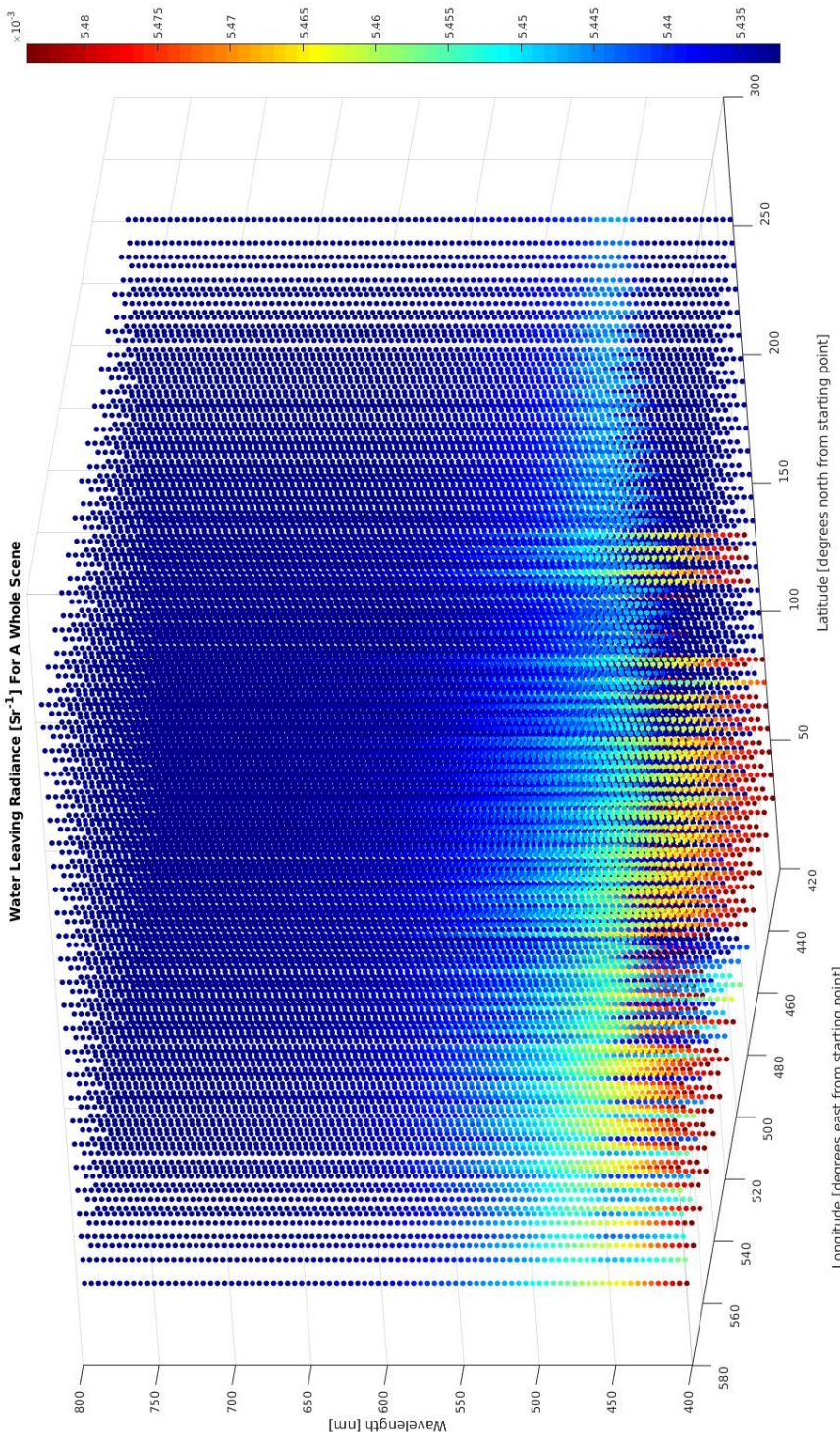
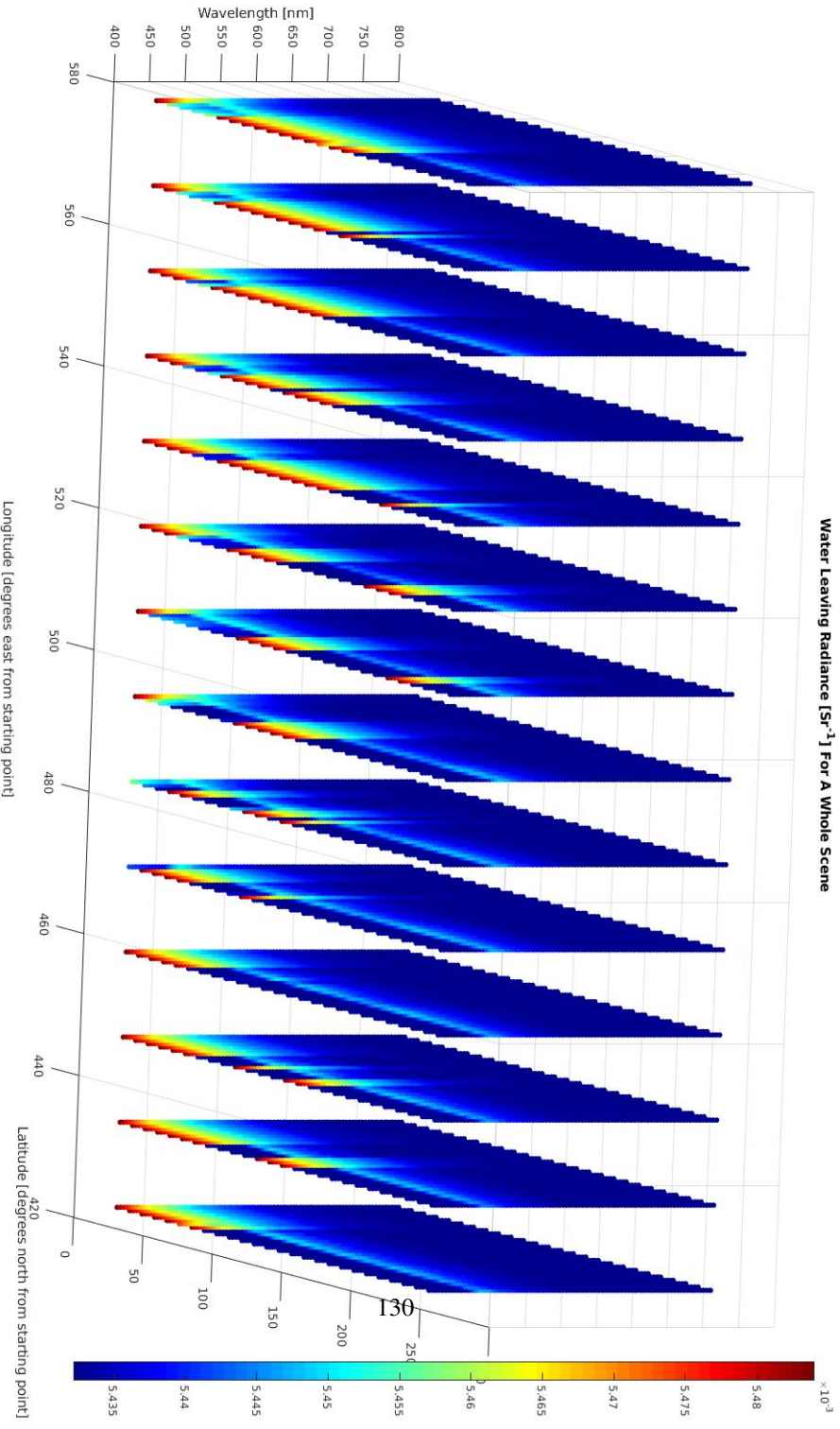


Figure 13.12: Illustration of water leaving radiance for a whole scene (view 4).



**Figure 13.13:** Illustration of water leaving radiance for a whole scene (view 5).



**Figure 13.14:** Illustration of water leaving radiance for a whole scene (view 6).

# Temporal Sensitivity Of Data Acquisition Analysis

This chapter presents the results regarding the temporal sensitivity of data acquisition analysis. The results are presented in two parts, i.e. regarding the tests performed by utilizing Panoply and the tests performed by utilizing the lookup table.

## 14.1 Panoply

As mention in chapter 8, Panoply was used in order to identify which part of the SINMOD dataset contains the changing chl\_a concentration values. The resulting area of interest included the x-axis values of 0 – 768 and the y-axis values of 470 – 578.

Figure 14.1 presents the Panoply illustration of the chl\_a concentration at three consecutive time frames, i.e. at time frame 160, 161 and 162. Thus, there is 1 hour in between the three illustrations. Figure 14.2 presents the same scene, for time frames 162, 167 and 172. Thus, there are 5 hours in between the three illustrations.

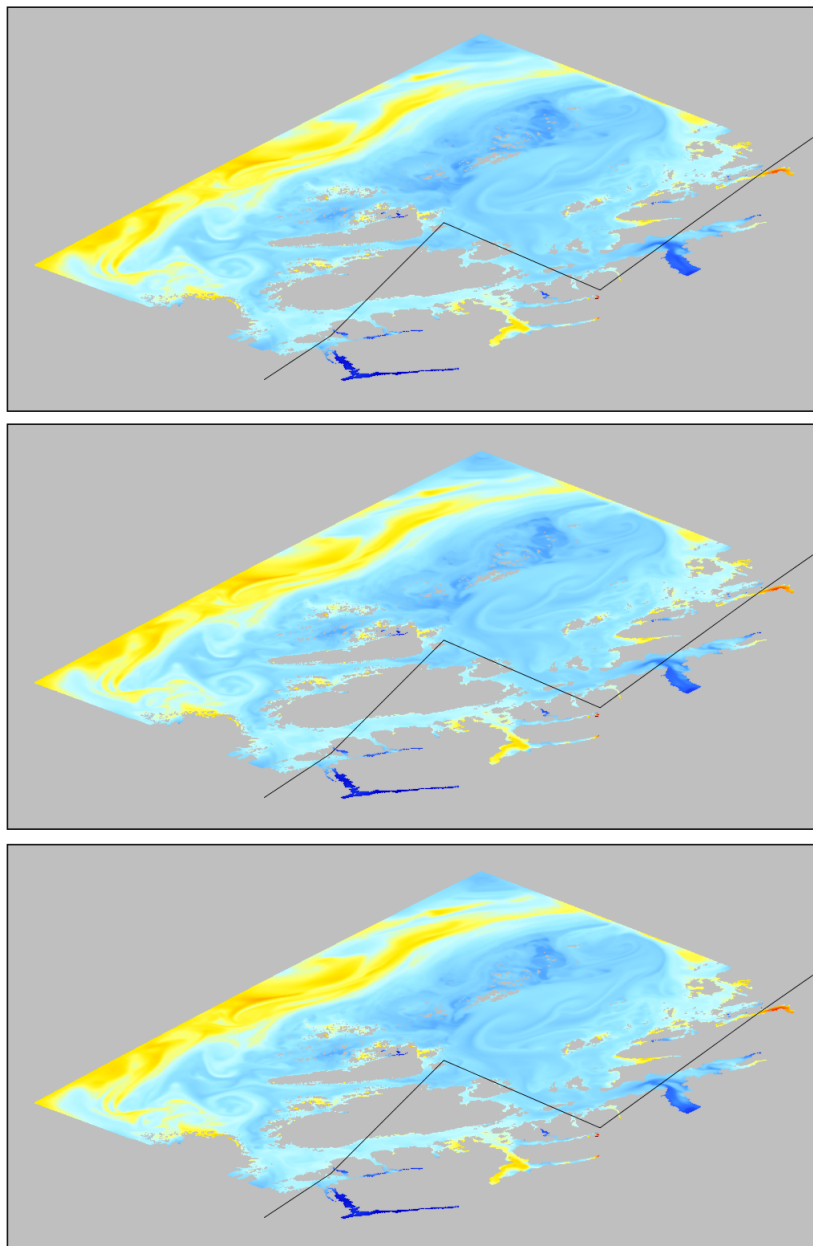


**Figure 14.1:** Illustrations from Panopoly at time stamp 160, 161 and 162.

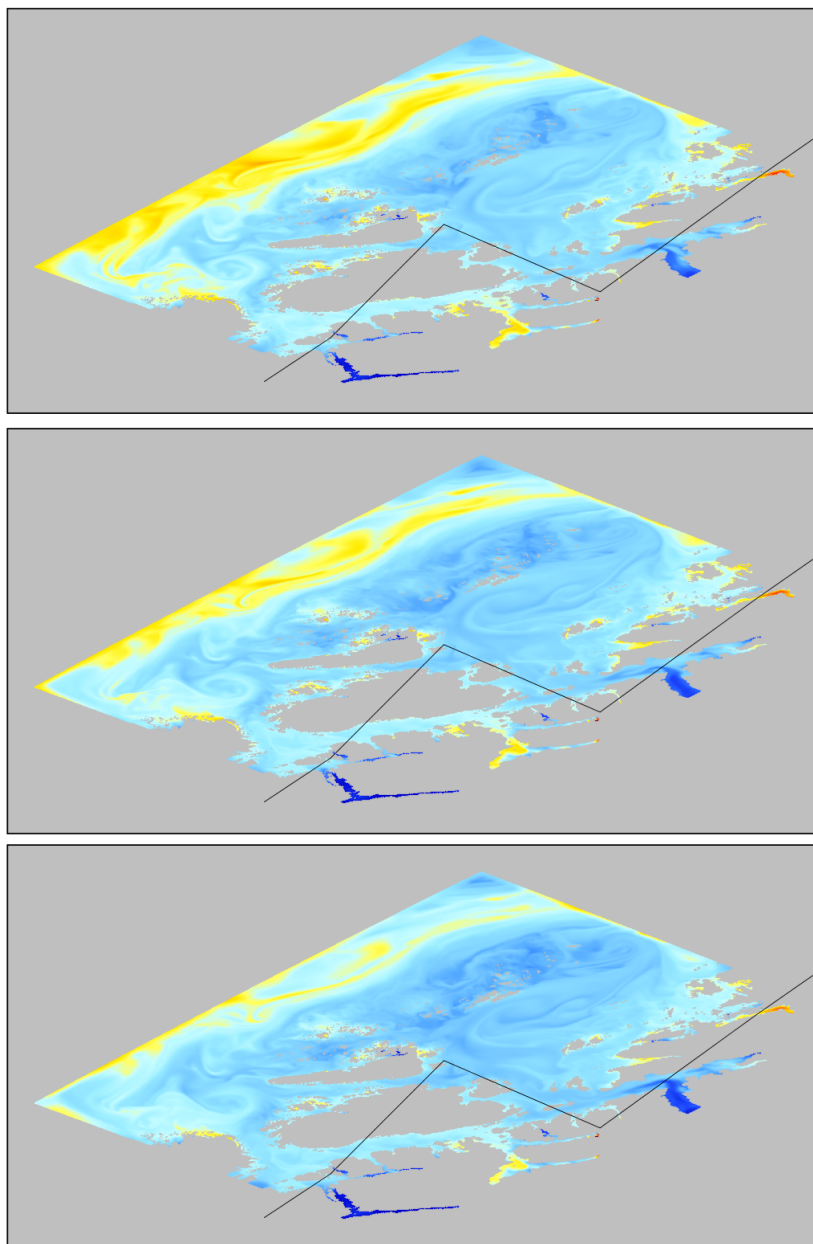
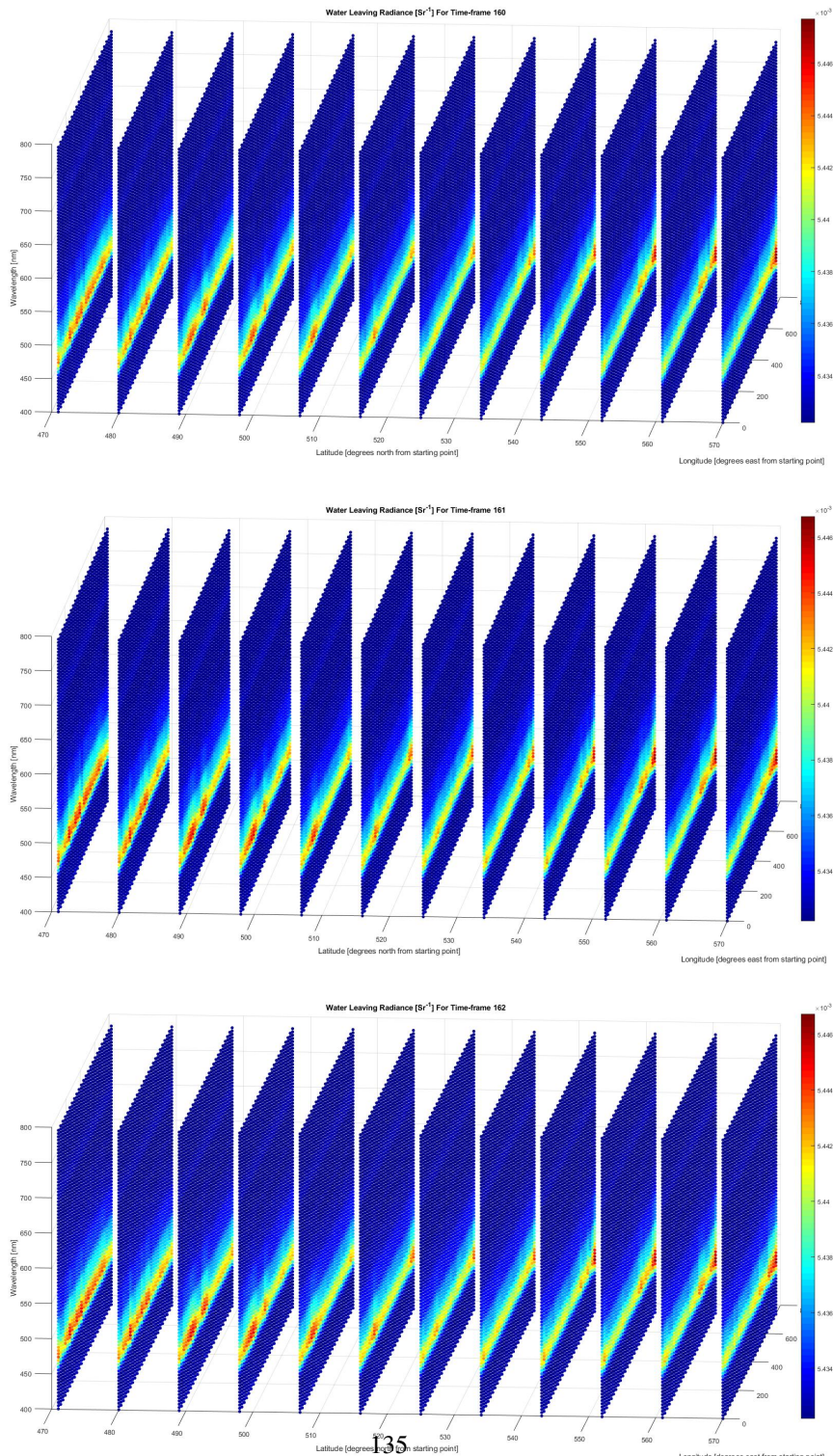


**Figure 14.2:** Illustrations from Panoply at time stamp 162, 167 and 172.

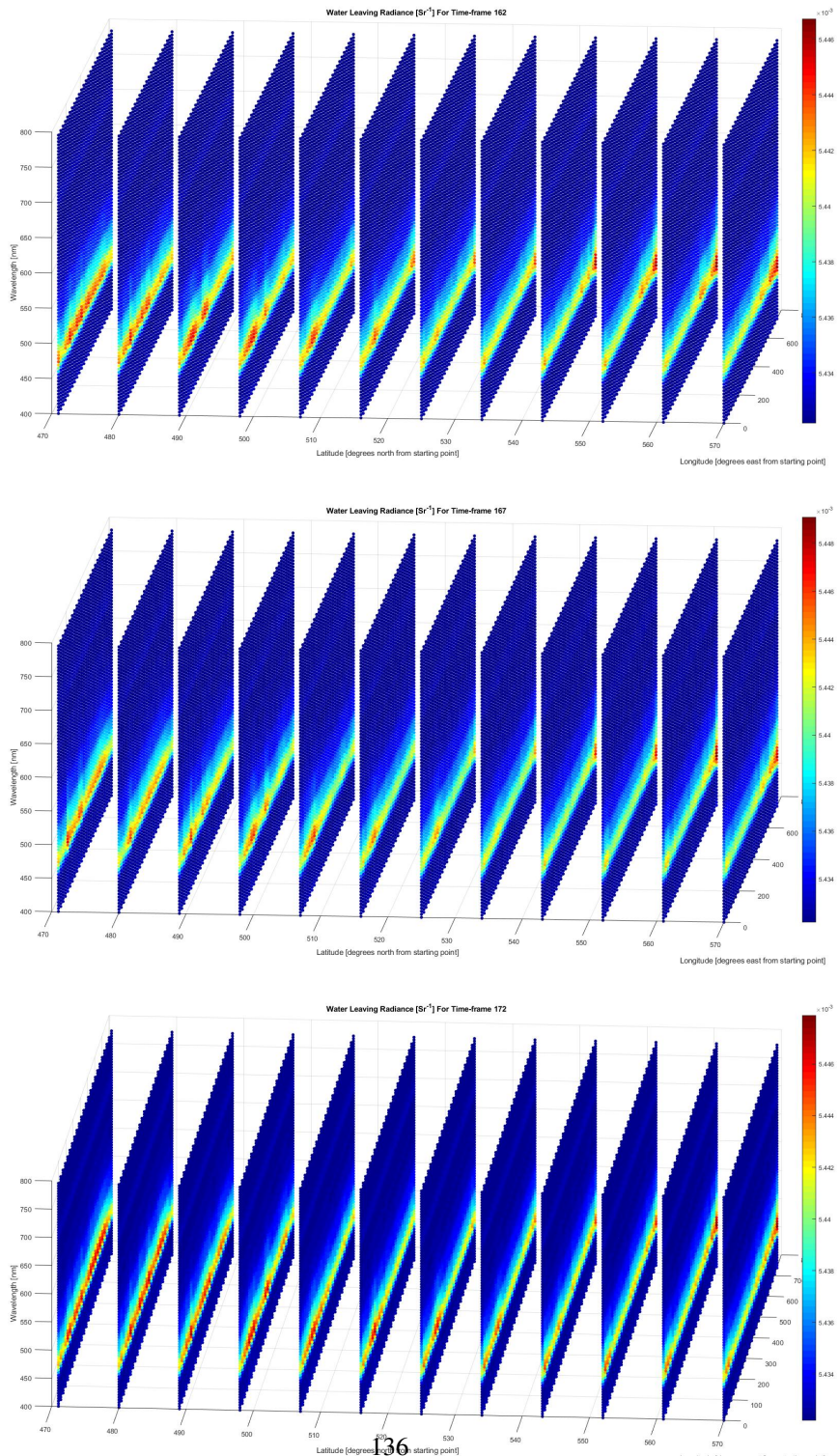
## 14.2 The Lookup Table

Figure 14.3 and 14.4 illustrate the water leaving radiance at the ocean surface for three different time frames each. Figure 14.3 presents the time frames 160, 161 and 162, i.e. frames with 1 hour in between them. Figure 14.4 on the other hand, presents the time frames 162, 167 and 172, i.e. frames with 5 hours in between them.

Figure 14.5 and 14.6 illustrate the variations between the time frames in a more straightforwardly manner. Figure 14.5 demonstrates the difference in water leaving radiance values between the frames 160 and 161, while figure 14.6 presents the the difference in water leaving radiance values for the frames 162 and 172.



**Figure 14.3:** Water leaving radiance [ $sr^{-1}$ ] from time frames 160, 161 and 162, respectively.



**Figure 14.4:** Water leaving radiance [ $\text{sr}^{-1}$ ] from time frame 162, 167 and 172, respectively.

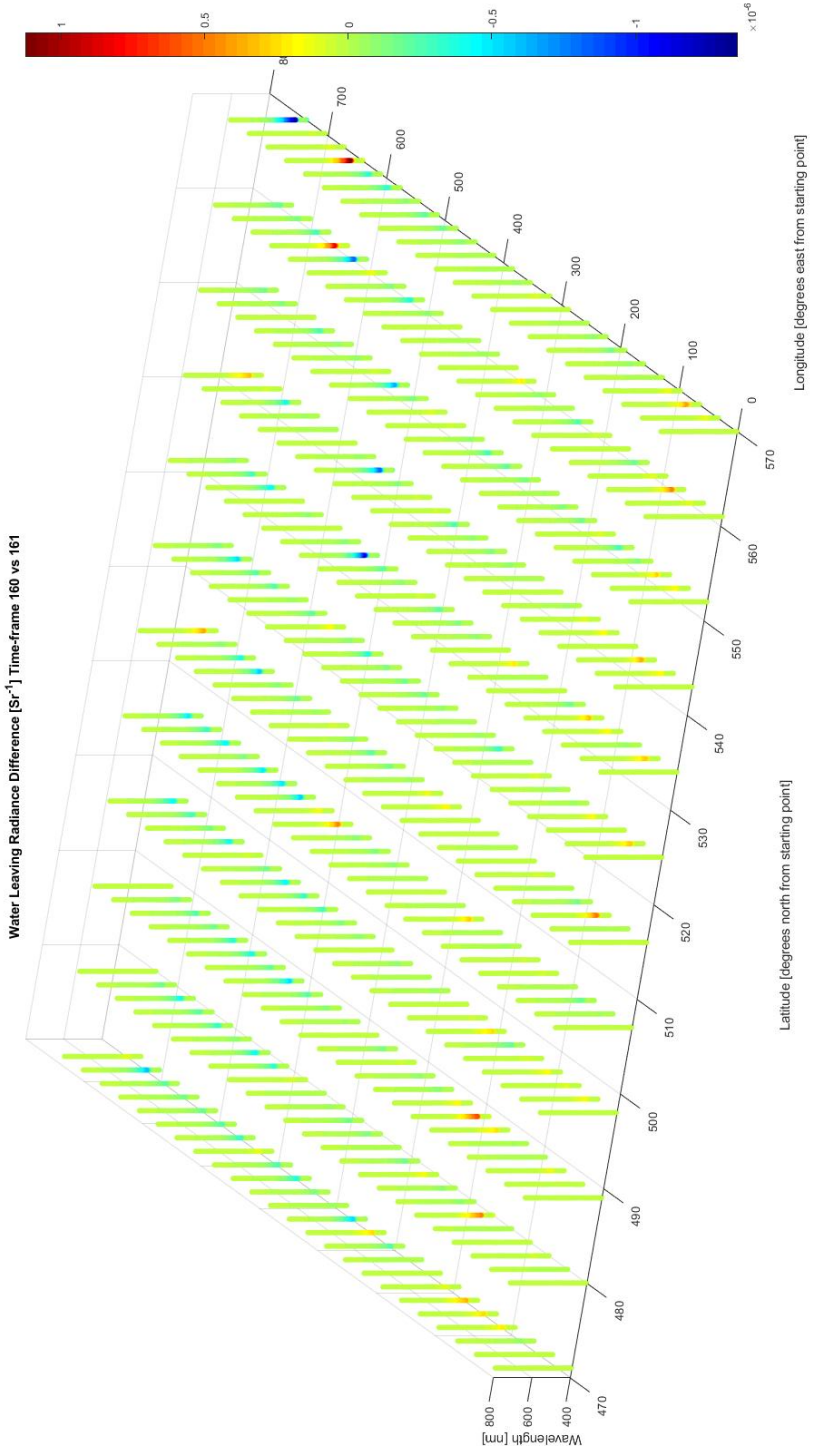


**Figure 14.5:** Water leaving radiance difference [ $\text{sr}^{-1}$ ] from time frame 160 to time frame 161.

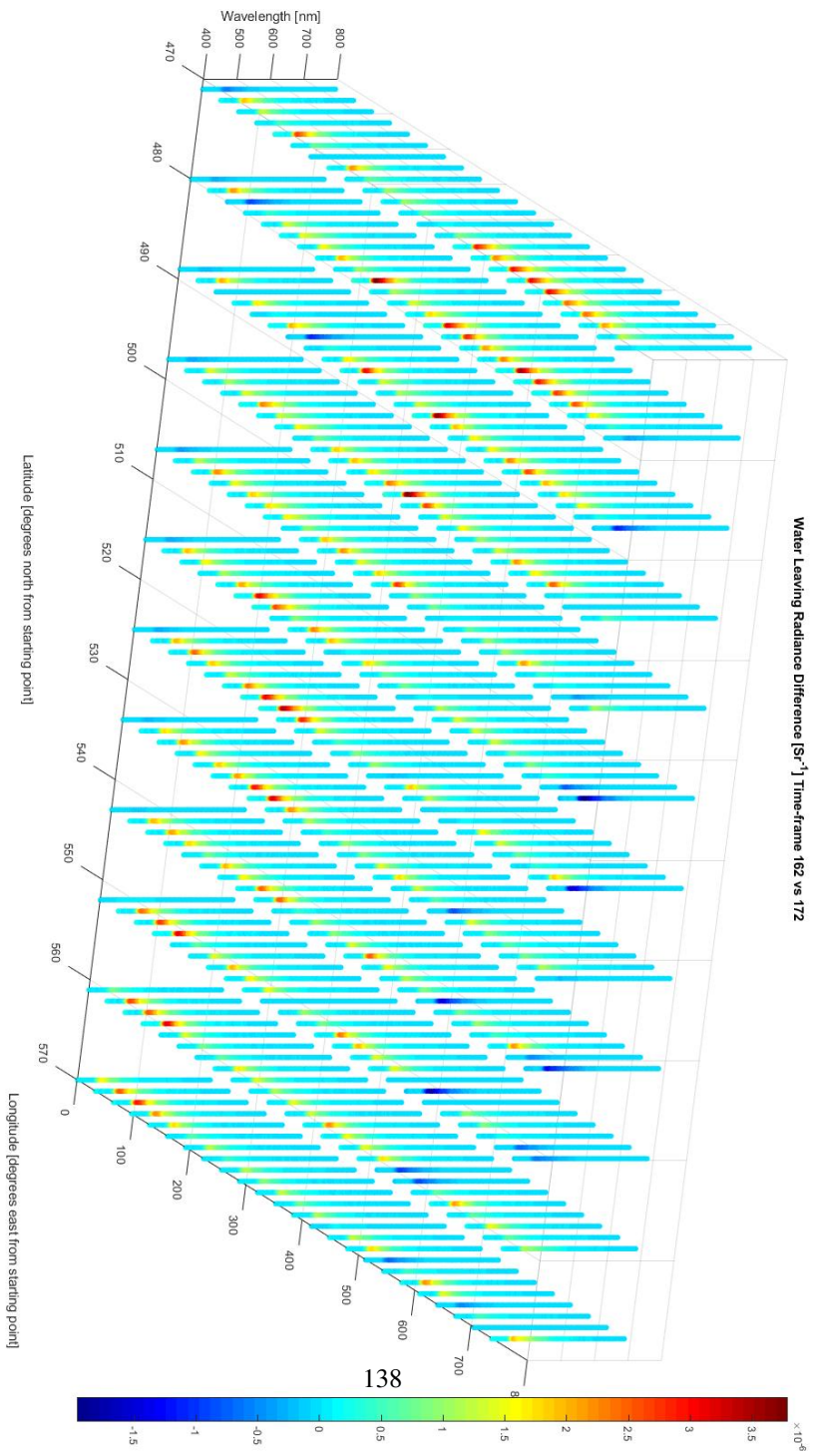


**Figure 14.6:** Water leaving radiance difference [ $\text{sr}^{-1}$ ] from time frame 162 to time frame 172.

Figure 14.7 and 14.8 present the same variations as figures 14.5 and 14.6, i.e. between time frames 160 and 161 and between the time frames 162 and 172, but given as change in percentage. More precisely, figure 14.7 presents the water leaving radiance difference from frame 160 to frame 161 as a percentage of the water leaving radiance values in frame 160. In the same manner, figure 14.8 presents the water leaving radiance difference from frame 162 to frame 172 as the percentage of the water leaving radiance values in frame 162.

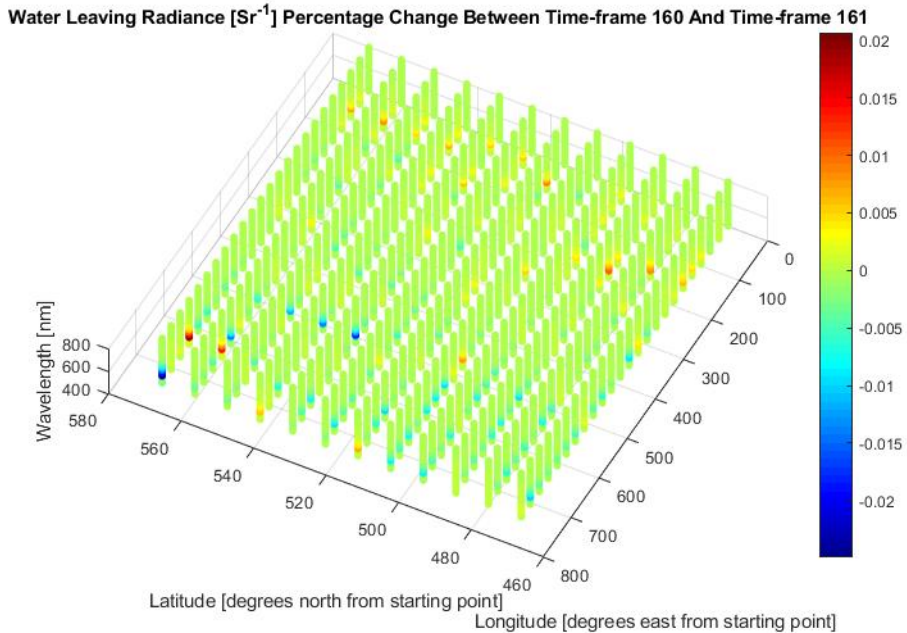


**Figure 14.7:** Water leaving radiance [ $\text{sr}^{-1}$ ] percentage change between the time frame 160 and the time frame 161.

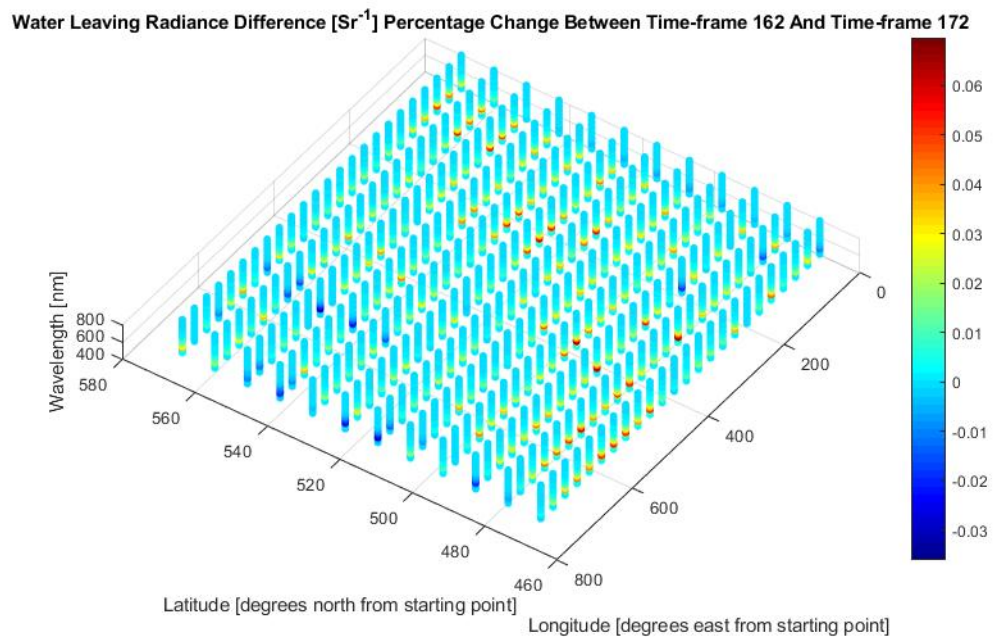


**Figure 14.8:** Water leaving radiance [ $sr^{-1}$ ] percentage change between the time frame 162 and the time frame 172.

Figures 14.9, 14.10 and 14.11 present the maximum water leaving radiance variations over 1 hour, 5 hours and 10 hours, respectively. Figure 14.12 presents the three time correlated variations in one figure. The red lines represent the 1 hour maximum water leaving radiance variation, the blue lines represent the 5 hours maximum water leaving radiance variation and the green lines represent the 10 hours maximum water leaving radiance variation.

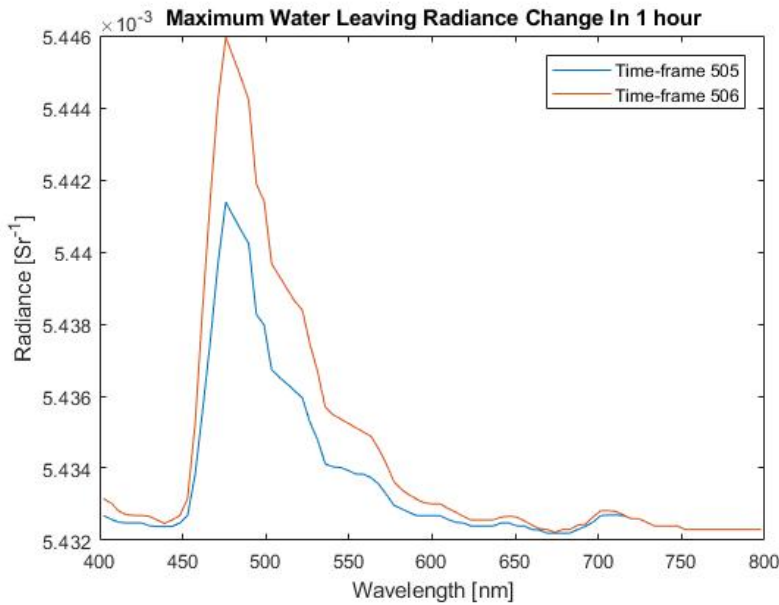


**Figure 14.9:** Maximum water leaving radiance change over 1 hour.

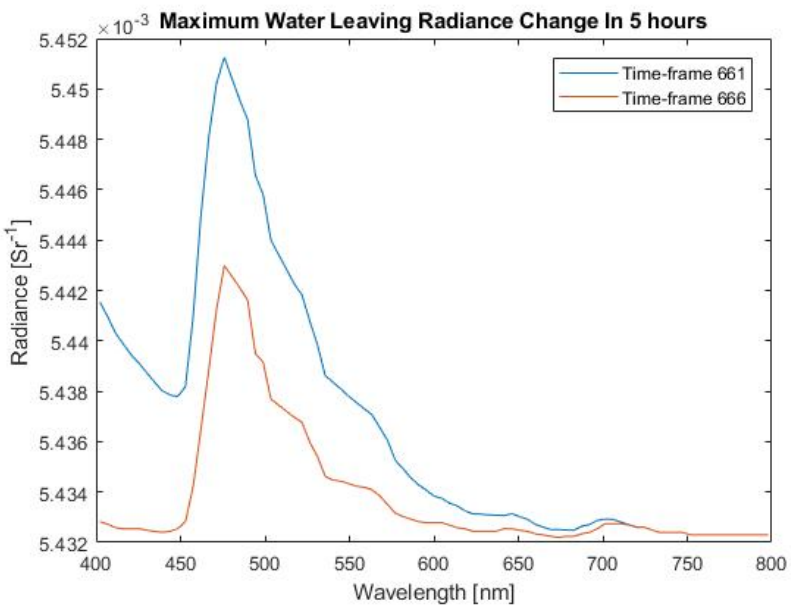


**Figure 14.10:** Maximum water leaving radiance change over 5 hours.

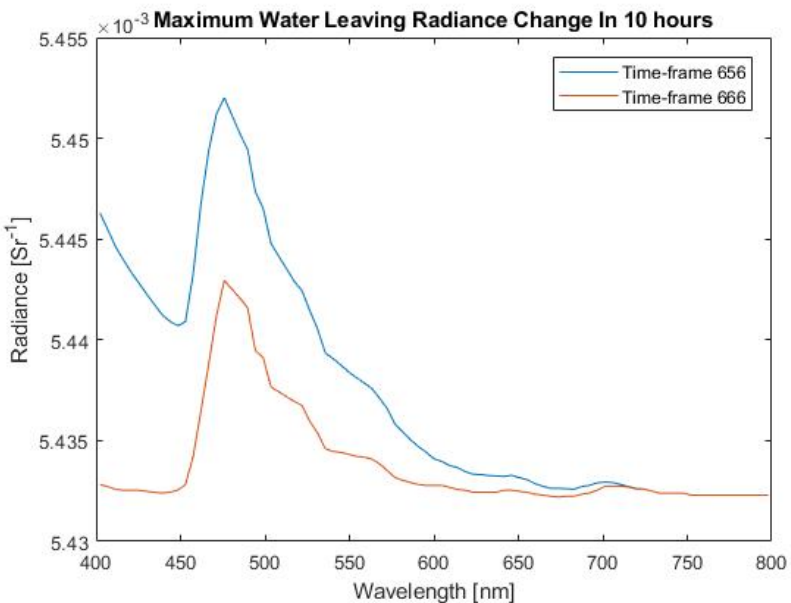


**Figure 14.11:** Maximum water leaving radiance change over 10 hours.

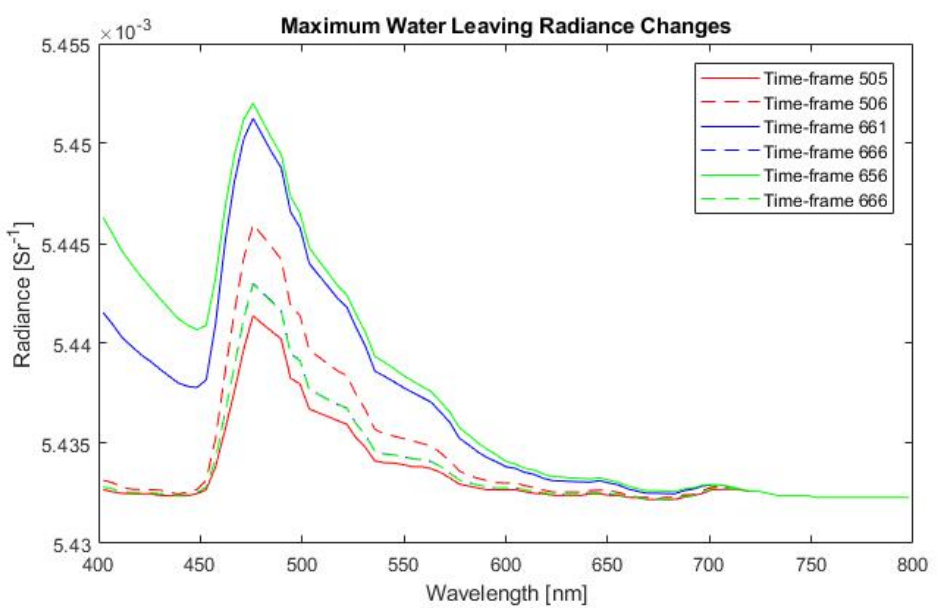


**Figure 14.12:** Maximum water leaving radiance change over 1 hour, 5 hours and 10 hours.

# User Friendly Interface For The Software

The general results include the possibility for the HYPSO mission, and other interested parties, to utilize the work and data created in this thesis at any time, without requiring help from the creator.

The python interface to PlanarRad is more automatic. It is no longer required to change the inputs of interest in several locations in a handful of files, but rather only in the input file. The created input Matlab file is the only file where the user is required to provide inputs. The computational time was shortened with approximately 25 minutes for each input parameter. That is, if four solar zenith angles are provided, the computational time of the RadPhyll Simulator is approximately 1 hour and 40 minutes shorter than the computational time of PlanarRad.

For specifics on the resulting user friendly program, i.e. the RadPhyll Simulator, see the documentation and user guide in appendix A.

## **Part IV**

# **Discussion and Conclusions**

# Discussion

## 16.1 Combining The MATLAB Files From The Preliminary Work

11 Matlab scripts were created in the preliminary work. These were altered and combined into two scripts.

## 16.2 Developing Batch Runs For PlanarRad

A resulting effect of batch runs being developed for PlanarRad was that all the input values can be specified in one input file, instead of manually providing all the input values and scrutinizing through the computer for several input files. The values of interest for the batch report can be specified.

The result from the test regarding whether the same results are produced regardless of whether one employs the GUI was expected, as the same program was operated, with the same input values. Nonetheless, the test was deemed necessary to ensure the batching worked as intended.

## 16.3 Examining Different Scenarios

This section, i.e. section 16.3, regards the examination of different scenarios, such as the effect on the water leaving radiance due to various solar angles. Firstly, several frequent observations, and the reason for their occurrences, will be presented. Then, effects of

various solar and viewing angles will be presented, as well as the effects of water clouds on the radiance at TOA.

### 16.3.1 Frequent Observations

In general, differences occurring between various viewing and/or solar angles are due to absorption and scattering in the atmosphere, as well as due to the ocean surface not being a Lambertian surface.

The radiance at the ocean surface due to atmospheric effects is small compared to the radiance at TOA due to atmospheric effects. This is expected, as the total attenuation through the atmosphere is the sum of free space path loss and attenuation caused by atmospheric absorption (Blattenberger [a]). The free space path loss regards the fact that the power level of a transmitted signal decreases at a rate inversely proportional to the distance traveled and proportional to the wavelength of the signal as it traverses the atmosphere (Blattenberger [b]). That is, the solar radiance will be stronger at TOA than at the ocean surface, as well as the distance where absorption and scattering can occur is smaller between the sun and TOA, than between the sun and the ocean surface.

The following sections will discuss dips and peaks that occur frequently for the resulting radiances presented in this chapter, as well as present the reason for these occurrences.

The water reflectance is high at wavelengths shorter than 500 nm, which corresponds to blue water (Gower et al. [2005]). The water reflectance gives a peak near 560 nm, corresponding to green water (Gower et al. [2005]). Chl.a fluorescence produces a narrow peak for the water reflectance at 685 nm (Gower et al. [2005]). These characteristics can be somewhat observed for resulting radiance due to atmospheric effects at TOA, as this radiance includes the radiance due to atmospheric effects at the ocean surface that has been reflected by the ocean surface and propagated to TOA.

The radiance due to atmospheric effects frequently decreases with increasing wavelengths. This is due to the absorption and scattering by gases and aerosols in the Earth's atmosphere. See sections 2.1.3 and 2.1.7.

The radiance due to atmospheric effects frequently results in a dip at 430-435 nm. This corresponds to the blue part of the visible spectrum, as illustrated in figure 12.8. This dip is below 700 nm. Thus, it is due to absorption by various elements in the sun's photosphere (Mobley). Specifically, the dip is due to absorption by calcium, iron and hydrogen (Starr [2005]).

The radiance due to atmospheric effects frequently results in a dip at 761 nm, i.e. in the infrared radiation. This dip is above 700 nm. Thus, it is due to absorption by atmospheric oxygen, the fact that the sun's irradiance is close to a blackbody spectrum, and due to absorption by water vapor (Mobley).

A dip in the resulting radiance due to atmospheric effects frequently occurs at 589 nm due to absorption by sodium in the sun's photosphere (Starr [2005]).

A peak in the water leaving radiance generally occurs at 476 nm. This is due to the chl\_a absorption, which is high for wavelengths 400 - 450 nm and 650 - 700 nm, and lowest at approximately 475 nm.

### 16.3.2 Solar Azimuth Angle

Figure 12.2 and 12.3 present the water leaving radiance at the ocean surface for various solar azimuth angles. They differ by figure 12.3 not including the solar azimuth angle of 180°.

The resulting water leaving radiance values with respect to the solar azimuth angle of 120°, represented by the yellow mark in figure 12.2, appears to be missing. However, figure 12.3 reveals that the values are approximately  $6.7 * 10^{-3} \text{ sr}^{-1}$ , which is the same value as for the water leaving radiance resulting from the solar azimuth angle of 180°. The water leaving radiance values resulting from the solar azimuth angles of 60° and 0° are roughly the same. This can also be observed in figure 12.3. This observation is expected due to the azimuthally symmetry of the scattering process, as presented in section 2.1.2. This holds when the medium is isotropic as well as the light is unpolarized, which is true for sunlight propagating through the atmosphere, as long as no cirrus clouds, ice fogs or similar, are present (Mobley). It also holds for natural waters. The scattering is generally divided into forward scattering and backward scattering. The backscatter fraction regards the fraction that is deflected through scattering angles greater than 90 deg. This quantity is fundamental to remote sensing, due to most of the light leaving the ocean in an upward direction is backscattered sunlight (Mobley). Thus, the observation of the difference between the resulting water leaving radiance with regard to whether the solar azimuth angle is greater than 90° or not, is due to the azimuthally symmetry and the backscattering effect.

Figure 12.4 illustrates the water leaving radiance at the ocean surface resulting from the solar azimuth angles of 0° and 60°. The resulting water leaving radiance values from the two solar azimuth angles vary in the same manner with respect to wavelengths. Both solar azimuth angles result in a peak at 476 nm. This peak occurs for all solar azimuth angles in figures 12.2 and 12.3 as well, and is due to absorption by various elements in the sun's photosphere (Mobley). The peaks have water leaving radiance values that are approximately  $1.3 * 10^{-5} \text{ sr}^{-1}$  higher than general water leaving radiance values for the two solar azimuth angles.

The difference between the resulting water leaving radiance with respect to utilizing the solar azimuth angle of 180° or 120°, and utilizing the solar azimuth angle of 60° or 0° is approximately  $1.25 * 10^{-3} \text{ sr}^{-1}$ .

### 16.3.3 Solar Zenith Angle

#### Radiance Due To Atmospheric Effects

The figures discussed in this section regard the radiance due to atmospheric effects. Figure 12.5 regards the resulting radiance at the ocean surface [ $W\ m^{-2}\ \mu m^{-1}\ sr^{-1}$ ], figure 12.6 presents the resulting radiance at TOA [ $W\ m^{-2}\ \mu m^{-1}\ sr^{-1}$ ], and figure 12.7 illustrates the difference between the two at the selected solar zenith angle of  $60^\circ$ .

Figure 12.5 illustrates the resulting radiance at the ocean surface with regard to four solar zenith angles, i.e.  $20^\circ$ ,  $40^\circ$ ,  $60^\circ$  and  $80^\circ$ . There is a small difference of approximately  $1 - 1.5 * 10^{-3}\ W\ m^{-2}\ \mu m^{-1}\ sr^{-1}$  between the radiance resulting from the solar zenith angles  $20^\circ$ ,  $40^\circ$  and  $60^\circ$  in consecutive order. The radiance at the ocean surface due to atmospheric effects resulting from the solar zenith angle  $80^\circ$  differs from the three presented radiances. The radiance resulting from the solar zenith angle  $80^\circ$  varies less with regard to wavelength and has a lower value between the wavelengths of 400 and 750 nm. However, with regard to the wavelengths between 750 and 800 nm, the radiance at the ocean surface due to atmospheric effects resulting from the solar zenith angle of  $80^\circ$ , is roughly the same value as the radiance resulting from the other three solar zenith angles. The biggest difference between the radiance at the ocean surface due to atmospheric effects resulting from the solar zenith angle  $80^\circ$  and the radiance resulting from the other three angles occurs at 400 nm, and has a value between  $3.5 * 10^{-3}$  and  $7 * 10^{-3}\ W\ m^{-2}\ \mu m^{-1}\ sr^{-1}$ . The solar zenith angle of  $20^\circ$  results in the greatest radiance. The second highest radiance results from the solar zenith angle  $40^\circ$ . The reason for these differences occurring are discussed in section 16.3.1. Dips in the resulting radiance occur at 439 nm, for all solar zenith angles, due to absorption by various elements in the Sun's photosphere. Dips in the resulting radiance also occur at 589 nm and 761 nm for all solar zenith angles. The dip at 589 nm occurs due to absorption by sodium in the sun's photosphere (Starr [2005]). The dip at 761 nm is explained in section 16.3.1.

Figure 12.6 presents the resulting radiance due to atmospheric effects, with regard to the four solar zenith angles, at TOA. The radiance at TOA resulting from the solar zenith angle of  $80^\circ$  differs from the radiance values at TOA resulting from the other three solar zenith angles, by resulting in a lower value for wavelengths 400 - 700 nm and varying less with regard to wavelength. The biggest radiance value difference is approximately  $20 - 40\ W\ m^{-2}\ \mu m^{-1}\ sr^{-1}$ . The solar zenith angle of  $20^\circ$  results in the greatest radiance at TOA due to atmospheric effects out of the presented solar zenith angles. The second highest radiance results from the solar zenith angle of  $40^\circ$ . The reason for these differences occurring are discussed in section 16.3.1. Dips in the resulting radiance at TOA due to atmospheric effects occur at 430 - 435 nm and at 761 nm regardless of solar zenith angle. The dip between 430 nm and 435 nm is due to absorption by calcium, iron and hydrogen in the sun's photosphere (Starr [2005]). The dip at 761 nm is explained in section 16.3.1.

Figure 12.7 compares the resulting radiance due to atmospheric effects at the ocean surface and at TOA, with regard to the solar zenith angle of  $60^\circ$ . Figure 12.7 illustrates how

small the radiance due to atmospheric effects is at the ocean surface compared to at TOA. This result is expected, and is discussed in section 16.3.1.

### Water Leaving Radiance

Figure 12.9 presents the resulting water leaving radiance at the ocean surface with regard to the solar zenith angles of  $20^\circ$ ,  $40^\circ$ ,  $60^\circ$  and  $80^\circ$ . The figure reveals that the solar zenith angle of  $60^\circ$  results in the highest water leaving radiance values, with a maximum of  $5.451 * 10^{-3} \text{ sr}^{-1}$ . This is due to multiple scattering, absorption and reflectance processes in both the ocean and in the atmosphere. The solar zenith angle of  $20^\circ$  results in the lowest water leaving radiance values, with a maximum of  $5.447 * 10^{-3} \text{ sr}^{-1}$ . These peaks occur at 476 nm.

Figure 12.9 also demonstrates that the solar zenith angle does not affect the wavelength dependent variations of the resulting water leaving radiance. The solar zenith angles affect the resulting water leaving radiance values between the wavelengths of approximately 470 to 570 nm. These wavelengths correspond to the colors light blue, green and yellow. This is due to the chl<sub>a</sub> absorption being low for these wavelengths, making the radiance more susceptible. The biggest water leaving radiance value difference due to variation in solar zenith angle has a value of approximately  $4 * 10^{-6} \text{ sr}^{-1}$ . This is a small difference, as it is  $7.34 * 10^{-2} \%$  of the lowest water leaving radiance value at the wavelength the difference occurs.

### 16.3.4 Viewing Angles

#### Radiance Due To Atmospheric Effects

The following sections regard the effects of the viewing angles on the radiance due to atmospheric effects.

#### Viewing Zenith Angles

Figure 12.14 presents the radiance at the ocean surface, resulting from atmospheric effects, for the three viewing zenith angles of  $0^\circ$ ,  $30^\circ$  and  $60^\circ$ . Figure 12.12 presents the same scenario, except for the illustrated radiance being at TOA, and the viewing zenith angle  $90^\circ$  being included. Figure 12.13 compares the described radiance at the ocean surface to the radiance at TOA by utilizing the viewing zenith angle of  $30^\circ$ .

Figure 12.14 reveals that the radiance at the ocean surface due to atmospheric effects resulting from the viewing zenith angle of  $60^\circ$  is higher in value than the resulting radiances from the viewing zenith angles of  $30^\circ$  and  $0^\circ$ , with approximately  $1.1 * 10^{-2} \text{ W m}^{-2} \mu\text{m}^{-1} \text{ sr}^{-1}$ . In general, the resulting radiance at the ocean surface decreases slightly with increasing wavelength. Two dips in the resulting radiance occur at 430 - 435 nm and 761 nm. These observations are explained in section 16.3.1.

The resulting radiance at TOA due to atmospheric effects with regard to the viewing zenith angle of  $90^\circ$  is not visible in figure 12.12, due to its values being zero at all wavelengths. The radiance resulting from the viewing zenith angle of  $60^\circ$  is higher than the radiances resulting from the viewing zenith angles of  $0^\circ$  and  $30^\circ$ , with approximately  $50 \text{ W m}^{-2} \mu\text{m}^{-1} \text{ sr}^{-1}$ . In general, the resulting radiance at TOA decreases with increasing wavelength. Two significant dips in the resulting radiance at TOA due to atmospheric effects occur at 430 - 435 nm and 761 nm. These observations are explained in section 16.3.1.

Figure 12.13 compares the resulting radiance at the ocean surface and at TOA, due to atmospheric effects, with regard to a viewing zenith angle of  $30^\circ$ . The viewing zenith angle of  $30^\circ$  was selected as it results in generic radiance values, and thus functions well for demonstration purposes. Figure 12.13 demonstrates how small-scale the radiance due to atmospheric effects is at the ocean surface compared to at TOA. This is discussed in section 16.3.1.

### **Viewing Azimuth Angles**

Figure 12.15 illustrates the resulting radiance due to atmospheric effects at the ocean surface with regard to four viewing azimuth angles, namely  $0^\circ$ ,  $60^\circ$ ,  $120^\circ$  and  $180^\circ$ . Figure 12.16 presents the same scenario, except for the resulting radiance being presented at TOA. Figure 12.17 compares the radiances at the ocean surface and the radiances at TOA. The viewing azimuth angle utilized in figure 12.17 is  $60^\circ$ .

Figure 12.15 demonstrates that the variation in resulting radiance at the ocean surface, with regard to the four viewing azimuth angles, is small. The resulting radiances vary in the same manner with regard to wavelength. Furthermore, the resulting radiance values are roughly the same, regardless of viewing azimuth angle. The biggest radiance value difference occurs between the viewing azimuth angles  $180^\circ$  and  $0^\circ$ , with a value of approximately  $1 * 10^{-3} \text{ W m}^{-2} \mu\text{m}^{-1} \text{ sr}^{-1}$ . Figure 12.16 presents the same observation. However, the difference in radiance value is approximately  $10 \text{ W m}^{-2} \mu\text{m}^{-1} \text{ sr}^{-1}$ . The viewing azimuth angle of  $180^\circ$  results in the biggest radiance at the surface due to atmospheric effects, out of the presented viewing azimuth angles, while the viewing azimuth angle of  $60^\circ$  generally results in the lowest radiance. In general, the resulting radiance at the ocean surface due to atmospheric effects decreases with increasing wavelength. Two significant dips in the resulting radiance occurs at 430 - 435 nm and at 761 nm, regardless of viewing azimuth angle. The dips are explained in section 16.3.1.

Figure 12.16 reveals that the greatest radiance due to atmospheric effects at TOA, results from the viewing azimuth angle of  $180^\circ$ . The second greatest radiance results from the viewing azimuth angle of  $120^\circ$ . The resulting radiance from the viewing azimuth angles of  $0^\circ$  and  $60^\circ$  are approximately the same. In general, the resulting radiance at TOA due to atmospheric effects decreases with increasing wavelength. Two significant dips in the resulting radiance at TOA occur at 430 - 435 nm and 761 nm, regardless of viewing azimuth angle. The explanations for these observations are presented in section 16.3.1.

Figure 12.17 compares the radiance at the ocean surface and at TOA, due to atmospheric effects, resulting from the viewing azimuth angle  $60^\circ$ . The resulting radiance at TOA is greater than the resulting radiance at the ocean surface. This is expected. The difference between the two resulting radiances decreases with increasing wavelengths. This is expected as the resulting radiance at TOA decreases with increasing wavelength.

## Water Leaving Radiance

The following sections regard the effect of the viewing angles on the water leaving radiance at the ocean surface.

### Viewing Zenith Angles

Figure 12.18 illustrates the water leaving radiance at the ocean surface resulting from various viewing zenith angles. The presented viewing zenith angles are  $120^\circ$ ,  $150^\circ$  and  $170^\circ$ , as defined by PlanarRad. Section 6.1 presents the viewing zenith angle definitions. The resulting water leaving radiance values vary with respect to the viewing zenith angle. Specifically, there is a difference of roughly  $3 * 10^{-2} \text{ sr}^{-1}$  between the water leaving radiance values resulting from the viewing zenith angles of  $170^\circ$  and  $120^\circ$ . In the same manner, there is a difference of approximately  $5.5 * 10^{-2} \text{ sr}^{-1}$  between the water leaving radiance values resulting from the viewing zenith angles of  $120^\circ$  and  $150^\circ$ . Furthermore, there is a difference of approximately  $9 * 10^{-2} \text{ sr}^{-1}$  between the water leaving radiance values resulting from the viewing zenith angles of  $170^\circ$  and  $150^\circ$ . The described water leaving radiance value differences are big enough for the resulting water leaving radiance values to appear as constant, i.e. the wavelength dependent variations are not noticeable in figure 12.18. These differences are due to the ocean surface not being Lambertian.

Figure 12.19, 12.20 and 12.21 present the water leaving radiance values resulting from the three viewing zenith angles independently. The objective is to present the wavelength dependent variations of the resulting water leaving radiance.

Figure 12.19 presents the water leaving radiance at the ocean surface resulting from the viewing zenith angle of  $120^\circ$ . The water leaving radiance peaks at 476 nm. The graphical top is present between approximately 450 and 580 nm. The wavelength dependent variations in the resulting water leaving radiance are mostly due to the chl\_a absorption discussed in section 16.3.1. The peak has a water leaving radiance value of approximately  $1.7 * 10^{-5} \text{ sr}^{-1}$  more than the generic water leaving radiance value for the viewing zenith angle of  $120^\circ$ .

Figure 12.20 illustrates the water leaving radiance resulting from the viewing zenith angle of  $150^\circ$ . The water leaving radiance value increases from approximately 450 nm until it peaks at 476 nm. The resulting water leaving radiance value then decreases until the wavelength of approximately 580 nm. The water leaving radiance peak resulting from the viewing zenith angle of  $150^\circ$  has a value of approximately  $1.4 * 10^{-5} \text{ sr}^{-1}$  more than the

generic water leaving radiance for the specified viewing zenith angle.

Figure 12.21 illustrates the water leaving radiance at the ocean surface resulting from the viewing zenith angle of  $170^\circ$ . The wavelength dependent variations in the resulting water leaving radiance can be observed in the same manner as for the water leaving radiance resulting from the viewing zenith angles of  $120^\circ$  and  $150^\circ$ . The water leaving radiance peak resulting from the viewing zenith angle of  $170^\circ$  has a value of approximately  $1.2 * 10^{-5} \text{ sr}^{-1}$  more than the generic water leaving radiance for the specified viewing zenith angle.

### **Viewing Azimuth Angles**

Figure 12.22 presents the water leaving radiance at the ocean surface resulting from various viewing azimuth angles. The presented viewing azimuth angles are  $0^\circ$ ,  $60^\circ$ ,  $120^\circ$  and  $180^\circ$ .

The viewing azimuth angle of  $0^\circ$  differs from the other three, which result in roughly the same water leaving radiance, by resulting in a water leaving radiance that is higher in value with approximately  $5.5 * 10^{-2} \text{ sr}^{-1}$ . The water leaving radiances resulting from the four viewing azimuth angles appear to be constant. However, figure 12.23, which presents the described scenario without the water leaving radiance resulting from the viewing azimuth angle of  $0^\circ$ , reveals that it is due to the difference between the water leaving radiance resulting from the viewing azimuth angle of  $0^\circ$  and the water leaving radiance resulting from the other three viewing azimuth angles.

Figure 12.23 further demonstrates that the water leaving radiance resulting from various viewing azimuth angles, varies similarly with regard to wavelength as the water leaving radiance resulting from various viewing zenith angles, as described in section 16.3.4. The water leaving radiance peak, resulting from the viewing azimuth angle of  $180^\circ$ , in figure 12.23 has a value of approximately  $1.6 * 10^{-5} \text{ sr}^{-1}$  more than the generic water leaving radiance value. Considering the three presented viewing azimuth angles, the highest water leaving radiance at the ocean surface results from the the viewing azimuth angle of  $180^\circ$ . The lowest water leaving radiance results from the viewing azimuth angle of  $120^\circ$ . The difference between the two is approximately  $2 * 10^{-6} \text{ sr}^{-1}$ . Section 16.3.1 presents the explanation for these results.

Figure 12.24 illustrates the water leaving radiance at the ocean surface resulting from the viewing azimuth angle of  $0^\circ$ . The resulting water leaving radiance varies, with respect to wavelength, in the same manner as the water leaving radiance resulting from the other three viewing azimuth angles. The water leaving radiance peak has a value of approximately  $1.7 * 10^{-5} \text{ sr}^{-1}$  more than the generic water leaving radiance value with regard to the viewing azimuth angle of  $0^\circ$ .

### 16.3.5 Clouds

Figure 12.28 presents the radiance at the ocean surface due to atmospheric effects, for a scenario with water clouds present above the ocean. Figure 12.29 presents the same scenario, but illustrates the radiance at TOA, rather than at the ocean surface. Figure 12.30 compares the resulting radiance at the ocean surface with the resulting radiance at TOA. Figure 12.31 illustrates the difference in resulting radiance at TOA due to atmospheric effects with respect to there being water clouds and there not being any clouds present.

Figure 12.28 reveals that the resulting radiance at the ocean surface generally decreases with increasing wavelength. Two dips in the resulting radiance of significant amplitudes occur at 439 and 761 nm. The dips are discussed in section 16.3.1.

The radiance illustrated in figure 12.29 is similar to the radiance presented in figure 12.28. The previously mentioned dips are observable in figure 12.29 as well.

Figure 12.30 demonstrates the difference between the resulting radiance at TOA and the resulting radiance at the ocean surface due to atmospheric effects when water clouds are present. The difference is generally approximately  $225 \text{ W m}^{-2} \mu\text{m}^{-1} \text{ sr}^{-1}$ . The resulting radiance is greater at TOA than at the ocean surface. The difference, i.e.  $225 \text{ W m}^{-2} \mu\text{m}^{-1} \text{ sr}^{-1}$ , is approximately  $9 * 10^5$  times bigger than the greatest radiance value at the surface.

Figure 12.31 illustrates the impact water clouds have on the radiance at TOA due to atmospheric effects. The resulting radiance is higher, for all wavelengths, when water clouds are present than when no clouds are present. The difference in resulting radiance value is generally of approximately  $200 \text{ W m}^{-2} \mu\text{m}^{-1} \text{ sr}^{-1}$ . This is a big difference, considering the highest resulting radiance when no clouds are present is of approximately  $140 \text{ W m}^{-2} \mu\text{m}^{-1} \text{ sr}^{-1}$ . The observed dips at 439 and 761 nm are of greater impact when water clouds are present, than when there are no clouds. This is due to clouds consisting of dry air, liquid water drops and sometimes ice particles (NASA [b]). The dip at 439 nm is due to absorption by water, while the dip at 761 nm is due to absorption by oxygen (Starr [2005]).

### 16.3.6 Comparison Between Several Presented Scenarios

#### Solar Azimuth Angle VS Solar Zenith Angle

A comparison between the effects of the solar azimuth and zenith angles on the water leaving radiance at the ocean surface will be presented. This comparison is based on figures 12.2 and 12.4 with regard to solar azimuth angles, and 12.9 with regard to solar zenith angles.

A comparison will not be presented regarding the effects of the solar azimuth and zenith

angles on the radiance at the ocean surface due to atmospheric effects. This is due to results regarding the radiance due to atmospheric effects for various solar azimuth angles not existing, as it is not an option in COART. In the same manner, a comparison will not be presented regarding the effect of solar azimuth and zenith angles on the radiance at TOA.

Figure 12.2 reveals that, regarding the presented solar azimuth angles, the greatest water leaving radiance at the ocean surface is of approximately  $6.7 * 10^{-3} \text{ sr}^{-1}$ , resulting from the solar azimuth angles of  $180^\circ$  and  $120^\circ$ , while the lowest is approximately  $5.4 * 10^{-3} \text{ sr}^{-1}$  and results from the solar azimuth angle of  $0^\circ$ . That is a variation in water leaving radiance resulting from different solar azimuth angles of approximately  $1.3 * 10^{-3} \text{ sr}^{-1}$ . The reasons for these differences are discussed in section 16.3.1.

Furthermore, figure 12.2 reveals that the solar azimuth angles of  $180^\circ$  and  $120^\circ$  result in approximately the same water leaving radiance, and that the solar azimuth angles of  $0^\circ$  and  $60^\circ$  result in similar water leaving radiance values. Figure 12.4 presents a closer view of the water leaving radiance resulting from the solar azimuth angles of  $0^\circ$  and  $60^\circ$ . The figure illustrates that the resulting water leaving radiance values are wavelength dependent, and have a water leaving radiance difference between them of approximately  $1.7 * 10^{-5} \text{ sr}^{-1}$ .

Figure 12.9 reveals that the water leaving radiance resulting from various solar zenith angles only differ from each other between the wavelengths of 460 and 600 nm. These are the wavelengths this section will regard. The highest water leaving radiance results from the solar zenith angle of  $60^\circ$ , and has a maximum value of  $5.451 * 10^{-3} \text{ sr}^{-1}$ . The lowest water leaving radiance, with regard to the presented solar zenith angles, results from the solar zenith angle of  $20^\circ$ , and has a maximum value of  $5.447 * 10^{-3} \text{ sr}^{-1}$ . Thus, the difference in maximum water leaving radiance resulting from different solar zenith angles is approximately  $4.3 * 10^{-6} \text{ sr}^{-1}$ . Section 16.3.1 discusses why these results occur.

## **Viewing Azimuth Angle VS Viewing Zenith Angle**

### **Radiance Due To Atmospheric Effects**

A comparison will be presented regarding the effects of viewing azimuth and zenith angles on the resulting radiance due to atmospheric effects, at the ocean surface and at TOA.

Regarding the resulting radiance due to atmospheric effects at the ocean surface, figure 12.14 is used with regard to viewing zenith angles, and figure 12.15 with regard to viewing azimuth angles. Regarding the resulting radiance due to atmospheric effects at TOA, figure 12.12 is used to present the results regarding viewing zenith angles and figure 12.16 regarding viewing azimuth angles.

Figure 12.14 reveals that the radiance due to atmospheric effects at the ocean surface resulting from various viewing zenith angles has values between 0 and  $1.9 * 10^{-2} \text{ W m}^{-2} \mu\text{m}^{-1} \text{ sr}^{-1}$ . Furthermore, it reveals that the difference between the highest radiance, re-

sulting from the viewing zenith angle of  $60^\circ$ , and the lowest radiance, resulting from the viewing zenith angle of  $0^\circ$ , is generally approximately  $11 * 10^{-3} W m^{-2} \mu m^{-1} sr^{-1}$ . This difference is due to the scattering in the atmosphere as well as the ocean surface not being a Lambertian surface, and thus does not reflect radiance equally into all directions.

Figure 12.15 reveals that the highest radiance, resulting from various viewing azimuth angles, at the ocean surface due to atmospheric effects, results from the viewing azimuth angle  $180^\circ$ . The lowest radiance results from the viewing azimuth angle of  $60^\circ$ . The difference between the two is generally approximately  $1 * 10^{-3} W m^{-2} \mu m^{-1} sr^{-1}$ . This is considerably lower than the difference in resulting radiance at the ocean surface due to atmospheric effects resulting from various viewing zenith angles. Furthermore, in general, the radiance values decrease with increasing wavelengths, as the radiance resulting from various viewing zenith angles also does. The reason for this is discussed in section 16.3.1.

Figure 12.12 reveals that the highest resulting radiance at TOA due to atmospheric effects, with regard to various viewing zenith angles, results from the viewing zenith angle of  $60^\circ$ , and has a maximum value of  $110 W m^{-2} \mu m^{-1} sr^{-1}$ . The lowest resulting radiance at TOA due to atmospheric effects, results from the viewing zenith angle of  $0^\circ$ , and has a maximum value of  $52 W m^{-2} \mu m^{-1} sr^{-1}$ . Thus, there is a difference of  $58 W m^{-2} \mu m^{-1} sr^{-1}$ . The resulting radiance decreases with increasing wavelengths, as explained in section 16.3.1.

Figure 12.16 reveals that the highest radiance at TOA due to atmospheric effects, with regard to various viewing azimuth angles, results from the viewing azimuth angle of  $180^\circ$ , and has a maximum value of  $64 W m^{-2} \mu m^{-1} sr^{-1}$ . The lowest radiance at TOA results from the viewing azimuth angles of  $0^\circ$  and  $60^\circ$ , and has a maximum value of  $51 W m^{-2} \mu m^{-1} sr^{-1}$ . Thus, there is a difference of  $13 W m^{-2} \mu m^{-1} sr^{-1}$  between the two. The radiance decreases with increasing wavelengths. The reason for this is discussed in section 16.3.1.

### **Water Leaving Radiance**

The following sections regard the resulting water leaving radiance at the ocean surface with respect to various viewing azimuth and zenith angles. Figure 12.18 regards the viewing zenith angles. Figure 12.22 regards the viewing azimuth angles.

Figure 12.18 reveals that various viewing zenith angles result in various water leaving radiance values at the ocean surface. The highest water leaving radiance has a value of approximately  $9 * 10^{-2} sr^{-1}$ , and results from the viewing zenith angle of  $150^\circ$ . The lowest water leaving radiance has a value of approximately  $2 * 10^{-3} sr^{-1}$ , and results from the viewing zenith angle of  $170^\circ$ .

Figure 12.22 reveals that various viewing azimuth angles result in various water leaving radiance values at the ocean surface. This is discussed in section 16.3.4. The highest water leaving radiance has a value of approximately  $6.3 * 10^{-2} sr^{-1}$ , and results from the view-

ing azimuth angle of  $0^\circ$ . The lowest water leaving radiance has a value of approximately  $5 * 10^{-3} \text{ sr}^{-1}$ , and results from the viewing azimuth angle of  $180^\circ$ .

## **Viewing Angles VS Solar Angles**

### **Radiance Due To Atmospheric Effects**

This section regards the resulting radiance at TOA due to atmospheric effects with various viewing zenith angles. Figure 12.12 reveals that the difference between the maximum value of the highest resulting radiance, and the maximum value of the lowest resulting radiance is of  $58 \text{ W m}^{-2} \mu\text{m}^{-1} \text{ sr}^{-1}$ . A dip in the resulting radiance occurs at 439 nm. In general, as presented in section 16.3.1, the resulting radiance decreases with increasing wavelength.

This section regards the resulting radiance at TOA due to atmospheric effects with various solar zenith angles. Figure 12.6 reveals that the difference between the maximum value of the highest resulting radiance, and the maximum value of the lowest resulting radiance is of approximately  $41 \text{ W m}^{-2} \mu\text{m}^{-1} \text{ sr}^{-1}$ . A dip in the resulting radiance occurs at 439 nm. In general, the resulting radiance decreases with increasing wavelength.

A comparison regarding the viewing azimuth angles and solar azimuth angles will not be presented, as it is not possible to vary the solar azimuth angle in COART.

## **Water Leaving Radiance**

This section regards the resulting water leaving radiance with various viewing zenith angles. Figure 12.18 reveals that the resulting water leaving radiance has values between  $3 * 10^{-3}$  and  $9 * 10^{-2} \text{ sr}^{-1}$ . That is a variation of  $8.7 * 10^{-2} \text{ sr}^{-1}$ .

This section regards the resulting water leaving radiance with various solar zenith angles. Figure 12.9 reveals that the water leaving radiance has maximum values between  $5.447 * 10^{-3}$  and  $5.451 * 10^{-3} \text{ sr}^{-1}$ . That is a variation of  $4 * 10^{-6} \text{ sr}^{-1}$ .

This section regards the resulting water leaving radiance with various viewing azimuth angles. Figure 12.22 reveals that the resulting water leaving radiance has values between  $5 * 10^{-3}$  and  $6.2 * 10^{-2} \text{ sr}^{-1}$ . That is a variation of  $5.7 * 10^{-2} \text{ sr}^{-1}$ .

This section regards the resulting water leaving radiance with various solar azimuth angles. Figure 12.2 reveals that the resulting water leaving radiance has values between  $5.45 * 10^{-3}$  and  $6.7 * 10^{-3} \text{ sr}^{-1}$ . That is a variation of  $1.25 * 10^{-3} \text{ sr}^{-1}$ .

## **Radiance At The Ocean Surface Due To Atmospheric Effects VS Water Leaving Radiance At The Ocean Surface**

The following sections will present a comparison of the resulting water leaving radiance

and the resulting radiance due to atmospheric effects, at the ocean surface.

The following comparison regards the effects of the solar zenith angle. It was performed with the viewing zenith angle  $110^\circ$  and the viewing azimuth angle  $0^\circ$ , as defined in PlanarRad and presented in section 6.1. Figure 12.10 and 12.11 present the difference between the resulting water leaving radiance and the radiance at the ocean surface due to atmospheric effects, with the solar zenith angles  $20^\circ$ ,  $40^\circ$ ,  $60^\circ$  and  $80^\circ$ . More precisely, the figures presents the result by taking the radiance due to atmospheric effects and subtracting the water leaving radiance from it. Therefore, the result illustrates how much bigger, or smaller, the radiance at the ocean surface due to atmospheric effects is than the water leaving radiance.

The following comparison regards the effects of the viewing zenith angle of  $30^\circ$ . It was performed with the solar zenith angle  $60^\circ$ , the viewing azimuth angle  $0^\circ$  and the viewing zenith angle  $30^\circ$ , as defined in COART. The viewing zenith angle  $30^\circ$  in COART corresponds to a viewing zenith angle  $120^\circ$  in PlanarRad. Figure 12.25 presents the radiance difference between the radiance due to atmospheric effects and the water leaving radiance, with the viewing zenith angle of  $30^\circ$ .

The following comparison regards the effects of the viewing azimuth angle. It was performed with the solar zenith angle  $60^\circ$  and the COART viewing zenith angle  $20^\circ$ , which corresponds to the viewing zenith angle of  $110^\circ$  in PlanarRad. Figure 12.26 and 12.27 illustrate the difference between the radiance at the ocean surface due to atmospheric effects and the water leaving radiance, with regard to the viewing azimuth angles  $0^\circ$ ,  $60^\circ$ ,  $120^\circ$  and  $180^\circ$ .

## 16.4 Creating A Lookup Table For Simulation Of A Whole Scene

### 16.4.1 The Creation Of A Lookup Table

This section will discuss the results regarding the creation of a lookup table. Several lookup tables were created, with regard to different solar and viewing angles. However, this section, i.e. section 16.4.1 presents the creation of only one, as the procedure was the same for all. Figure 13.2 regards the water leaving radiance at the ocean surface for different SINMOD data points, i.e. for different values of the chl<sub>a</sub> concentration. The presented water leaving radiance is calculated by PlanarRad. Figure 13.3 presents the absorption due to chl<sub>a</sub> concentration and due to water for the same SINMOD data points. Figure 13.4 illustrates the same scenario, but only for the wavelengths 400 - 700 nm. Figure 13.5 illustrates the chl<sub>a</sub> scattering for the same SINMOD data points. Figure 13.7 presents the water scattering for the SINMOD data points. Figure 13.6 compares the water leaving radiance at the ocean surface calculated by PlanarRad for a chosen SINMOD data point, and the water leaving radiance at the ocean surface for the same chl<sub>a</sub> concentration

value calculated by utilizing the lookup table. Figure 13.8 presents several resulting water leaving radiance values calculated by the lookup table together with several water leaving radiance calculations for other data points by PlanarRad.

Figure 13.2 presents the water leaving radiance at the ocean surface for seven SINMOD data points. The resulting water leaving radiance from a chl<sub>a</sub> concentration value of  $0.0 \text{ mg chl}_a \text{ m}^{-3}$  differs from the resulting water leaving radiance from the other six chl<sub>a</sub> concentration values, as it does not vary in the same manner with regard to wavelengths. The water leaving radiance values resulting from the remaining six chl<sub>a</sub> concentration values are wavelength dependent as discussed in section 16.3. Furthermore, the resulting water leaving radiance values peak at the wavelength of 476 nm. This is, as explained in section 16.3.1, due to the chl<sub>a</sub> absorption, which is high for wavelengths 400 - 450 nm and 650 - 700 nm. The absorption is lowest at approximately 475 nm, thus a peak in the water leaving radiance occurs at this wavelength.

Figure 13.2 further reveals that the difference between the largest water leaving radiance peak, which results from the chl<sub>a</sub> concentration value of  $0.3 \text{ mg chl}_a \text{ m}^{-3}$ , and the smallest peak, which results from the chl<sub>a</sub> concentration value of  $1.8 \text{ mg chl}_a \text{ m}^{-3}$ , is small. The difference is approximately  $1.5 * 10^{-5} \text{ sr}^{-1}$ . The resulting water leaving radiance from the chl<sub>a</sub> concentration value of  $0.0 \text{ mg chl}_a \text{ m}^{-3}$  is not included in the previous statement, as it does not have a peak.

Figure 13.2 demonstrates that the higher chl<sub>a</sub> concentration, the less the water leaving radiance between 450 and 600 nm. This is due to the chl<sub>a</sub> absorption at these wavelengths, as can be seen in figure 13.4. The figure reveals that the higher the chl<sub>a</sub> concentration, the more absorption, i.e. the less water leaving radiance.

Figure 13.3, which presents the absorption due to chl<sub>a</sub> concentration and pure water, reveals two perceptible peaks at 450 and 670 nm. The higher the chl<sub>a</sub> concentration, the higher the absorption. This is expected as chlorophyll concentrations result in increased absorption near 450 nm in satellite optical data (Gower and King [2014]).

Figure 13.5 presents the scattering due to chl<sub>a</sub> concentration for the varying SINMOD data points. The scattering values are evenly spaced for the different data points, with approximately  $1 * 10^{-8} \text{ m}^{-1}$  in between each consecutive chl<sub>a</sub> concentration value. The greater the chl<sub>a</sub> concentration, the more scattering. This is expected, due to chlorophyll concentrations resulting in increased scattering from the ocean, especially near 550 nm, i.e. green light (Gower and King [2014]). This can be seen in figure 13.5.

Figure 13.7 presents the water scattering for the SINMOD data points. The scattering values are the same for all the presented data points. This is to say, the chl<sub>a</sub> concentration does not affect the scattering. This is expected, as the figure illustrates the pure water scattering. The variables affecting the water scattering is the water temperature, salinity and viewing angle at the different data points. The salinity is generally the same for all data points, while the viewing angle's effect is negligible. The temperature does not vary ade-

quately to result in a difference in resulting scattering. The greatest temperature difference is of  $8.42 * 10^{-1} C$ .

Figure 13.6 compares the resulting water leaving radiance calculated by PlanarRad to the resulting water leaving radiance calculated by the lookup table for the chl\_a concentration value of  $3.409 * 10^{-1} mg chl\_a m^{-3}$ . The results are identical.

Figure 13.8 presents several water leaving radiance values calculated by the lookup table together with several water leaving radiance values calculated by PlanarRad. The lookup table resulting water leaving radiance values fit perfectly and follow the same wavelength dependent variations as the resulting water leaving radiance values calculated by PlanarRad.

### 16.4.2 Simulating A Whole Scene

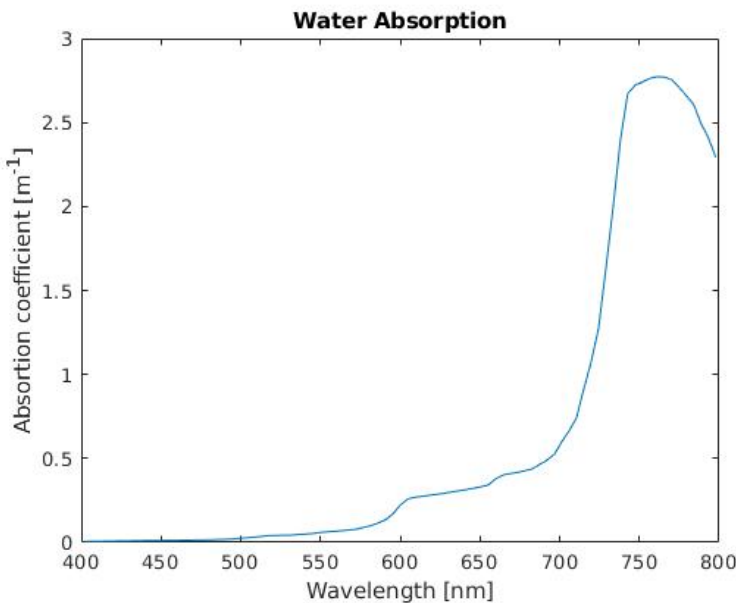
Figures 13.9, 13.10, 13.11, 13.12, 13.13 and 13.14 present the same result from different views. The figures present a 4D chart representing the water leaving radiance for a whole scene. The water leaving radiances were calculated using the lookup table.

Figure 13.9 presents a confusing first impression. However, the figure reveals that the wavelengths from 550 to 800 nm result in small water leaving radiance values compared to the lower wavelengths. The highest water leaving radiance values result from the wavelengths between 400 and 500 nm. This is expected as water leaving radiance generally peaks at 476 nm, as discussed in section 16.3.1. The reason for high water leaving radiance values at only certain locations are due to the fact that a time frame from the SINMOD data is being simulated in the figure. There are only higher values of chl.a concentration at certain points in the data set.

Figure 13.10 presents a more straightforwardly illustration, as the inner values of the illustrated cube are more visible than in figure 13.9. The same phenomena are revealed in figure 13.10 as in figure 13.9, i.e. that certain data points have higher water leaving radiance values, and that the wavelengths greater than approximately 550 - 600 nm result in low water leaving radiance values regardless of the amount of chl.a concentration. Figure 13.11 presents the scene from the latitude perspective instead of from the longitude perspective.

Figure 13.12 presents the resulting water leaving radiance cube with the perspective from above the scene. The data points with high water leaving radiance values are more visible in this figure. The resulting light blue color resulting at around 500 nm is stable over the entire scene, regardless of the water leaving radiance values in the lower wavelengths. This is due to the water absorption spectrum, illustrated in figure 16.1.

Figure 13.13 reveals how the water leaving radiance values decrease as the wavelengths increase. The difference between the high and low resulting water leaving radiance values are of approximately  $4.5 * 10^{-5} sr^{-1}$ . This is a relatively small difference, as it is



**Figure 16.1:** Absorption by water.

$8.28 * 10^{-1}\%$  of the resulting water leaving radiance at most wavelengths, i.e. of the value  $5.435 * 10^{-3} \text{ sr}^{-1}$  which corresponds to the dark blue color in the figure.

The last illustration of the scene, i.e. figure 13.14, demonstrates how the chl\_a concentration values, and their respective water leaving radiance values, are distributed over the data points.

## 16.5 Temporal Sensitivity Of Data Acquisition Analysis

### 16.5.1 Panoply

Figure 14.1 presents the Panoply illustration of the chl\_a concentration at three consecutive time stamps. That is, there is one hour in between each of the frames. Figure 14.2 presents the same scene, but with five hours in between each frame.

Figure 14.1 reveals that difference between the three time frames is small. Figure 14.2 reveals that there is a significant difference between the three time frames.

## 16.5.2 The Lookup Table

Figure 14.3 and 14.4 present the water leaving radiance at the ocean surface for three different time frames each. Figure 14.3 presents time frames with one hour in between each frame. Figure 14.4 presents time frames with five hours in between each frame.

Figure 14.3 reveals that the water leaving radiance values do vary. The colors in the figure are in the same range for all three frames. Thus the images can be directly compared. The differences in water leaving radiance are small-scale. The water leaving radiance values are given in  $10^{-3} \text{ sr}^{-1}$ .

Figure 14.4 reveals a more significant water leaving radiance difference between the three presented frames, than in figure 14.3. The color bars for the frames 162 and 172 are identical. However, the color bar for frame 167 has a larger value range. That is, the color red does not represent the same water leaving radiance value for the three frames. Nonetheless, there is more variation in the water leaving radiance in this figure than in figure 14.4.

Figure 14.5 illustrates the difference in water leaving radiance value between time frames with one hour in between, while figure 14.6 presents the the difference in water leaving radiance for time frames with 10 hours in between.

Figure 14.5 reveals that generally the difference in water leaving radiance values is approximately between  $0 \text{ sr}^{-1}$  and  $2.5 * 10^{-7} \text{ sr}^{-1}$ . Furthermore, the figure reveals that several water leaving radiance value differences are of  $1 * 10^{-6} \text{ sr}^{-1}$ .

Figure 14.6 demonstrates that generally the is a difference in water leaving radiance values of around  $0 - 5 * 10^{-7} \text{ sr}^{-1}$ , and that there are several data points with water leaving radiance value difference of approximately  $1.5 * 10^{-6} \text{ sr}^{-1}$ . Furthermore, figure 14.6 reveals that there are certain data points with a water leaving radiance difference of approximately  $2.5 - 3.5 * 10^{-6} \text{ sr}^{-1}$ .

Figure 14.7 and 14.8 present the same water leaving radiance differences as figures 14.5 and 14.6, i.e. for time frames with one hour difference in between them and for time frames with ten hours in between them. Figure 14.7 and 14.8 differ by presenting the water leaving radiance differences as change in percentage.

Figure 14.7 reveals that for most of the data points the water leaving radiance difference in percentage is around  $0 - 2.5 * 10^{-3} \%$ , and that certain data points result in a water leaving radiance difference of approximately  $1.5 * 10^{-2} \%$ . In the same manner, figure 14.8 reveals that generally the water leaving radiance difference in percentage is around  $0 - 2 * 10^{-2} \%$ , with certain data points resulting in a difference of approximately  $6 * 10^{-2} \%$ . The water leaving radiance variation presented in figure 14.8 varies from four times to eight times more than the water leaving radiance variation presented by figure 14.7.

Figures 14.9, 14.10, 14.11 and 14.12 present the maximum water leaving radiance varia-

tions over one hour, five hours, ten hours and all together, respectively. The results presented by figures 14.9, 14.10 and 14.11 are discussed in the following sections.

Figure 14.9 illustrates the water leaving radiance for time frames 505 and 506. The maximum chl<sub>a</sub> concentration difference between the two time frames is of  $4.146 * 10^{-1} \text{ mg chl}_a \text{ m}^{-3}$ , and occurred at the *x* and *y* values of 1 and 552 respectively. The chl<sub>a</sub> concentration values at the given data point were  $9.479 * 10^{-1} \text{ mg chl}_a \text{ m}^{-3}$  and  $5.333 * 10^{-1} \text{ mg chl}_a \text{ m}^{-3}$  for the time frames 505 and 506 respectively. Figure 14.9 reveals that this corresponds to a water leaving radiance difference of approximately  $5 * 10^{-6} \text{ sr}^{-1}$ .

Figure 14.10 illustrates the water leaving radiance for time frame 661 and 666. The maximum chl<sub>a</sub> concentration difference between the two time frames is of  $5.174 * 10^{-1} \text{ mg chl}_a \text{ m}^{-3}$ , and occurred at the *x* value of 71 and *y* value of 523. The chl<sub>a</sub> concentration values at the given data point were  $2.581 * 10^{-1} \text{ mg chl}_a \text{ m}^{-3}$  and  $7.755 * 10^{-1} \text{ mg chl}_a \text{ m}^{-3}$  for the time frames 661 and 666 respectively. Figure 14.10 reveals that this corresponded to a water leaving radiance difference of approximately  $8 * 10^{-6} \text{ sr}^{-1}$ .

Figure 14.11 presents the water leaving radiance for time frames 656 and 666. The maximum chl<sub>a</sub> concentration difference between the two time frames is of  $5.464 * 10^{-1} \text{ mg chl}_a \text{ m}^{-3}$ , and occurred at the *x* value of 106 and *y* value of 523. The chl<sub>a</sub> concentration values at the given data point were  $2.327 * 10^{-1} \text{ mg chl}_a \text{ m}^{-3}$  and  $7.791 * 10^{-1} \text{ mg chl}_a \text{ m}^{-3}$  for the time frames 656 and 666 respectively. Figure 14.11 revels that this chl<sub>a</sub> concentration difference results in a water leaving radiance difference of approximately  $1 * 10^{-5} \text{ sr}^{-1}$ .

Figure 14.12 presents the discussed water leaving radiances variations in one figure.

## 16.6 User Friendly Interface For The Software

The user friendly program is efficient and straightforwardly regarding adding atmospheric effects, due to all the necessary data acquisition and calculations having been performed beforehand.

Regarding the calculations of the atmospheric effects, an offset will occur if the aerosol model is not perfect. However, this does not mean that spectral information in the water leaving radiance is lost, but rather that there is a small offset (Storvold [2018a]).

For discussion regarding the specific results presented by the RadPhyll Simulator, such as results from various solar angles, see appendix A. For discussion regarding the different possibilities of the program, see the user guide in appendix A.

# Conclusion

## 17.1 Combining The MATLAB Files From The Preliminary Work

An effect of the altering of the MATLAB scripts from the preliminary work is that less code lines are required to be modified, as well as less data having to be transferred between scripts for every new run. This saves a lot of computational time as the data transmission had to be performed manually. The combination of the 11 scripts also affected the robustness of the scripts, as human error is less prevalent.

The simulation process of calculating radiance due to geophysical variables was simplified. That is, it is less dependent on several input files and manual inputs. The new system is more user friendly, as it is more straightforwardly, as well as easier to alter the input variables in order to create new results.

## 17.2 Developing Batch Runs For PlanarRad

The development of batch runs for PlanarRad resulted in the computational time being shortened, due to the new input file allowing several values to be specified at once for a specific input variable. This is not possible in the initial PlanarRad version.

Due to the fact that the values of interest can be specified for the batch report, the report is more straightforwardly than the individual reports created from each run by PlanarRad. The individual reports consist of a manifold of possible values of interest, presented over 29072 lines and 311 columns.

## **17.3 Examining Different Scenarios**

### **17.3.1 Solar Azimuth Angle**

The water leaving radiance at the ocean surface resulting from various solar azimuth angles, results in the same wavelength dependent pattern, i.e. regardless of solar azimuth angle. A significant peak occurs at 476 nm. The water leaving radiance resulting from the solar azimuth angles of  $120^\circ$  and  $180^\circ$  are identical, while the water leaving radiance resulting from the solar azimuth angles of  $0^\circ$  and  $60^\circ$  are similar. The solar azimuth angles of  $180^\circ$  and  $120^\circ$  result in the highest water leaving radiance, followed by the solar azimuth angle of  $60^\circ$ . The lowest water leaving radiance results from the solar azimuth angle of  $0^\circ$ . The difference of utilizing solar azimuth angles less than or greater than  $90^\circ$  results in a significant difference, i.e. a difference equal to 22.94% of the water leaving radiance resulting from solar azimuth angles of less than  $90^\circ$ . Thus, the selection of solar azimuth angle is of importance.

### **17.3.2 Solar Zenith Angle**

#### **Radiance Due To Atmospheric Effects**

There is a small difference between the resulting radiance due to atmospheric effects at the ocean surface with regard to the solar zenith angles  $20^\circ$ ,  $40^\circ$  and  $60^\circ$ . The radiance resulting from the solar zenith angle of  $80^\circ$  varies less with regard to wavelength, and is lower with regard to the wavelengths between 400 and 750 nm. Thus, the solar zenith angle of  $80^\circ$  is preferable compared to the remaining angles with regard to water leaving radiance observance. This is due to the radiance due to atmospheric effects not being the radiance of interest, and thus it is of interest to minimize both the value and the wavelength dependent variation of it.

The radiance at TOA due to atmospheric effects resulting from the solar zenith angle of  $80^\circ$  differs from the radiance values resulting from the other three solar zenith angles, by resulting in a lower radiance for wavelengths 400 - 700 nm, as well as varying less with regard to wavelength. The solar zenith angle of  $80^\circ$  is therefore preferred over the remaining presented solar zenith angles.

The resulting radiance at TOA due to atmospheric effects should be considered to a higher degree than the radiance at the ocean surface due to atmospheric effects when considering favorable solar zenith angle. This is due to the radiance resulting from atmospheric effects being small at the ocean surface compared to at TOA.

## **Water Leaving Radiance**

The solar zenith angle of  $60^\circ$  results in the highest water leaving radiance at the ocean surface with regard to the various solar zenith angles, i.e.  $20^\circ$ ,  $40^\circ$ ,  $60^\circ$  and  $80^\circ$ . Thus, the solar zenith angle of  $60^\circ$  is the preferred solar zenith angle for water leaving radiance observation, as it is less complicated to observe and examine a radiance that has higher resulting values.

### **17.3.3 Viewing Angles**

#### **Radiance Due To Atmospheric Effects**

##### **Viewing Zenith Angles**

The radiance at the ocean surface due to atmospheric effects resulting from the viewing zenith angle of  $60^\circ$  is higher in value than the resulting radiances from the viewing zenith angles of  $30^\circ$  and  $0^\circ$ . Thus, the viewing zenith angle should be selected to  $0^\circ$  or  $30^\circ$  rather than  $60^\circ$  if the water leaving radiance is to be observed. The viewing zenith angles' are defined as in COART. Section 6.1 presents this definition.

The resulting radiance at TOA due to atmospheric effects with the viewing zenith angle  $60^\circ$  is higher than the resulting radiances with the viewing zenith angles of  $0^\circ$  and  $30^\circ$ . This suggests that for observance of water leaving radiance at TOA, a viewing zenith angle of  $0^\circ$  or  $30^\circ$  should be utilized. This is due to the fact that the discussed radiance is due to atmospheric effects and does not include the water leaving radiance. It is desirable to keep the resulting radiance as small as possible.

The resulting radiance at the ocean surface due to atmospheric effects was revealed to be small-scale compared to the resulting radiance at TOA due to atmospheric effects, when compared with a viewing zenith angle of  $30^\circ$ . That is, the radiance at TOA is of greater impact than than the radiance at the ocean surface.

The viewing zenith angle does affect the resulting radiance, but not with regard to wavelength dependent variations. More precisely, the viewing zenith angle affects the general radiance values, but not the occurrence of peaks and dips.

##### **Viewing Azimuth Angles**

The resulting radiance values at the ocean surface due to atmospheric effects are roughly the same regardless of viewing azimuth angle. The same holds for the resulting radiance at TOA due to atmospheric effects. However, the largest resulting radiance difference is bigger at TOA then at the ocean surface. This implies that regardless of whether one observes the radiance due to atmospheric effects at the ocean surface or at TOA, the viewing azimuth angle does not significantly affect the result.

The resulting radiance due to atmospheric effects at TOA is greater than the resulting radiance due to atmospheric effects at the ocean surface, when comparing them with regard to viewing azimuth angle.

### Water Leaving Radiance

#### Viewing Zenith Angles

There is a difference in the resulting water leaving radiance at the ocean surface for the three viewing zenith angles  $120^\circ$ ,  $150^\circ$  and  $170^\circ$ , which are defined as in PlanarRad. The viewing zenith angle definition is presented in section 6.1. The viewing zenith angle of  $170^\circ$  results in the lowest water leaving radiance of the three viewing zenith angles. The viewing zenith angle of  $150^\circ$  results in the highest water leaving radiance. The differences in resulting water leaving radiances are huge, regarding that the water leaving radiance resulting from the viewing zenith angle of  $150^\circ$  is approximately 22 times the water leaving radiance resulting from the viewing zenith angle of  $170^\circ$ .

Regardless of viewing zenith angle the water leaving radiance at the ocean surface peaks at 476 nm. The peak has roughly the same value above the general water leaving radiance value regardless of viewing zenith angle. Furthermore, the graphical top occurs between 450 and 580 nm, regardless of viewing zenith angle. Thus, the wavelength dependent variations in the resulting water leaving radiance values are not affected by various viewing zenith angles.

#### Viewing Azimuth Angles

The viewing azimuth angle of  $0^\circ$  differs from the others, by resulting in a water leaving radiance that is higher with approximately  $5.5 * 10^{-2} \text{ sr}^{-1}$ .

The viewing azimuth angle of  $180^\circ$  results in the highest water leaving radiance at the ocean surface, out of the three viewing azimuth angles  $60^\circ$ ,  $120^\circ$  and  $180^\circ$ . The viewing azimuth angle of  $120^\circ$  results in the smallest water leaving radiance. However, the difference between the two is small. Furthermore, the resulting water leaving radiance varies with regard to wavelength in the same manner regardless of viewing azimuth angle. Thus, the peaks occur at the same wavelength and have values with approximately the same value above the general water leaving radiance value, regardless of viewing azimuth angle.

### 17.3.4 Clouds

The difference between the resulting radiance at TOA and the resulting radiance at the ocean surface, due to atmospheric effects, when water clouds are present is huge. The resulting radiance at TOA is greater than the resulting radiance at the ocean surface.

The impact water clouds have on the radiance at TOA due to atmospheric effects is that the resulting radiance is higher for all wavelengths when water clouds are present. The observed dips, at 439 and 761 nm, are bigger when water clouds are present as well.

### 17.3.5 Comparison Between Several Presented Scenarios

This section regards the comparisons of solar azimuth angles and solar zenith angles, viewing azimuth angles and viewing zenith angles, viewing angles and solar angles, and the radiance at the ocean surface due to atmospheric effects and the water leaving radiance at the ocean surface.

#### Solar Azimuth Angles VS Solar Zenith Angles

One of the differences between the effects on the water leaving radiance at the ocean surface with regard to solar azimuth and solar zenith angles, is that the resulting water leaving radiance due to solar zenith angle variation only varies significantly from 460 to 600 nm. The water leaving radiance resulting from various solar azimuth angles varies for all wavelengths. Furthermore, the variation in the resulting water leaving radiance with regard to solar zenith angle, i.e. between 460 and 600 nm, is small compared to the one resulting from the solar azimuth angles.

#### Viewing Azimuth Angle VS Viewing Zenith Angle

#### Radiance Due To Atmospheric Effects

The viewing zenith angles affect the resulting radiance at the ocean surface due to atmospheric effects more than the viewing azimuth angles do. Thus, the viewing zenith angles should be of higher consideration.

The radiance at TOA due to atmospheric effects with regard to viewing zenith angles result in a higher maximum value, as well as a slightly higher maximum value for the lowest resulting radiance, than the radiance at TOA due to atmospheric effects resulting from various viewing azimuth angles. Furthermore, the differences between the radiances resulting from various viewing zenith angles are greater than the differences between the radiances resulting from various viewing azimuth angles. This is expected, partly due to non Lambertian surfaces, such as the ocean surface, usually displaying some degree of reflectance anisotropy (Disney), and thus the definition of a Lambertian surface has an effect. Each point of a Lambertian surface reflects intensity in a cosine pattern (Mobley), as illustrated in figure 17.1. Section 2.1.8 presents theory regarding surfaces. However, the observation is mostly due to the scattering due to atmospheric gasses and aerosols in the atmosphere being more dependent on viewing zenith angle than on viewing azimuth angle. This is a result of the variation of the viewing zenith angle affecting the distance from the observance point to the observed point on the ocean surface, as can be seen in figure

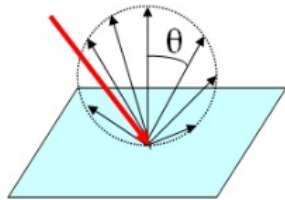


**Figure 17.1:** Illustration of a Lambertian surface. Originally presented in Mobley.

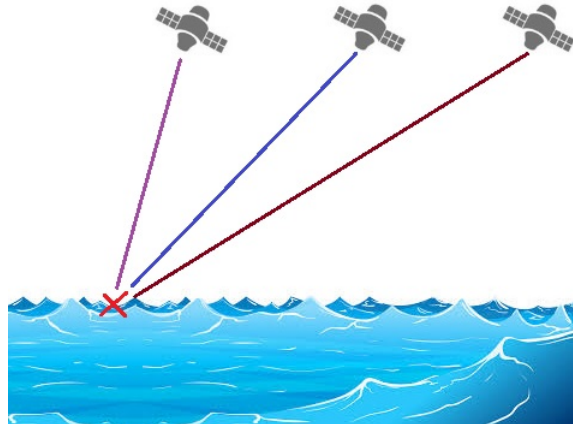


**Figure 17.2:** Illustration of the observation distance being correlated to the viewing zenith angle.

17.2. The variation of the viewing azimuth angle does not have this effect. This distance variation affects the area of possible scattering. Section 2.1.7 presents theory regarding atmospheric correction. Thus, the variation of viewing zenith angle has a greater effect on the observed radiance due to atmospheric effects than the variation of viewing azimuth angle has.

Disregarding the radiance at TOA due to atmospheric effects resulting from the viewing zenith angle of  $60^\circ$ , the radiance values resulting from the remaining two viewing zenith angles, are approximately the same as the radiance values resulting from the viewing azimuth angles. This suggests that the viewing zenith angle of  $60^\circ$  is inferior, as it introduces a lot of radiance at TOA due to atmospheric effects, compared to the other viewing zenith angles.

The radiance at TOA due to atmospheric effects resulting from various viewing azimuth angles varies less than the radiance resulting from various viewing zenith angles. Thus, the selection of viewing azimuth angle is of less importance than the selection of viewing

zenith angle.

### **Water Leaving Radiance**

The highest water leaving radiance value resulting from various viewing zenith angles is approximately  $2.7 * 10^{-2} \text{ sr}^{-1}$  higher than the highest resulting water leaving radiance from various viewing azimuth angles. The lowest water leaving radiance value resulting from various viewing zenith angles is approximately  $3.10^{-3} \text{ sr}^{-1}$  lower than lowest water leaving radiance resulting from various viewing azimuth angles.

Regardless of viewing zenith or azimuth angles, the graphical top in the resulting water leaving radiance occurs between wavelengths 450 and 600 nm. Thus, there is no variation in wavelength dependent variations.

### **Viewing Angles VS Solar Angles**

#### **Radiance Due To Atmospheric Effects**

The dip in resulting radiance due to atmospheric effects at 439 nm occurs for all resulting radiances, regardless of viewing angle or solar angle. Furthermore, the radiance at TOA due to atmospheric effects resulting from various viewing zenith angles varies more than the radiance resulting from various solar zenith angles.

#### **Water Leaving Radiance**

The water leaving radiance at the ocean surface resulting from various viewing zenith angles varies more than the water leaving radiance resulting from various solar zenith angles. Therefore, the selection of viewing zenith angle is of greater impact than the selection of solar zenith angle.

The water leaving radiance resulting from various viewing azimuth angles varies more than the water leaving radiance resulting from various solar azimuth angles. Thus, the selection of viewing azimuth angle is of greater impact than the selection of solar azimuth angles.

#### **Radiance At The Ocean Surface Due To Atmospheric Effects VS Water Leaving Radiance At The Ocean Surface**

Solar zenith angles always result in larger water leaving radiance than radiance at the ocean surface due to atmospheric effects. This is due to the fact that the water leaving radiance has not yet propagated through any media above the ocean surface, while the solar radiance has propagated from TOA to the ocean surface, and has thus been scattered and absorbed along the way. The solar zenith angle resulting in the biggest difference between the water

leaving radiance and radiance due to atmospheric effects is  $80^\circ$ . The solar zenith angle resulting in the smallest difference between the water leaving radiance and the radiance due to atmospheric effects is  $20^\circ$ . Thus, if the radiance just above the ocean surface is to be observed for all wavelengths, i.e. 400 - 800 nm, the solar zenith angle can be any angle, as the resulting water leaving radiance is greater than the radiance due to atmospheric effects regardless. However, as the difference between the water leaving radiance and the radiance at the ocean surface due to atmospheric effects resulting from the solar zenith angle of  $80^\circ$  is approximately 614 times bigger than the difference resulting from the solar zenith angle of  $20^\circ$ , the angle of  $80^\circ$  is preferable with regard to water leaving radiance observation at the ocean surface.

The radiance at the ocean surface due to atmospheric effects resulting from various solar zenith angles varies more than the water leaving radiance resulting from various solar zenith angles. This is due to the fact that the solar radiance has propagated from TOA to the ocean surface, and is thus more susceptible to scattering and absorption variation with regard to solar zenith angle variation, than the water leaving radiance is. Thus, the solar zenith angle has a greater impact on the radiance at the ocean surface due to atmospheric effects than on the water leaving radiance. However, as mentioned in the previous section, the water leaving radiance always results in a greater value than the radiance at the ocean surface due to atmospheric effects.

The water leaving radiance is always greater than the radiance at the ocean surface due to atmospheric effects, for the wavelengths 400 - 800 nm, when utilizing the viewing zenith angle of  $30^\circ$ , as defined by COART. Section 6.1 presents this definition. In general, the difference between the resulting water leaving radiance and the resulting radiance at the ocean surface due to atmospheric effects increases as the wavelengths increase.

For the three viewing azimuth angles  $60^\circ$ ,  $120^\circ$  and  $180^\circ$  the difference between the resulting radiance at the ocean surface due to atmospheric effects and the resulting water leaving radiance is roughly nonexistent. For the viewing azimuth angle of  $0^\circ$  however, the water leaving radiance is larger for all wavelengths, i.e. 400 - 800 nm. The difference between the water leaving radiance and the radiance at the ocean surface due to atmospheric effects resulting from the viewing azimuth angle of  $0^\circ$  is almost 47 times bigger than the difference resulting from any of the other three presented viewing azimuth angles. That is, unless the viewing azimuth angle of  $0^\circ$  is used, the resulting water leaving radiance and the resulting radiance due to atmospheric effects will be approximately the same. However, the resulting water leaving radiance is always slightly bigger. In general, the difference between the resulting water leaving radiance and the resulting radiance due to atmospheric effects increases as the wavelengths increase.

## **17.4 Creating A Lookup Table For Simulation Of A Whole Scene**

### **17.4.1 The Creation Of A Lookup Table**

The water leaving radiance calculated by PlanarRad and the water leaving radiance calculated by the lookup table are identical. The lookup table resulting water leaving radiance values follow the same wavelength dependent variations as the resulting water leaving radiance values from PlanarRad. This is beneficial as it suggests the lookup table works as intended. Thus, the lookup table can be used in order to perform computations for large batches in significantly less time.

### **17.4.2 Simulating A Whole Scene**

The simulation of a whole scene revealed that the locations resulting in high water leaving radiance values are spread out geographically, and more frequent at lower wavelengths.

The wavelengths from approximately 550 to 800 nm result in small water leaving radiance values, compared to the lower wavelengths, regardless of the chl<sub>a</sub> concentration value. The highest water leaving radiance values occur between the wavelengths of 400 and 440 nm. The second highest resulting water leaving radiance values occur at the wavelengths between 440 and 460 nm. The remaining water leaving radiance values of significance occur between the wavelengths of 460 and 520 nm.

## **17.5 Temporal Sensitivity Of Data Acquisition Analysis**

### **17.5.1 Panoply**

The conclusion from the temporal sensitivity of data acquisition analysis performed with Panoply is that the variation of chl<sub>a</sub> concentration over the time period of one hour is small. Furthermore, it revealed that the variation over the time period of five hours might be of importance.

### **17.5.2 The Lookup Table**

The conclusion from the temporal sensitivity of data acquisition analysis performed with the lookup table is that there is greater variation in water leaving radiance values over a time period of ten hours than over a time period of one hour, as is expected. Moreover, the longer time period of observance, the greater the maximum water leaving radiance variation.

## 17.6 User Friendly Interface For The Software

The combination and altering of the files and processes created in this thesis into one user friendly and straightforwardly program was successful. It is possible for any interested party to utilize the work and data created in this thesis.

There are many possible use cases for the simulation tool. It is easy to visualize the results. NetCDF files are great for working with big data sets containing a lot of information.

The development of the RadPhyll Simulator has made the calculation and computation of water leaving radiance just above the ocean surface given chl<sub>a</sub> concentration, as well as of radiance at TOA due to atmospheric effects, less complicated and more temporal efficient.

The five different versions were successful and thus it is possible to calculate water leaving radiance [ $sr^{-1}$ ] for user specified chl<sub>a</sub> concentration values [ $mg\ chl\_a\ m^{-3}$ ], as well as for user specified viewing angle, i.e. from a list of predefined angles, in addition. Furthermore, it is possible to calculate water leaving radiance [ $sr^{-1}$ ] for a whole scene. Moreover, it is possible to calculate radiances at TOA [ $W\ m^{-2}\ \mu m^{-1}\ sr^{-1}$ ] due to atmospheric effects, given type of clouds, viewing azimuth angle, viewing zenith angle and solar zenith angle. Lastly, it is possible to present, and plot, water leaving radiance [ $sr^{-1}$ ] for various solar zenith angles, solar azimuth angles, viewing zenith angles and/or viewing azimuth angles.

## 17.7 Summary

The motivation for this thesis included providing information regarding the effects of various solar and viewing angles, as well as various weather, on the resulting radiance. Providing information regarding the temporal sensitivity of data acquisition, to the overall mission, was also a motivation. This was achieved.

The objective of the overall mission includes simulating what the different sensors on board of the different robot agents record. The work presented in this thesis aids this purpose.

The contributions of this thesis to existing work, as presented in section 1.4, includes the combination of several small and specific processes into one big system. The presented solution performs the process of calculating a hyperspectral cube as seen by a sensor at TOA from specific geophysical and atmospheric variables. Furthermore, being able to specify personal geophysical variable values is not common (Lapadatu [2018]). The following sections summarize these aspects in more detail. Section 1.4 includes a complete presentation.

The simulation is performed by revising, upgrading and utilizing the simulation created in the preliminary work. There are no programs, procedures or models available regarding the process of simulating geophysical variables in the ocean as a hyperspectral cube observed at TOA. Existing procedures involve combining several, more specific, models. The available option is expensive. The provided process in this thesis is a non commercial option where the only required inputs are the geophysical variables one wishes to simulate and the properties of the mediums of interest. Simulated TOA radiance values coincide well with real world data.

The process of converting geophysical variables to absorption, scattering and attenuation is required as there are no general programs for this purpose. Scripts were computed. The results were applied as inputs to the batch runs developed for the software PlanarRad. The batch runs were developed by altering existing software.

Several atmospheric radiative transfer models exist. However, the user can not specify the water leaving radiance. Thus, the user must manually calculate the total effect of the atmosphere. The process presented in this thesis combines all the separate calculations into one process. Thus, as an alternative to existing remote sensing tools, that use real satellite data, the simulation tool uses output data from the coupled physical and ecological ocean model SINMOD to calculate the resulting spectral response in radiance.

There are no publicly available lookup tables for obtaining water leaving radiance given geophysical variables in the ocean. Therefore, lookup tables were created in order to be able to calculate water leaving radiance more temporal efficiently.

It is challenging to compare different viewing and solar angles with regard to water leaving radiance from different existing reports. This holds for the comparison of radiance at TOA as well. Therefore, an examination was performed in this thesis, where different combinations of viewing angles and solar angles are used in order to examine specific scenarios on the same underlying chl\_a concentration values.

The temporal sensitivity analysis of data acquisition performed in this thesis regards the oceans outside of Norway, and is not based on satellite data, as existing temporal sensitivity analyses are, but rather on actual chl\_a concentration data.

The RadPhyll Simulator was developed in order to make the calculation and computation of water leaving radiance just above the ocean surface given chl\_a concentration, as well as of radiance at TOA due to atmospheric effects, less complicated and more rapid. The software differs from existing software, by being developed as one whole system, i.e. the several specific processes needed for the radiance computation are combined. That is, utilizing the developed program the user needs only specify inputs in one input file, and is not required to transfer data between several different software.

The presented results can be utilized by the hyperspectral remote sensing field, as well as by parties interested in ocean color. Furthermore, the results are of specific interest

for satellite missions, as the expected observed radiance can be simulated. That is, the simulation tool can be used for simulating how different geophysical variables translate to spectral radiance, and how the medium around it affects the values (Lapadatu [2018]). Simulation of how the atmosphere affects the radiance values for different wavelengths, different solar angles, different viewing angles and different weather is useful.

The simulation tool is intended to be used for feasibility and analytic studies during the HYPSO space mission design phase, as well as improve the mission operations of a possibly custom-designed hyperspectral imaging satellite that is configured to observe specific targets. This includes design and validation of the hyperspectral instrument, spacecraft attitude control during imaging, data processing algorithms and data products. Improved trade-off studies in payload design would be possible by simulating the TOA radiometry reaching a detector.

### 17.7.1 Effects On The Various Types Of Radiance

Tables 17.1, 17.2 and 17.3 presents a concise summary of the effects of different solar and viewing angles on the water leaving radiance, and on the radiance due to atmospheric effects at the ocean surface and at TOA.

**Table 17.1:** Summarized conclusion regarding solar and viewing angles' effect on the water leaving radiance at the ocean surface.

Type of angle	Effect
Solar azimuth	The utilization of solar azimuth angles less than or grater than $90^\circ$ results in a difference of $1.25 * 10^{-3} \text{ sr}^{-1}$ .
Solar zenith	The solar zenith angle of $60^\circ$ results in the highest radiance (with regard to the discussed solar zenith angles).
Viewing azimuth	The viewing azimuth angle of $0^\circ$ results in the highest radiance (with regard to the discussed viewing azimuth angles).
Viewing zenith	Results in different radiance values with regard to selected viewing zenith angles.
Viewing VS solar	The selection of viewing angles is of greater impact than the selection of solar angles. The resulting water leaving radiance is larger than the resulting radiance due to atmospheric effects at the ocean surface regardless of solar or viewing angles.

**Table 17.2:** Summarized conclusion regarding solar and viewing angles' effect on the radiance at the ocean surface due to atmospheric effects.

Type of angle	Effect
Solar zenith	The radiance resulting from the solar zenith angle of 80° varies less with regard to wavelength, and is lower for wavelengths between 400 and 750 nm.
Viewing zenith	The viewing zenith angle of 60° results in the highest radiance (with regard to the discussed viewing zenith angles).
Viewing azimuth	The resulting radiance values are roughly the same, regardless of viewing azimuth angle.
Viewing zenith VS viewing azimuth	The viewing zenith angles affect the resulting radiance more than the viewing azimuth angles do.

**Table 17.3:** Summarized conclusion regarding solar and viewing angles' effect on the radiance at TOA due to atmospheric effects.

Type of angle	Effect
Solar zenith	The radiance resulting from the solar zenith angle of 80° differs by resulting in a lower radiance for wavelengths 400 - 700 nm, as well as varies less with regard to wavelength.
Viewing zenith	The viewing zenith angle of 60° results in the highest radiance (with regard to the discussed viewing zenith angles).
Viewing azimuth	The resulting radiance values are roughly the same regardless of viewing azimuth angle.
Viewing zenith VS viewing azimuth	The selection of viewing azimuth angle is of less importance than the selection of viewing zenith angle.
Viewing zenith VS solar zenith	The resulting radiance varies more with respect to selected viewing zenith angle, than with respect to selected solar zenith angle.

## 17.8 Further Work

In the nearest future the results presented in this thesis will be used by PhD candidates. Further into the future, the simulation tool will be used by the HYPSO mission (Lapadatu [2018]).

Examining how different parameters in the water body, such as ocean state and depth, affect the water leaving radiance is of interest. Examining how the camera specifications affects the recorded radiance is also of interest. Furthermore, it is of interest to examine how different phase functions in PlanarRad affect the resulting water leaving radiance. A suggestion of a phase function that could be examined is the Fournier-Forand function, as it does a better job of reproducing the shapes of ocean phase functions than the Henyey-Greenstein phase function, or any other previously developed analytical model does (Lapadatu [2018]).

Further work regarding the RadPhyll Simulator includes, as mentioned in detail in the user guide in appendix A, creating additional lookup tables, obtaining more data from COART, and altering the script in order to create the possibility of combining the versions that calculate water leaving radiance with the COART (atmospheric effects) version.

# **Part V**

# **Appendices**

# Documentation And User Guide For The RadPhyll Simulator

## A.1 Introduction

The Radiance given Chlorophyll Simulator (RadPhyll Simulator) is a program developed in order to make the calculation and computation of water leaving radiance just above the ocean surface given chlorophyll a (chl.a) concentration, as well as of radiance at TOA due to atmospheric effects, less complicated and more rapid.

The RadPhyll Simulator is a MATLAB script developed in MATLAB R2018b. The data utilized by the program is generated by utilizing PlanarRad version 0.9.5 beta 2015\_07\_17 on Linux with Ubuntu 16.04 (Xenial Xerus), as well as a Python interface for running PlanarRad in batches. This python interface is written in Python 2.7.12 for Ubuntu 16.04 (Xenial Xerus). However, neither PlanarRad nor the python interface are necessary for utilizing the program. The program can be run on any operating system that supports MATLAB R2018b, or similar MATLAB versions. There are several versions of the program, presented with descriptions in table A.1. Several of the program versions require the SINMOD dataset, i.e. the *plankton.nc* file presented in section 3.1, to be available.

**Table A.1:** Description of the available program versions.

The RadPhyll Simulator versions	Description
The manual chl_a values version	Calculates water leaving radiance [ $sr^{-1}$ ] for user specified chl_a concentration values [ $mg\ chl\_a\ m^{-3}$ ]
The manual chl_a values version with specific viewing angles	Calculates water leaving radiance [ $sr^{-1}$ ] for user specified chl_a concentration values [ $mg\ chl\_a\ m^{-3}$ ] and viewing zenith or azimuth angle [deg].
The whole scene version	Calculates water leaving radiance [ $sr^{-1}$ ] for a whole scene. The user is required to specify which geographical area and time frame from the SINMOD dataset should be used to obtain the chl_a concentration values.
The COART (atmospheric effects) version	Calculates radiances at TOA [ $W\ m^{-2}\ \mu m^{-1}\ sr^{-1}$ ] due to atmospheric effects, given type of clouds, viewing azimuth angle, viewing zenith angle and solar zenith angle.
The general angle variation demonstration version	Calculates water leaving radiance [ $sr^{-1}$ ]. The results can be presented and plotted for various pre-defined solar and viewing angles.

Five versions of the program are available. The versions are the manual chl\_a values version, the manual chl\_a values version with specific viewing angles, the whole scene version, the COART (atmospheric effects) version and the general angle variation demonstration version. The manual chl\_a values version regards the user specifying the chl\_a concentration values of interest. The manual chl\_a values version with specific viewing angles regards the user specifying the chl\_a concentration values of interest, as well as the viewing zenith or azimuth angle of interest. The whole scene version regards the user specifying which geographical area and time frame from the SINMOD dataset should be used to obtain the chl\_a concentration values. This version has a plotting option. The COART (atmospheric effects) version regards computing the radiance at TOA due to atmospheric effects. The general angle variation demonstration version regards presenting, and plotting if desired, water leaving radiance resulting from different solar zenith and azimuth angles, as well as different viewing zenith and azimuth angles. There are four solar zenith angles and four solar azimuth angles available. Furthermore, there are three viewing zenith angles and four viewing azimuth angles available.

The program is based on PlanarRad and COART, and utilizes the lookup tables created in this thesis, as discussed in chapter 7. The manual chl.a values version, manual chl.a values version with specific viewing angles, whole scene version and general angle variation demonstration version are based on the SINMOD dataset. That is to say, the COART (atmospheric effects) version is the only version that is not based on the SINMOD data set. Due to the utilization of the lookup tables, the chl.a concentration values must be in the range of 0.0 to 1.8  $mg\ chl\_a\ m^{-3}$ .

Regardless of which version is selected the wavelengths are defined as the wavelengths of interest for the HYPSO mission, i.e. 400 - 800 nm. The wavelengths can not be changed as the acquired radiation data, as well as the lookup tables, utilized in the program is calculated with regard to the HYPSO mission wavelengths. The calculations were performed in PlanarRad, COART and MATLAB beforehand, and thus are not performed directly in the program.

The program generates, depending on the selected version, the resulting water leaving radiance or the resulting radiance at TOA due to atmospheric effects.

The program can be ran directly from MATLAB, or through a command-line by typing  
`./matlab -nodisplay -nosplash -nodesktop -r "run('directory-path/RadPhyll.m');exit;" | tail -n +11` while in the directory containing MATLAB. The input file must be run separately beforehand.

## A.2 The Input File

It is required for the input file "Input\_RadPhyll.m" to be run before the program is run. This is due to the fact that the input file creates, and saves, files necessary for the program to run. The input file needs to be run every time the inputs are changed, otherwise the changes will not be applied.

The first input required by the user regards which version of the program is to be run. This is specified in the variable *input\_version*. Table A.2 presents the available input values. Figure A.1 illustrates the version selection in the input file.

**Table A.2:** Available input values to the variable *input\_version*.

<b>Input value to <i>input_version</i></b>	<b>Selected version</b>
0	The manual chl_a values version
1	The manual chl_a values version with specific viewing angles
2	The whole scene version
3	The COART (atmospheric effects) version
4	The general angle variation demonstration version

```
% For version and input variables explanations, see the program documentation.

% Please choose version
%
% ~ "0" = Manual Chl_a Values Version
% ~ "1" = Manual Chl_a Values Version With Specific Viewing Angles
% ~ "2" = Whole Scene Version
% ~ "3" = COART (Atmospheric Effects) Version
% ~ "4" = General Angle Variation Demonstration Version

input_version = 2;
```

**Figure A.1:** Illustration of version selection in the program input file.

### A.3 The Manual Chl\_a Values Version

The manual chl<sub>a</sub> values version provides the possibility of calculating water leaving radiance [ $sr^{-1}$ ] for user specified chl<sub>a</sub> concentration values [ $mg\ chl\_a\ m^{-3}$ ].

In order to run the manual chl<sub>a</sub> values version the chl<sub>a</sub> concentration must be specified. This is specified in a list called *input\_chl\_a\_values\_manual*. The user can provide as many chl<sub>a</sub> concentration values as desired.

The values used in the lookup table were calculated with the sun zenith angle of 40°, the sun azimuth angle of 0°, the viewing zenith angle of 130° and the viewing azimuth angle of 180°. Since this version calculates water leaving radiance, and thus uses values obtained by utilizing PlanarRad, the viewing zenith angle is defined as in PlanarRad. Section 6.1 presents details regarding the viewing zenith angle definition. Thus, these angles are applicable for the output water leaving radiance values as well.

When the manual chl<sub>a</sub> values version of the program is ran the water leaving radiance values are calculated, and saved in an .mat output file called *output\_RadPhyll\_manual*, as well as in a .csv file called *output\_RadPhyll\_manual.csv*.

The output file will consist of one row for every chl<sub>a</sub> concentration value specified. Each row will consist of 87 radiance values, one for each wavelength band. The first row in the output file will be a header with information. Figure A.3 presents an example of an output.

Table A.3 presents the input variables for the manual chl<sub>a</sub> values version, as well explanations for each variable. Figure A.2 illustrates the manual chl<sub>a</sub> values version part of the input file.

**Table A.3:** The manual chl<sub>a</sub> values version input variables.

Input variable	Explanation
input_chl_a_values_manual	Chl <sub>a</sub> values of interest

---

```

%% Manual chl_a Values Version

input_chl_a_values_manual = [ ];

% Insert chl_a values you wish to use as input to PROGRAM NAME

input_chl_a_values_manual(1) = 0.3409;
input_chl_a_values_manual(2) = 0.12;

input_number_of_values_manual = length(input_chl_a_values_manual);

```

**Figure A.2:** The manual chl<sub>a</sub> values section in the program input file.

	A	B	C
1	resulting_radiance_LU_1	resulting_radiance_LU_2	resulting_radiance_LU_3
2	0.0054336046	0.0054334182	0.0054331318
3	0.00546736	0.00546554	0.00546374

**Figure A.3:** The manual chl<sub>a</sub> values version of the program output example.

## A.4 The Manual Chl<sub>a</sub> Values Version With Specific Viewing Angles

The manual chl<sub>a</sub> values version with specific viewing angles provides the possibility of calculating water leaving radiance [ $sr^{-1}$ ] given user specified chl<sub>a</sub> concentration values [ $mg\ chl\_a\ m^{-3}$ ], as well as the possibility for the user to select viewing angles from a list of predefined angles.

PlanarRad was employed to obtain the water leaving radiance values which were applied in the creation of the lookup tables, see section 7 for details. In the table L.a, in the reports generated by PlanarRad, every row represents a certain zenith angle, i.e. the numbers in each row represent different azimuth angles for that specific zenith angle. Every column in the table represents a certain azimuth angle, and thus the numbers in each column represent different zenith angles for that specific azimuth angle. The azimuth angles range from  $0^\circ$  to  $345^\circ$ , and increment with  $15^\circ$ . Thus there are 24 azimuth angles available. The zenith angles range from  $0^\circ$  to  $180^\circ$ , and increment with  $10^\circ$ . However, around the zenith angle of  $90^\circ$  the incrementation is not exactly  $10^\circ$ . The available zenith angles around the mentioned angle are  $80^\circ$ ,  $87^\circ$ ,  $92^\circ$  and  $100^\circ$ . The employed python script removes the first and last zenith angles, due to them being end caps. Thus, 18 zenith angles are available for further calculations. Furthermore, azimuth angles will only be regarded from  $0^\circ$  to  $180^\circ$ . Zenith angles will only be regarded from  $100^\circ$  to  $170^\circ$  as this corresponds to looking down towards the ocean surface. That is to say, the specified zenith angles provide the water leaving radiance.

The resulting water leaving radiance with regard to different viewing azimuth angles is

not linear. Thus, it is onerous to create an accurate lookup table with regard to different azimuth angles. The resulting water leaving radiance with regard to different viewing zenith angles is not linear either. Thus, it is onerous to create an accurate lookup table with regard to different viewing zenith angles. Therefore, PlanarRad was run seven times for different chl\_a concentration values, and the resulting water leaving radiance was retrieved for different viewing azimuth and zenith angles. The retrieved water leaving radiance values were used in order to create 11 lookup tables. Thus, the lookup tables are able to calculate water leaving radiance for different chl\_a concentration values with regard to different viewing angles. These lookup tables can not calculate the water leaving radiance for other viewing angles than the ones calculated in PlanarRad, but are able to calculate the water leaving radiance for other chl\_a concentration values with regard to the selected viewing angles.

Each lookup table consists of seven rows, i.e. one row for each of the seven chl\_a concentration values. 4 of the 11 lookup tables regard the viewing zenith angles. The available viewing zenith angles are 100°, 120°, 140° and 160°. The remaining seven lookup tables regard the viewing azimuth angles. The available viewing azimuth angles are 0°, 30°, 60°, 90°, 120°, 150° and 180°. The specified viewing zenith angles were retrieved from the L\_a tables by utilizing the indices starting at [10,12] and ending at [16,12]. The specified viewing azimuth angles were retrieved from the L\_a tables by utilizing the indices starting at [13,0] and ending at [13,12].

The intention is that the user can specify one of these viewing zenith or azimuth angles, as well as chl\_a concentration values of interest. The program will select the correct lookup table and calculate the resulting water leaving radiance for the given chl\_a concentration value with regard to the given viewing zenith or azimuth angle.

In order to run the manual chl\_a values version with specific viewing angles, the user must specify one or more chl\_a concentration value, as in the manual chl\_a values version. These values are saved in a list. Furthermore, the user must specify *input\_type\_several*, i.e. which viewing zenith or azimuth angle to utilize. Only one viewing angle can be selected each run. These inputs are saved and applied in the script *RadPhyll.m*.

The solar azimuth angle used in the computation of the water leaving radiance was 0°, while the solar zenith angle was 40°. The viewing zenith angle applied when obtaining water leaving radiance with respect to viewing azimuth angle was 130°. The viewing azimuth angle used when obtaining water leaving radiance with respect to viewing zenith angle was 180°.

The resulting water leaving radiance values are saved in an *.mat* output file titled *output\_RadPhyll\_several*, as well as in a *.csv* file called *output\_RadPhyll\_several.csv*.

The output file will consist of one row for every chl\_a concentration value specified. Each row will consist of 87 radiance values, one for every wavelength band. The first row in the output file will be a header with information.

---

```

%% Manual chl_a Values Version With Specific Viewing Angles

input_chl_a_values_several = [ ];

% Choose specific viewing angle of interest
% ~ "0" = Zenith angle: 100
% ~ "1" = Zenith angle: 120
% ~ "2" = Zenith angle: 140
% ~ "3" = Zenith angle: 160
% ~ "4" = Azimuth angle: 0
% ~ "5" = Azimuth angle: 30
% ~ "6" = Azimuth angle: 60
% ~ "7" = Azimuth angle: 90
% ~ "8" = Azimuth angle: 120
% ~ "9" = Azimuth angle: 150
% ~ "10" = Azimuth angle: 180

input_type_several = 0;

% Insert chl_a values you wish to use as input
input_chl_a_values_several(1) = 0.3409;
input_chl_a_values_several(2) = 0.12;

input_number_of_values_several = length(input_chl_a_values_several);

```

**Figure A.4:** Illustration of the section of the input file of the program regarding the manual chl.a values version with specific viewing angles.

Table A.4 presents the input variables for manual chl.a values version with specific viewing angles, as well as explanations for each variable. Figure A.4 illustrates the manual chl.a values version with specific viewing angles part of the input file.

**Table A.4:** The manual chl.a values version with specific viewing angles input variables.

Input variable	Explanation
input_chl_a_values_several	Chl.a values of interest
input_type_several	Select specific viewing angle of interest

## A.5 The Whole Scene Version

The whole scene version provides the possibility of calculating water leaving radiance [ $sr^{-1}$ ] for a whole scene, i.e. time frame, from the SINMOD dataset, given coordinates, time frame, spacing, and whether or not to accept *-nan* values as input.

In order to run the whole scene version of the RadPhyll Simulator several inputs must be specified by the user. The coordinates of interest are specified through the latitude starting and ending point, the longitude starting and ending point, as well as the spacing for the two. The *x*-inputs correspond to latitude, while the *y*-inputs correspond to longitude. The spacing specifies how many of the values from the SINMOD dataset in between the starting and ending points should be employed, i.e. how many values the water leaving radiance should be calculated for. As an example, a spacing of five corresponds to utilizing every *fifth<sup>th</sup>* value in between the starting and ending values.

Other required inputs are the time frame, i.e. which time frame from the SINMOD dataset to obtain the chl\_a concentration values from, and whether or not to accept *-nan* values. 1 represents *yes*, while 0 represents *no*. The SINMOD dataset includes some *-nan* values, thus if one selects not to accept these, the program will use the closest geographical non-nan value instead.

When the whole scene version is ran the water leaving radiance is calculated for each chl\_a concentration value specified, by utilizing a lookup table. The resulting water leaving radiance values are saved as a hyperspectral cube. It is possible to plot the whole scene, by setting the variable *input\_plotting\_answer\_whole\_scene* to 1. This can be specified in the section regarding the whole scene version in the program input file.

The values used in the lookup table were calculated with the sun zenith angle of 40°, the sun azimuth angle of 0°, the viewing zenith angle of 130° and the viewing azimuth angle of 180°. Since this version calculates water leaving radiance, and thus utilizes values obtained by utilizing PlanarRad, the viewing zenith angle is defined as in PlanarRad. Section 6.1 presents details. Thus, these angles are applicable for the output water leaving radiance values as well.

The resulting water leaving radiance is saved in an *.mat* output file called *output\_RadPhyll\_whole\_scene*, as well as in a *.csv* file called *output\_RadPhyll\_whole\_scene.csv*.

The output file will consist of several rows and columns with water leaving radiance values. The amount of rows will equal to the amount of *x*-values, i.e. the number of latitude coordinates for a certain longitude coordinate. The amount of columns will equal to the amount of *y*-values, i.e. the number of longitude coordinates for a certain latitude coordinate, multiplied with 87, i.e. the number of wavelength bands. The correct way to interpret the output file is that each row represents a latitude coordinate, while the columns represent longitude coordinates as well as wavelength band information. The first *number of y* columns represent the first wavelength band, the next *number of y* columns represent the second wavelength band etc. The first row in the output file will be a header with information.

The output resulting from the whole scene version is ordinarily large, and thus not every program can open or process it. Excel generally can open the output file.

Table A.5 presents the input variables for the whole scene version, as well as variables explanations. Figure A.5 illustrates the part of the program input file regarding the whole scene version.

**Table A.5:** The whole scene version input variables.

Input variable	Explanation
input_x_start	Latitude [degrees north from starting point] starting coordinate
input_x_end	Latitude [degrees north from starting point] ending coordinate
input_y_start	Longitude [degrees east from starting point] starting coordinate
input_y_end	Longitude [degrees east from starting point] ending coordinate
input_time	Specific time frame of interest in the SINMOD dataset
input_x_spacing	Latitude spacing
input_y_spacing	Longitude spacing
input_nan_answer	Whether or not to accept -nan values
input_plotting_answer_whole_scene	Wheter or not to plot the resulting scene

```
%% Whole Scene Version

% Insert coordinates of interest (x,y and time)
%
%   ~ x: Latitude [degrees north from starting point]
%   ~ y: Longitude [degrees east from starting point]
%   ~ time: Time frame

input_x_start = 423;
input_x_end = 579;

input_y_start = 31;
input_y_end = 256;

input_time = 501;

% Insert x spacing of interest
% NB! "(input_x_end - input_x_start)/input_x_spacing" must result in an integer (not float)!

input_x_spacing = 12;

% Insert y spacing of interest
% NB! "(input_y_end - input_y_start)/input_y_spacing" must result in an integer (not float)!

input_y_spacing = 9;

% Do you wish for "-nan" values to be accepted?
%
%   ~ "1" = Yes
%   ~ "0" = No

input_nan_answer = 0;

% Do you wish to plot the results?
%
%   ~ "1" = Yes
%   ~ "0" = No

input_plotting_answer_whole_scene = 0;
```

**Figure A.5:** The section of the program input file regarding the whole scene version.

## A.6 The COART (Atmospheric Effects) Version

The COART (atmospheric effects) version provides the possibility of calculating radiances at TOA [ $W\ m^{-2}\ \mu m^{-1}\ sr^{-1}$ ] due to atmospheric effects, given type of clouds, viewing azimuth angle, viewing zenith angle and solar zenith angle as inputs. The resulting outputs are calculated by utilizing COART.

Two possibilities are available regarding the selection of cloud types, namely *no clouds* and *water clouds*. Granted that *no clouds* is selected, the user must specify viewing azimuth angle, viewing zenith angle or solar zenith angle. The user can specify several of the mentioned as well. However, in that case, the different angles will not be combined, but rather outputted as three different output files. It is required that all inputs are specified, regardless of whether all are of interest to the user or not.

If the viewing azimuth angle is specified by the user, the remaining angles are defined as listed below:

- Solar zenith angle of  $60^\circ$
- Viewing zenith angle of  $20^\circ$

If the viewing zenith angle is specified by the user, the remaining angles are defined as listed below:

- Solar zenith angle of  $60^\circ$
- Viewing azimuth angle of  $0^\circ$

If the solar zenith angle is defined by the user, the remaining angles are defined as listed below:

- Viewing zenith angle of  $20^\circ$
- Viewing azimuth angle of  $0^\circ$

If the user specifies usage of water clouds, the viewing angles and solar angle are defined as listed below:

- Solar zenith angle of  $60^\circ$
- Viewing azimuth angle of  $0^\circ$
- Viewing zenith angle of  $20^\circ$

All angles are defined as in COART. Section 6.1 presents the angle definitions.

The resulting radiance at TOA is saved in an *.mat* output file called *output\_RadPhyll\_COART\_type of angle\_angle*, as well as in a *.csv* file called *output\_RadPhyll\_COART\_type of angle\_angle.csv*.

The output file will consist of one row, representing the chosen angle, with 87 values representing the 87 wavelength bands. The first row in the output file will be a header with

information.

Table A.6 presents the input variables for the COART (atmospheric effects) version, as well as explanations for the variables. Figure A.6 illustrates the input file, with regard to The COART (atmospheric effects) version.

**Table A.6:** The COART (atmospheric effects) version input variables.

<b>Input variable</b>	<b>Explanation</b>
input_clouds_answer	Choose between "No clouds" and "Water clouds"
input_COART_viewing_az	Choose viewing azimuth angle (available angles: 0, 60, 120, 180, all four)
input_COART_viewing_zen	Choose viewing zenith angle (available angles: 0, 30, 60, all three)
input_COART_solar_zen	Choose solar zenith angle (available angles: 20, 40, 60, 80, all four)

---

```
%>> COART (Atmospheric Effects) Version

% Insert type of clouds of interest
%   ~ "0" = No clouds
%   ~ "1" = Water clouds

input_clouds_answer = 1;

% The following inputs are of interest if "No clouds" was selected above

% Insert viewing azimuth angle of interest

% Available viewing azimuth angles:
%   ~ 0
%   ~ 60
%   ~ 120
%   ~ 180
%   ~ "1000" = All four

input_COART_viewing_az = 0;

% Insert viewing zenith angle of interest

% Available viewing zenith angles:
%   ~ 0
%   ~ 30
%   ~ 60
%   ~ "1000" = All three

input_COART_viewing_zen = 0;

% Insert solar zenith angle of interest

% Available solar zenith angles:
%   ~ 20
%   ~ 40
%   ~ 60
%   ~ 80
%   ~ "1000" = All four

input_COART_solar_zen = 40;
```

**Figure A.6:** The input file, with regard to The COART (atmospheric effects) version.

## A.7 The General Angle Variation Demonstration Version

The general angle variation demonstration version provides the possibility of calculating water leaving radiance [ $sr^{-1}$ ], given whether or not to output the resulting water leaving radiance for various solar zenith angles, solar azimuth angles, viewing zenith angles and/or viewing azimuth angles. Furthermore, the user must specify whether or not the results should be plotted. The resulting water leaving radiance is computed by utilizing computed values from PlanarRad, that have been saved in the script *RadPhyll.m*.

The available sun zenith angles are  $20^\circ$ ,  $40^\circ$ ,  $60^\circ$  and  $80^\circ$ . The available sun azimuth angles are  $0^\circ$ ,  $60^\circ$ ,  $120^\circ$  and  $180^\circ$ . The available viewing zenith angles are  $120^\circ$ ,  $150^\circ$  and  $170^\circ$ . The available viewing azimuth angles are  $0^\circ$ ,  $60^\circ$ ,  $120^\circ$  and  $180^\circ$ . The viewing zenith angles are defined as in PlanarRad. Section 6.1 presents details regarding the viewing zenith angle definition.

Granted that the user specifies to plot the solar zenith angles, all four will be plotted together. The same holds regarding solar azimuth angles. Granted that the user specifies to plot the viewing zenith angles, all three will be plotted together. However, if the user specifies to plot the viewing azimuth angles, angle  $60^\circ$ ,  $120^\circ$  and  $180^\circ$  are plotted together, while angle  $0^\circ$  is plotted in a separate plot. This is due to the resulting water leaving radiance with the viewing azimuth angle  $0^\circ$  is much higher, i.e. approximately  $6.23 * 10^{-2} sr^{-1}$  compared to  $5.45 * 10^{-3} sr^{-1}$ , than the resulting water leaving radiance with the other three viewing azimuth angles.

The varying of solar zenith angles is computed with the remaining angles set as follows:

- Solar azimuth  $0^\circ$
- Viewing zenith  $170^\circ$
- Viewing azimuth  $0^\circ$

The varying of solar azimuth angles is computed with the remaining angles set as follows:

- Solar zenith  $20^\circ$
- Viewing zenith  $170^\circ$
- Viewing azimuth  $0^\circ$

The varying of viewing zenith angles is computed with the remaining angles set as follows:

- Solar zenith  $40^\circ$
- Solar azimuth  $0^\circ$
- Viewing azimuth  $0^\circ$

The varying of viewing azimuth angles is computed with the remaining angles set as follows:

- Solar azimuth  $0^\circ$

- Solar zenith 40°
- Viewing zenith 130°

The resulting water leaving radiance is saved in an *.mat* output file called *output\_RadPhyll\_variation\_type of angle*, as well as in a *.csv* file called *output\_RadPhyll\_variation\_type of angle.csv* for every option, i.e. one for the solar zenith angles, one for the solar azimuth angles, one for the viewing zenith angles and one for the viewing azimuth angles.

The output file will consist of one row for every specified angle. Each row will consist of 87 values, representing the 87 wavelength bands. The first row in the output file will be a header with information.

Table A.7 presents the input variables for the general angle variation demonstration version, as well as the explanations for the variables. Figure A.7 presents some of the inputs from the input file regarding the general angle variation demonstration version.

**Table A.7:** The general angle variation demonstration version input variables.

Input variable	Explanation
input_var_sun_zenith_angle	Whether or not it is desired to output a general sun zenith angle variation demonstration. The sun zenith angles 20, 40, 60 and 80 will be presented.
input_var_sun_zenith_angle_plot	Whether or not the sun zenith angle results should be plotted.
input_var_sun_azimuth_angle	Whether or not it is desired to output a general sun azimuth angle variation demonstration. The sun azimuth angles 0, 60, 120 and 180 will be presented.
input_var_sun_azimuth_angle_plot	Whether or not the sun azimuth angle results should be plotted.
input_var_viewing_zenith_angle	Whether or not it is desired to output a general viewing zenith angle variation demonstration. The viewing zenith angles 120, 150 and 170 will be presented.
input_var_viewing_zenith_angle_plot	Whether or not the viewing zenith angle results should be plotted.
input_var_viewing_azimuth_angle	Whether or not it is desired to output a general viewing azimuth angle variation demonstration. The viewing azimuth angles 0, 60, 120 and 180 will be presented.
input_var_viewing_azimuth_angle_plot	Whether or not the viewing azimuth results should be plotted.

```

%% General Angle Variation Demonstration Version

% Do you wish to output a general sun zenith angle variation demonstration?
% (The sun zenith angles 20, 40, 60 and 80 will be presented)
%   ~ "0" = No
%   ~ "1" = Yes

input_var_sun_zenith_angle = 0;

% Do you wish to plot the results?
% ~ "0" = No
% ~ "1" = Yes

input_var_sun_zenith_angle_plot = 0;

% Do you wish to output a general sun azimuth angle variation demonstration?
% (The sun azimuth angles 0, 60, 120 and 180 will be presented)
%   ~ "0" = No
%   ~ "1" = Yes

input_var_sun_azimuth_angle = 0;

% Do you wish to plot the results?
%   ~ "0" = No
%   ~ "1" = Yes

input_var_sun_azimuth_angle_plot = 0;

% Do you wish to output a general viewing zenith angle variation demonstration?
% (The viewing zenith angles 120, 150 and 170 will be presented)
%   ~ "0" = No
%   ~ "1" = Yes

```

**Figure A.7:** Some of the inputs from the input file of the program regarding the general angle variation demonstration version.

## A.8 Expanding The RadPhyll Simulator

This section regards how the developed program can be further developed if desirable.

The program can be further developed by creating additional lookup tables. This would result in additional scenarios available to the program. Additional lookup tables could also be utilized in order to vary the solar and viewing angles in the whole scene version of the program. To obtain this, PlanarRad, preferably the batch version, must be utilized.

Obtaining more data from COART and including it in the program is another method to expand the program. Such additional data can regard the resulting radiance values with respect to various atmospheres, various maritime aerosol models and various stratospheric aerosol models.

Furthermore, the developed software can be improved by altering the script in order to create the possibility of combining the versions that calculate water leaving radiance with the COART (atmospheric effects) version. This would result in total radiances at TOA, i.e. including radiance due to atmospheric effects as well as the water leaving radiance. Inputs can be created in order to select how the water leaving radiance should be calculated, i.e. which solar and viewing angles to utilize, as well as which atmospheric model to utilize.

# Appendix B

## The Lookup Tables

This appendix presents the created water leaving radiance [ $sr^{-1}$ ] lookup tables with regard to different viewing angles. The lookup tables are presented as figures, i.e. figure B.1 - B.11, as each lookup table consists of 609 values. The lookup table values are available in the simulation tool RadPhyll, in the primary script *RadPhyll.m*. The viewing azimuth angle used in the creation of the viewing zenith angle lookup tables is  $180^\circ$ . The viewing zenith angle used in the creation of the viewing azimuth angle lookup tables is  $130^\circ$ , as defined in PlanarRad, see section 6.1. The resulting maximum values are given by the maximum value on the z-axes.

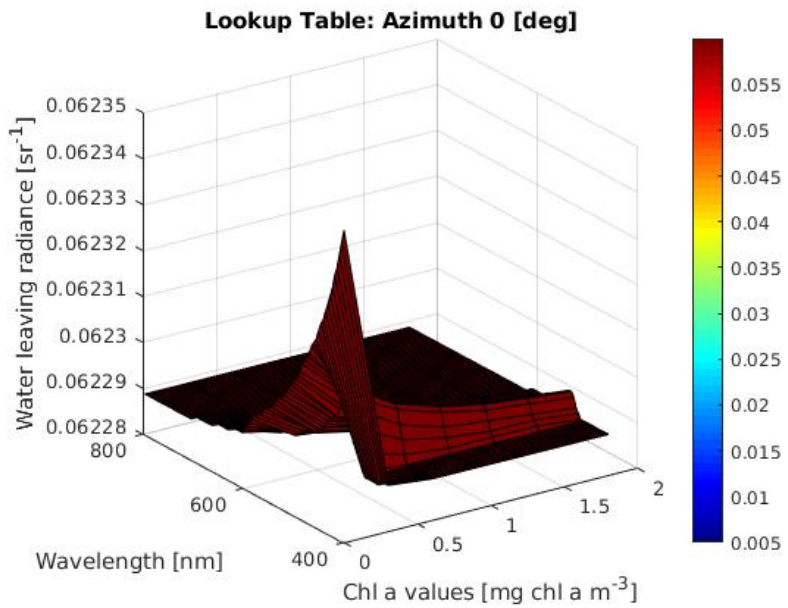


**Figure B.1:** Lookup table for the viewing azimuth angle of  $0^\circ$ .

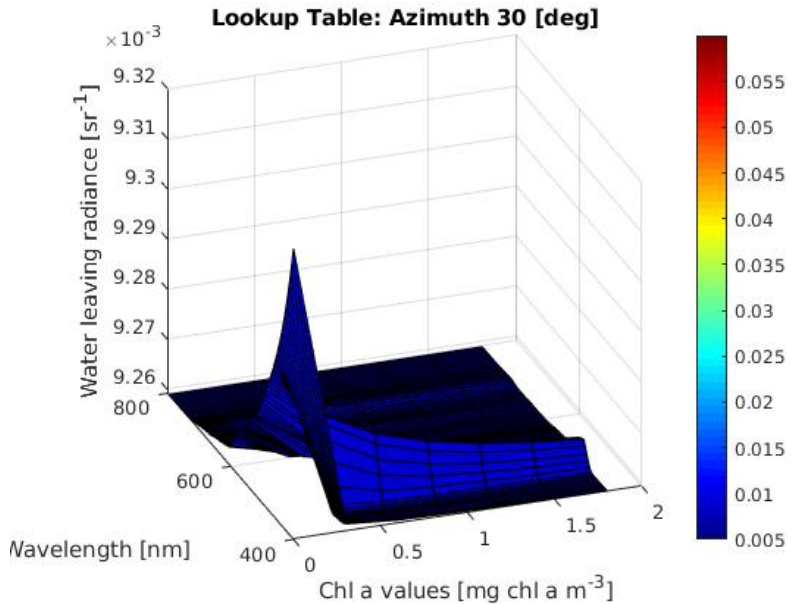


**Figure B.2:** Lookup table for the viewing azimuth angle of  $30^\circ$ .

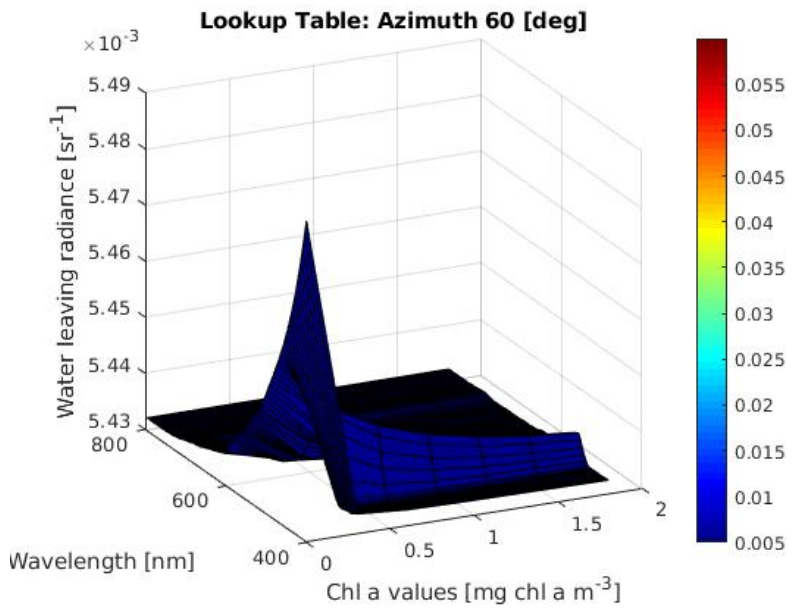


**Figure B.3:** Lookup table for the viewing azimuth angle of  $60^\circ$ .

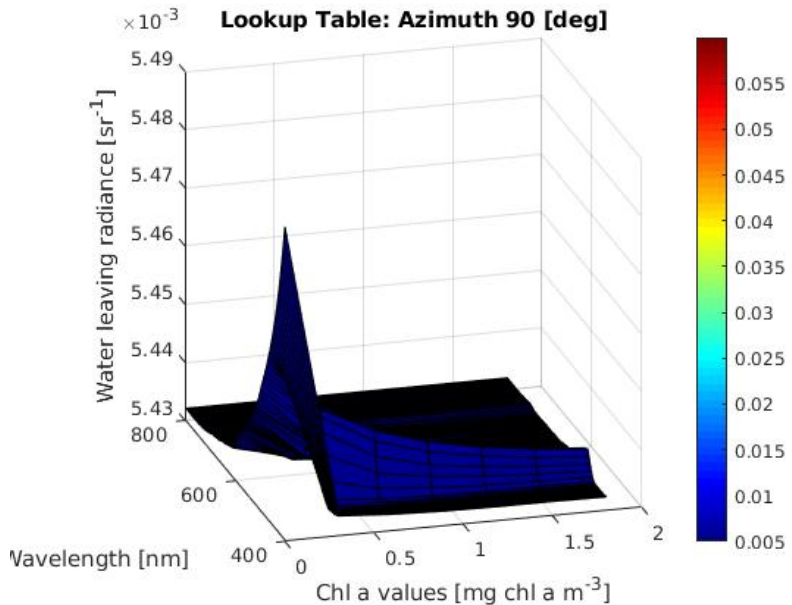


**Figure B.4:** Lookup table for the viewing azimuth angle of  $90^\circ$ .

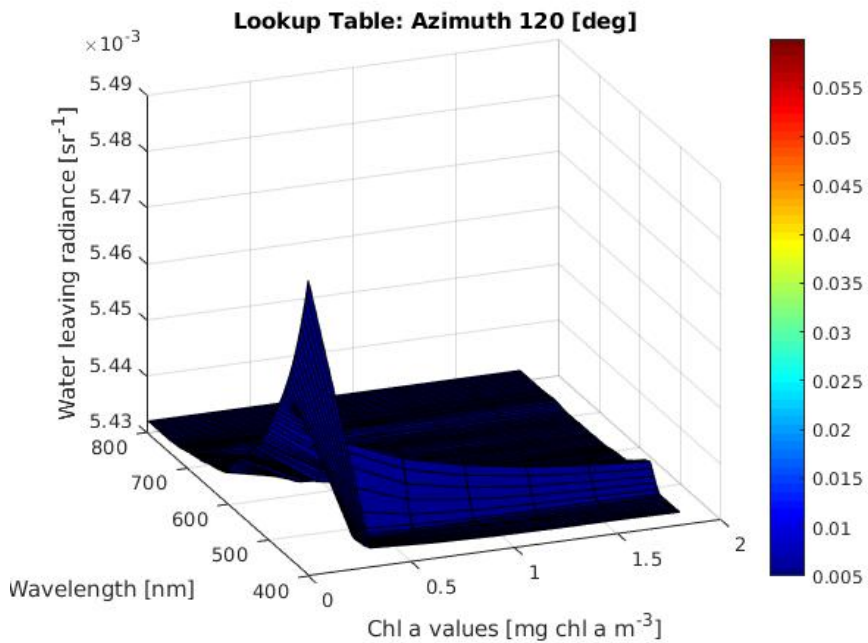


**Figure B.5:** Lookup table for the viewing azimuth angle of  $120^\circ$ .

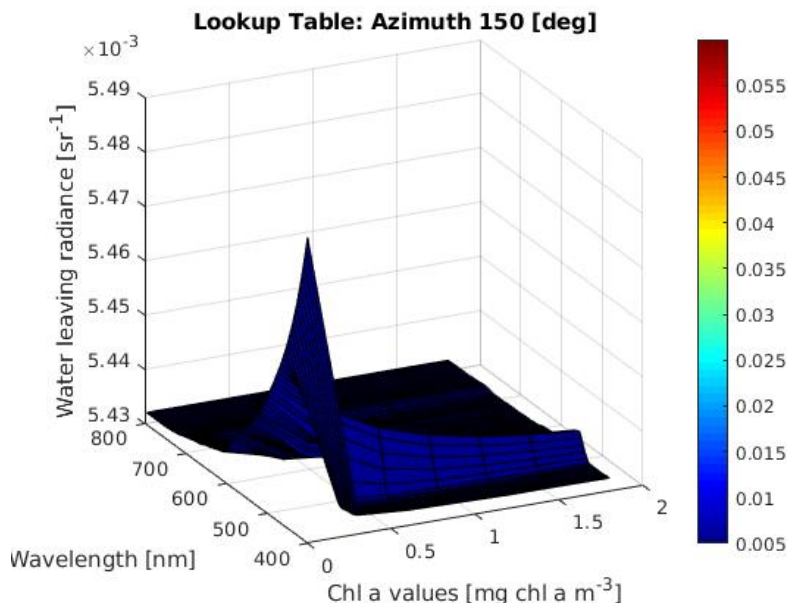


**Figure B.6:** Lookup table for the viewing azimuth angle of  $150^\circ$ .

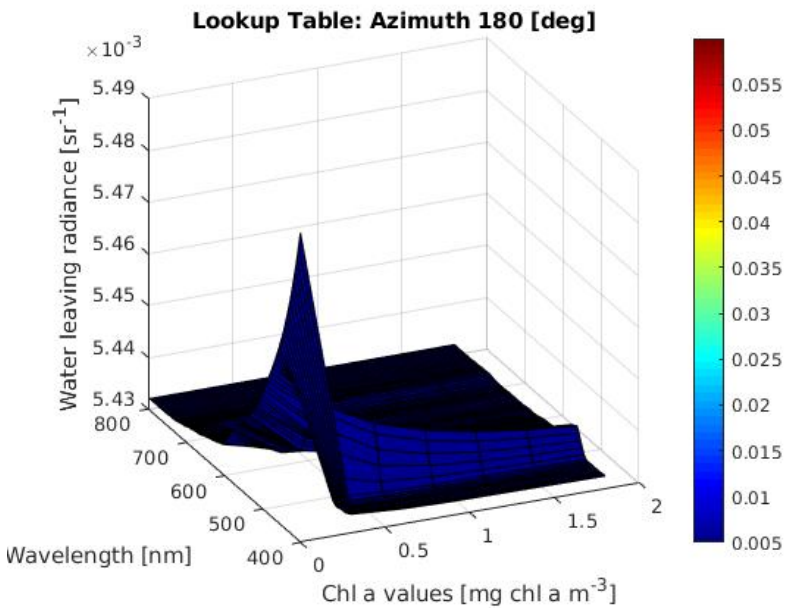


**Figure B.7:** Lookup table for the viewing azimuth angle of 180°.

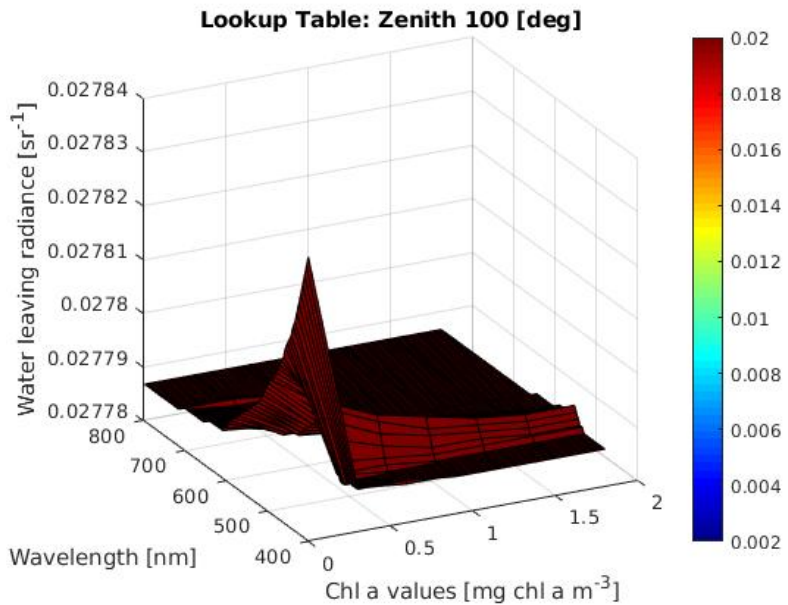


**Figure B.8:** Lookup table for the viewing zenith angle of 100°.

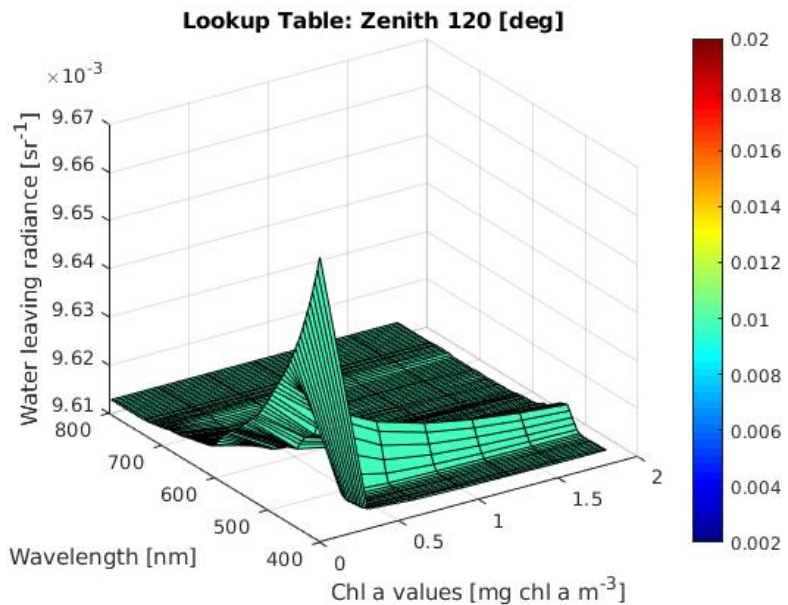


**Figure B.9:** Lookup table for the viewing zenith angle of 120°.

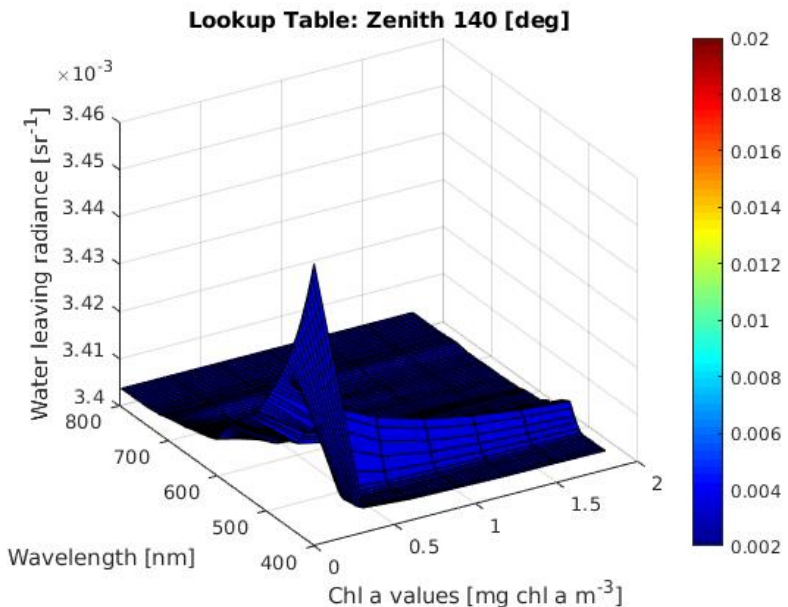


**Figure B.10:** Lookup table for the viewing zenith angle of 140°.

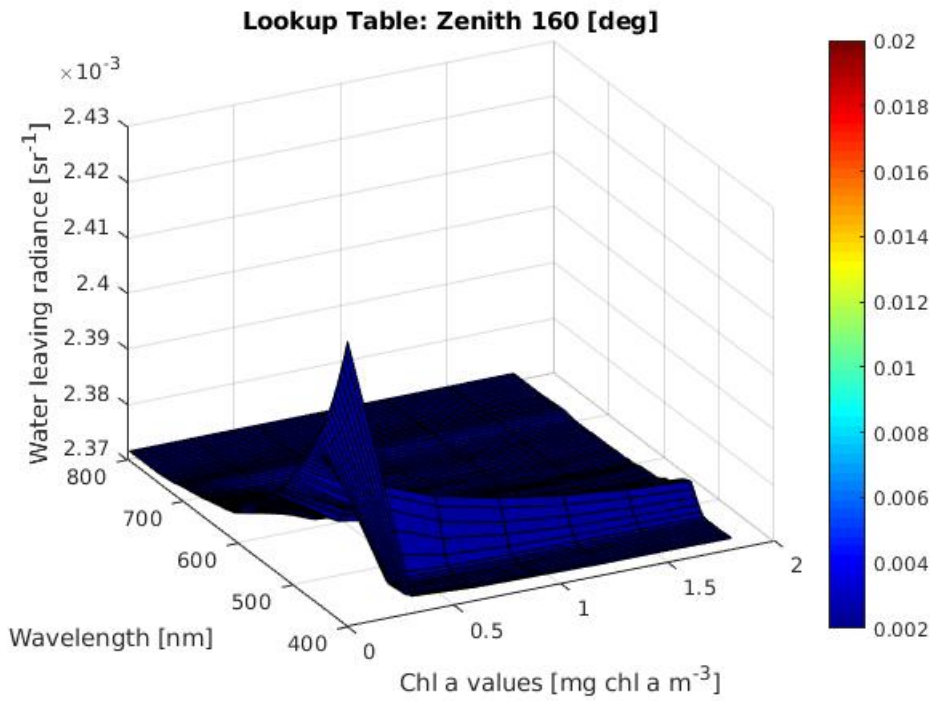


**Figure B.11:** Lookup table for the viewing zenith angle of 160°.

# Conference Paper

A conference paper has been submitted to whispers 2019 based on the work presented in this thesis. The conference paper is currently pending. Whispers is a workshop on hyperspectral image and signal processing arranged by The IEEE Geoscience and Remote Sensing Society (Couturier-Doux). Whispers 2019 is held in Amsterdam, The Netherlands, 24 - 26 September.

The workshop regards hyperspectral data processing, which includes, among other processing types, processing of images, from the ground using satellite sensors, up to astrophysical data, as well as models of the sensed scene, including physical considerations (Couturier-Doux).

The submitted conference paper is presented in this appendix.

# SIMULATION TOOL FOR HYPER-SPECTRAL IMAGING FROM A SATELLITE

Monica Lapadatu, Sivert Bakken, Mariusz E. Grøtte, Morten Alver, Tor A. Johansen

Center for Autonomous Marine Operations and Systems

Department of Engineering Cybernetics

Norwegian University of Science and Technology (NTNU)

Trondheim, Norway

## ABSTRACT

This paper presents a tool created for simulating the expected radiance from oceanic geophysical parameters through the atmosphere as perceived by a hyperspectral remote sensing satellite. The effects of varying off-nadir viewing angles, solar zenith angles and the presence of water clouds on the resulting radiance has been analyzed, and simulated top-of-atmosphere (TOA) radiance values coincide well with real world data.

**Index Terms**— Simulation, hyperspectral, satellite, ocean color, radiative transfer.

## 1. INTRODUCTION

Ocean color remote sensing satellites are currently being used for maritime observation and surveillance, e.g. monitoring of phytoplankton, zooplankton, river plumes, oil spills, water sediments and ice. Past and present operational satellites are mainly concerned with multispectral data, but hyperspectral sensors are being considered more frequently for upcoming missions [1, 2]. By utilizing hyperspectral sensors it is expected to enhance the capabilities to detect targets of interest and estimate their characteristics [3]. Experimental space-based hyperspectral sensors include HICO and Hyperion [4, 5].

This paper focuses on the simulation of TOA radiance as perceived by a hyperspectral sensor in Low Earth Orbit, as well as simulation of water leaving radiance at the ocean surface.

The objective is to analyze different scenarios with varying off-nadir viewing angles, solar zenith angles and the presence of water clouds. As an alternative to existing remote sensing tools, e.g. SeaDAS, SNAP and Ocean Virtual Laboratory, that use real satellite data, the simulation tool uses output data from the coupled physical and ecological ocean model SINMOD to calculate the resulting spectral response in radiance. Further, estimated atmospheric effects at TOA are added. The result is the hyperspectral image cube sensed at TOA.

The simulation tool is intended to be used for feasibility and analytical studies during the space mission design phase, as well as improve the mission operations of a possibly custom-designed hyperspectral imaging satellite that is configured to observe specific targets. This includes design and validation of the hyperspectral instrument, spacecraft attitude control during imaging, data processing algorithms and data products.

The common way to simulate geophysical variables in the ocean as hyperspectral radiance received by a satellite sensor is to combine the underwater radiative transfer code HydroLight and the atmospheric code MODTRAN [6]. Both HydroLight and MODTRAN are commercial software, and they are not designed to work together.

Via PlanarRad and COART, open-source alternatives, a system of lookup tables were computed to make the simulation process more time effective. A temporal sensitivity of data acquisition analysis was performed, and a user friendly interface for radiance simulation was developed.

The theory is based on [6], i.e. ocean optics, which regards light and radiometry, optical oceanography, absorption, scattering, optical constituents of the ocean, radiative transfer theory, remote sensing, atmospheric effects and the bidirectional reflection distribution function.

## 2. SYSTEM OVERVIEW

The simulation tool is based on the utilization of a hyperspectral imager, as described in [7]. Furthermore, a dataset, titled the SINMOD data, is utilized in combination with the program PlanarRad in order to calculate water leaving radiance from the ocean surface. The radiance due to atmospheric effects is calculated utilizing the program COART. Combining the two results in the hyperspectral radiance at TOA.

### 2.1. The SINMOD data

SINMOD is developed by SINTEF [8, 9]. It is based on the primitive Navier-Stokes equations and uses a regular horizontal grid and z-layers. High resolution simulations are achieved using a nesting scheme where larger scale simulations provide outer boundary conditions for higher resolution simulations. The top level domain covers the Norwegian Sea and Arctic Ocean in 20 km horizontal resolution, and the resolution is increased by a factor of 5 through each nesting step. The model forcing includes atmospheric reanalysis data from Era Interim [10] and climatological freshwater runoff data. Tidal dynamics are applied on the outer boundaries of the top level domain, based on 8 tidal components from TPXO [11].

The model calculates physical oceanographic variables such as surface elevation, current speed, temperature and salinity. The ecological model additionally estimates nutrient concentrations (nitrate, silicate, ammonium), phytoplankton (diatoms and flagellates), zooplankton (*Calanus finmarchicus* and *C. glacialis*) and variables such as heterotrophic nanoflagellates, microzooplankton, and fast and slow sinking detritus.

### 2.2. PlanarRad

HydroLight is well suited for mapping geophysical variables to spectral signatures [6]. However, as HydroLight is a commercial software, PlanarRad, a functionally similar open source alternative, was utilized instead.

PlanarRad is a free open source code for modelling light in natural waters or other homogeneous scattering and absorbing media [12]. PlanarRad produces nearly identical results to HydroLight [13]. PlanarRad is a C++ implementation of the invariant embedded numerical integration technique for calculating radiative transfer in plane-parallel media with an opaque bottom boundary [12]. It is based on the algorithm described in [6].

### 2.3. COART

Coupled Ocean and Atmosphere Radiative Transfer (COART) is a tool provided by NASA. The tool is able to calculate and simulate radiance and irradiance at any levels in the atmosphere and ocean.

The COART model was based on the Coupled Discrete Ordinate Radiative Transfer (CDISORT) code, which was developed from DISORT. DISORT is a publicly distributed software for radiative transfer, provided by NASA [14].

### 2.4. The lookup tables

Several lookup tables were created with the purpose of saving computational time for the calculation of water leaving radiance at the ocean surface. The lookup tables are especially relevant for computation of whole scenes instead of individual pixels. MATLAB and PlanarRad were utilized in order to compute the lookup tables. MATLAB was utilized to read the chl<sub>a</sub> concentration values from the SINMOD dataset and calculate the absorption, attenuation and scattering for the PlanarRad input files. PlanarRad calculated the water leaving radiance for the selected chl<sub>a</sub> concentration values.

### 2.5. Temporal sensitivity of data acquisition analysis

A lookup table was utilized together with MATLAB in order to perform a temporal sensitivity of data acquisition analysis. The objective was to acquire a understanding of the water leaving radiance variation with regard to time. The analysis was performed by identifying several consecutive time frames from the SINMOD dataset with variation in the chl<sub>a</sub> concentration values. The water leaving radiance was calculated for the specified values. The analysis was performed for time periods of one hour, five hours and ten hours.

### 2.6. Software

A software program is developed in order to make the calculation and computation of water leaving radiance just above the ocean surface given chl<sub>a</sub> concentration, as well as of radiance at TOA due to atmospheric effects, less complicated and more rapid.

The main program is a MATLAB R2018b script. The utilized data was generated by PlanarRad, as well as a Python 2.7.12 interface for running PlanarRad in batches, initially developed by Daniel Marrable. Neither PlanarRad nor the python interface are necessary for utilizing the program, which exists in five versions. Several of the versions require the SINMOD dataset to be available. The program generates, depending on the selected version, the resulting water leaving radiance or the resulting radiance at TOA. One version of the program regards the user specifying the chl<sub>a</sub> concentration values of interest. Another regards the user also specifying the viewing zenith or azimuth angle of interest. The third version regards the user specifying which geographical area and time frame from the SINMOD dataset should be utilized to obtain the chl<sub>a</sub> concentration values. The radiance at TOA due to atmospheric effects can be computed. The final version regards presenting and plotting water

leaving radiance resulting from different solar zenith and azimuth angles, as well as different viewing zenith and azimuth angles.

Regardless of which version is utilized the wavelengths are defined as 400 - 800 [nm]. The chl<sub>a</sub> concentration values must be in the range of 0.0 to 1.8 [mg chl<sub>a</sub> m<sup>-3</sup>].

## 3. RESULTS

The case study considers a hyperspectral imager with spectral range of 400 - 800 nm and spectral resolution of 5 nm [7].

The utilized SINMOD data consists of approximately one month of recorded data with a temporal resolution of 1 hour, produced from model domain covering the areas outside of Mid Norway, including Hitra, Frya, Froan and Frohavet in 160 m horizontal resolution. The surface layer thickness is 3 m on average, but varies with surface elevation. The variables included are temperature [°C], chlorophyll in the surface layer [mg chl<sub>a</sub> m<sup>-3</sup>], chlorophyll integrated over 0 - 50 meter per square metre [mg chl<sub>a</sub> m<sup>-2</sup>], and the concentration of diatoms [mmol N m<sup>-3</sup>] and flagellates [mmol N m<sup>-3</sup>] in the surface layer.

Viewing zenith angles are defined differently by PlanarRad, as presented in [15], and COART, as presented in [16].

COART was prescribed to calculate radiances [ $W\ m^{-2}\ \mu m^{-1}\ sr^{-1}$ ] at multiple wavelengths from 0.4 [ $\mu m$ ] to 0.8 [ $\mu m$ ]. The output, presented at TOA and at the ocean surface, represent only the radiances due to atmospheric effects.

The utilized solar zenith angle was 60°. The trace gas amounts of  $CO_2$  and  $CH_4$  values were set as recommended by COART. The MODTRAN maritime model was utilized as the mixed layer aerosol, while the stratospheric aerosol was set to utilize a background model. The aerosol loading was specified by the aerosol optical thickness at 0.5 [ $\mu m$ ] of 0.2. The depth was set to 0 meters, with a bottom albedo of 0. Modelling a black surface prevents the COART outputs to include values of reflected radiance from the ocean surface.

### 3.1. Solar azimuth angles

The sun zenith angle was 20°. The resulting water leaving radiance values were obtained from the viewing azimuth angle of 0° and the viewing zenith angle of 170°. The angles are defined as in PlanarRad.

The water leaving radiance resulting from solar azimuth angle of 120° and 180° are roughly the same. The same holds for the water leaving radiance resulting from solar azimuth angles of 60° and 0°. The water leaving radiance resulting from the solar azimuth angle of 180° is higher than the water leaving radiance resulting from the solar azimuth angle of 60°.

### 3.2. Solar zenith angles

PlanarRad utilized a solar azimuth angle of 0°. The resulting water leaving radiance at the ocean surface was retrieved with the viewing azimuth angle 0° and the viewing zenith angle 170°.

COART utilized the previously presented inputs. The viewing zenith angle was 20°, while the viewing azimuth angle was 0°. The results were, after calculating the reflected radiance from the surface to TOA, the radiance due to atmospheric effects [ $W\ m^{-2}\ \mu m^{-1}\ sr^{-1}$ ] at the ocean surface and at TOA.

There is a small difference, of approximately 1-1.5  $W\ m^{-2}\ \mu m^{-1}\ sr^{-1}$ , between the resulting radiance due to atmospheric effects at the ocean surface with regard to the solar zenith angles 20°,

$40^\circ$  and  $60^\circ$ . The radiance resulting from the solar zenith angle of  $80^\circ$  varies less with regard to wavelength, and is lower between the wavelengths 400 [nm] and 750 [nm].

The radiance at TOA resulting from the solar zenith angle of  $80^\circ$  differs from the radiance resulting from the other three solar zenith angles, by being lower for the wavelengths 400 - 700 [nm]. The radiance resulting from the solar zenith angle of  $80^\circ$  varies less with regard to wavelength than the resulting radiance from the other three solar zenith angles.

The resulting water leaving radiance at the ocean surface with regard to various solar zenith angles differ from each other between 460 nm and 600 nm. The resulting water leaving radiance due to various solar azimuth angles differ from each other for all wavelengths. It can be inferred that the resulting water leaving radiance varies more with regard to solar azimuth angle than with solar zenith angle.

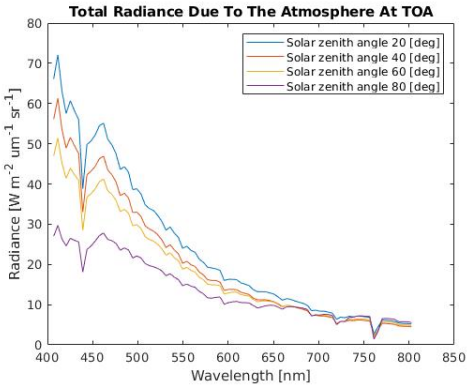


**Fig. 1.**

Radiance at TOA due to atmospheric effects, with regard to solar zenith angles.

### 3.3. Viewing azimuth angles

PlanarRad utilized the viewing zenith angle  $130^\circ$ , the solar azimuth angle  $0^\circ$  and the solar zenith angle  $40^\circ$ .

The test performed by COART was executed with the inputs as previously presented, and with the viewing zenith angle  $20^\circ$  and the viewing azimuth angle at every  $60^\circ$  from  $0^\circ$  to  $180^\circ$ .

The resulting radiance, both at the ocean surface and at TOA, due to atmospheric effects is roughly the same, regardless of viewing azimuth angle. The viewing azimuth angle resulting radiance does not vary as much as the viewing zenith angle resulting radiance.

The viewing azimuth angles of  $60^\circ$ ,  $120^\circ$  and  $180^\circ$  result in roughly the same water leaving radiance, while the viewing azimuth angle of  $0^\circ$  differs from these by resulting in a water leaving radiance that is higher with approximately  $0.055 \text{ sr}^{-1}$ . Of the viewing

azimuth angles of  $60^\circ$ ,  $120^\circ$  and  $180^\circ$ , the angle  $180^\circ$  results in the highest water leaving radiance, while the angle  $120^\circ$  results in the smallest. The difference is approximately  $2 * 10^{-6} [\text{sr}^{-1}]$ .

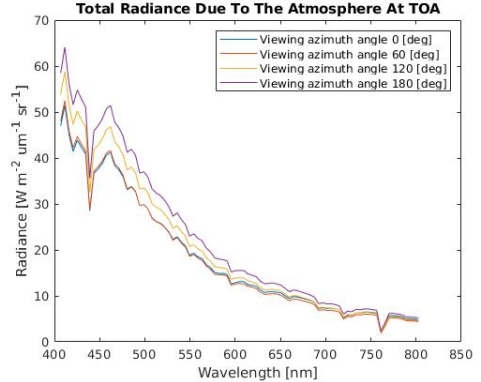


**Fig. 2.**

Radiance due to atmospheric effects at TOA, with regard to viewing azimuth angles.

### 3.4. Viewing zenith angles

PlanarRad utilized the viewing azimuth angle  $0^\circ$ , the solar azimuth angle  $0^\circ$  and the solar zenith angle  $40^\circ$ . The test performed by COART was executed with the azimuth and zenith radiance output angles of  $0^\circ$  and every  $30^\circ$  from  $0^\circ$  to  $90^\circ$ , respectively.

The radiance due to atmospheric effects at the ocean surface resulting from the viewing zenith angle of  $60^\circ$  is higher than the resulting radiances from the angles of  $30^\circ$  and  $0^\circ$ , with approximately  $0.011 \text{ W m}^{-2} \mu\text{m}^{-1} \text{ sr}^{-1}$ . Likewise, the resulting radiance due to atmospheric effects at TOA from the viewing zenith angle of  $60^\circ$  is higher than the resulting radiances from the viewing zenith angles of  $30^\circ$  and  $0^\circ$ , with approximately  $50 \text{ W m}^{-2} \mu\text{m}^{-1} \text{ sr}^{-1}$ .

The resulting water leaving radiance values at the ocean surface differ with regard to viewing zenith angles. The utilized angles are  $120^\circ$ ,  $150^\circ$  and  $170^\circ$ . The viewing zenith angle of  $170^\circ$  results in the lowest water leaving radiance, while the angle of  $150^\circ$  results in the highest. The resulting water leaving radiance varies roughly the same with regard to variation in the viewing zenith angle as with regard to variation in viewing azimuth angle.

### 3.5. Clouds

COART was utilized to perform a test regarding the presence of water clouds. The spherical water clouds were specified to be from 3 km to 4 km of the size  $10 \text{ RE} [\mu\text{m}]$  and  $200 \text{ liquid water path [g/m]}$ .

Figure 4 presents the impact of water clouds on the radiance at TOA due to atmospheric effects. The resulting radiance is higher

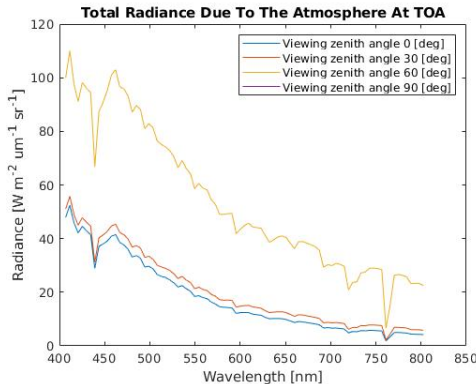


**Fig. 3.**

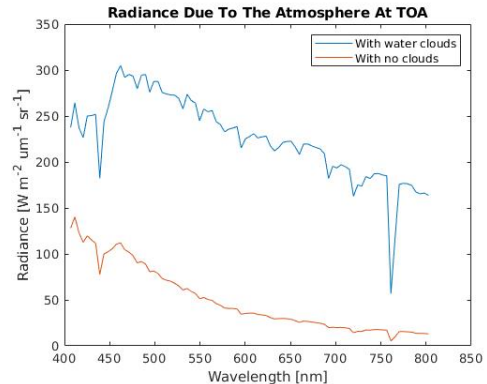


**Fig. 4.**

Radiance due to atmospheric effects at TOA,  
with regard to viewing zenith angles.

when water clouds are present than when no clouds are present, with approximately  $200 \text{ W m}^{-2} \mu\text{m}^{-1} \text{ sr}^{-1}$ .

### 3.6. The lookup tables

The resulting water leaving radiance is identical regardless of whether it is computed by PlanarRad or by the lookup table. This suggests the lookup table works as intended. Figure 5 presents several water leaving radiance values calculated by the lookup table together with several water leaving radiance values calculated by PlanarRad. The lookup table resulting water leaving radiance values fit perfectly and follow the same wavelength dependent variations as the resulting water leaving radiance values from PlanarRad.

### 3.7. Temporal sensitivity of data acquisition analysis

The temporal sensitivity analysis for the time period of one hour revealed that generally the water leaving radiance varies with 0 – 0.0025%, and with approximately 0.015% for certain data points. The temporal sensitivity analysis for the time period of five hours revealed that generally the water leaving radiance varies with 0 – 0.02%, and with approximately 0.06% for certain data points. The water leaving radiance variation over the period of ten hours varies from four to eight times more than the variation over the period of one hour. The longer the time period, the bigger the water leaving radiance variation.

## 4. FUTURE WORK

Suggested further work includes examining how different parameters in the water body, such as ocean state and depth, affect the water leaving radiance. Examining how the camera specifications affects the recorded radiance is also of interest.

Result 3. Radiance due to atmospheric effects at TOA,  
with regard to water clouds.

## 5. CONCLUSIONS

The simulation tool can be utilized for simulating how different geophysical variables translate to spectral radiance, and how the medium around it affects the values. It is also useful for simulating how the atmosphere affects the radiance values for various wavelengths, angles and weather. Improved trade-off studies in payload design would be possible by simulating the TOA radiometry reaching a detector.

The resulting radiance is higher when water clouds are present than when no clouds are present. The resulting water leaving radiance is almost identical regardless of whether it is computed by PlanarRad or by the lookup table. The temporal sensitivity analysis revealed that the longer the time period, the bigger the water leaving radiance variation.

The resulting radiance due to atmospheric effects with the solar zenith angle of  $80^\circ$  differs from other angles, both with regard to radiance at the surface and at TOA, by resulting in lower values. The solar zenith angles affect the water leaving radiance less than the solar azimuth angles do. The resulting radiance due to atmospheric effects are roughly the same regardless of viewing azimuth angle. The radiance due to atmospheric effects resulting from the viewing zenith angle of  $60^\circ$  is higher than for  $30^\circ$  and  $0^\circ$ , both at the ocean surface and at TOA. The resulting water leaving radiance values at the ocean surface differ significantly with regard to viewing zenith angles.

## 6. ACKNOWLEDGEMENTS

This work was supported by the Norwegian Research Council through the Centre of Autonomous Marine Operations and Systems (NTNU AMOS) (grant no. 223254), the MASSIVE project (grant

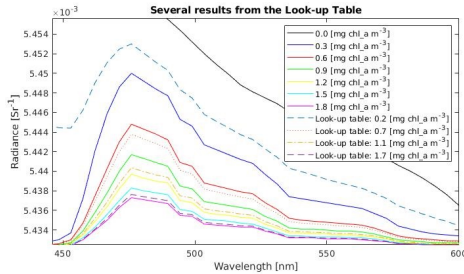


**Fig. 5.**

Result 4. Water leaving radiance calculated by the lookup table and PlanarRad.

no. 270959).

We are grateful to Ingrid Ellingsen and SINTEF Ocean for assisting with the SINMOD simulation data.

## 7. REFERENCES

- [1] Amir Ibrahim, Bryan Franz, Ziauddin Ahmad, Richard Healy, Kirk Knobelspiesse, Bo-Cai Gao, Chris Proctor, and Peng-Wang Zhai. Atmospheric correction for hyperspectral ocean color retrieval with application to the hyperspectral imager for the coastal ocean (hico). *Remote Sensing of Environment*, 204:60–75, 2018.
- [2] Joseph D Ortiz, Dulci M Avouris, Stephen J Schiller, Jeffrey C Luval, John D Lekki, Roger P Tokars, Robert C Anderson, Robert Shuchman, Michael Sayers, and Richard Becker. Evaluating visible derivative spectroscopy by varimax-rotated, principal component analysis of aerial hyperspectral images from the western basin of lake erie. *Journal of Great Lakes Research*, 2019.
- [3] M Guelman and F Ortenberg. Small satellite's role in future hyperspectral earth observation missions. *Acta Astronautica*, 64(11):1252–1263, 2009.
- [4] Darryl J. Keith, Blake A. Schaeffer, Ross S. Lunetta, Richard W. Gould Jr., Kenneth Rocha, and Donald J. Cobb. Remote sensing of selected water-quality indicators with the hyperspectral imager for the coastal ocean (hico) sensor. *International Journal of Remote Sensing*, 35(9):2927–2962, 2014.
- [5] M. Soukup, J. Gailas, D. Fantin, A. Jochemsen, C. Aas, P. J. Baecck, L. Benhadj, S. Lives, B. Delauré, M. Menenti, B. G. H. Gorte, S. E. Aria Hosseini, M. Esposito, and C. N. van Dijk. Hyperscout: Onboard processing of hyperspectral imaging data on a nanosatellite. In *Small Satellites, System and Services Symposium (4S), Valletta, Malta*, 2016.
- [6] Curtis Mobley. Ocean optics web book.
- [7] F. Sigernes. Basic hyperspectral imaging. *TTK20 Hyperspectral remote sensing - lecture notes*, Norwegian University of Science and Technology, Trondheim.
- [8] Dag Slagstad and Thomas A. McClamans. Modeling the ecosystem dynamics of the Barents Sea including the marginal ice zone: I. Physical and chemical oceanography. *Journal of Marine Systems*, 58(1-2):1–18, October 2005.
- [9] Paul Wassmann, Dag Slagstad, Christian Wexels Riser, and Marit Reigstad. Modelling the ecosystem dynamics of the Barents Sea including the marginal ice zone: II. Carbon flux and interannual variability. *Journal of Marine Systems*, 59(1-2):1–24, January 2006.
- [10] Dick P Dee, SM Uppala, AJ Simmons, Paul Berrisford, P Poli, S Kobayashi, U Andrae, MA Balmaseda, G Balsamo, d P Bauer, et al. The era-interim reanalysis: Configuration and performance of the data assimilation system. *Quarterly Journal of the royal meteorological society*, 137(656):553–597, 2011.
- [11] Gary Egbert and Lana Erofeeva. The osu topex/poseidon global inverse solution tpxo.
- [12] Jon Hedley. A three-dimensional radiative transfer model for shallow water environments. *Optics Express* 16.
- [13] John Hedley. Planarrad result sheet for hydrolight comparison.
- [14] Zhonghai Jin. A note on coart and its input.
- [15] John Hedley. Brdf of a material with isotropic phase function.
- [16] Zhonghai Jin. View geometry web.

# Bibliography

Takafumi Hirata. Marine phytoplankton ecology using satellite and in situ observation and model. URL <https://en.wikipedia.org/wiki/Azimuth>.

F. Sigernes, M. E. Grøtte, J. Veisdal, E. H-LIVERMORE, J. Fortuna, E. F. Prentice, M. Syrjasuo, K. Rajan, and T. A. Johansen. Pushbroom hyper spectral imager version 6 (hsi v6) part list – final prototype. 2018.

Curtis Mobley. Ocean optics web book. URL <http://www.oceanopticsbook.info/>.

F. Sigernes. Basic hyperspectral imaging. *TTK20 Hyperspectral remote sensing - detailed lecture notes*, 2018.

National Snow and Ice Data Center. Polar stereographic projection and grid. URL [https://nsidc.org/data/polar-stereo/ps\\_grids.html](https://nsidc.org/data/polar-stereo/ps_grids.html).

John Hedley. Brdf of a material with isotropic phase function, a. URL [http://www.planarrad.com/index.php?title=BRDF\\_of\\_a\\_material\\_with\\_isotropic\\_phase\\_function](http://www.planarrad.com/index.php?title=BRDF_of_a_material_with_isotropic_phase_function).

Zhonghai Jin. A note on coart and its input, a. URL <https://clouds.larc.nasa.gov/jin/rtnote.html>.

National Research Council. Assessing the requirements for sustained ocean color research and operations. *Washington, DC: The National Academies Press*.

Evelyn Honoré-Livermore. Kick-off.

Monica Lapadatu. Simulation of hyperspectral imaging of algal blooms from satellites, 2018. URL <http://folk.ntnu.no/moniclap/TTK4550/>.

Warren J. Smith. *Modern Optical Engineering - The Design of Optical Systems. 3rd Edition*. McGraw-Hill, 2000.

Chein-I Chang. *Hyperspectral Imaging: Techniques for Spectral Detection and Classification*. Springer Science Business Media, ISBN 978-0-306-47483-5, 2003.

John Hedley. Planarrad, b. URL <http://www.planarrad.com/index.php?title=PlanarRad>.

Morten Omholt Alver. Private communication by email, 2018.

Tor Arne Johansen. Smallsat-related projects, autumn 2018.

Amir Ibrahim, Bryan Franz, Ziauddin Ahmad, Richard Healy, Kirk Knobelspiesse, Bo-Cai Gao, Chris Proctor, and Peng-Wang Zhai. Atmospheric correction for hyperspectral ocean color retrieval with application to the hyperspectral imager for the coastal ocean (hico). *Remote Sensing of Environment*, 204:60–75, 2018.

Joseph D Ortiz, Dulci M Avouris, Stephen J Schiller, Jeffrey C Luvall, John D Lekki, Roger P Tokars, Robert C Anderson, Robert Shuchman, Michael Sayers, and Richard Becker. Evaluating visible derivative spectroscopy by varimax-rotated, principal component analysis of aerial hyperspectral images from the western basin of lake erie. *Journal of Great Lakes Research*, 2019.

M Guelman and F Ortenberg. Small satellite's role in future hyperspectral earth observation missions. *Acta Astronautica*, 64(11):1252–1263, 2009.

Darryl J. Keith, Blake A. Schaeffer, Ross S. Lunetta, Richard W. Gould Jr., Kenneth Rocha, and Donald J. Cobb. Remote sensing of selected water-quality indicators with the hyperspectral imager for the coastal ocean (hico) sensor. *International Journal of Remote Sensing*, 35(9):2927–2962, 2014. doi: 10.1080/01431161.2014.894663. URL <https://doi.org/10.1080/01431161.2014.894663>.

M. Soukup, J. Gailas, D. Fantin, A. Jochemsen, C. Aas, P. J. Baeck, L. Benhadj, S. Livens, B. Delauré, M. Menenti, B. G. H. Gorte, S. E. Aria Hosseini, M. Esposito, and C. N. van Dijk. Hyperscout: Onboard processing of hyperspectral imaging data on a nanosatellite. In *Small Satellites, System and Services Symposium (4S), Valletta, Malta*, 2016.

Gunhild Berget and Trygve Fossum. Coordinated hyperspectral imaging from small satellite, drone and surface vehicles.

Mariusz E. Grøtte. Scientific feedback presentation.

Gene C. Feldman. Nasa seadas. URL <https://seadas.gsfc.nasa.gov/>.

ESA. Snap, a. URL <https://step.esa.int/main/toolboxes/snap/>.

ESA. Ocean virtual laboratory, b. URL <https://ovl-project.oceandatalab.com/overview>.

John Hedley. Private communication by email, 2018.

John M. Wallace and Peter V. Hobbs. *Atmospheric Science An Introductory Survey*. 2 edition, 2006.

- N. A. Scott and A. Chedin. A fast line-by-line method for atmospheric absorption computations: The automatized atmospheric absorption atlas. *J. Appl. Meteorol.*, 20:802–812, 1981.
- S. Y. Kotchenova, E. F. Vermote, R. Matarrese, and F. J. Klemm. Validation of a vector version of the 6s radiative transfer code for atmospheric correction of satellite data. part i: Path radiance. *Applied Optics*, 45:6762–6774, 2006.
- P. Eriksson, S. A. Buehler, C.P. Davis, C. Emde, and O. Lemke. Arts, the atmospheric radiative transfer simulator, version 2. *Journal of Quantitative Spectroscopy and Radiative Transfer*, 112:1551 – 1558, 2011.
- I. M. Chapman, D. A. Naylor, B. G. Gom, R. R. Querel, and P. Davis-Imhof. Btram: An interactive atmospheric radiative transfer model. *The 30th Canadian Symposium on Remote Sensing*, 30:22–25, 2009.
- Z. Jin, T. P. Charlock, K. Rutledge, K. Stamnes, and Y. Wang. An analytical solution of radiative transfer in the coupled atmosphere-ocean system with rough surface. *Applied Optics*, 45:7443–7455, 2006a.
- Charlie Zender. Welcome to the crm homepage. URL <http://dust.ess.uci.edu/crm/index.shtml>.
- Paul van Delst. Community radiative transfer model (crtm). URL <https://www.ssec.wisc.edu/~paulv/Fortran90/CRTM/Developmental/>.
- J. P. Gastellu-Etchegorry, V. Demarez, V. Pinel, and F. Zagolski. Modelling radiative transfer in heterogeneous 3-d vegetation canopies. *Remote Sensing of Environment*, 58: 131–156, 1996.
- Knut Stamnes, S. C. Tsay, W. Wiscombe, and Kolf Jayaweera. Numerically stable algorithm for discrete-ordinate-method radiative transfer in multiple scattering and emitting layered media. *Applied Optics*, 27:2502–2509, 1988.
- Y. Xie, M. Sengupta, and J. Dudhia. A fast all-sky radiation model for solar applications (farms): Algorithm and performance evaluation. *Solar Energy*, 135:435–445, 2016.
- Q. Fu and K.-N Liou. Parameterization of the radiative properties of cirrus clouds. *Journal of the Atmospheric Sciences*, 50:2008–2025, 1993.
- F. J. Martin-Torres and A. Kutepov, A. Dudhia, O. Gusev, and A.G. Feofilov. Accurate and fast computation of the radiative transfer absorption rates for the infrared bands in the atmosphere of titan. *Geophysical Research Abstracts*, 7735, 2003.
- D. P. Edwards. *GENLN2: A general line-by-line atmospheric transmittance and radiance model, Version 3.0 description and users guide*. National Center for Atmospheric Research, Boulder, Co, NCAR/TN-367-STR, 1992.
- Bernhard Mayer, Arve Kylling, Claudia Emde, Robert Buras, Ulrich Hamann, Josef Gasteiger, and Bettina Richter. *libRadtran user's guide*. 2017.

A. Berk, L. S. Bernstein, G. P. Anderson, P. K. Acharya, D. C. Robertson, J. H. Chetwynd, and S. M. Adler-Golden. Modtran cloud and multiple scattering upgrades with application to aviris. *Remote Sensing of Environment*, 65:367–375, 1998.

Rune Storvold. Private communication by email, 2018a.

Yunfeng Lv, Zhongqiu Sun, and Yunsheng Zhao. Measurement of water-leaving radiance on smooth water surfaces at different viewing angles using high-resolution spectroradiometer. *Chinese Optics Letters*, 10:62801, 2012.

Menghua Wang. Effects of ocean surface reflectance variation with solar elevation on normalized water-leaving radiance. *Applied Optics*, 45:4122–4128, 2006.

NASA. Multi-angle imaging spectroradiometer, a. URL <https://misr.jpl.nasa.gov/Mission/>.

Menghua Wang. Ioccg lecture series 2014-atmospheric correction. URL [http://www.ioccg.org/training/SLS-2014/Wang\\_Section5\\_atm\\_corr\\_Case1\\_2014.pdf](http://www.ioccg.org/training/SLS-2014/Wang_Section5_atm_corr_Case1_2014.pdf).

Howard R. Gordon and Kenneth J. Voss. Modis normalized water-leaving radiance algorithm theoretical basis document. URL [https://modis.gsfc.nasa.gov/data/atbd/atbd\\_mod18.pdf](https://modis.gsfc.nasa.gov/data/atbd/atbd_mod18.pdf).

Jian Li, Liqiao Tian, Qingjun Song, Zhaoxia Sun, Hongjing Yu, and Qianguo Xing. Temporal variation of chlorophyll-a concentrations in highly dynamic waters from unattended sensors and remote sensing observations. URL <https://www.ncbi.nlm.nih.gov/pmc/articles/PMC6111722/>.

Yosef Z. Yacobi. Temporal and vertical variation of chlorophyll a concentration, phytoplankton photosynthetic activity and light attenuation in lake kinneret: possibilities and limitations for simulation by remote sensing. *Journal of Plankton Research*, 28: 725–736, 2006. doi: <https://doi.org/10.1093/plankt/fbl004>.

Hongqing Wang, C. M. Hladik, Wenrui Huang, K. Milla, L. Edmiston, M. A. Harwell, and J. F. Schalles. Detecting the spatial and temporal variability of chlorophyll-a concentration and total suspended solids in apalachicola bay, florida using modis imagery. *International Journal of Remote Sensing*, 31:439–453, 2010.

McGraw-Hill. *Encyclopedia of Science and Technology* (5th ed.). 1993.

CIE. *International Lighting Vocabulary. Number 17.4. CIE, 4th edition.* ISBN 978-3-900734-07-7, 1987.

Leslie D. Stroebel and Richard D. Zakia. *Focal Encyclopedia of Photography* (3rd ed.). Focal Press, p. 115. ISBN 0-240-51417-3, 1993.

James M. Palmer. *The SI system and SI units for Radiometry and photometry*. Archived from the original (PDF), 2012.

ISO. *Thermal insulation — Heat transfer by radiation — Physical quantities and definitions*. ISO 9288:1989. ISO catalogue. Retrieved 2015-03-15., 1989.

Inc. Sequoia Scientific. Hydrolight. URL <https://www.sequoiasci.com/product/hydrolight/>.

IOCCG, Platt T., Hoepffner N., Stuart V., and Brown C. (eds.). Why ocean colour? the societal benefits of ocean-colour technology. *Reports of the International Ocean-Colour Coordinating Group*, (No. 7), 2008.

Geir Johnsen, Zsolt Volent, Egil Sakshaug, Fred Sigernes, and Lasse H. Pettersson. *Remote sensing in the Barents Sea*. Tapir Academic Press, Trondheim. 630 pp. ISBN 978-82-519-2461-0, 2009.

T.J. Petzold. Volume scattering functions for selected ocean waters. *Scripts Inst. Oceanogr. Report*, pages 72–78, 1972.

Seelye Martin. *An Introduction to Ocean Remote Sensing (second edition)*. Cambridge University Press, ISBN 978 1 107 01938 6, 2014.

Rune Storvold. *Atmospheric effects*. 2018b.

A.F.H. Goetz. Three decades of hyperspectral remote sensing of the earth: A personal view. *Remote Sensing of Environment*, pages 5–16, 2009.

Dag Slagstad and Thomas A. McClanahan. Modeling the ecosystem dynamics of the Barents Sea including the marginal ice zone: I. Physical and chemical oceanography. *Journal of Marine Systems*, 58(1-2):1–18, October 2005. URL <http://www.sciencedirect.com/science/article/B6VF5-4H98T19-1/2/e4b73b9ffefe92c45c7b28e227ffcde1>.

Paul Wassmann, Dag Slagstad, Christian Wexel Riser, and Marit Reigstad. Modelling the ecosystem dynamics of the Barents Sea including the marginal ice zone: II. Carbon flux and interannual variability. *Journal of Marine Systems*, 59(1-2):1–24, January 2006. ISSN 0924-7963. URL <http://www.sciencedirect.com/science/article/B6VF5-4J140YJ-1/2/14301cbdd82f300a5035491d9e072b35>.

Dick P Dee, SM Uppala, AJ Simmons, Paul Berrisford, P Poli, S Kobayashi, U Andrae, MA Balmaseda, G Balsamo, d P Bauer, et al. The era-interim reanalysis: Configuration and performance of the data assimilation system. *Quarterly Journal of the royal meteorological society*, 137(656):553–597, 2011.

Gary Egbert and Lana Erofeeva. The osu topex/poseidon global inverse solution tpxo. URL <http://volkov.oce.orst.edu/tides/global.html>.

Bill Casselman. Stereographic projection. URL <http://www.ams.org/publicoutreach/feature-column/fc-2014-02>.

UCAR. Network common data form (netcdf), a. URL <https://www.unidata.ucar.edu/software/netcdf/>.

UCAR. An introduction to netcdf, b. URL [https://www.unidata.ucar.edu/software/netcdf/docs/netcdf\\_introduction.html](https://www.unidata.ucar.edu/software/netcdf/docs/netcdf_introduction.html).

MathWorks. Read data from variable in netcdf data, a. URL <https://se.mathworks.com/help/matlab/ref/ncread.html>.

MathWorks. Import netcdf files and opendap data, b. URL [https://se.mathworks.com/help/matlab/import\\_export/importing-network-common-data-form-netcdf-files-and-opendap-data.html](https://se.mathworks.com/help/matlab/import_export/importing-network-common-data-form-netcdf-files-and-opendap-data.html).

Dr. Robert B. Schmunk. Panoply netcdf, hdf and grib data viewer. URL <https://www.giss.nasa.gov/tools/panoply/>.

John Hedley. A three-dimensional radiative transfer model for shallow water environments. *Optics Express* 16, pages 21887–21902, 2008.

John Hedley. Planarrad result sheet for hydrolight comparison, c. URL [http://www.planarrad.com/images/f/f2/Pr\\_hl\\_report.pdf](http://www.planarrad.com/images/f/f2/Pr_hl_report.pdf).

Zhonghai Jin. Coupled ocean and atmosphere radiative transfer (coart), b. URL <https://clouds.larc.nasa.gov/jin/coart.html>.

R. R. Bidigare, M. E. Ondrusek, J. H. Morrow, and D. A. Kiefer. In vivo absorption properties of algal pigments. *Ocean Optics X, Proc.*, SPIE 1302:290–302, 1990.

H. Buiteveld, J. M. H. Hakvoort, and M. Donze. The optical properties of pure water. URL <https://omlc.org/spectra/water/data/buiteveld94.txt>.

Bohren and Huffman. Mie. URL <http://scatterlib.wikidot.com/mie>.

UCL. Diatoms. URL <https://www.ucl.ac.uk/GeolSci/micropal/diatom.html>.

Barry S. C. Leadbeater and John C. Green. *Flagellates: Unity, Diversity and Evolution*. Taylor and Francis Limited, 2000.

Eyvind Aas. The refractive index of phytoplankton. *INSTITUTE REPORT SERIES*, 1981.

Xiaodong Zhang, Lianbo Hu, and Ming-Xia He. Scattering by pure seawater: Effect of salinity. *Optics Express*, 17(7):5698–5710, 2009.

Arnold L. Gordon. Ocean stratification. URL [https://eesc.columbia.edu/courses/ees/climate/lectures/o\\_strat.html](https://eesc.columbia.edu/courses/ees/climate/lectures/o_strat.html).

Daniel Marrable. Github: planarradpy, a. URL <https://github.com/marrabld/planarradpy>.

Daniel Marrable. Private communication by email, 2019.

James E. Smith and Ravi Nair. *Virtual Machines: Versatile Platforms For Systems And Processes (The Morgan Kaufmann Series in Computer Architecture and Design)*. ISBN 1-55860-910-5, 2005.

John Hedley. Installation from source on linux, d. URL [http://www.planarrad.com/index.php?title=Installation\\_from\\_source\\_on\\_Linux](http://www.planarrad.com/index.php?title=Installation_from_source_on_Linux).

John Hedley. Planarrad, e. URL [http://www.planarrad.com/index.php?title=Previous\\_versions](http://www.planarrad.com/index.php?title=Previous_versions).

Daniel Marrable. Welcome to planarradpy's documentation!, b. URL <https://marrabld.github.io/planarradpy/>.

Z. Jin, T.P. Charlock, K. Rutledge, K. Stammes, and Y. Wang. Analytical solution of radiative transfer in the coupled atmosphere-ocean system with a rough surface. *Applied Optics*, 45:7443–7455, 2006b.

MATLAB. 1-d data interpolation (table lookup). URL <https://se.mathworks.com/help/matlab/ref/interp1.html>.

MathWorks. .mat file extension, c. URL <https://www.reviversoft.com/file-extensions/mat>.

Jasmine Nahorniak. Hico hyperspectral imager for the coastal ocean. URL <http://hico.coas.oregonstate.edu/>.

Kirt Blattenberger. Atmospheric absorption (specific attenuation), a. URL <http://www.rfcafe.com/references/electrical/atm-absorption.htm>.

Kirt Blattenberger. Free space path loss - friis equation, b. URL <http://www.rfcafe.com/references/electrical/path-loss.htm>.

J. Gower, S. King, G. Borstad, and L. Brown. Detection of intense plankton blooms using the 709 nm band of the meris imaging spectrometer. *International Journal of Remote Sensing*, 26(9):2005–2012, 2005.

Cecie Starr. *Biology: Concepts and Applications*. Thomson Brooks/Cole, ISBN 978-0-534-46226-0, 2005.

NASA. What are clouds made of? are they more likely to form in polluted air or in pristine air?, b. URL <https://pmm.nasa.gov/education/content/what-are-clouds-made-are-they-more-likely-form-polluted-air-or-pristine-air>.

Jim Gower and Stephanie King. *Remote Sensing of the African Seas*. Springer Science+Business Media Dordrecht, DOI 10.1007/978-94-017-8008-7\_2, 2014.

Dr. Mathias Disney. Principles and practice of remote sensing. URL <https://slideplayer.com/slide/2448300/>.

Vincent Couturier-Doux. Whispers 2019. URL <http://www.ieee-whispers.com/conference-info/>.

